TECHNISCHE UNIVERSITÄT MÜNCHEN

Department of Chemistry and Catalysis Research Center
Chair of Technical Electrochemistry

Operando Characterization of Fundamental Reaction Mechanisms and Degradation Processes in Lithium-Ion and Lithium-Oxygen Batteries

Johannes Wandt

Vollständiger Abdruck der von der Fakultät für Chemie der Technischen Universität München zur Erlangung des akademischen Grades eines

Doktors der Naturwissenschaften (Dr. rer. nat.)

genehmigten Dissertation.

Vorsitzender:	Prof. Dr. Klaus Köhler
Prüfer der Dissertation:	1. Prof. Hubert A. Gasteiger (Ph.D.)
	2. Prof. Dr. Tom Nilges
	3. Prof. Dr. Rüdiger-A. Eichel

Diese Dissertation wurde am 08.07.2017 bei der Technischen Universität München eingereicht und durch die Fakultät für Chemie am 10.07.2017 angenommen.

Abstract

The investigation of fundamental mechanisms and especially aging processes in lithium-ion and lithium-oxygen batteries is the overarching topic of this PhD thesis. For a comprehensive understanding of the battery aging processes it is necessary to connect the macroscopic observation ("capacity fading") with the underlying microscopic changes. The main goal of this thesis is the development of novel spectro-electrochemical techniques for the time resolved observation of processes occurring during battery charge and discharge. A major advantage of this so-called *operando* analysis is the capability of detecting thermodynamically unstable reaction intermediates which is not possible with classical *ex situ* analysis. In the first part of this thesis, a novel battery cell design for *operando* electron paramagnetic resonance spectroscopy (EPR) is developed and benchmarked. *Operando* EPR spectroscopy is then used for the detection of lithium dendrites on lithium metal anodes and lithium metal plating on graphite anodes. Furthermore, it is shown that singlet oxygen is evolved during the charging process in aprotic lithium-oxygen batteries. In the second part of this thesis, transition metal dissolution from layered metal oxide cathode materials and its subsequent deposition on the graphite anode is studied by *operando* x-ray absorption (XAS) spectroscopy. In the final part of this thesis, the aging processes of commercially produced 18650 type graphite/LFP cells are investigated by *in situ* neutron diffraction in combination with a detailed electrochemical analysis.

Kurzfassung

Das grundlegende Thema dieser Doktorarbeit ist die Untersuchung der Reaktionsmechanismen und insbesondere der Alterungsprozesse in Lithium-Ionen und Lithium-Sauerstoff Batterien. Für ein tiefgreifendes Verständnis der Batteriealterung ist es notwendig die makroskopischen Beobachtungen ("abnehmende Kapazität") mit den zugrunde liegenden mikroskopischen Veränderungen zu verknüpfen. Das Ziel dieser Arbeit ist die Entwicklung neuartiger spektroelektrochemischer Methoden, um die ablaufenden Prozesse zeitaufgelöst direkt während des Zyklierens zu untersuchen. So lassen sich im Gegensatz zur klassischen *ex situ* Analytik zum Beispiel auch thermodynamisch instabile Zwischenprodukte erfassen. Im ersten Abschnitt wird eine elektrochemische Batteriezelle für *operando* Elektronenspinresonanz (ESR) Spektroskopie entwickelt. Diese wird dann eingesetzt um die Entstehung von Lithium Dendriten auf Lithiummetall Anode und das Abscheiden von metallischem Lithium auf Graphit Anoden zu untersuchen. Des Weiteren wird mittels *operando* ESR Spektroskopie gezeigt, dass Singulett Sauerstoff beim Ladevorgang in aprotischen Lithium-Sauerstoffbatterien auftritt. Im zweiten Abschnitt wird zeit- und ortsaufgelöste Röntgenabsorptionsspektroskopie (XAS) eingesetzt um die Metallauflösung von Kathodenmaterialen zu untersuchen. Im dritten Abschnitt werden Alterungsprozesse in kommerziell produzierten Lithium-Ionen Batterien mittels *in situ* Neutronendiffraktionsmessungen in Kombination mit einer detaillierten elektrochemischen Charakterisierung untersucht.

Contents

List of Acronyms

Abbreviation	Description
BEV	Battery electric vehicle
CE	Coulombic efficiency
DEMS	Differential electrochemical mass spectroscopy
DMC	Dimethyl carbonate
EC	Ethylene carbonate
EMC	Ethyl methyl carbonate
EPR	Electron paramagnetic resonance
ESR	Electron spin resonance
EXAFS	Extended x-ray absorption fine structure
FEC	Fluoroethylene carbonate
FEP	Fluorinated ethylene propylene
LEDC	Lithium ethylene dicarbonate
LCO	Lithium cobalt oxide
LFP	Lithium iron phosphate
LMO	Lithium manganese oxide
LTO	Lithium titanate
NCA	Lithium nickel cobalt aluminum oxide
NMC	Lithium nickel manganese cobalt oxide
NMR	Nuclear magnetic resonance
OEMS	On-line electrochemical mass spectrometry
PES	Prop-1-ene-1,3-sultone
PTFE	Polytetrafluoroetyhlene
SEI	Solid electrolyte interphase
TEMP	2,2,6,6-Tetramethylpiperidine
TEMPO	(2,2,6,6-Tetramethylpiperidin-1-yl)oxyl
TTF	Tetrathiafulvalene
VC	Vinylene carbonate
XANES	X-ray absorption near-edge structure
XAS	X-ray absorption spectroscopy
XRD	X-ray diffraction

1 Introduction

The year 2016 marked the 25th anniversary of the introduction of the lithium-ion battery technology by Sony in 1991.[1] Sony's commercialization of the lithium-ion battery did not come out of the blue, but followed 15 years of research in related battery systems. As early as 1976, Stanley Whittingham proposed a secondary battery consisting of a lithium metal anode and a titanium disulfide intercalation cathode.[2;3] Lithium containing transition metal oxides like $LiCoO_2$ and $LiMn_2O_4$, which would later be used in the first lithium-ion batteries as intercalation cathode materials, were already described in the early 1980s by John B. Goodenough and Michael Thackeray.[4;5] Throughout the 1980s, intensive research was directed towards the development of a reversible lithium metal anode by companies like Exxon and Moli Energy, but safety and cycle life remained an unsolved challenge.[6] Still, this work contributed important material and processing knowledge for the field of lithium based secondary batteries.[7] In Sony's first lithium-ion battery, the inherently unsafe lithium metal anode was replaced by a carbonaceous soft carbon intercalation anode;[1] this was enabled by pioneering work on the carbon/electrolyte interaction by Jeff Dahn and co-workers published in 1990.[8] At first, the lithium-ion battery was targeted at the rapidly evolving consumer electronics market and especially the "3 C's" of computations, communications and cameras.[7] With an energy density of about 200 Wh L^{-1} and 80 Wh kg^{-1}, Sony's first lithium-ion battery already outperformed the state of the art nickel metal hydride battery.[1;7] Since then, lithium-ion technology has rapidly evolved, with specific energy more than doubling and costs declining by a factor of about ten,[9] opening up new markets like electro-mobility and grid storage/stabilization.[10;11]

The year 2016 marked not only the 25th anniversary of the lithium-ion battery. It was also the first year in which atmospheric carbon dioxide concentration passed the 400 ppm threshold, which compares to 280 ppm in the mid-18th century and peak concentrations of less than 300 ppm in the past 400.000 years.[12;13] For the containment of carbon dioxide driven anthropogenic global warming, the electrification of the transport sector and the replacement of fossil fuels in the energy sector are of central importance, as these two sectors contribute 23% and 42% to total carbon dioxide

emissions (numbers for 2015).[14] In order to be competitive in these fields, a further significant improvement of overall battery performance will be necessary within the next few years. For the successful mass market penetration of battery electric vehicles, a driving range of 300 miles is considered necessary to overcome the "range anxiety" of potential customers.[15] According to an estimation by BMW, a 300 miles driving range requires an increase of the specific energy by a factor of 2.5 in comparison to the 120 Wh kg^{-1} (cell level) of the current BMW i3.[10] Another major challenge for battery electric vehicles is the comparably high prize of battery packs in comparison to internal combustion engines. At the current prize of about 250 \$ kWh^{-1}, a battery pack providing a 300 mile driving range would cost over 20.000 \$ which is not acceptable for a compact car.[15] A recent systematic review by Nykvist and Nilsson revealed that battery costs have rapidly fallen by approximately 14% annually between 2007 and 2014 and will continue to do so.[16] But even if the goal of the US Department of Energy of 125 \$ kWh^{-1} can be reached, a 300 mile battery pack would still amount to about 10.000 \$.[15] The requirements for the driving range might be eased if reasonably fast charging times could be achieved. In this respect, the power capability of the battery cell is a key parameter. A high specific power, expressed in W kg^{-1}, is important both for fast energy uptake during fast charging or regenerative breaking and for fast energy release during car acceleration. For quantification of the rate capability of a battery, the so-called C-rate is a useful measure. The C-rate correlates the applied current (in A) to the nominal battery capacity (in Ah), e.g. at a 1C rate the battery is fully charged (or discharged) in one hour and at a 0.2C rate in five hours, respectively. State of the art lithium-ion batteries have a very good rate capability for the discharge process, e.g. the BMW i3 battery pack can be completely discharged within 12 minutes (= 5C) without a significant capacity loss.[10] In contrast, the rate capability for the charging process is much worse and charging rates above 1C severely limit the battery cycle life of state of the art lithium-ion batteries.[17] New battery materials will be necessary for improvements of the specific energy and power, while simultaneously reducing battery costs. This has to be achieved without compromising the life time of the battery and especially the safety. Recent incidents of self-igniting lithium-ion batteries on the Boeing 787 Dreamliner and the Samsung Galaxy Note 7 have emphasized the paramount importance of battery safety.[18]

1.1 Working Principle of a Lithium-Ion Battery

The main components of a lithium-ion battery are the active materials in the negative and positive electrode and the liquid electrolyte. According to common convention in the field of lithium-ion batteries, the negative electrode is called anode and the positive electrode is called cathode throughout this work, following the nomenclature of the discharge reaction. A typical lithium-ion battery contains graphite as anode active material which can reversibly intercalate lithium ions during battery charge and de-intercalate lithium ions during discharge ($Li^+ + e^- + C_6 \underset{\text{discharge}}{\overset{\text{charge}}{\rightleftharpoons}} LiC_6$). On the cathode side, a transition metal oxide like $LiCoO_2$ is used from which lithium ions are extracted during charge and inserted during discharge ($LiCoO_2 \underset{\text{discharge}}{\overset{\text{charge}}{\rightleftharpoons}} Li_{1-x}CoO_2 + x\,Li^+ + x\,e^-$). The cell reaction for such a lithium-ion battery is simply the sum of the half cell reactions ($LiCoO_2 + x\,C_6 \underset{\text{discharge}}{\overset{\text{charge}}{\rightleftharpoons}} Li_{1-x}CoO_2 + x\,LiC_6$). This kind of cell chemistry is called intercalation chemistry because the active materials, also referred to as hosts, retain their general structure during lithium intercalation and

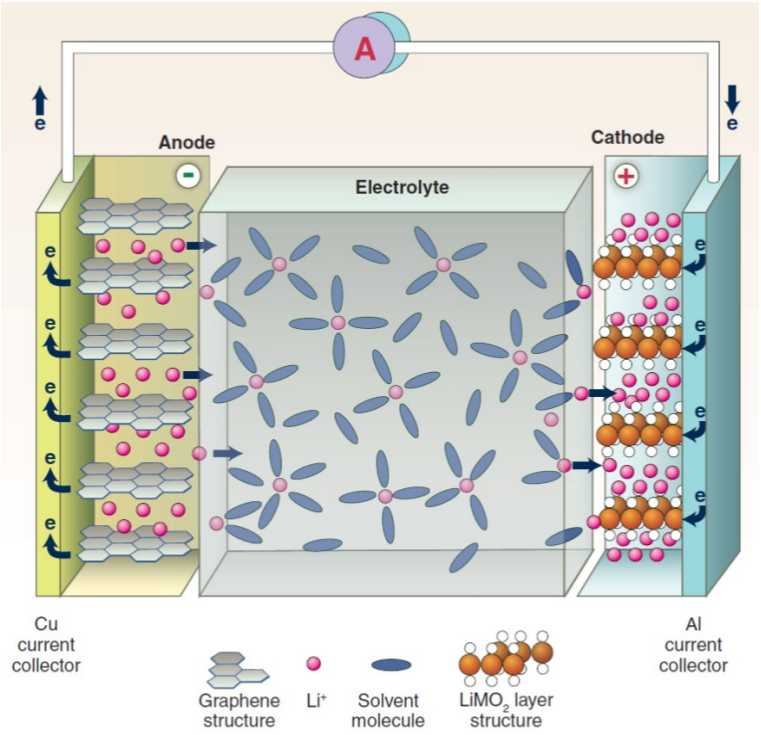

Figure 1.1 Working principle and main components of a lithium-ion battery. Image from reference [11]. Reprinted with permission from AAAS.

deintercalation.[1] It is also the host material which is getting oxidized or reduced during battery operation (e.g. $Co^{3+} \rightleftharpoons Co^{4+}$) while lithium ions shuttle between the electrodes, hence the alternative name "rocking chair battery" for a lithium-ion battery. The ionic conductivity between the electrodes is provided by an aprotic electrolyte containing a lithium salt while a porous polyolefine separator prevents short circuiting.[20] In this section, the most important aspects regarding the basic cell components (anode/cathode active materials and electrolyte) are briefly reviewed.

Graphite is the standard anode active material because it offers a high specific capacity of 372 mAh g^{-1} and a low and flat working potential of 100 to 200 mV vs. Li/Li^+. The characteristic potential profile of graphite can be assigned to the well known staging behavior.[21] In $Li_{0.5}C_6$ (stage II) two graphene sheets separate each lithium layer whereas in $Li_{1.0}C_6$ (stage I) the graphene and lithium layers alternate.[22] For lower intercalation degrees ($x < 0.5$ in Li_xC_6), the mechanism of lithium intercalation is still controversial.[23] The magnetic and electronic properties of the graphite intercalation compounds change drastically upon lithium intercalation, for example the c-axis conductivity (perpendicular to graphene layers) is three orders of magnitude higher in LiC_6 in comparison to pristine graphite.[22;24;25;26] The potential of the lithium intercalation into graphite is well below the thermodynamic stability limit of all aprotic electrolyte solvents. Therefore, stable cycling of a graphite electrode is only possible because of the so-called solid electrolyte interphase (SEI), a concept first introduced by Emanuel Peled in 1979.[27] The SEI is a several nano meter thick passivation layer which forms in the very first charge and consists of inorganic and organic electrolyte reduction products like lithium fluoride, lithium carbonate and lithium ethylene dicarbonate (LEDC);[28] it prohibits ongoing electrolyte reduction as it is electronically insulating but allows lithium ion diffusion, thereby enabling reversible lithium intercalation and deintercalation in graphite.[29;30] In a state of the art lithium-ion battery, the limitation of the charging current arises at the graphite electrode.[17] The low working potential of the graphite electrode (100 to 200 mV above Li/Li^+ potential) is advantageous in terms of cell potential and specific energy, but poses the risk of undesired lithium metal plating upon battery charge. At high charging currents, the cell polarization can drive the potential of the graphite electrode below the Li/Li^+ potential and plating of metallic lithium becomes thermodynamically possible. Lithium plating has to be prevented as it causes irreversible capacity loss and also poses a

[1] The term "intercalation" was first used in the 1950s for chemical intercalation into graphite.[19] Within the battery community the term "intercalation chemistry" was introduced by S. Whittingham in 1976.[2]

serious safety hazard, as discussed in more detail in the next chapter.[31]

The spinel type lithium titanate (LTO) is an alternative anode active material with a specific capacity of 175 mAh g^{-1} and working potential of 1.55 V vs. Li/Li^+.[32] On the one hand, the comparably high potential makes LTO an interesting anode material for cells with a high charging rate capability, as the above mentioned lithium plating side reaction is not taking place.[33] On the other hand, the high working potential significantly limits the cell potential and therefore the specific energy. There have been attempts to use novel high voltage cathode materials to achieve reasonable cell potentials also in combination with an LTO anode,[33;34] but in the end LTO anodes will probably be excluded from cells which are designed for high specific energy densities.

Hard carbons are another interesting group of anode active materials. In general, the term hard carbon refers to disordered carbonaceous materials which cannot be graphitized at high temperatures. Depending on the preparation method, hard carbons have specific capacities ranging from 200 to almost 1000 mAh g^{-1}.[35] Hard carbons exhibit a sloped potential profile which is intermediate between graphite and LTO,[8;35] making them promising anode materials for applications which require fast charging and a high specific energy. Hard carbons were used in Sony's second generation lithium-ion battery in 1992 before being replaced by graphite which offers a higher energy density (in Wh L^{-1}).[1] In the near future, the necessity for higher charging rates might cause a revival of hard carbons as anode materials.

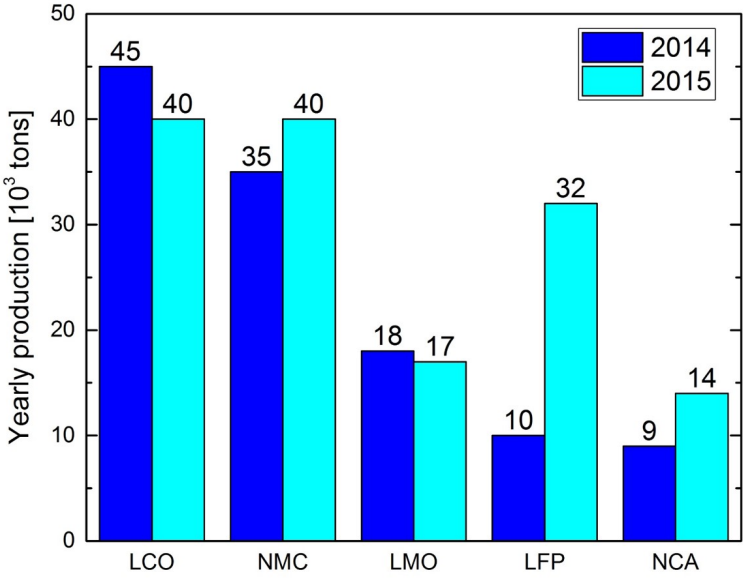

Figure 1.2 Annual global production of LCO, NMC, LMO, LFP and NCA cathode materials for the years 2014 and 2015. Note that the NMC value includes materials of different Ni, Co and Mn content. Data provided by Christophe Pillot.[36]

On the cathode side, several different active materials are commonly used in state of the art lithium-ion batteries; Figure 1.2 shows the yearly global production for the five most common cathode materials for the years 2014 and 2015. Most cathode materials are lithium containing transition metal oxides. There is a class of layered transition metal oxides including $LiCoO_2$ (LCO), $LiNi_{0.8}Co_{0.15}Al_{0.05}O_2$ (NCA) and $LiNi_xMn_yCo_zO_2$ (NMC, with x + y + z = 1) which all have an α-$NaFeO_2$ –type structure and there are also a few spinel materials like $LiMn_2O_4$.[37] For NMC, the atomic ratio of the transition metals Ni, Mn and Co can be varied and is indicated by subscripts (e.g. NMC111 = $LiNi_{1/3}Mn_{1/3}Co_{1/3}O_2$). Currently, NMC111 is the most commonly used material, but other stochiometries like NMC532, NMC622 and NMC811 are under development (see next section). The only commonly used non-oxide cathode material is the phospho-olivine $LiFePO_4$ (LFP) which was first described in 1997 by the Goodenough group.[38] While the different cathode materials all have specific advantages and disadvantages, one can make a simple comparison of the specific energy and intrinsic material safety as shown in Table 1.1. For all cathode materials except LFP, the practically achievable specific capacity is lower than the theoretical capacity if the entire lithium could be extracted during charge ($x < 1$ in $LiCoO_2 \xrightarrow{\text{charge}} Li_{1-x}CoO_2 + x\,Li^+ + x\,e^-$). The amount of lithium which is extracted during battery charge is controlled by the upper cut-off potential. NCA delivers the highest practical specific energy of 750 Wh kg^{-1}, followed by LCO and NMC111 with around 600 Wh kg^{-1}. LMO and LFP give lower practical specific energies of 500 and 450 Wh kg^{-1} which is due to their lower capacity and potential, respectively. The intrinsic safety characteristics of a cathode material improve with the onset temperature of oxygen release. Once oxygen is released at elevated temperatures, it can cause the ignition of the electrolyte and therefore contribute to a so-called thermal runaway.[39] According to Table 1.1, the layered oxidizes LCO, NCA and NMC can release oxygen at relatively low temperatures of 150, 160 and 210 °C, respectively. In contrast, the spinel LMO has as significantly higher onset temperature of 265 °C, while the phospho-olivine LFP does not release oxygen at all in the relevant temperature range because of the covalent oxygen bonding within the phosphate anion. In general, for cathode materials, specific energy and intrinsic material safety show opposing trends. Except for LCO, all cathode materials listed in Table 1.1 are currently used in battery electric vehicles (BEV) by major car producers.[7;10]

A standard electrolyte in a lithium-ion battery contains a mixture of cyclic and linear alkyl carbonates as solvents and $LiPF_6$ as conducting salt. The cyclic alkyl carbon-

Table 1.1 Selected electrochemical and chemical properties of lithium-ion cathode materials. The first specific capacity is the practically achievable value, the one in brackets is the theoretical value. The average potential is the midpoint voltage at a C/20 rate. LFP does not show any oxygen release.

	Spec. energy [10] [Wh kg^{-1}]	Spec. capacity [7] [mAh g^{-1}]	Average potential [7] [V vs. Li/Li^+]	Oxygen release [39] [°C]
LCO	600	155 (274)	3.9	150
NMC	600	160 (278)	3.8	210
NCA	750	180 (279)	3.7	160
LMO	500	100-120 (148)	4.0	265
LFP	410	160 (170)	3.4	-

ates enable the dissolution of the conducting salt due to their high dielectric constants, while the linear carbonates decrease the solvent viscosity to optimize the ionic conductivity.[40] The most commonly used cyclic carbonate is ethylene carbonate (EC), for the linear carbonates dimethyl carbonate (DMC) or ethyl methyl carbonate (EMC) are typically used. For the last 25 years, ethylene carbonate has been an indispensable electrolyte component as it forms an SEI which prevents solvent co-intercalation and resulting graphite exfoliation.[8] $LiPF_6$ is used as standard conducting salt as it offers good overall properties and especially because it passivates the aluminum current collector. The latter is not the case for most other conducting salts like, for example, bis(trifluoromethane)sulfonimide lithium salt (LiTFSI).[41] In order to improve the cycle and calendric life of lithium-ion batteries, small quantities of so-called electrolyte additives are used. Most electrolyte additives are reduced on the graphite electrode within the first charge and form a more stable and passivating SEI.[42] In commercial cells the most common electrolyte additives are vinylene carbonate (VC) and prop-1-ene-1,3 sultone (PES).[43] The structures of these electrolyte components are listed in Figure 1.3.

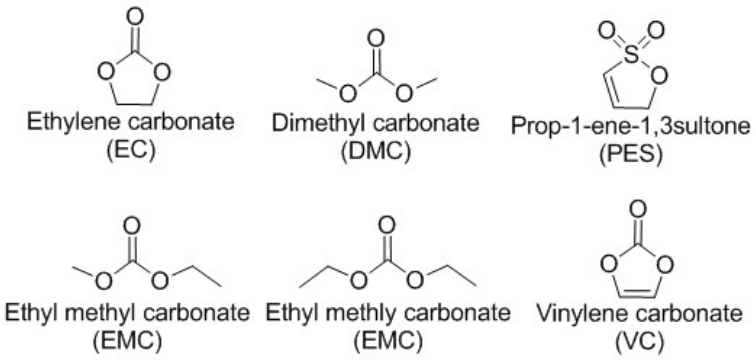

Figure 1.3 Structures of most common electrolyte solvents, conducting salts and additives.

1.2 Next Generation Lithium Ion Batteries

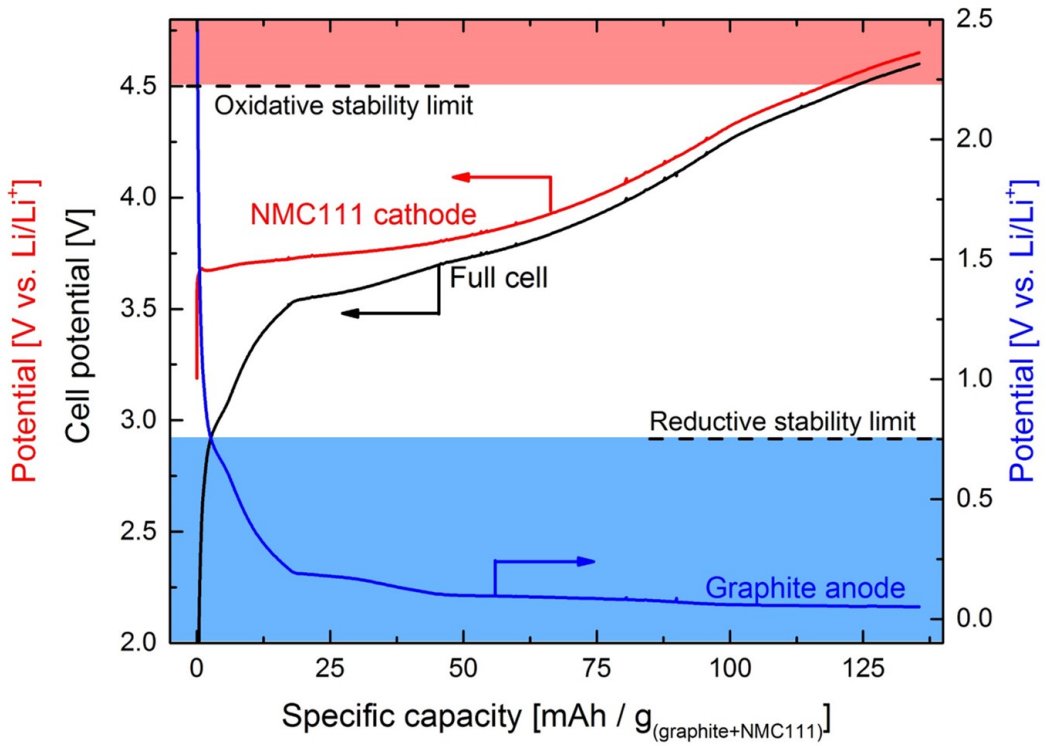

Figure 1.4 Potential profile of an NMC111 cathode, a graphite anode and the resulting cell potential during the first battery charge (C/10 rate). The electrode potentials are measured against an internal lithium reference electrode. The areas shaded in blue and red color indicate regions of cathodic and anodic electrolyte instability.

Figure 1.4 shows typical anode and cathode potential profiles and the resulting cell potential during the charge of a graphite/NMC111 cell. The specific energy of the cell is the area under the black curve (spec. energy [Wh kg^{-1}] = voltage [V] x spec. capacity [Ah kg^{-1}]). There are two general possibilites for increasing the specific energy, i) increase the cell potential and ii) increase the specific capacity. The only option for increasing the cell potential is to increase the working potential of the cathode as the graphite anode already operates very close to the lower boundary of the lithium metal potential. The specific cell capacity is currently limited by the cathode materials, with achievable specific capacites between 120 and 180 mAh g^{-1} (see Table 1.1) in comparison to 372 mAh g^{-1} for graphite. Therefore, in the short and mid term, the specific energy of state of the art lithium-ion batteries can gradually be improved by closing the gap between theoretical and practical specific capacity for NMC based cathode materials (see Table 1.1). This can be achieved by increasing the charging cut-off potential as shown in Figure 1.4. It is possible to entirely delithiate NMC111

if the material is charged to 5.0 V vs. Li/Li^+.[44] The close to linear capacity increase at potentials above 4.2 V vs. Li/Li^+ leads to an almost quadratic increase in specific energy upon increasing the charging cut-off potential.[45] Unfortunately, cut-off potentials of higher than 4.4 V (vs. graphite) severely reduce battery life because the cathode potential exceeds the stability limit of the battery electrolyte (see Figure 1.4), causing electrochemical electrolyte oxidation which is accompanied by massive transition metal dissolution from the cathode active material.[45;46;47] The latter is probably caused by acidic etching due to protic electrolyte oxidation products.[48;49] Transition metal ions can diffuse through the electrolyte and precipitate on the graphite anode where they inhibit the passivating function of the SEI and catalyze electrolyte reduction. While the exact mechanism of this transition metal triggered side reaction on the graphite electrode is still heavily debated, this process is considered to be the main reason for the fast capacity fading of NMC cells cycled to high cut-off potentials.[45;46] In addition to the electrochemical electrolyte oxidation, the NMC cathode material itself is also chemically unstable at high delithiation degrees ($x < 0.2$ in Li_xMO_2). Our group recently reported that both normal NMC and lithium and manganese rich layered "high-energy NMC" (HE-NMC) irreversibly release oxygen from the particle surface according to $MO_2 \longrightarrow MO + \frac{1}{2}\,O_2$ which is also believed to further contribute to electrolyte decomposition.[50;51] As a consequence, the choice of upper cut-off potential for graphite/NMC cells is a compromise between improving the specific capacity while retaining a sufficient battery life. Alternatively, the utilization of the NMC cathode material can also be improved by increasing the nickel content. For the same cut-off potential of 4.3 V vs. Li/Li^+ (about 4.2 V cell potential), NMC811 shows a reversible capacity of 200 mAh g^{-1} and a specific capacity of 760 Wh kg^{-1} which compares to 160 mAh g^{-1} and 600 Wh kg^{-1} for NMC111.[10;52] As a downside, the propensity for oxygen release also scales with the nickel content, which can be rationalized by the similarity in composition of NMC811 ($LiNi_{0.8}Mn_{0.1}Co_{0.1}O_2$) and NCA ($LiNi_{0.8}Co_{0.15}Al_{0.05}O_2$) which is well known for facile oxygen release.[51]. In addition to improving NMC, entirely new cathode materials offering higher potentials and/or specific capacites are currently beeing explored. Possible candidates are the $LiNi_{0.5}Mn_{1.5}O_2$ spinel[53] with an average potential of 4.7 V and a capacity of about 120 to 140 mAh g^{-1} or the above mentioned high-energy NMC[54;55] with a specific capacity of about 250 mAh g^{-1}.[10]

On the anode side, the addition of small quantities of novel anode active materials like silicon (3600 mAh g^{-1} for $15\,Li^+ + 15\,e^- + 4\,Si \longrightarrow Li_{15}Si_4$)[56] to a graphite electrode is

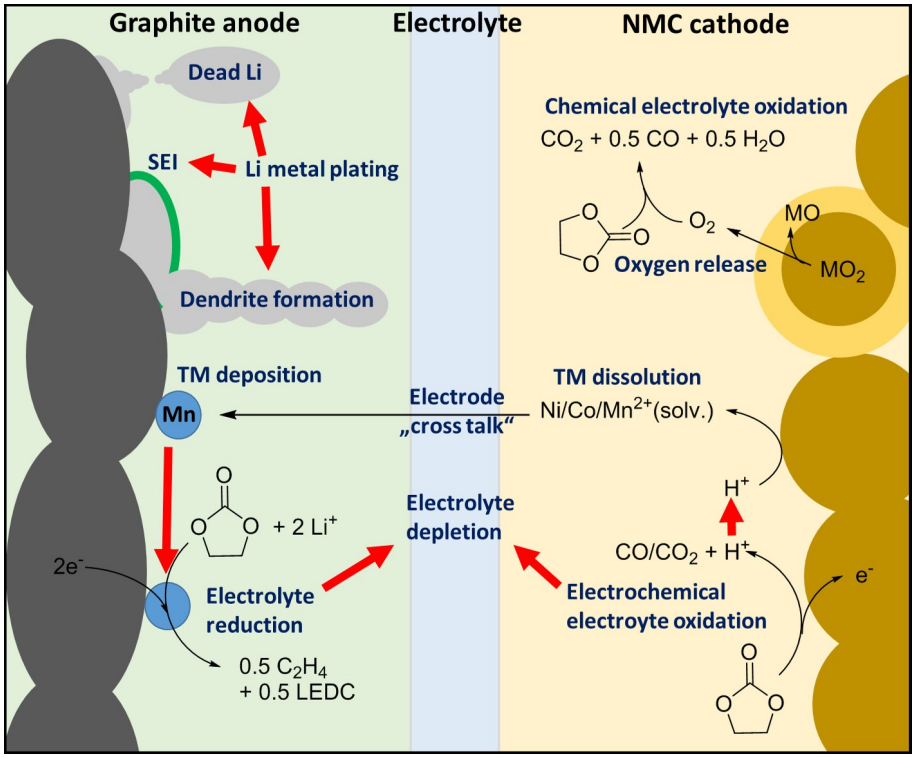

Figure 1.5 Scheme of undesired side reactions in lithium-ion batteries which are investigated within this PhD project.

already used for improving the specific capacity.[7;57] The use of high silicon contents, or even pure silicon, is hampered by its massive volume expansion and contraction upon lithium intercalation and deintercalation of up to 300%, causing particle cracking and ongoing SEI formation. Various mitigation strategies like nano-structuring have been investigated but so far no reversible silicon anode is available.[58]

In the long term, lithium metal would be the ideal anode material due to its very high specific capacity of 3860 mAh g^{-1}. Unfortunately, the lithium plating process ($Li^+ + e^- \longrightarrow Li$) does not occur homogeneously over the electrode but forms micro-structured dendrites.[59] It is generally accepted that dendrite formation increases with the geometric plating current density (in mA cm^{-2}) but, despite more than 30 years of intensive research, the fundamental mechanism of the process is still controversial.[60;61;62] Dendrite growth has been attributed to electric field inhomogeneities,[63] lithium ion concentration gradients,[64;65] preferred lithium deposition at kinks/defect sites[66;67], or even mechanical stress within the electrode,[62] but so far no model can explain all experimentally observed dendrite growth patterns. In fact, dendrite growth has been observed to take place at the tip[62;68], in the middle,[67] and also at the base[68;69] of existing dendrites and to be either directed towards the counter

electrode or occur randomly and undirected.[67;69;70]
Approaches for the reduction or total suppression of lithium dendrite formation have mainly focused on electrolyte additives to improve the SEI properties and to achieve a more homogeneous current distribution or on strong mechanical barriers to prevent internal short circuits, but so far with limited success only.[59] The consequence of lithium dendrite formation is ongoing electrolyte and active lithium loss due to permanent SEI renewal on the freshly exposed lithium metal surface. Also, during the stripping process, lithium metal can loose electronic contact to the electrode and form so-called "dead lithium". Furthermore, lithium dendrite formation is a serious safety hazard due to the above mentioned possibility of internal shorts. The consequences of lithium dendrite formation on lithium metal anodes and undesired lithium plating on graphite electrodes (see previous chapter) are similar, but the nature of these two processes is different. On graphite electrodes, lithium plating is an undesired side reaction which can be prevented by using proper charging conditions while lithium dendrite formation appears to be intrinsic to the (desired) lithium plating/stripping process on lithium metal anodes.
Figure 1.5 visualizes lithium-ion battery side reactions and their interconnections which are investigated in this PhD thesis. The diffusion of reaction products from one electrode to the other in combination with further side reactions is referred to as "electrode crosstalk".

1.3 Beyond Lithium-Ion Cell Chemistry

While specific capacities of lithium-ion batteries gradually approach their physico-chemical limits, significantly higher specific energies might be obtained with entirely new battery concepts like lithium-sulfur and lithium-oxygen.[9;71] These novel battery technologies are sometimes referred to as "beyond lithium-ion batteries" as they do not rely on intercalation chemistry. In recent years, the aprotic lithium-oxygen battery has received much attention due to its outstanding theoretical specific capacity and energy of 1170 Ah kg^{-1} and 3460 Wh kg^{-1}.[72;73] A recent estimation by Gallagher and co-workers has raised doubts though, whether the practically achievable energy density of lithium-oxygen cells could exceed advanced lithium-ion cells.[74]

The lithium-oxygen cell consists of a lithium metal anode, an oxygen-breathing porous cathode and an aprotic electrolyte. During discharge, oxygen is reduced within the porous cathode forming Li_2O_2 as discharge product according to $2\,Li^+ + 2\,e^- + O_2 \rightleftharpoons Li_2O_2$. The thermodynamic potential of the Li_2O_2 formation is 2.96 V vs. Li/Li^+. During charge, the reaction is reversed and oxygen is evolved. The discharge reaction is not a direct two-electron reduction but consists of two steps. The first step is a one electron reduction forming the highly reactive superoxide radical ($O_2 + e^- \longrightarrow O_2^{\bullet -}$) which quickly combines with a lithium ion, forming LiO_2. The subsequent step is either a second electrochemical one-electron reduction ($LiO_2 + Li^+ + e^- \longrightarrow Li_2O_2$) directly at the electrode surface or a chemical disproportionation ($2\,LiO_2 \longrightarrow Li_2O_2 + O_2$) which can also take place in the bulk electrolyte.[75;76] Hard Lewis acids, like poorly solvated Li^+, favor the second one-electron reduction, while soft Lewis acids, like well solvated Li^+ or bulky tetra alkyl ammonium cations, favor the chemical disproportionation.[76;77;78]

While the discharging mechanism is fairly well understood, mechanistic understanding of the charging reaction is very limited. In contrast to the discharge process, no solution based superoxide species are formed during charge.[79] There is theoretical and experimental evidence for a two step mechanism which is initiated by the topotactic and non-stochiometric Li_2O_2 delithiation ($Li_2O_2 \longrightarrow Li_{2-x}O_2 + x\,Li^+ + x\,e^-$) followed by further oxidation and oxygen evolution ($Li_{2-x}O_2 \longrightarrow$ (2-x) Li^+ + (2-x) $e^- + O_2$).[80;81;82] This charging mechanism is plausible and matches most experimental data, but it does not explain the observed side reactions taking place during charge. An important measure of undesired side reactions is the e-/O_2 ratio which should equal 2.00 for the reversible Li_2O_2 formation. For the discharge in standard

ether based electrolytes with a standard carbon cathode, e-/O_2 ratios very close to 2.00 in combination with e-/Li_2O_2 ratios better than 2.20 have been reported, indicating that Li_2O_2 is indeed the main discharge product.[83] Minor amounts of discharge side reaction products, like lithium acetate and lithium carbonate, can be attributed to the chemical reaction of highly reactive superoxide with electrolyte and of Li_2O_2 with the carbon support.[84;85] During battery charge, e-/O_2 ratios are always worse than 2.60 for a variety of electrolyte solvents, conducting salts and cathode materials, indicating a strong contribution of undesired side reactions.[86;87;88] Furthermore, carbon dioxide evolution due to oxidation of the carbon support is observed at potentials as low as 3.5 V vs. Li/Li^+;[89] this is remarkable, considering that carbon is stable towards electrochemical oxidation to potentials of well above 4.0 V vs. Li/Li^+.[90] In the last few years, a variety of different electrolyte compositions and cathode materials has been investigated, but so far no truly reversible lithium-oxygen cell chemistry could be achieved.[91] For a more targeted search for stable cell components, a better understanding of the charging side reactions will be required.

In addition to the intrinsic complexity of the lithium-oxygen cell chemistry, scientific progress has been significantly hampered because of irreproducible results and insufficient reporting of experimental details.[93] In this respect, a publication by Peter Bruce and co-workers on a tetrathiafulvalene (TTF) redox mediator is a rather unfortunate example.[92] The publication has received a lot of attention as it claims 100 fully reversible charge/discharge cycles. According to the redox mediator concept, TTF is supposed to decrease the charging overpotential by acting as a soluble electron hole carrier. Within this concept, TTF is first oxidized at the carbon electrode, forming TTF^+, which then oxidizes Li_2O_2 according to $2\,TTF^+ + Li_2O_2 \longrightarrow 2\,TTF + 2\,Li^+ + O_2$. In order to ensure the catalytic role of TTF, it is important to compare the capacity of the Q(TTF/TTF^+) couple to the actual cell capacity Q(cell). For the above mentioned study, Q(TTF/TTF^+) can only be calculated within a factor of 10 (0.01 to 0.1 mAh) as the electrolyte volume is stated to be between 40 and 400 μL. No reason for this unusual deviation/uncertainty in electrolyte volume is given. The total cell capacity is even more obscured as i) the capacity is normalized to the weight of the gold electrode (mAh g_{Au}^{-1}), ii) the gold loading is only stated within a facor of over 30 (0.15 to 5 mg cm^{-2}), and iii) no geometric surface area of the gold electrode is given. Assuming[2] an electrode diameter of 10 mm and using the above mentioned gold load-

[2] In other lithium-oxygen studies published around the same time, the Bruce group used standard Swagelok cells.[84;89;94]

ing range, a value for Q(cell) of 0.035 to 1.175 mAh can be calculated. It is possible to narrow down the actual Q(cell) value by graphical back-integration of differential electrochemical mass spectrometry (DEMS) curves plotted in the supplementary information. The resulting cell capacity $Q(cell)_{DEMS}$ of 0.033 mAh (dashed horizontal line in Figure 1.6) matches very well to the lower range of Q(cell) of 0.035 mAh which corresponds to a gold loading of 0.15 mg cm^{-2}. This means that the entire cell capacity is very well within the range of $Q(TTF/TTF^{+})$; accordingly, TTF might simply act stochiometrically as active material rather than as catalytic redox mediator as claimed in the article. This is supported by more carefully designed studies carried out by the Janek and McCloskey groups, who found no positive impact of TTF on lithium-oxygen cycling behavior. [91;95]

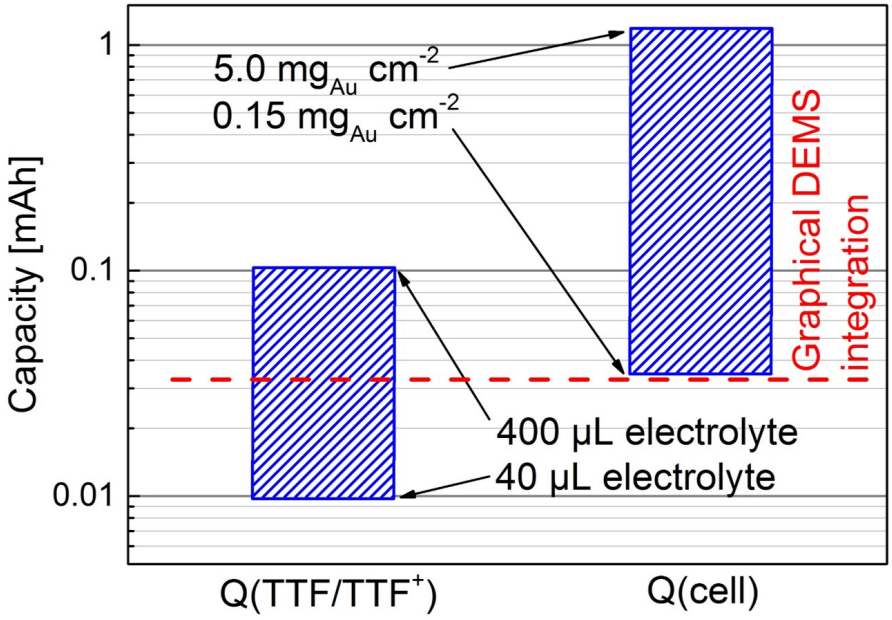

Figure 1.6 Case study of a high impact lithium-oxygen publication based on insufficient and misleading experimental data. [92] Comparison of the possible ranges for $Q(TTF/TTF^{+})$ and Q(cell) according to the information available within the publication and actual cell capacity ($Q(cell)_{DEMS}$, red dashed line) determined by graphical back-integration of DEMS curves shown in the supplementary information.

The reason for the huge deviation (factor > 30) in the stated gold loading remains mysterious, especially if one considers the fabrication method of the nano porous gold electrode used by Bruce and co-workers; [96] this is produced by dealloying of a 12 carat white gold leaf (1/1 Au/Ag mass ratio, Noris Blattgold GmbH, Germany) with an area specific weight of 0.23 mg cm^{-2}. Accordingly, the electrode loading of 0.15 mg cm^{-2}, as indirectly determined via DEMS back integration, is very reasonable. In contrast, it is absolutely inconceivable how a loading higher than 0.23 mg cm^{-2} could be obtained

and the motivation for stating a range from 0.15 to 5 mg cm^{-1} is up to speculation. It has been recognized within the battery community that this kind of irreproducible research is a significant impediment for the scientific progress and as a consequence new protocols for evaluation and reporting of experimental data for lithium-oxygen cells have recently been suggested.[93;97]

1.4 Operando Characterization: Necessity and Challenges

In battery research, test cells are often treated as some kind of black box. A bias is applied to the cell, for example a constant current, and the system response, in this case the cell potential, is recorded. Then, output parameters, like discharge capacity or coulombic efficiency, are analyzed based on *assumed* cell reactions. Finally, cell components are systematically altered in order to optimize the observed output parameters. While this is a reasonable approach which has been successfully applied for decades, there are cases in which it is necessary to take a closer look into the black box to gain a detailed understanding of the *actual* cell reactions. In this respect, the early research in the field of aprotic lithium-oxygen batteries is an interesting "historic" case study.

The concept of the aprotic lithium-oxygen battery was first described in 1996 in a seminal publication by K. M. Abraham.[72] Their cell consisted of a lithium metal anode, a typical lithium-ion battery polymer electrolyte[3] containing a carbonate solvent and $LiPF_6$ as conducting salt, and a porous carbon sheet without active material as cathode. In oxygen atmosphere, the cell showed a capacity of 1600 mAh g_{carbon}^{-1} for several charge/dischare cycles. In discharged electrodes, Li_2O_2 was qualitatively detected by Raman spectroscopy and decoloring of a $KMnO_4$ solution. Further backup experiments were carried out to confirm the assumed cell chemistry. First, a cell was discharged in pure argon which showed no discharge capacity; then, a fresh (undischarged) cell was charged in oxygen atmosphere which only showed a negligible charge capacity. The former experiment was interpreted to confirm that oxygen was a necessary reactant during discharge; the latter experiment was interpreted to rule out direct electrochemical electrolyte oxidation as the main charging reaction. The occurrence of a reversible O_2/Li_2O_2 cell chemistry was the logical conclusion of this thorough analysis. In the following years, a series of highly cited studies investigated the presumed lithium-oxygen cell chemistry in liquid carbonate based electrolytes. While many of these studies were methodically correct, the data analysis of purley electrochemical experiments (e.g. charge/discharge cycling, rotating disc experiments

[3]The lithium-oxygen concept was serendipitously discovered during an *in situ* gas phase infrared (IR) spectroscopy study on the SEI formation on graphite electrodes.[98] The SEI formation process was studied at a potential of about 0.8 V vs. Li/Li^+ where no lithium intercalation but oxygen reduction can take place. Oxygen was accidentally introduced through a leaking syringe for IR sample extraction.

and impedance spectroscopy) was based on the implicit assumption of a reversible O_2/Li_2O_2 cell chemistry.[99;100;101;102] Finally, in 2011 two groups independently discovered that an entirely different cell chemistry takes place in carbonate containing electrolytes.[103;94] The superoxide radical, initally formed during discharge, undergoes a nucleophilic ring opening reaction with propylene carbonate, forming various organic degradation products.[4] These degradation products are then oxidized to carbon dioxide in the subsequent charge. Therefore, the charge/discharge reaction in carbonate electrolytes is carried by irreversible electrolyte decomposition rather than the assumed reversible O_2/Li_2O_2 chemistry. For the discovery of the actual cell chemistry, the use of quantitative analytic techniques like differential electrochemical mass spectroscopy (DEMS) played a key role as they identified Li_2O_2 as a minor side product during discharge, rather than the stoichiometric main product.

In general, an analytical technique can by applied under *ex situ*, *in situ* or *operando* conditions.[5] In a typical *ex situ* experiment a cell first undergoes a certain cycling or aging procedure and then the component of interest (e.g. the cathode or anode) is harvested and analyzed. *Ex situ* analysis is the standard option as the sample can be prepared following the specific requirements of the respective analytical technique. A classical example for a battery related *ex situ* analysis is the determination of cross over transition metals on graphite electrodes by flame spectroscopy.[105;106] In contrast, *in situ* and *operando* analysis is carried out directly within the battery cell without additional sample preparation. Usually *in situ* and *operando* analysis are non-destructive, making it possible to continue with battery cycling thereafter. Furthermore, the sample is investigated in its "natural environment" which excludes experimental artefacts during sample preparation. As a downside, *in situ* and *operando* analysis is usually more complicated for most analytical techniques because the sample cannot be specially prepared. Additional complexity is added by the simultaneous presence of all other cell components, which might lead to overlapping signals or impede the signal assignment. The difference between *in situ* and *operando* analysis is the following: in an *in situ* experiment the spectrum/diffractogram is recorded while the electrochemistry is stopped, in an *operando* experiment the spectrum/diffractogram is recorded in parallel with cell cycling. Usually an experiment is carried out under *in situ*, rather

[4] The reaction between propylene carbonate and superoxide had already been described in 1991 by Aurbach and co-workers.[104]

[5] There is no standarized nomenclature for the terms *ex situ*, *in situ* and *operando*. Some authors use the term *in situ* also for *operando* experiments. Depending on the research community the term "*in operando*" might be used instead of "*operando*".

than *operando*, conditions if i) the recording time of a spectrum/diffractogram is long on the relevant electrochemical time scale ("time resolution") or ii) if battery operation and analytical technique exclude each other. A typical example for the former case is *in situ* neutron diffraction, in which a long integration time is necessary for a reasonable signal to noise ratio;[107] a typical example for the latter case is an *in situ* nuclear magnetic resonance (NMR) set up, in which the same copper disc acts as battery current collector and NMR detector.[108] These two studies are ony individual examples; depending on the experimental design and set up it is also possible to use neutron diffraction and NMR in *operando* conditions.[109;110]

The unique strength of *operando* techniques is the possibility to investigate cells in a state of non-equilibrium and observe transient processes or detect thermodynamically unstable intermediates. An archetypical example of such a phenomenon is the lithium metal plating reaction on graphite electrodes. During fast or low temperature battery charging, lithium plating might be kinetically favored, but there is a thermodynamic driving force for chemical reintercalation of metallic lithium into the underlying graphite particle ($x\mathrm{Li} + \mathrm{Li}_y\mathrm{C}_6 \longrightarrow \mathrm{Li}_{x+y}\mathrm{C}_6$, $x + y \leq 1$). Thus, during the subsequent open circuit period or sample preparation time following battery charge, metallic lithium quickly "disappears"; as a consequence an *ex situ* analysis inevitably underestimates the amount of lithium plating.[111]

For *operando* experiments, the electrochemical cell must be fully compatible with the specific requirements of the respective analytical technique. In recent years, dedicated *operando* battery cells have been developed for most common spectroscopic and diffraction based techniques.[112] For most spectroscopic techniques, the battery housing is a major challenge, as it must be permeable for electromagnetic waves of a certain wavelength and in case of magnetic resonance spectroscopy also for a magnetic field. There are various cell designs for *operando* NMR spectroscopy which consist of a plastic bag or special polymer housing.[113] For *operando* UV/Vis spectroscopy, cells with a quartz glass windows sealed in standard pouch bag have been developed.[114] For x-ray absorption spectroscopy (XAS), cells with x-ray windows consisting of polymer foils (e.g. Kapton®or Mylar®) with a thickness of a few μm are used.[115] For x-ray diffraction it is even possible to use a standard pouch cell which also works for lab based x-ray sources, though synchrotron radiation offers a better time resolution and signal to noise ratio.[116] There is a variety of analytical techniques which require ultra high vacuum in order to reach a sufficiently long mean free path for electrons. For these techniques the presence of liquid electrolyte with finite vapor pressure is the main

obstacle. *Operando* scanning electron microscopy (SEM) can be carried out if a polymer or ionic liquid based electrolyte without vapor pressure is used.[69] In recent years, the development of differentially pumped endstations has enabled the investigation of electrochemical systems with standard liquid electrolytes by x-ray photoelectron spectroscopy (XPS).[117]

So far, electron paramagnetic resonance spectroscopy (EPR)[6] has not yet been used for *operando* investigation of battery materials and systems. It has been the main goal of this PhD thesis to develop a battery cell for *operando* EPR spectroscopy. The development process is covered in Section 2.1. *Operando* EPR spectroscopy is then used to study three different phenomena. In Section 3.1.1, the formation of lithium dendrites on lithium metal anodes and the role of current density and electrolyte additives is investigated. It is demonstrated that *operando* EPR can semi-quantitatively detect lithium metal dendrites in presence of a huge excess of bulk metallic lithium in the anode by exploiting the so-called skin depth effect. In Section 3.1.2, lithium metal plating on graphite electrodes is investigated. Despite the important role of this side reaction for fast charging, analytical techniques capable of directly and quantitatively detecting plated lithium metal are very rare. One such example is the *in situ* neutron diffraction study carried out by Zinth et al.[118] In Section 3.1.3, *operando* EPR spectroscopy is used in combination with a chemical spin trap to prove the occurrence of singlet oxygen during the charging process of an aprotic lithium-oxygen battery. The highly reactive singlet oxygen is probably the missing link in the mechanistic understanding of the so far puzzling charging side reaction in aprotic lithium-oxygen batteries.

In Section 3.2, synchrotron based *operando* XAS spectroscopy is used for the investigation of transition metal dissolution and deposition in NMC/graphite cells. These experiments are carried out in a special cell design which enables both time and spatial resolution. This is the first *operando* XAS study on the transition metal deposition reaction and significant differences in comparison to previous *ex situ* studies are observed.

The studies in Sections 3.1 and 3.2 all rely on special *operando* cell designs and target one specific side reaction. In contrast, in Section 3.3, a commercially produced 18650-type cell is investigated by *in situ* neutron diffraction. The goal of this study is not to observe a single side reaction, but rather to obtain a comprehensive picture of the general aging mechanism taking place within the cell.

[6] Also referred to as electron resonance spectroscopy (ESR).

2 Experimental Methods

2.1 Operando Electron Paramagnetic Resonance Spectroscopy

In EPR spectroscopy, an external magnetic field B_0 is applied to a sample to align the unpaired spins, which can then be excited by an electromagnetic wave according to $h\nu = g\beta B_0$, where h is the Planck's constant, ν is the frequency of the electromagnetic wave, β is the Bohr magneton and g is the material specific spectroscopic g-value. Standard lab based EPR spectrometers use an X-band microwave source with a frequency between 9 and 10 GHz which requires a magnetic field of about 350 mT to fulfill the resonance condition for g-values close to the free electron ($g_e = 2.0023$). In principle, EPR spectroscopy can be used for any sample containing unpaired spins, for example organic radicals or paramagnetic transition metal ions. The combination of EPR spectroscopy with electrochemistry, first mentioned in 1958,[119] is frequently used in organic and metal organic chemistry to study redox reactions[120;121] because i) in most one-electron redox reactions either the educt or the product has an odd number of electrons and is therefore EPR active and ii) the electrochemical electrode potential can be continuously adjusted, which is not possible with chemical oxidation/reduction agents. To the best of our knowledge, there is only a single study ("preliminary note")[122] on *in situ* EPR spectroscopy with a battery context, while *in situ*/*operando* NMR is frequently used for battery research.[123;124] This might have to do with practical complications in the development of *operando* EPR cells for battery applications. The main challenges are the presence of metal current collectors which can shield off the microwave as well as the necessity of high dielectric solvents (see previous chapter) causing the attenuation of microwave power. The dielectric constant of ethylene carbonate ($\epsilon = 89.78$ at 25 °C) is even higher than that of water which is typically considered to be a high-loss solvent in EPR spectroscopy.[41] Depending on size and shape of the current collectors and their orientation within the cavity, the magentic field modulation might also induce eddy currents which can cause experimental artefacts in the recorded EPR spectra.[125] Further challenges are the geometric

constraints within the cavity (10 mm diameter) and high demands on sealing. The latter is especially critical because battery cell chemistry can be strongly affected by trace amounts of water and for a typical battery experiment the cell might have to be functional in ambient atmosphere for up to 30 hours (e.g. C/10 cycle plus cell mounting and signal calibration).[126]

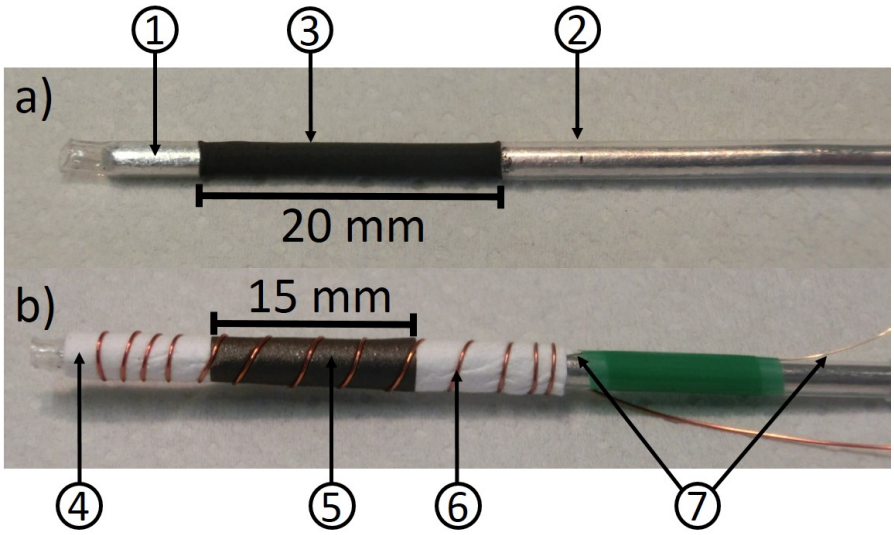

Figure 2.1 Images of the concentric *operando* EPR cell design a) during assembly and b) fully assembled. The configuration shown in this image contains LFP and graphite as active materials for the inner and the outer electrode.

The *operando* EPR cell developed within the course of this PhD project is shown in Figure 2.1. It is a concentric cell design with one electrode directly attached to the central wire and one electrode wrapped around this central electrode with a porous separator wound in between the electrodes. The cell is assembled starting with the central wire (1) (2 mm diameter) which acts both as current collector for the inner electrode and mechanical support. To prevent a short circuit, the central wire is covered by fluorinated ethylene propylene (FEP) heat shrink tubes (2), leaving out 20 mm close to the lower end. The inner electrode (3) is directly coated onto the exposed central wire. The viscosity of the ink is critical to achieve a homogeneous coating; to this end, the cell has to be rotated along its axis during coating and the entire ink drying process. The coating thickness is controlled by the thickness of the heat shrink tubes. Afterwards, a glass fiber separator (4) and the outer electrode (5) are attached with a thin wire (6) which also acts as the second current collector. The outer electrode is coated onto a porous polyolefine separator. The active material is facing outwards for direct electronic contact to the current collector wire while the

inwards facing polyolefine separator, once filled with electrolyte, provides ionic contact with the inner electrode. In this set up, a sufficient in-plane conductivity of the outer electrode is important to achieve a homogeneous current distribution across the entire electrode. The amount of conductive additive has to be adjusted according to the intrinsic conductivity of the active material. In the last step, a reference electrode (7), consisting of partially delithiated LFP coated onto insulated aluminum wire (0.1 mm diameter), is carefully introduced in between two layers of glass fiber separator and attached with battery electrolyte compatible tape.
In this cell design, EPR spectra show signals arising both from the inner and the outer electrode, so one can can choose the placement of working and counter electrodes based on practical considerations. An obvious exception to this is lithium metal foil, which can only be used as inner electrode. The material of the central and outer metal wires is either copper or aluminum, depending on the working potential of the respective electrode materials. The exact cell configurations used for the three *operando* EPR studies (see Sections 3.1.1, 3.1.2 and 3.1.3) are listed in Table 2.1. Further details regarding the cell assembly and used materials can be found in the respective sections. Note that the entire cell assembly can be carried out outside of the glove box if the electrode active materials are not air sensitive (e.g. LFP, pristine graphite).

Table 2.1 Cell configurations of *operando* EPR cell used within this PhD thesis.

Project	Outer electrode	Inner electrode	Outer Wire	Central Wire
Li dendrites	LFP	Li metal	Al	Cu
Li plating	Graphite	LFP	Cu	Al
Singlet oxygen	Vulcan carbon	LFP	Al	Al

The concentric alignment of the electrodes in our cell design (Figure 2.1) is similar to the coaxial cell design which is typically used for electrochemical EPR experiments in organic or metal organic chemistry.[125] In this coaxial cell, also referred to as Allendoerfer cell,[127] the working electrode consists of a thin wire in the form of a finely wound shallow pitched helix which is flush with the quartz glass tube; the cell is flooded with electrolyte and a second wire inside the helix serves as counter electrode. Only the small electrolyte fraction in between the helix and inner wall of the quartz glass tube is EPR active as the entire central part, containing the largest portion of the electrolyte and the counter electrode, is shielded off from the external microwave. This is advantageous because i) it reduces microwave losses in electrolytes with a high dielectric constant and ii) radicals produced at the counter electrode do not contribute to the

EPR signal. In summary, the entire cell concept of the Allendoerfer cell is based on excluding the inner part of the helix from the microwave. In contrast, in our cell design the inner part of the helix (formed by the outer current collector wire) is exactly the region of interest as this is where the battery electrodes are placed. Therefore it is important to wind the helix wide enough to ensure full and homogeneous microwave penetration of the cell. In other words, our cell design and the Allendorfer cell appear to be similar but the fundamental cell concept is exactly contrary.

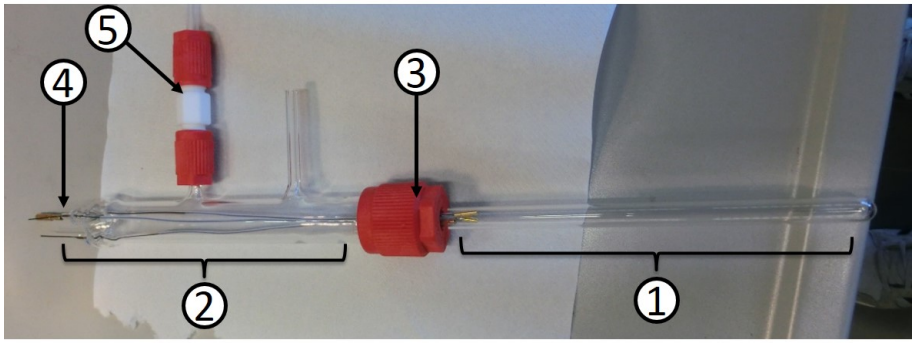

Figure 2.2 Image of the special housing for the *operando* EPR cell which allows cell cycling in a defined atmosphere.

After cell assembly, electrolyte is added directly onto the glass fiber separator and the cell is introduced into the housing. There are two different housings available for the *operando* EPR cell. The standard housing consists of a quartz glass tube (6 mm outer diameter, 0.5 mm wall thickness) which is sealed with a UV hardening two-component glue (UV glue 5023, BEST Klebstoffe, Germany). The glue does not contain protic solvents and does not produce water upon hardening. To remove residual water, the glue is dried under static vacuum over activated $CaCl_2$ for two weeks. Figure 2.2 shows the second type of housing in which the atmosphere can be controlled. It consists of a quartz glass tube (1) (10 mm outer diameter, 1.0 mm wall thickness) and a lid (2) which are connected by a gas tight tube fitting (3) (Bola, Germany). The lid contains three tungsten feed-through wires (4) which are connected to the actual cell by mini banana plugs (1 mm, Bürklin, Germany) and a connection (5) (Bola, Germany) for gas purging. A polytetrafluoroethylene (PTFE) spacer is used to center the EPR cell in the quartz glass tube.

The housing shown in Figure 2.2 was mainly used for the singlet oxygen project to carry out the battery charge in an atmosphere of defined oxygen partial pressure (see Section 3.1.3). Furthermore, it was used for an interesting isotope labeling experiment for the elucidation of the two different mechanisms involved in the 2,2,6,6-tetramethyl-

piperidin-1-yl-oxyl (TEMPO) formation (see Section 3.1.3). In this experiment, the predischarged electrode contained "normal" $Li_2{}^{16}O_2$ while the cell atmosphere was $^{17}O_2$ enriched. The different nuclear spin of $I = 0$ for ^{16}O and $I = 5/2$ for ^{17}O cause a different hyperfine splitting, making it possible to trace back the origin of the oxygen atom in the TEMPO molecule (e.g. TEMP^{16}O and TEMP^{17}O) as shown in Figure 2.3a.[128] The onset of the TEMP^{17}O formation seems to be delayed (Figure 2.3b), which would be consistent with the mechanism presented in Section 3.1.3, but the data was not published because of the low TEMP^{17}O signal intensity and the resulting uncertainty in the determination of the exact onset point.

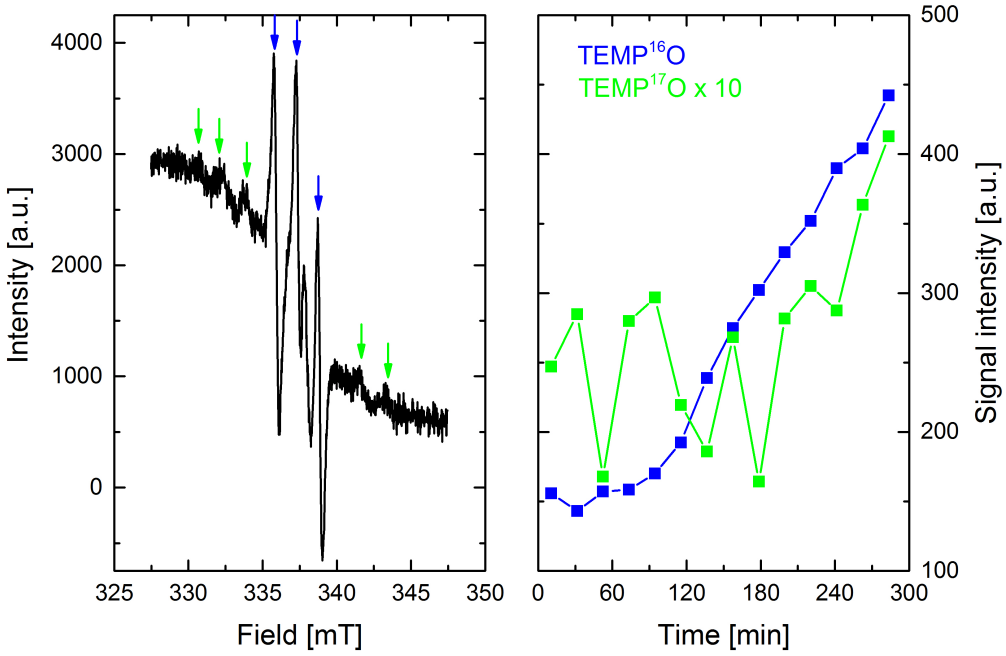

Figure 2.3 Electrochemical $Li_2{}^{16}O_2$ oxidation (= cell charge) in the presence of the TEMP spin trap in a $^{17}O_2$ enriched atmosphere with a current of 60 mA $g_{carbon}{}^{-1}$; a) final *operando* EPR spectrum showing TEMP^{16}O (blue markers) and TEMP^{17}O (green markers) and b) TEMP^{16}O and TEMP^{17}O signal intensities as a function of charging time.

For the electrochemical performance of the *operando* EPR cell it is important that a glass fiber separator is used (Figure 2.1). In initial experiments, a polyolefine (Celgard®) separator was used instead of the glass fiber separator. Figure 2.4a shows potential profiles recorded in the *operando* EPR cell with a polyolefine separator, lithium as anode and LFP as cathode (blue and green line for two nominally identical cells). Both cells show voltage spikes followed by total contact loss, but only during cell discharge and never during charge. The fact that the potential spikes only occur

during discharge excludes short circuits due lithium dendrites as possible origin because lithium is stripped during cell discharge. Figure 2.4b shows the potential profile in an identical *operando* EPR cell (lithium/LFP) in which a glass fiber separator is used instead of the polyolefine separator. It is evident that the voltage spikes do not occur in the glass fiber cell. It is not entirely clear what causes the potential spikes in the polyolefine separator cell and why they do not occur in the glass fiber cell, but it might be related to cell expansion and contraction upon cycling (e.g. mossy lithium formation and partial dissolution on the lithium metal anode). The glass fiber separator can act as a buffer towards this volume change as it is about 500 μm (= two layers) thick and compressible, while the polyolefine separator is only 50 μm (= two layers) thick and not compressible.

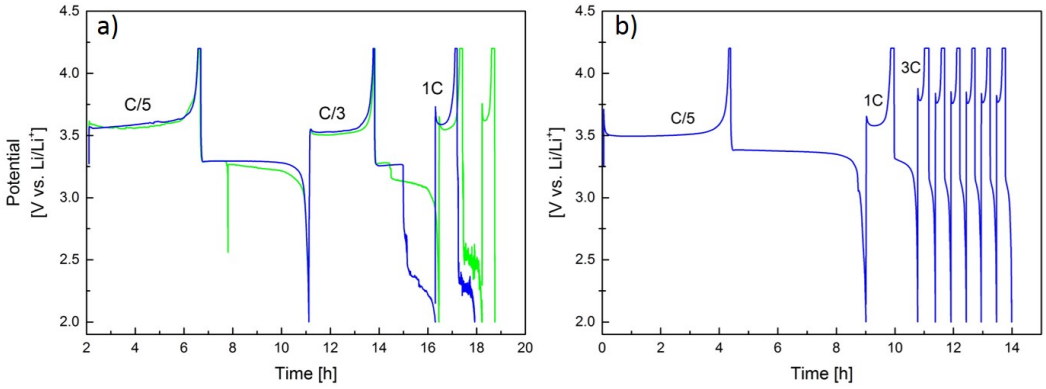

Figure 2.4 Potential profiles of an *operando* EPR lithium/LFP cell with a thin and rigid polyolefine separator (a) or a thick and compressible glass fiber separator (b); the green and blue curves in a) show two nominally identical experiments.

2.2 Operando X-Ray Absorption Spectroscopy

X-ray absorption spectroscopy is a structural characterization technique based on the photoelectric effect. An x-ray beam is used to excite an electron from an inner shell of an atom in the sample, creating a core hole. The filling of the core hole by an electron from a higher shell is accompanied by the emission of an x-ray photon. Both x-ray absorption and x-ray fluorescence can be used for detection. In the former mode, the x-ray source, sample and detector are arranged in a 180 degree geometry, in the latter in a 45 degree geometry. For light elements like sulfur and first-row transition metals usually K-edge absorption is used with element specific absorption energies of 2.47 keV for sulfur and 5 to 10 keV for first-row transition metals. For heavy atoms, the L-edge is more commonly used because of the high K-edge energy. For example, the platinum K-edge has an energy of 78.4 keV while the L-edge energy is 13.9 keV. Usually a synchrotron serves as x-ray source because of the high intensity and wide continuous spectral range.

X-ray absorption spectroscopy can be subdivided into x-ray absorption near-edge structure (XANES) and extended x-ray absorption fine structure (EXAFS) spectroscopy. A XANES spectrum is measured close to the absorption edge and contains information on the amount (height of edge jump) and the oxidation state (exact edge position) of the respective atom. EXAFS is based on the inelastic scattering of the photo electron with neighboring atoms. From the interference pattern, measured at energies up to several hundered eV's above the absorption edge, it is possible to determine the distance and amount of neighboring atoms and deduce the local geometry of the scattering atom. In contrast to diffraction techniques, no long range order is required for EXAFS analysis.

X-ray absorption spectroscopy is a common tool in battery research and has already been applied under *in situ*/*operando* conditions. *Operando* XANES is especially popular for the investigation of the complex discharge mechanism in lithium-sulfur cells, as it can differentiate between terminal and internal sulfur atoms in polysulfides and thereby determine the average polysulfide chain length (e.g., Li_2S_x with $1 \leq x \leq 8$).[129;130;131;132] In most studies, an averaged signal from both the sulfur cathode and the polysulfide containing electrolyte in the separator is measured. In contrast, a special *operando* XAS cell design developed by our group allows the selective measurement in either the anode, cathode or separator.[131] The concept of this *operando* XAS cell, which operates in fluorescence mode, is shown in Figure 2.5a.

One side of the flat, rectangular electrodes and the separator (10 x 10 mm) is pressed against the front plate of the cell which contains a 2 mm tapered hole serving as the x-ray window. The window is sealed with an aluminized Kapton® foil (100 nm Al-film on 8 μm Kapton®) which is an air and water permeation barrier. For the sulfur K-edge at 2.47 keV the 8 μm aluminized Kapton® foil has a transmission of about 50%, for the iron K-edge at 7.11 keV a transmission of over 80% is reached even if a second (non-aluminized) 25 μm thick Kapton® foil is additionally added for enhanced mechanical stability of the window. The penetration depth into the respective electrodes is about 50 μm at 2.47 keV and about 500 μm at 7.11 keV. It is important to obtain a homogeneous electrochemical reaction over the entire electrode area because only the uppermost part of the electrodes and the separator is measured (50 to 500 μm penetration depth versus 10 mm electrode side length). The cell (1) is mounted in a 45 angle with respect to the incoming x-ray beam (2) and the detector (3) as shown in Figure 2.5b. The size of the incoming x-ray beam has to be adjusted according to the required spatial resolution. Figure 2.5 c shows the top view of the x-ray window (without Kapton® foil) with the aluminum current collector cube (4), the cathode (5) (120 μm thickness), two compressed gass fiber separators (6) (about 350 μm thickness), the anode (7) (120 μm thickness) and the copper current collector cube (8). The dashed red line represents the size (100 x 1000 μm) and orientation of the incoming x-ray beam used for the spatially resolved XAS experiments. In most beamlines, the beam can be focused in one direction and is cut by slits in the other. In contrast to focusing, cutting with slits causes a significant loss of the incident beam intensity. The advantage of slits is a very well defined and sharp beam width while focusing yields a rather broad peak-like intensity distribution. Therefore the beam is cut in horizontal direction and focused in the vertical direction.

In the beginning of a spatially resolved XAS experiment, detailed mapping has to be carried out to determine the exact position of the electrodes. Note, that the aluminized Kapton® is not permeable for visible light and a standard optical fluorescence screen is therefore not helpful. Mapping is based on line scans (Figure 2.5d) of the total fluorescence intensity using a certain, fixed x-ray energy. The cell sample stage is moved in μm-steps in horizontal or vertical direction while the beam position and energy are kept constant. In order to reduce the time of line scans, the total fluorescence is measured without spectral resolution. As a consequence, a "copper line scan" (see red line in Figure 2.5 d), measured with a fixed x-ray energy slightly above the copper edge, is also sensitive to other elements with a slightly lower K-edge energy (e.g. Mn,

Fe, Co). The copper line scan is carried out to determine the position of the current collector/anode interface. A line scan of a metal contained in the cathode active material is carried out to determine the position of the cathode/separator interface. In combination with the known thickness of anode, cathode and separator a detailed map of the cell interior is obtained and measuring positions for the *operando* XAS experiment can be defined. Figure 2.5d shows the successful mapping of a preaged LTO/NMC cell. The steep decline of the red curve (copper line scan) at x = 3.5 mm corresponds to the current collector/LTO interface. The maximum of the green line (manganese line scan) in a similar x-position corresponds to manganese deposited in the LTO electrode. The steep increase of the green curve at x = 3.7 mm corresponds

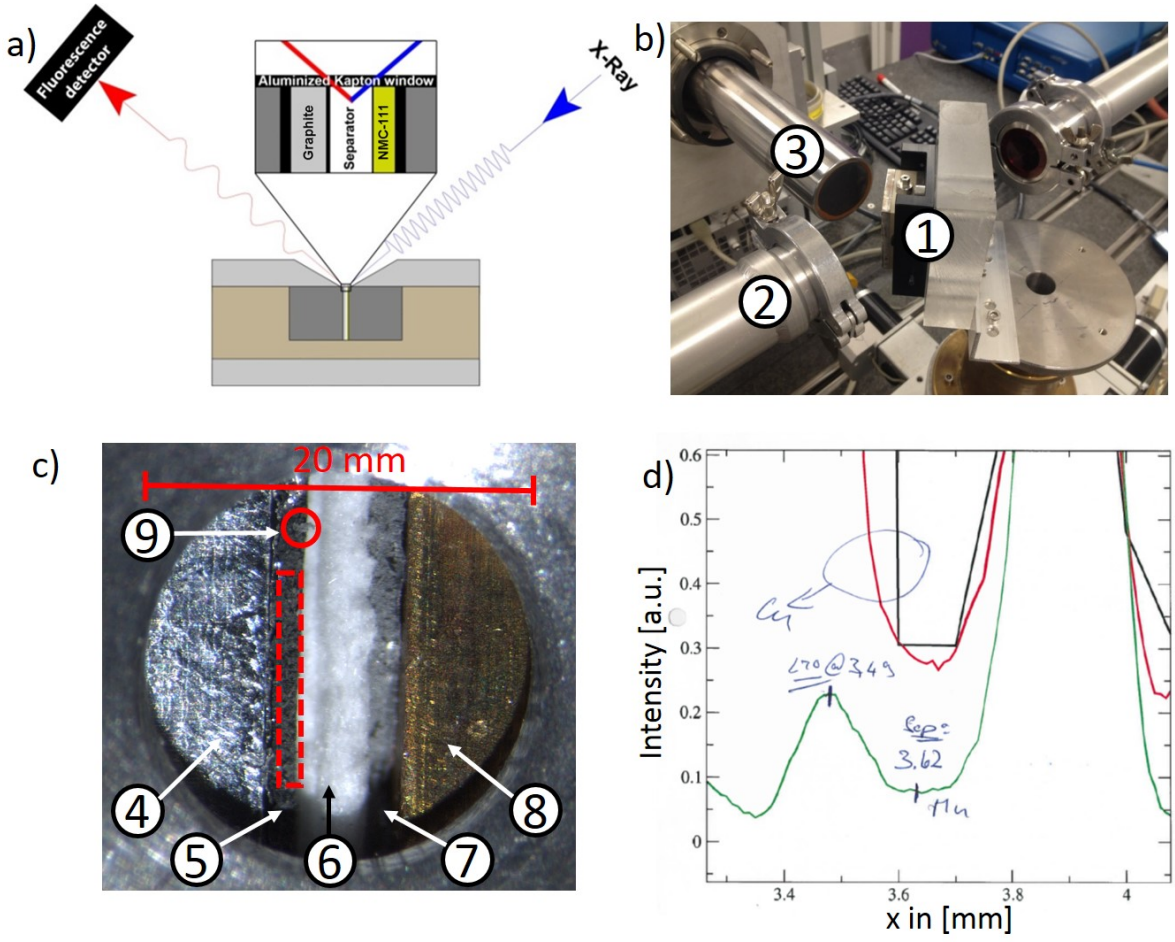

Figure 2.5 a) General concept of *operando* XAS cell with spatial resolution (Image adjusted from open access article [131]); b) Fluorescence set-up with 45 degree angle between the cell (1), the incoming x-ray beam (2) and the detector (3); c) Microscope image of an LTO/NMC cell without the aluminized Kapton® foil window with size and orientation of x-ray beam (red dashed line) and detached LTO particle (red circle); d) Mapping line scans for determination of the electrode and separator positions.

to the separator/NMC electrode interface. Two factors have to be considered for the correct interpretation of the line scans: i) the cell is mounted in a 45 degree angle, so moving the sample stage by a distance d results in an effective displacement of cos(d) and ii) the fluorescence intensity measured with a beam width in x-direction of Δx in position p gives an averaged value for $p \pm \Delta x/2$.
The general electrochemical performance of the XAS cell design is very good. The potential curve shown in Figure 1.4 (Section 1.2, page 8) was measured in the XAS cell and looks identical to a potential profile in a standard cell design. The XAS cell can be cycled for up to one week with a similar capacity retention as a standard cell design. A major problem are cycling conditions which cause heavy gassing; the resulting pressure increase first causes bending out and then rupture of the Kapton® window. Therefore, experiments with harsh cycling conditions like high cut-off potentials are currently limited to a few hours.
A major challenge for the study of the transition metal deposition at the anode (Section 3.2) is the presence of small detached cathode active material particles. The amount of transition metal deposited in the anode electrode is typically on the order of 1 mmol/$L_{electrode}$, where $L_{electrode}$ refers to the volume of the anode electrode (in liter) including graphite active material and electrode porosity. In comparison, the transition metal amount in a solid NMC particle is about 50 mol/L_{NMC} (ρ_{NMC} = 4.72 g cm^{-3}) which is four to five orders of magnitude more than the expected concentration increase in the anode. As a consequence, even a μm-sized particle of cathode active material which may have gotten detached from the cathode during the cell assembly can dominate the transition metal XAS spectra measured in the anode position if it comes to rest on the anode close to the x-ray window. In Figure 2.5c, the red circle shows a rather big detached LTO particle. To avoid this problem, adhesion of the cathode coating has to be essentially perfect and electrode cutting and cell assembly has to be carried out very carefully.

2.3 In Situ Neutron Diffraction

Neutron diffraction is based on scattering of cold neutrons and can be used to identify the crystalline phases in a sample. By Rietveld analysis of a neutron diffractogram it is possible to determine the atomic structure, lattice parameters, and particle size of crystalites. Neutron diffraction is a very expensive technique as it requires a nuclear reactor as neutron source, but it has several advantages over the more readily available x-ray diffraction (XRD). Neutron diffraction is much more sensitive for light elements, such as lithium, than XRD which is important for lithium-ion battery materials. Furthermore, the penetration depth of neutrons is so high that it is truly bulk sensitive and can even be applied for standard 18650-type cells in their normal metal housing, which is not possible with XRD.[133] This is a huge advantage as there are factors influencing the aging behavior of large format cells which cannot be properly studied in smaller lab cells like Swagelok cells or specially designed *in situ*/*operando* cells. Examples of such factors are inhomogeneous heat distribution[134;135] and current collector positioning.[136]

Neutron diffraction has been applied both under *in situ* and *operando* conditions for battery research;[137;138;139;109] *in situ* experiments are more common though, because the recording time for a neutron diffractogram of several hours is long in comparison to typical battery cycling times. At the neutron reactor FRMII (Garching, Germany) there are two different neutron diffractometer beamlines, SPODI and STRESS-SPEC, which are suitable for the investigation of 18650-type cells.[140;141] The method development for diffraction studies with 18650 cells is already completed for both beamlines.[142;143;144;118]

3 Results

This Section contains the journal articles comprising this PhD thesis. Publications are not presented in chronological order, but rather grouped thematically.
Section 3.1 shows the *operando* EPR studies. The EPR project has been carried out in collaboration with Prof. Rüdiger-A. Eichel, Prof. Josef Granwehr and Peter Jakes from the Institute of Energy and Climate Research - Fundamental Electrochemistry (IEK-9) at the Forschungszentrum Jülich (Germany). In the first publication (Section 3.1.1), the development of the *operando* EPR cell design is described and then the formation of lithium dendrites on lithium metal anodes is investigated. In the second publication (section 3.1.2),which will be submitted for publication soon, *operando* EPR is used for the quantitative detection of lithium plating on graphite anodes. In the third publication (Section 3.1.3), *operando* EPR is used in combination with a chemical spin trap to investigate singlet oxygen evolution during charging of aprotic lithium-oxygen batteries.
Section 3.2 presents the first *operando* XAS spectroscopy study on transition metal dissolution and redeposition in graphite/NMC cells. The experiments presented in this study are carried out with time and spatial resolution making use of the previously described cell design. The XAS project has been carried out in collaboration with Prof. Moniek Tromp from the Van't Hoff Institute for Molecular Sciences at the University of Amsterdam (Netherlands).
In Section 3.3 neutron diffraction is used for the investigation of capacity loss mechanisms in commercially produced 18650 type graphite/LFP cells. This project has been carried out in collaboration with the VW-VM Forschungsgesellschaft mbH & Co. KG (Ellwangen, Germany) and the Heinz Maier-Leibnitz Zentrum (MLZ) in Munich (Germany).

3.1 Operando Electron Paramagnetic Resonance Studies

3.1.1 Lithium Dendrite Formation On Lithium Metal Anodes

This section presents the article "*Operando* Electron Paramagnetic Resonance Spectroscopy - Formation of Mossy Lithium on Lithium Anodes during Charge-Discharge Cycling" which was submitted in August 2014 and accepted for publication in the peer reviewed Journal *Energy & Environmental Science* in February 2015. It is an open access article distributed under the terms of the Creative Commons Attribution 3.0 Unported Licence. The publication was presented on international conferences, for example at the 226th Meeting of The Electrochemical Society in Chicago (USA) in May 2015 (Abstract Number: #652). The permanent weblink to the article is http://pubs.rsc.org/-/content/articlehtml/2015/ee/c4ee02730b.
The paper describes the development and electrochemical benchmarking of our concentric battery cell design for *operando* EPR spectroscopy. The lithium/LFP potential profile and achievable specific capacity is very similar for the *operando* EPR cell in comparison to a standard Swagelok cell. The *operando* EPR cell also has a reasonable rate capability; the discharge capacity starts to deviate from a standard cell design at a 1C rate. The main reason for the lower capacity at high rates is probably the lack of compression. To the best of our knowledge, this is the first detailed *operando* EPR study with a battery context. The only other battery related *in situ*/*operando* EPR study was published in 1995 by Zhuang et al. as "preliminary note", using *in situ* EPR spectroscopy in a flat cell for the study of lithium intercalation into graphite.[122]
The formation of micro-structured mossy/dendritic lithium[1] has been studied since the early 1980s, but so far no satisfactory solution has been found. Most studies on lithium metal plating rely on microscopic techniques which can give valuable information regarding the exact structure and location of lithium dendrites but are non-quantitative;[145;146;147] furthermore, the assessment of microscopic images is by nature rather subjective. The difficulty for the (semi-) quantitative detection of lithium metal dendrites is the simultaneous presence of a large excess of "bulk lithium" in the lithium anode. In this study we show that it is possible to semi-quantitatively

[1] There are several different terms which are generally used to describe micro-structured lithium, e.g. lithium moss, lithium dendrites and lithium filaments. There is no clear definition for these terms.

detect lithium dendrites by exploiting the so-called skin effect. The penetration depth of the microwave into lithium metal is about 1 μm, which is similar to the size of micro-structured mossy/dendritic lithium but orders of magnitgude smaller than the dimension of the lithium foil. The same concept was previously used by Clare Grey and co-workers in the same context for NMR spectroscopy,[123] but the penetration depths for the NMR radiofrequency into lithium metal is about 10 μm, making NMR less sensitive than EPR for detection of micro-structured lithium.
In this study we investigate the influence of current density and electrolyte composition on the reversibility of the lithium plating/stripping process. The electrolyte additive fluoroethylene carbonate (FEC) is found to markedly reduce the formation of micro structured lithium. This results has recently been confirmed by a publication of Aurbach and co-workers.[148]

Author contributions

J.W. and C.M. developed the *operando* EPR cell. J.W., C.M. and P.J. carried out the EPR experiments. J.W., P.J., and J.G. carried out the data analysis. J.W. and J.G. wrote the manuscript. All authors discussed the data and commented on the results.

Energy & Environmental Science

PAPER

Cite this: *Energy Environ. Sci.*, 2015, **8**, 1358

Operando electron paramagnetic resonance spectroscopy – formation of mossy lithium on lithium anodes during charge–discharge cycling

Johannes Wandt,[a] Cyril Marino,*[a] Hubert A. Gasteiger,[a] Peter Jakes,[b] Rüdiger-A. Eichel[bcd] and Josef Granwehr*[b]

Received 27th August 2014
Accepted 13th February 2015

DOI: 10.1039/c4ee02730b

www.rsc.org/ees

The formation of mossy lithium and lithium dendrites so far prevents the use of lithium metal anodes in lithium ion batteries. To develop solutions for this problem (*e.g.*, electrolyte additives), *operando* measurement techniques are required to monitor mossy lithium and dendrite formation during electrochemical cycling. Here we present a novel battery cell design that enables *operando* electron paramagnetic resonance (EPR) spectroscopy. It is shown that time-resolved *operando* EPR spectroscopy during electrochemical cycling of a lithium-metal/$LiFePO_4$ (LFP) cell provides unique insights into the lithium plating/dissolution mechanisms, which are consistent with *ex situ* scanning electron microscopy (SEM) analysis. To demonstrate the viability of the *operando* EPR method, two cells using different electrolytes were studied. When using an electrolyte containing fluoroethylene carbonate (FEC) additive, a higher reversibility of the lithium anode and reduced formation of micro-structured (mossy/dendritic) lithium were observed.

Broader context

The expanding market for portable electronic devices and the emerging electric transportation sector create an increasing demand for rechargeable high energy density batteries. One option to significantly increase the energy density would be the use of metallic lithium anodes due to the light weight and very low potential of lithium. Unfortunately, the use of lithium anodes with commonly used liquid aprotic electrolytes has so far been prevented by the formation of micro-structured lithium during battery charge – so called dendritic or mossy lithium – which both consumes active lithium and liquid electrolyte and also poses a serious safety hazard. In this study, we present electrochemical *operando* EPR (electron paramagnetic resonance) spectroscopy as a novel tool to study the formation of lithium dendrites in real-time and under realistic conditions. As a case study, we investigate the extent of the formation of micro-structured lithium in lithium/lithium iron phosphate cells in the absence or presence of fluoroethylene carbonate additive, which is known to reduce dendrite formation. The results provided by a detailed EPR line shape analysis and supported by *ex situ* SEM images clearly show that *operando* EPR spectroscopy is a powerful diagnostic technique, yielding valuable information that is not accessible by commonly used microscopic techniques.

Introduction

Lithium metal would be an ideal battery anode material due to its high specific capacity (3860 mA h g^{-1}) and its very low potential (−3.04 V *vs.* standard hydrogen electrode), thus enabling outstanding gravimetric energy densities. A lithium metal anode combined with lithium- and manganese-rich layered metal oxide cathodes would enable an energy density increase of Li-ion battery systems by 50% to ≈300 W h kg_{system}^{-1} compared to currently used graphite anodes.[1] The development of a reliable lithium anode is especially critical for new cell chemistries, such as Li–Sulfur and Li–Air, in order to realize their potential gravimetric energy densities.[1–4] According to Sion Power, a leading developer of Li–S batteries, the *"generation of porous 'mossy' Li deposits"* is one of *"two major mechanisms limiting Li–S cycle life".*[5] A variety of strategies to *"master the Li–electrolyte interface"*,[6] ranging from ceramic blocking layers[7–9] and advanced charging procedures[10] to organic or inorganic electrolyte additives,[11,12] have been investigated with only limited success so far.[13]

Despite significant scientific effort and large investments of battery makers over the last 40 years, the lithium metal anode in combination with liquid electrolytes has not been successfully commercialized[14] (the only exception are liquid solvent free lithium–polymer batteries). This is mainly due to the formation of micro-structured (mossy/dendritic) lithium during battery charge, which reduces cell life due to irreversible electrolyte consumption[15] and also poses a serious safety threat due to the possibility of internal cell shortening.[16,17]

[a]*Technical Electrochemistry, Technische Universität München, Garching, Germany. E-mail: cyril.marino@psi.ch*

[b]*Institute of Energy and Climate Research (IEK-9), Forschungszentrum Jülich, Jülich, Germany. E-mail: j.granwehr@fz-juelich.de*

[c]*RWTH Aachen University, Institute of Physical Chemistry, Aachen, Germany*

[d]*Jülich Aachen Research Alliance (JARA), Section JARA-Energy, Aachen, Germany*

This journal is © The Royal Society of Chemistry 2015

These persistent problems led to the use of graphite as anode material instead of metallic lithium by Sony in 1991, paving the way for modern Li-ion battery technology.[18,6] Graphite can reversibly intercalate and deintercalate lithium ions, thus enabling excellent cycle life over several thousand cycles.[19] However, the intercalation potential for lithium ions into graphite is very close to the Li/Li^+ potential, which can cause plating of metallic lithium on the graphite particles if the battery is charged at low temperatures or with high *C*-rates.[20–26] Lithium plating on graphite usually takes place in a dendritic morphology and therefore impairs both cell life and safety due to the abovementioned reasons.[25,27] Accordingly, researchers have tried to find electrolyte compositions and additives to prevent or at least reduce lithium plating and dendrite formation.[28–30] Since lithium plating on graphite is partially reversible at open circuit conditions, detailed studies of dendrite formation require *operando* rather than *in situ*/*ex situ* techniques.

Most studies on lithium plating and dendrite formation are based on microscopy techniques. Optical spectroscopy has been successfully applied in both *in situ*[31,32] and *operando*[33,34] setups but is limited by the low resolution. In contrast, scanning electron microscopy (SEM) shows better resolution but is restricted to polymer electrolyte cells for *in situ*[35] or *operando* experiments.[16] At the current stage, there are only very few analytical techniques available that give quantitative or semi-quantitative information about the occurrence of micro-structured lithium during cell cycling under *operando* conditions. In 2010, Bhattacharyya and co-workers introduced electrochemical *in situ* and *operando* ^{7}Li-NMR spectroscopy,[36] which has since then also been used by other groups.[37–39] NMR spectroscopy can provide valuable insights as exemplified by the *operando* imaging of lithium dendrites by Chandrashekar *et al.*[37] Still, one disadvantage of *operando* NMR is the low spectral resolution due to the inability to use magic angle spinning. As another analytical approach that is applicable during electrochemical cell cycling, *operando* electron magnetic measurements have recently been presented by Gershinsky and co-workers for the investigation of conversion materials such as $FeSb_2$.[40]

In this work we propose to use *operando* electron paramagnetic resonance (EPR) spectroscopy as a new analytical technique for the semi-quantitative determination of mossy or dendritic lithium, henceforth referred to as "micro-structured lithium" (as suggested by Bhattacharyya and co-workers[36]). With EPR spectroscopy, the detection of micro-structured lithium on the anode surface is based on the EPR resonance caused by the conduction electrons in metallic lithium, whereas Li^+-ions are EPR inactive. In comparison to NMR spectroscopy, EPR is expected to show a higher sensitivity per unit volume due to the higher gyromagnetic ratio of electron spins and a higher selectivity for dendrite detection due to the roughly ten times smaller skin depth of EPR microwaves in comparison to NMR radiowaves.

A new electrochemical cell setup suitable for *operando* EPR spectroscopy during electrochemical cycling is introduced. We investigate the morphological changes of a lithium metal anode during cycling of a $Li/LiFePO_4$ (LFP) cell as case study to demonstrate the capabilities of electrochemical *operando* EPR spectroscopy. First, our new cell design is validated by a comparison of the electrochemical performance with a standard cell design. Next, the evolution of the EPR resonance of metallic lithium is analyzed using a standard electrolyte with or without fluoroethylene carbonate (FEC) additive, which is known to reduce lithium dendrite formation.[29,30,41] The results obtained by *operando* EPR spectroscopy, supported by a detailed EPR lineshape analysis, are confirmed by *ex situ* scanning electron microscopy (SEM) images.

Materials and methods

Operando cell design

Fig. 1 shows a schematic drawing of the *operando* EPR cell. A coaxial cell design for electrochemical EPR spectroscopy has previously been suggested by Zhuang *et al.*[42] We use a tubular design with a concentric arrangement of the cell components to meet the geometric constrains of the EPR spectrometer. A central copper wire (1 mm diameter, 99.9%, Alfa Aesar) serves as anode current collector and is wrapped with lithium metal foil (450 μm thickness, 25 mm length, 99.9%, Chemetall, Germany). PTFE heat shrink tubes (Deray PTFE, Autec, Germany) confine the lithium anode on both sides to prevent a short circuit. A glass–fiber separator (250 μm thickness, 40 mm length, glass microfiber filter 691, VWR) is rolled around the lithium anode. The LFP electrode (20 mm length), which is coated directly onto a Celgard separator (C480), is assembled with the separator facing inwards. A helical aluminum wire (0.5 mm diameter, 99.999%, Alfa Aesar) serves as cathode current collector. The cell is enclosed by a quartz glass tube (6 mm outer diameter, 0.5 mm wall thickness, QSIL, Germany). The combination of an electrode coated directly onto the porous separator and the aluminum wire as current collector ensures ionic conduction between anode and cathode without shielding off the microwaves. Electrolyte (500 μL) is added directly onto the glass–fiber separator inside the glass tube using an Eppendorf pipette. The cell is sealed on both ends with capillary wax and dried inside the glove box for several hours.

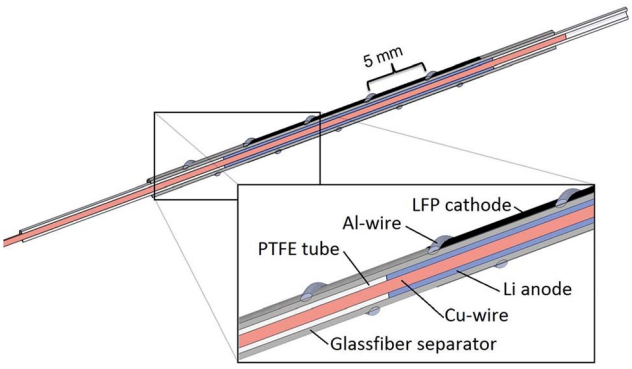

Fig. 1 Design of electrochemical operando EPR cell. The surrounding quartz glass tube is omitted for clarity.

Electrode and electrolyte preparation

The LFP electrodes were prepared by gap bar coating using an ink composed of 80 wt% carbon coated LFP (1 μm, 2.5 wt% C, 15 $m^2 g^{-1}$, Clariant), 10 wt% Super C65 (Timcal), 10 wt% PVDF (Kynar HSV900, Arkema) and *N*-methyl pyrrolidone (99.5%, Sigma-Aldrich) as solvent. The ink was prepared by homogenizing all components in a planetary mixer (ARV-310CE, Thinky) for 20 minutes at 2000 rpm. It was coated either onto a Celgard C480 separator for EPR experiments (250 μm wetfilm thickness, loading: ≈3.9 mg_{LFP} cm^{-2}) or onto an aluminum foil for SEM experiments (350 μm wet film thickness, loading: *ca.* 5.8 mg_{LFP} cm^{-2}). After coating and solvent evaporation at 60 °C, rectangular electrodes (20 mm × 7 mm) were cut out with a scalpel or round electrodes (10 mm diameter) were punched out with a precision punch (Hohsen, Japan). The electrodes were dried in dynamic vacuum at 95 °C for 12 hours in a glass oven (Büchi, Switzerland). The different LFP loadings for the EPR and SEM experiments are necessary to achieve the same current density (in mA cm_{Li}^{-2}) on the lithium anode due to the concentric cell setup of the *operando* EPR cell. As electrolyte, 1 M lithium hexafluorophosphate ($LiPF_6$) in a mixture of ethylene carbonate (EC) and ethyl methyl carbonate (EMC) (LP57, BASF) was used either as received or after the addition of 10 wt% of FEC (Solvay Chemistry). Cell assembly and preparation of SEM samples was carried out inside an argon-filled glove box (MBraun, O_2 and H_2O less than 0.1 ppm).

Electrochemical testing

Electrochemical testing was done with a VMP3 potentiostat (Bio-Logic, France). After at least 12 hours at open circuit, the cells were cycled between 2.0 and 4.2 V *vs.* Li/Li^+. The cells were charged in a CCCV mode (CV step until current dropped to 20% of current for *C*/5 charge) and discharged galvanostatically with the following cycling procedure: (i) one *C*/5 cycle (≡0.23 mA cm_{Li}^{-2}); (ii) one 1*C* cycle (≡1.15 mA cm_{Li}^{-2}); (iii) six 3*C* cycles (≡3.45 mA cm_{Li}^{-2}); (iv) one *C*/1.5 cycle (≡0.76 mA cm_{Li}^{-2}). The *C*-rate is calculated with respect to the nominal capacity of the LFP electrode and the current density is normalized to the lithium surface area. Notice that the current density (in mA cm^{-2}) is higher for the lithium electrode than for the LFP electrode due to the concentric cell design.

SEM experiment

SEM images were recorded on a JEOL JCM-6000 SEM (secondary electron imaging, 15 kV accelerating voltage). The lithium electrodes (17 mm diameter) for the SEM analysis were cycled against LFP electrodes (10 mm diameter) in a custom-made cell described previously.[43] An additional Celgard separator was placed between the lithium anode and the glass–fiber separator to prevent damaging the micro-structured lithium surface by the removal of the glass–fiber separator, since it typically strongly sticks to the lithium surface after very few cycles. In contrast, the Celgard separator does not get penetrated by lithium filaments within the limited number of cycles used in this study, so that it can be removed without damaging the lithium anode surface. This is confirmed by the absence of hydrogen gas evolution upon immersing the removed Celgard separator into water; the same observation was reported by Gallus *et al.*[44] After cycling, the cells were transferred back into the glove box and the lithium electrode was harvested. The lithium electrodes were washed twice with 500 μL dimethyl carbonate (DMC) in order to remove $LiPF_6$ and EC residues and dried in vacuum for 15 minutes. The cells were transferred into the SEM using a conductive carbon tape (Plano, Germany) and a sample holder that limited the contact to ambient atmosphere to a few seconds; a short air contact has been reported to have no impact on the microscopic structure of dendritic lithium surfaces.[35] To determine the thickness of the micro-structured lithium layer, a special sample holder was used, in which the lithium electrode was bent down by 90°.

EPR spectroscopy

EPR spectra were recorded on a Bruker ElexSys E-540 continuous-wave (cw) X-band EPR spectrometer, equipped with an ER 4108 TMHS resonator operating at 9.897 GHz. Microwave power was set to 1.00 mW. Sweeps were performed with 5 mT width and a center field of 353.2 mT. As is common practice, the cw EPR spectra were recorded as first derivatives of the signal with respect to the external magnetic field B_0. The field modulation frequency was set to 100 kHz, and the modulation amplitude was 0.1 mT. EPR spectra were recorded continuously during cell cycling. Each spectrum took 1 min to record, which represented the temporal resolution of the two-dimensional time-resolved EPR data.

The EPR signal caused by Fe^{3+} is generally much wider than the signal from metallic Li.[45,46] It could be suppressed by using a relatively low modulation amplitude and by performing a zeroth order baseline correction.

EPR data analysis

A quantitative analysis of EPR spectra from conduction electrons in metals needs to take the diffusion of electrons in and out of the skin of the conductor into account.[47] Since the phase of the microwave field used to excite the spins changes as a function of depth into the conductor, the shape of the EPR resonances varies as a function of the geometry and thickness of the conductor. This complicates the quantification of the EPR signal, since the number of contributing spins is not simply proportional to the area under the integrated experimental spectrum, as conventionally assumed for the determination of spin concentrations.[48] An exact quantification requires either a calibration with a set of samples that cover the full range of lineshapes observed experimentally or a theoretical model that can be used to fit the experimental resonances. Nonetheless, as long as the signal is dominated by a single resonance and the lineshape does not change drastically, integration of the experimental first derivative spectrum, followed by the calculation of the area under the obtained spectrum, provides at least a relative measure of changes in the number of spins contributing to the signal. If a lineshape change occurs quickly, the continuity of the signal amplitude

 This journal is © The Royal Society of Chemistry 2015

can be used as a qualitative test whether a complete recalibration is required. To minimize systematic errors caused by deviations of the cell positioning and orientation in the EPR resonator, the amplitude was normalized to the amplitude of the pristine cell at the beginning of electrochemical cycling. Besides its simplicity, this method has the advantage that it is very robust.

Theoretical expressions for the lineshape of conduction EPR signals have been derived for flat plates of various thicknesses d[47] and for spherical metal particles with different radii a.[49] For porous or micro-structured lithium, no theoretical lineshape and amplitude models are currently available. Since the expressions for flat plates and for spherical particles agree with each other in the limit of thicknesses and radii that are either very small or very large compared with the skin depth δ of the metal, we use an empirical approach, validated by comparison with SEM images at selected positions within the cycling protocol, to relate EPR lineshapes with the dimension of the structures of deposited lithium.

For conductor structures that are much smaller or much bigger than δ, the resonance can be represented as a superposition of the absorptive part χ'' and the dispertive part χ' of the complex susceptibility,[50]

$$\chi = \chi''\cos(\phi) + \chi' \sin(\phi) \quad (1)$$

where the phase ϕ between the two components characterizes the asymmetry of the resonance. Since conduction EPR resonances are isotropic in the limit of sufficiently high electronic conductivity, χ'' gives rise to a Lorentzian with half width at half height Δ, located at position B_{res}, and χ' represents the corresponding dispersion line. Using $B_{res} = h\nu_0/g\beta_e$, where h is Planck's constant, ν_0 is the microwave frequency and β_e is the Bohr magneton, B_{res} is related to the Landé g factor. Therefore the spectrum can be characterized using only the parameters g, Δ and ϕ. The experimentally measured first derivative signal was fitted using

$$I(B_0) = I_0\left[\frac{\sin(\phi)}{\Delta^2 + (B_0 - B_{res})^2} - 2(B_0 - B_{res})\frac{\cos(\phi)\Delta + \sin(\phi)(B_0 - B_{res})}{\left(\Delta^2 + (B_0 - B_{res})^2\right)^2}\right], \quad (2)$$

where I_0 is the amplitude of the signal, which is assumed to be proportional to the number of contributing spins and an instrumentation-dependent constant factor. In addition, qualitative features of the sample geometry can be deduced from Δ and ϕ. For example, $\phi \sim \pi/2$ indicates that $d \gg \delta$ and $\phi \sim 0$ suggest $d \ll \delta$.[51]

Results

Electrochemistry

The new *operando* EPR cell design was validated by comparing the voltage profiles and the electrochemical performance with our custom made standard cell design with a spring compressed circular electrode stack, which has been described in a previous publication.[43] Fig. 2 shows the initial $C/5$ and the sixth $3C$ cycle. The $C/5$ cycles for all cells (Fig. 2a) show a flat voltage plateau around 3.5 V *vs.* Li/Li^+, which is typical for LFP.[52] The polarization is low during charge and discharge for both cell designs, with a slightly lower overpotential for the cell with the FEC additive. The $3C$ cycles (Fig. 2b) show a significantly higher overpotential and lower charging capacity for the *operando* cell design. In the absence of FEC, both the EPR and the standard cell show a second voltage plateau during $3C$ discharge, which is caused by changing overpotentials of the lithium counter electrode during the first cycles with higher current density.

Fig. 2c compares the rate capability of the *operando* EPR cells and the standard cell design. They all yield specific capacities of ≈150 mA h g_{LFP}^{-1} at $C/5$. The moderate deviation from the theoretical specific energy of 170 mA h g_{LFP}^{-1} is within the range that is typically observed in practical LFP cells,[52–56] particularly since our LFP electrodes were not optimized for high rates. Above $C/1.5$, the standard cell performs better, still maintaining ≈130 mA h g_{LFP}^{-1} at $3C$ compared to only ≈100 mA h g_{LFP}^{-1} for the *operando* EPR cell. The main reasons for the reduced rate performance of the *operando* EPR cells are (i) the limited electric contacting of the LFP electrode by the aluminum wire, which increases the ohmic resistance, and (ii) the lack of compression compared to the metal spring compression in the standard cell design.[43] While the limited contact area of the LFP electrode with the current collector might negatively affect the homogeneity of the current distribution at high C-rates, this effect would be the same with and without the FEC additive. Despite these minor shortcomings, our *operando* EPR cell clearly shows essentially identical cycling behavior at low C rates to that of optimized conventional battery cells.

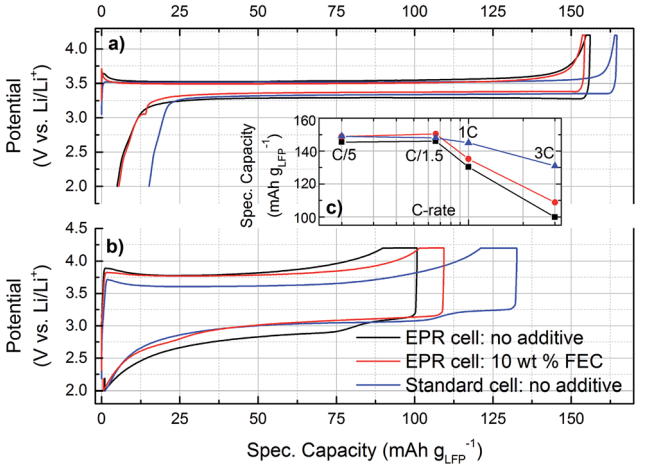

Fig. 2 Voltage profiles at (a) $C/5$ and (b) $3C$ of the *operando* EPR cells containing electrolyte without additive (black) or with 10 wt% FEC (red), and of a standard cell design (blue) for comparison. (c) Comparison of the rate capability of these cells.

Li-EPR resonance during electrochemical cycling

Fig. 3 shows the evolution of the EPR signal and the voltage curves for the cell with standard electrolyte and with FEC additive. The EPR signal shows a significant difference for both cells already during the first cycle. With standard electrolyte, the Li EPR intensity increases during charge (≡non-uniform lithium plating) and hardly decreases during discharge (≡Li anode dissolution). In contrast, the increase is less pronounced with FEC-containing electrolyte and is completely reversible during the first cycle.

For subsequent cycles at higher *C*-rates, the EPR signal for the cell with standard electrolyte further increases during every charge without significantly decreasing during discharge. With FEC-containing electrolyte, the EPR signal also increases during charge, but decreases again during discharge, implying a better reversibility of the anode processes. Still, during the six 3*C*-cycles the EPR signal does not completely reverse during discharge, thus also causing a steady increase for the cell containing FEC electrolyte. An interesting detail, highlighting the adequate time resolution of the *operando* EPR technique, is the kink in the EPR signal with decreasing current density during the constant voltage charging step, observed during all six 3*C*-charges in FEC electrolyte (see middle panel in Fig. 3). At the end of the cycling procedure, the relative EPR signal with standard electrolyte exceeds the signal from the cell with FEC electrolyte by about a factor seven.

Fig. 4a–c compare the EPR spectra of the cells without and with FEC additive at different times. Both resonances show the asymmetric shape expected for metallic lithium. The shift of the center of the two lines with respect to each other is caused by a different resonance frequency of the resonator when loaded with the two cells. Both pristine cells at the beginning of cycling show a similar linewidth and a lineshape with $\phi \sim \pi/2$. Without additive, linewidth and asymmetry diminish within about 15 min and then remain fairly constant. With FEC additive, the EPR resonance changes significantly during the first cycle, but it is essentially reversible. Once charging at an increased rate, the shape of the resonance changes to a width and asymmetry similar to the cell without additives within two minutes.

The result of a least-squares fit of the EPR spectra, using a model consisting of two lines according to eqn (2), is shown for the cell with standard electrolyte in Fig. 4d, f and h and for the FEC cell in Fig. 4e, g and i. With a single line, no satisfactory fit was possible. Fig. 4d and e show the amplitude of the two components *(green and blue)* for the two cells, relative to the sum of both amplitudes at the beginning of cycling. These amplitudes are proportional to the number of contributing spins. The width and the asymmetry for both fitted signal components are shown as a function of time in Fig. 4f and g and Fig. 4h and i respectively. The two components show different characteristics during the first charge–discharge cycle for the

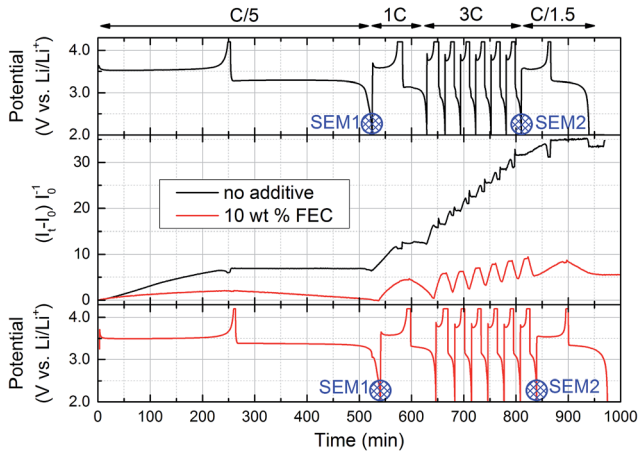

Fig. 3 Overview of cycling of *operando* EPR cells containing electrolyte without additive (black) and with 10 wt% FEC (red). Top and bottom panel: Voltage profiles according to cycling procedure shown above top panel; blue 'SEM1' and 'SEM2' markers indicate positions where *ex situ* SEM images of lithium anodes were recorded. Central panel: Normalized intensity of EPR signal, obtained by calculating the area under the numerically integrated experimental first derivate Li spectrum.

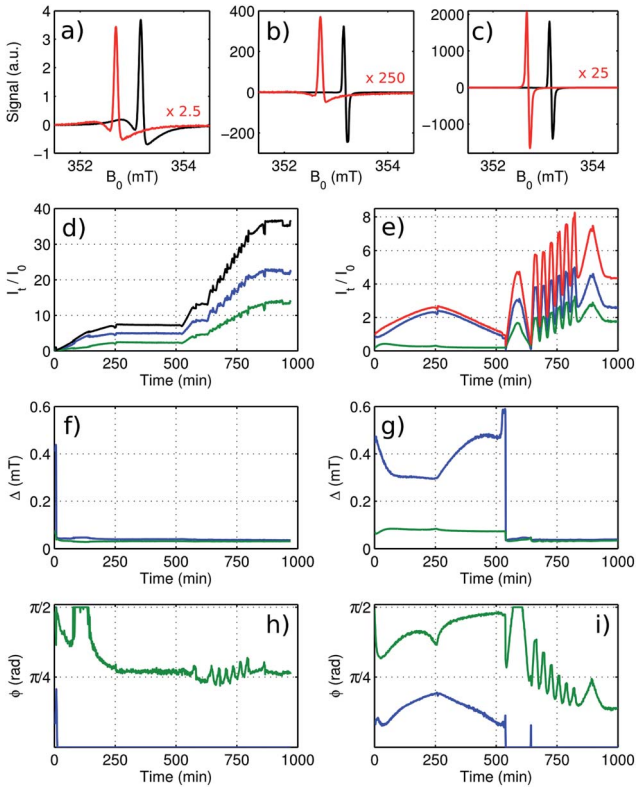

Fig. 4 Analysis of time-resolved EPR of metallic Li for cell containing electrolyte without additives (black) and cell containing electrolyte with 10 wt-% FEC (red). The spectra at the beginning of cycling (a), at the end of the first cycle (b), corresponding to position SEM1 in Fig. 3, and at the end of the last 3*C* cycle (c), corresponding to position SEM2 in Fig. 3, are compared. The red spectra are scaled as indicated in each panel. The resonances were fitted using a model with two phase-shifted Lorentzian lines. The amplitudes for the broader (blue) and for the narrower component (green) are shown for the cell without additives (d) and the FEC-containing cell (e). The sum of both components is shown in black and red for each cell. The width and the asymmetry of each component is shown for the cell without additives (f and h) and for the FEC-containing cell (g and i).

This journal is © The Royal Society of Chemistry 2015

FEC cell and for the first few minutes for the cell with standard electrolyte, indicating that these components are caused by two structurally different domains. The narrow component *(green color)* with $\Delta \sim 0.1$ mT shows a high asymmetry, $\phi \sim \pi/2$, which indicates that it is originating from bulk lithium of the anode. The broader component *(blue color)* with $\Delta \sim 0.3$–0.5 mT and an intermediate asymmetry, $\phi \sim \pi/6$, shows a reversible amplitude change by more than a factor two. At the same time the bulk lithium from the anode gets shielded by the additional metal on its surface, causing a signal decrease. Starting with the second cycle for the FEC cell, both linewidths abruptly adjust to a similar value and the amplitudes start to progress synchronously. The same effect is observed more gradually right from the beginning of cycling for the cell with standard electrolyte. This indicates that from that point, a distribution of ϕ rather than multiple distinct components is causing the observed lineshape.

During the first cycle for the cell with FEC additive and during the first few minutes for the cell with standard electrolyte, the asymmetry of the two components varies noticeably, albeit not drastically, and the two amplitudes are not changing synchronously, hence the area of the integrated signal does not lead to quantitative information about the relative number of spins contributing to the signal. Nonetheless, since the signal amplitude is dominated by the broader of the two components (which is not the visually dominant feature in Fig. 4a), the signal amplitudes as obtained by integration and by fitting differ from each other by less than 20%. For subsequent cycles, the lineshapes vary only weakly such that the relative amplitude changes obtained from calculating the area under the integrated experimental spectrum can be taken as semi-quantitative. Therefore this simple and robust method is suitable to quantify the relative growth of the porous layer of metallic lithium on top of the lithium anode during electrochemical cycling.

SEM images

SEM images of cycled lithium electrodes, shown in Fig. 5 and 6, were recorded after the *C*/5-cycle (position SEM1 in Fig. 3) and after the sixth 3*C*-cycle (position SEM2 in Fig. 3).

After the first cycle (SEM1), differences on the lithium electrode surface can already be detected by eye, as shown in the two insets in Fig. 5a and c. Note that one must only consider the central part of the lithium electrodes, as the LFP counter electrode has a smaller diameter than the lithium electrode (10 mm *vs.* 17 mm). The electrode containing standard electrolyte is partially covered by micro-structured lithium, which clearly protrudes from the electrode surface (Fig. 5a). The electrode containing FEC electrolyte shows black spots with hardly any three dimensional structure. According to the SEM images, at some of these black spots there is still a very thin layer of residual micro-structured lithium grouped around holes in the dense lithium surface. At other sites, the micro-structured lithium had dissolved completely, leaving behind bare holes. In contrast, the micro-structured lithium layer is thick and intact in the standard electrolyte. At some sites the micro-structured

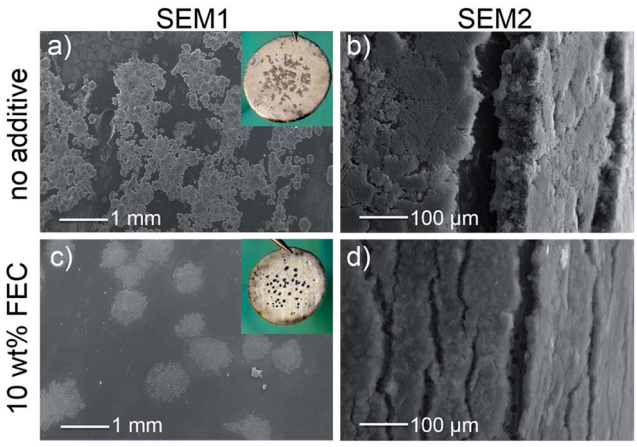

Fig. 5 *Ex situ* SEM images of cells containing standard electrolyte (top row) and electrolyte with 10 wt% FEC (bottom row). Images were recorded after the *C*/5 cycle (a and c) and after the sixth 3*C* cycle (b and d). Lithium electrodes in (b) and (d) were bent down by 90° using a special sample holder to show the cross section of the micro-structured lithium layer on top of the underlying lithium surface. Notice the different lengthscales of images (a,c and b,d).

lithium layer was slightly damaged during the SEM sample preparation, revealing holes that would otherwise be covered by the micro-structured lithium film. Several other groups have also reported the occurrence of similar holes on cycled lithium electrodes.[38,57–59]

After the sixth 3*C* cycle (SEM2), both electrodes were covered with a thick film of micro-structured lithium. To compare the amount of micro-structured lithium, SEM images were taken from electrodes that had been bent down 90° to expose the cross section of the micro-structured layer, as shown in Fig. 5b and d. Based on these images, the thickness of the micro-structured film was determined to be 66 ± 5 µm with the standard electrolyte and 20 ± 2 µm with the FEC additive.

In the electrode cycled with FEC electrolyte, discrete and uniformly shaped holes with a diameter of about 10 µm could be observed in the cracks (Fig. 5d), whereas the rest of the lithium surface appears to be unchanged. In contrast, the underlying lithium surface in the standard electrolyte was very inhomogeneous and rough, containing large holes and canyon-like structures (not visible in Fig. 5b).

The holes in the lithium anode surface seem to affect the growth of micro-structured lithium, which is supported by two further observations: Fig. 6a shows three holes and a thin layer of residual micro-structured lithium after the first *C*/5-cycle in FEC electrolyte. It can clearly be seen that the micro-structured lithium grows out of the hole and then spreads over the lithium surface. This mechanism is also consistent with Fig. 6b, where part of the micro-structured lithium film had been separated during SEM sample preparation but was still attached to the electrode, thus revealing its lower side. The lithium particles on the lower side are arranged in the exact same pattern as the holes on the corresponding lithium surface. This further confirms that the micro-structured lithium layer is only connected to the underlying lithium surface by a few contact points

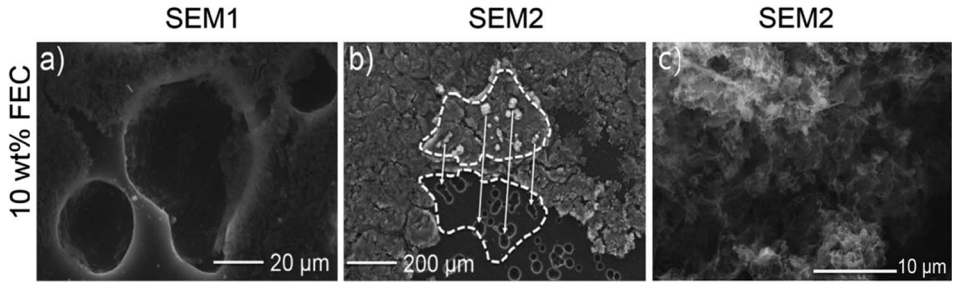

Fig. 6 *Ex situ* SEM images showing specific surface structures of lithium electrodes cycled with FEC additive. (a) Close-up recorded after the initial *C*/5 cycle. (b) Surface section where a patch of micro-structured lithium had been turned over during sample preparation (after the sixth 3*C* cycle), revealing the metallic lithium anode below. Craters on the anode surface and the matching connecting lithium particles on the lower side of the micro-structured lithium are indicated by white arrows. (c) Lithium micro-structures forming on the lithium electrode upon cycling, recorded at higher resolution. Pore structures are of micrometer size with sub-micrometer pore wall thickness, which is smaller than the skin depth δ of the microwaves used for the EPR experiments.

through the holes. Limited contact between the micro-structured lithium layer and the underlying lithium surface has already been reported in 1990 by Yamaki *et al.*[60] and has also been observed more recently by Orsini *et al.*[35] and by Steiger *et al.*[34] on cross section SEM images. The porosity of micro-structured lithium is depicted in Fig. 6c with an increased resolution, showing that the pore wall dimensions are in the sub-micrometer range. Very similar structures of the micro-structured lithium layer have been previously reported by other groups.[37,57]

Discussion

Interpretation of EPR results

The microwave irradiation used to induce electron spin transitions is subject to a finite penetration depth into the 'bulk' lithium-metal anode owing to the skin effect. At 9.5 GHz, the skin depth is $\delta \approx 1.1$ μm,[61,62] which is two orders of magnitude smaller than the thickness of the Li anode. Only a small fraction of the Li metal is contributing to the EPR signal, which is therefore proportional to the surface area of the lithium anode rather than to its volume. If, during charging, more lithium is deposited smoothly on the anode, the signal does not change appreciably. The experimentally observed amplitude change can be caused by an increase of the Li metal surface area or by a reduction of the electrical conductivity, which would increase δ. The latter would also cause a significant lineshape change. This is neither observed for the cell without additives after the first few minutes nor during fast cycling for the FEC cell, therefore it is anticipated that the EPR signal largely scales with the surface area. The formation of lithium micro-structures (mossy/dendritic) with a thickness of about 1–2 μm, which is comparable to δ, has been reported[35] and was observed in the SEM images (Fig. 6c), with pore wall diameters at least an order of magnitude smaller. Hence the newly formed surface micro-structures are penetrated by the microwave field and, due to the increased surface area and supported by the growth direction perpendicular to the magnetic microwave field lines, contribute to the observed EPR signal increase. The formation of lithium micro-structures is further supported by the change of the line asymmetry from $\phi \sim \pi/2$ for the pristine cell, which originates from lithium metal that is much thicker than δ, to $\phi \sim 0$ during cell cycling, which indicates a thickness of the micro-structure walls smaller than δ.[51]

The rate of the linewidth change for the FEC cell at the beginning of the 1*C* cycle shows an approximately five times higher value than the rate for the cell with standard electrolyte at the beginning of the *C*/5 cycle. This indicates that although the FEC cell is more robust toward the formation of micro-structured lithium, once it starts to build, it becomes the dominant form of lithium deposition. This micro-structured lithium could be considered non-locally as surface lithium with an increased time T_D it takes a spin to diffuse through the skin depth. The result would be a decreased linewidth and an increased line symmetry,[49] as observed for the FEC cell after the first cycle and for the cell without additives quickly after starting the initial charging. Furthermore, when electrical contact is lost, the porous surface would behave more like isolated lithium metal with small dimensions. Corresponding line widths have been reported to narrow substantially, depending on the size of the structure.[63]

Comparing EPR and SEM results

For the two electrolytes, both *operando* EPR spectroscopy and *ex situ* SEM analysis reveal a different lithium plating/stripping behavior already during the first cycle, which is caused by the improved properties of the solid/electrolyte interface (SEI) in the FEC-containing electrolyte. The FEC additive is known to be reduced and polymerize at lithium potential, thus forming a very flexible SEI layer.[29,30,41,64] The latter was supported by a recent study on the chemical composition of the surface film formed on silicon anodes in the presence of FEC by Markevich *et al.*[64] Besides an improved mechanical flexibility, the SEI formed in FEC-containing electrolytes also has an increased ionic conductivity,[30] which results in a more homogeneous current distribution.[15,58,65] As a consequence, lithium plating in the FEC-containing electrolyte can be expected to occur rather homogeneously in comparison to the standard electrolyte, which is reflected by the less pronounced increase of the EPR signal and the continuously large linewidth during the first

 This journal is © The Royal Society of Chemistry 2015

charge. Because of the homogeneous and rather compact lithium deposition according to the moderate increase of the EPR signal, most lithium plated during first charge is stripped during first discharge and the EPR signal returns to its initial value after the first cycle for the FEC-containing cell.

In contrast, the SEI that forms in the standard carbonate-based electrolyte mainly consists of lithium salts (such as LiF, Li_2CO_3 and Li_2O) formed by irreversible electrolyte reduction.[66] Due to its composition the SEI shows poor adhesion to the lithium surface and cannot withstand significant volume changes.[15] Accordingly, already during first charge the non-uniform lithium deposition and the corresponding volumetric expansion results in mechanical stress on the SEI at sites of preferred lithium plating; this causes the SEI to break, and fresh lithium is exposed to the electrolyte. Although fresh lithium has been shown to react with the electrolyte within seconds,[67] the new SEI on the exposed lithium is thinner than on the rest of the electrode. Further lithium deposition will therefore preferentially take place at these sites, causing the growth of micro-structured (mossy/dendritic) lithium during the first charge. During the subsequent discharge, the EPR signal hardly decreases in the standard electrolyte, which is consistent with SEM images showing a significant amount of residual micro-structured lithium after the first cycle. This is due to the dissolution of 'bulk' lithium from the lithium anode, while the main part of the micro-structured lithium is not dissolved.

The dissolution of bulk lithium rather than micro-structured lithium is a direct consequence of the limited contact points between the micro-structured lithium layer and the underlying lithium anode, as shown in Fig. 6b. If the contact points dissolve during discharge before all the micro-structured lithium has been oxidized, the micro-structured lithium layer loses electric contact to the anode and becomes electrochemically inactive, forming so called 'dead lithium'.[57] This mechanism, which is also consistent with the EPR data, is in very good agreement with recent results published by Steiger *et al.*, who follow the development of micro-structured lithium by optical microscopy and also observe limited contact points ("stems") as previously mentioned.[34]

The occurrence of non-uniform lithium plating during the first cycle is in accordance with literature. In our experiments, the geometric current density during the initial *C*/5 cycle was 0.23 mA cm_{Li}^{-2}. Several other groups have also reported non-uniform lithium plating (dendrites, moss or particles) at similar[11,59,68] or even lower[33] current densities in liquid electrolytes without film-forming additives. Stark el al. observed the formation of discrete lithium particles already during the first couple of seconds of lithium plating in EC/DMC electrolyte,[12] which is consistent with the instantaneous increase of the EPR signal on the first charge.

During subsequent cycles the increased current density causes an accumulation of micro-structured lithium in both electrolytes as consistently shown by the increasing EPR signal and by SEM images. It is generally accepted that an increase in charging current density also enhances the formation of micro-structured lithium.[35,58,59,65]

The lithium plating/stripping process seems to be almost completely irreversible during cell cycling with standard electrolyte due to the lack of EPR signal decrease during discharge phases, whereas it is at least partially reversible with the FEC containing electrolyte. The similarity of the linewidth and asymmetry for the two cells at faster cycling rates indicates that the build-up of the signal-inducing lithium structure is similar for both cells, but the decrease during discharge proceeds differently.

The growth of the micro-structured lithium layer during cycling takes place at the interface with the metallic lithium anode, where new lithium micro-structures growing out of the holes pushes away the old layer of micro-structured lithium.[34] This preferential lithium plating on the lithium metal surface is favored over lithium plating on top of the micro-structured layer due to the poor electronic conductivity of the latter.

Conclusions

An *operando* EPR cell was developed to perform EPR spectroscopy during electrochemical cycling. These measurements provided time-resolved semi-quantitative information about the plating and stripping of metallic lithium on lithium-metal anodes, which is particularly useful for investigating the formation of micro-structured lithium (mossy/dendritic). The method is complementary to optical and electron microscopic techniques that have their strength in monitoring the morphology of the electrode surface in turn.

The potential of *operando* EPR was explored by comparing two cells, the first one containing a standard electrolyte and the other one with an FEC additive to the electrolyte that is known to reduce the formation of micro-structured lithium (mossy/dendritic). Based on the EPR signal intensity and lineshape, it was shown that lithium deposition during electrochemical cell cycling was much more reversible when using FEC additive. The EPR results were confirmed by *ex situ* SEM images that were recorded at selected positions using identically cycled cells.

Owing to the high sensitivity of the EPR technique, already the early stages of the formation of lithium micro-structures in lithium batteries could be monitored. As compared to *operando* NMR,[36] the EPR experiment is considerably more sensitive, and since microwave frequencies instead of radiofrequencies are used, the skin depth is significantly smaller. Therefore EPR excites a thinner layer on the lithium metal surface, providing information with higher surface localization.

The presented interpretation of *operando* EPR data was based on the empirical extension of theoretical findings that for flat surfaces and for spherical particles of analogous dimensions the same lineshapes are observed. In addition, very characteristic lineshape changes are observed when going from structures that are large to structures that are small compared with the skin depth of the microwave field used to excite the spins. It was deduced, supported by SEM images, that the same qualitative lineshape changes are observed when changing from a smooth lithium anode with a thickness much larger than the skin depth to porous lithium with wall thickness smaller than the skin depth. In principle, it should be possible to

interpret the data quantitatively. A suitable procedure was sketched, yet theoretical expressions of conduction EPR signals from porous metallic lithium must first be derived.

Acknowledgements

We would like to thank Hans Kungl (IEK-9) for very helpful discussions, Magnus Graf (IEK-9) for experimental support with the EPR measurements, Johannes Landesfeind (TUM) for valuable support with the SEM measurements, and Yi-Chun Lu (Chinese University of Hongkong) for contributions to the *operando* EPR cell design. TUM gratefully acknowledges the financial support by BMW AG and by the Bavarian Ministry of Economic Affairs and Media, Energy and Technology under the auspices of the EEBatt project. IEK-9 gratefully acknowledges funding from the German Federal Ministry of Education and Research (BMBF-project DESIREE, grant number 03SF0477A).

References

1 K. G. Gallagher, S. Goebel, T. Greszler, M. Mathias, W. Oelerich, D. Eroglu and V. Srinivasan, *Energy Environ. Sci.*, 2014, **7**, 1555–1563.
2 J. Christensen, P. Albertus, R. S. Sanchez-Carrera, T. Lohmann, B. Kozinsky, R. Liedtke, J. Ahmed and A. Kojic, *J. Electrochem. Soc.*, 2012, **159**, R1–R30.
3 P. Bruce, S. Freunberger, L. Hardwick and J.-M. Tarascon, *Nat. Mater.*, 2012, **11**, 19–30.
4 Y.-X. Yin, S. Xin, Y.-G. Guo and L.-J. Wan, *Angew. Chem., Int. Ed. Engl.*, 2013, **52**, 13186–13200.
5 Y. Mikhaylik, I. Kovalev, R. Schock, K. Kumaresan, J. Xu and J. Affinito, *Meet. Abstr. Electrochem. Soc.*, 2009, **902**, 216.
6 J.-M. Tarascon, *Philos. Trans. R. Soc., A*, 2010, **368**, 3227–3241.
7 J. B. Bates, *US Pat.*, 5314765, 1994.
8 S. J. Visco and Y. S. Nimon, *US Pat.*, 7645543 B2, 2010.
9 S. J. Visco, E. Nimon, B. Katz, *US Pat.*, 7282296, 2007.
10 A. Aryanfar, D. Brooks, B. V Merinov, W. A. Goddard, A. J. Colussi and M. R. Hoffmann, *J. Phys. Chem. Lett.*, 2014, **5**, 1721–1726.
11 F. Ding, W. Xu, G. L. Graff, J. Zhang, M. L. Sushko, X. Chen, Y. Shao, M. H. Engelhard, Z. Nie, J. Xiao, X. Liu, P. V. Sushko, J. Liu and J.-G. Zhang, *J. Am. Chem. Soc.*, 2013, **135**, 4450–4456.
12 J. K. Stark, Y. Ding and P. A. Kohl, *J. Electrochem. Soc.*, 2013, **160**, D337–D342.
13 J. T. Vaughey, G. Liu and J.-G. Zhang, *MRS Bull.*, 2014, **39**, 429–435.
14 W. Xu, J. Wang, F. Ding, X. Chen, E. Nasybulin, Y. Zhang and J.-G. Zhang, *Energy Environ. Sci.*, 2014, **7**, 513–537.
15 D. Aurbach, E. Zinigrad, Y. Cohen and H. Teller, *Solid State Ionics*, 2002, **148**, 405–416.
16 M. Dollé, L. Sannier, B. Beaudoin, M. Trentin and J.-M. Tarascon, *Electrochem. Solid-State Lett.*, 2002, **5**, A286–A289.
17 K. J. Harry, D. T. Hallinan, D. Y. Parkinson, A. A. Macdowell and N. P. Balsara, *Nat. Mater.*, 2013, **12**, 1–6.
18 K. Ozawa, *Solid State Ionics*, 1994, **69**, 212–221.
19 H. Buqa, D. Goers, M. Holzapfel, M. E. Spahr and P. Novák, *J. Electrochem. Soc.*, 2005, **152**, A474–A481.
20 M. C. Smart, B. V. Ratnakumar, L. Whitcanack, K. Chin, M. Rodriguez and S. Surampudi, *IEEE Aerosp. Electron. Syst. Mag.*, 2002, **17**, 16–20.
21 P. Arorat, R. E. White and M. Doyle, *J. Electrochem. Soc.*, 1998, **145**, 3647–3667.
22 S. S. Zhang, K. Xu and T. R. Jow, *J. Power Sources*, 2006, **160**, 1349–1354.
23 M. C. Smart and B. V. Ratnakumar, *J. Electrochem. Soc.*, 2011, **158**, A379–A389.
24 M. Dubarry, C. Truchot, B. Y. Liaw, K. Gering, S. Sazhin, D. Jamison and C. Michelbacher, *J. Electrochem. Soc.*, 2012, **160**, A191–A199.
25 Z. Li, J. Huang, B. Yann Liaw, V. Metzler and J. Zhang, *J. Power Sources*, 2014, **254**, 168–182.
26 M. C. Smart, B. L. Lucht, S. Dalavi, F. C. Krause and B. V. Ratnakumar, *J. Electrochem. Soc.*, 2012, **159**, A739–A751.
27 L. Gireaud, S. Grugeon, S. Laruelle, B. Yrieix and J.-M. Tarascon, *Electrochem. Commun.*, 2006, **8**, 1639–1649.
28 O. Crowther and A. C. West, *J. Electrochem. Soc.*, 2008, **155**, A806–A811.
29 R. McMillan, H. Slegr, Z. Shu and W. Wang, *J. Power Sources*, 1999, **81–82**, 20–26.
30 R. Mogi, M. Inaba, S.-K. Jeong, Y. Iriyama, T. Abe and Z. Ogumi, *J. Electrochem. Soc.*, 2002, **149**, A1578–A1583.
31 K. Nishikawa, T. Mori, T. Nishida, Y. Fukunaka, M. Rosso and T. Homma, *J. Electrochem. Soc.*, 2010, **157**, A1212–A1217.
32 T. Nishida, K. Nishikawa, M. Rosso and Y. Fukunaka, *Electrochim. Acta*, 2013, **100**, 333–341.
33 J. Steiger, D. Kramer and R. Mönig, *J. Power Sources*, 2014, **261**, 112–119.
34 J. Steiger, D. Kramer and R. Mönig, *Electrochim. Acta*, 2014, **136**, 529–536.
35 F. Orsini, A. Du Pasquier, B. Beaudoin and J. M. Tarascon, *J. Power Sources*, 1998, **76**, 19–29.
36 R. Bhattacharyya, B. Key, H. Chen, A. S. Best, A. F. Hollenkamp and C. P. Grey, *Nat. Mater.*, 2010, **9**, 504–510.
37 S. Chandrashekar, N. M. Trease, H. J. Chang, L.-S. Du, C. P. Grey and A. Jerschow, *Nat. Mater.*, 2012, **11**, 311–315.
38 N. Schweikert, A. Hofmann, M. Schulz, M. Scheuermann, S. T. Boles, T. Hanemann, H. Hahn and S. Indris, *J. Power Sources*, 2013, **228**, 237–243.
39 F. Poli, J. S. Kshetrimayum, L. Monconduit and M. Letellier, *Electrochem. Commun.*, 2011, **13**, 1293–1295.
40 G. Gershinsky, E. Bar, L. Monconduit and D. Zitoun, *Energy Environ. Sci.*, 2014, **7**, 2012–2016.
41 A. V. Cresce, S. M. Russell, D. R. Baker, K. J. Gaskell and K. Xu, *Nano Lett.*, 2014, **14**, 1405–1412.
42 L. Zhuang and J. Lu, *Rev. Sci. Instrum.*, 2000, **71**, 4242–4248.
43 S. Meini, M. Piana, N. Tsiouvaras, A. Garsuch and H. A. Gasteiger, *Electrochem. Solid-State Lett.*, 2012, **15**, A45–A48.
44 D. R. Gallus, R. Schmitz, R. Wagner, B. Hoffmann, S. Nowak, I. Cekic-Laskovic, R. W. Schmitz and M. Winter, *Electrochim. Acta*, 2014, **134**, 393–398.

 This journal is © The Royal Society of Chemistry 2015

45 P. Jakes, E. Erdem, A. Ozarowski, J. van Tol, R. Buckan, D. Mikhailova, H. Ehrenberg and R.-A. Eichel, *Phys. Chem. Chem. Phys.*, 2011, **13**, 9344–9352.
46 E. Erdem, V. Mass, A. Gembus, A. Schulz, V. Liebau-Kunzmann, C. Fasel, R. Riedel and R.-A. Eichel, *Phys. Chem. Chem. Phys.*, 2009, **11**, 5628–5633.
47 F. Dyson, *Phys. Rev.*, 1955, **98**, 349–359.
48 G. R. Eaton, S. S. Eaton, D. P. Barr and R. T. Weber, *Quantitative EPR*, Springer, Vienna, 2010.
49 R. H. Webb, *Phys. Rev.*, 1967, **158**, 225–233.
50 V. Sitaram, A. Sharma, S. Bhat, K. Mizoguchi and R. Menon, *Phys. Rev. B: Condens. Matter Mater. Phys.*, 2005, **72**, 035209.
51 G. Feher and A. F. Kip, *Phys. Rev.*, 1955, **98**, 337–348.
52 A. K. Padhi, K. S. Nanjundaswamy and J. B. Goodenough, *J. Electrochem. Soc.*, 1997, **144**, 1188–1194.
53 K. Zaghib, J. Shim, A. Guerfi, P. Charest and K. A. Striebel, *Electrochem. Solid-State Lett.*, 2005, **8**, A207–A210.
54 D. Y. W. Yu, K. Donoue, T. Inoue, M. Fujimoto and S. Fujitani, *J. Electrochem. Soc.*, 2006, **153**, A835–A839.
55 C. Fongy, A.-C. Gaillot, S. Jouanneau, D. Guyomard and B. Lestriez, *J. Electrochem. Soc.*, 2010, **157**, A885–A891.
56 C. Fongy, S. Jouanneau, D. Guyomard, J. C. Badot and B. Lestriez, *J. Electrochem. Soc.*, 2010, **157**, A1347–A1353.
57 I. Yoshimatsu, T. Hirai and J. Yamaki, *J. Electrochem. Soc.*, 1988, **135**, 2422–2427.
58 D. Aurbach, Y. Gofer and J. Langzam, *J. Electrochem. Soc.*, 1989, **136**, 3198–3205.
59 M. Arakawa, S. Tobishima, Y. Nemoto and M. Ichimura, *J. Power Sources*, 1993, **43–44**, 27–35.
60 J. Yamaki, in *40th Int. Soc. Electrochem. Meet.*, 1990, pp. 150–151.
61 R. B. Lewis and T. R. Carver, *Phys. Rev. Lett.*, 1964, **12**, 693–695.
62 M. Höhne, *Phys. Status Solidi B*, 1978, **85**, 525–534.
63 K. Saiki, T. Fujita, Y. Shimizu, S. Sakoh and N. Wanda, *J. Phys. Soc. Jpn.*, 1972, **32**, 447–450.
64 E. Markevich, K. Fridman, R. Sharabi, R. Elazari, G. Salitra, H. E. Gottlieb, G. Gershinsky, A. Garsuch, G. Semrau, M. A. Schmidt and D. Aurbach, *J. Electrochem. Soc.*, 2013, **160**, A1824–A1833.
65 J. Yamaki, S. Tobishima, K. Hayashi, K. Saito, Y. Nemoto and M. Arakawa, *J. Power Sources*, 1998, **74**, 219–227.
66 D. Aurbach, *J. Power Sources*, 2000, **89**, 206–218.
67 M. Odziemkowski and D. E. Irish, *J. Electrochem. Soc.*, 1992, **139**, 3063–3074.
68 N. Schweikert, R. Heinzmann, A. Eichhöfer, H. Hahn and S. Indris, *Solid State Ionics*, 2012, **226**, 15–23.

3.1.2 Lithium Plating on Graphite Anodes

This section presents the article "Quantitative and Time Resolved Detection of Lithium Plating and Reintercalation on Graphite Anodes in Lithium Ion Batteries". At the time of the submission of this PhD thesis, this article has not yet been submitted for publication. This study was presented on international conferences, for example on the 231st Meeting of The Electrochemical Society in New Orleans (USA) in May 2017 (Abstract Number: #318).

This study is the follow-up project of the publication discussed in Section 3.1.1 and focuses on the time resolved and quantitative detection of lithium plating on graphite anodes by *operando* EPR spectroscopy. As discussed in Section 1.1, lithium plating on graphite anodes is of high interest for state of the art lithium-ion batteries as it limits the charging rate. Despite the importance of this side reaction, there is no analytical technique, besides neutron diffraction (see previous section), available for the time resolved and quantitative detection of plated lithium metal on graphite anodes. There are a few purely electrochemical techniques that can indicate whether lithium plating has occurred during charge, for example by distinct features in the potential profiles during subsequent OCV or battery discharge.[149;150] Recently Dahn and co-workers showed that lithium plating reduces the coulombic efficiency and can be indirectly detected in this way.[151] All of these techniques are simple and elegant, especially as they do not require any special experimental set up, but they also contain little more information other than whether lithium plating generally occurred or not. In addition, microscopy can be used to determine the structure and location of plated lithium, but it is also non-quantitative and can only be used *ex situ* to monitor "dead lithium".[152]

This study contains the entire method development for the detection of lithium metal plating on graphite anodes by *operando* EPR. During normal high rate or low temperature battery charge, lithium plating always takes place in parallel with the desired lithium intercalation reaction and also the chemical reintercalation of plated lithium metal. For the method development, model experiments are carried out which separate these reactions. First, the reversible graphite intercalation and deintercalation is studied. The electronic properties of Li_xC_6 change drastically as a function of the lithium content x, as discussed in Section 1.1. The change in conductivity causes a phase shift and change in resonator quality factor which induces artefacts in the recorded EPR spectra. In this study, we present a correction method which is based on the simultaneous recording of an inert EPR reference. In the second model experiment, forced lithium plating onto fully intercalated LiC_6 is investigated. A method to deconvolute

the spectral components and to quantify the lithium metal amount is developed. In the final experiment, lithium plating during "normal" low temperature charge as a function of the C-rate is investigated. It is possible to quantify the amount of plated lithium and to calculate the corresponding lithium plating current. This data will be very useful for the validation of numerical simulations of fast charging processes.

Author contributions

H.G. and J.W. developed the general concept for this study. J.W. and P.J. carried out the EPR experiments. J.W. and J.G. carried out the data analysis. J.W. wrote the manuscript. All authors discussed the data and commented on the results.

Quantitative and Time Resolved Detection of Lithium Plating and Reintercalation on Graphite Anodes in Lithium Ion Batteries

Author list in alphabetic order

Eichel[2,3], Gasteiger[1], Granwehr[2,4], Jakes[2], Wandt[1]

[1]Technische Universität München, Institute for Technical Electrochemistry, Germany
[2] Forschungszentrum Jülich, Institut für Energie- und Klimaforschung, Grundlagen der Elektrochemie (IEK-9), 52425 Jülich, Germany
[3] RWTH Aachen University, Institut für Physikalische Chemie, 52074 Aachen, Germany
[4] RWTH Aachen University, Institut für Technische und Makromolekulare Chemie, 52074 Aachen, Germany

* corresponding authors

Abstract

The ability of fast and safe charging is critical for the success of lithium ion batteries for automotive applications. In state of the art lithium ion batteries the charging rate is limited by the onset of lithium plating on the graphite anode. Despite its high importance, so far no analytical technique has been available for directly measuring lithium plating during battery charge. Herein, we introduce *operando* electron paramagnetic resonance (EPR) spectroscopy as the first technique capable of the time resolved and quantitative detection of lithium metal plating in lithium ion batteries. In an exemplary study the C-rate dependence of lithium metal plating during low temperature charging at -20 °C is investigated. It is possible to quantify the amount of dead lithium and observe the chemical reintercalation of plated lithium metal. The time-resolved and quantitative information accessible with *operando* EPR spectroscopy will be very useful for the optimization of fast charging procedures, testing of electrolyte additives and model validation.

Introduction

Lithium ion batteries (LIB) are a key technology for the electrification of the transport sector. According to estimates by OEMs, an increase in the charging current by a factor of about 3 is necessary to achieve mass market penetration of battery electric vehicles over the next few years.[1,2] In state of the art LIBs the limitation of the charging current is arising at the graphite anode[3,4] into which Li ions intercalate upon charge:

$$Li^+ + e^- + C_6 \longrightarrow Li_xC_6 \quad \text{with } (0 \le x \le 1) \tag{1}$$

The reversible potential of the Li intercalation reaction (equation 1) is only 100 to 200 mV above the Li/Li^+ potential.[5] This is advantageous in terms of energy density but poses the risk of undesired lithium metal plating upon battery charge:

$$Li^+ + e^- \longrightarrow Li \tag{2}$$

Lithium plating becomes thermodynamically favorable in regions of the graphite electrode where the local potential drops below the Li/Li^+ potential due to liquid (electrolyte) and solid (graphite) phase mass transport limitations[6] and/or limited charge transfer kinetics[7] of the intercalation reaction. The importance of each of these factors for the propensity of lithium plating heavily depends on temperature,[6,8] active material loading[2] and electrode design parameters (e.g. porosity and tortuosity),[9] but in general lithium plating is favored by high charging currents and/or at low charging temperatures.[10,11] It is very important to reduce the amount of lithium plating during battery charge to a minimum as it causes capacity loss due to active lithium and electrolyte consumption, decreases the rate capability due to impedance build-up and also poses a serious safety hazard due to internal shorting.[11] Accordingly, the charging current of a LIB is limited to the maximum intercalation rate (equation 1), just before lithium plating (equation 2) sets in.

For a given graphite electrode this limiting charging current mainly depends on temperature and state of charge (SOC) of the graphite electrode. In order to design a safe and fast charging protocol, which varies the applied charging current over time to approach but never exceed the limiting current, detailed knowledge regarding the onset of lithium plating as a function of temperature and SOC is required. For the reliable detection of lithium plating a time resolved *operando* technique is necessary as metallic lithium can chemically reintercalate into the graphite anode under open circuit condition and could therefore partially or totally "disappear" during the sample preparation prior to an *ex situ* analysis:

$$y\,Li + Li_xC_6 \longrightarrow Li_{x+y}C_6 \quad (\text{with } x+y \le 1) \tag{3}$$

There are a couple of purely electrochemical techniques based on the shape of potential curves[12–14] or the coulombic efficiency[15,16] that can detect whether lithium plating has generally occurred during charge. While these techniques are simple and elegant and are suitable for all cell formats, they contain little or no information regarding the onset point and amount of lithium plating. *In situ* neutron diffraction has been successfully applied to monitor the Li reintercalation (equation 3) in 18650 full cells.[17,18] Furthermore, it has been demonstrated that electron paramagnetic resonance

(EPR)[19] and nuclear magnetic resonance (NMR)[20,21] spectroscopy are capable of detecting lithium metal within a coke/graphite electrode, but so far no time resolved detection of lithium metal plating during normal cell charge has been shown with any of these techniques.

In this publication, we demonstrate that electrochemical *operando* EPR spectroscopy can be used for the time resolved and quantitative detection of lithium metal plating on the graphite electrode during battery charge. While processes (1) to (3) would all occur simultaneously under high current and/or low temperature charge, we will first show model experiments in which reactions (1) and (2) are separated and can therefore be studied individually. Afterwards the "normal" low temperature charge in which all three processes occur simultaneously will investigated.

***Operando* EPR Cell Design**

The cell design of the *operando* EPR cell that can be directly cycled within the cavity of the EPR spectrometer is shown in Figure 1a and b and is described in more detail in our previous publications.[22,23] It consists of a graphite working electrode and a lithium iron phosphate (LFP) based counter and reference electrode; the cell does not contain any metallic lithium in its initial state and the occurrence of a metallic lithium EPR signal during charge can therefore be directly assigned to lithium plating on the graphite electrode. A small quantity of manganese(II) oxide (MnO), placed outside of the cell, is used as an inert EPR reference as explained later. Figure 1c shows potential profiles as measured in the *operando* EPR cell, which at low rates (C/10) display the staging behavior typical for the graphite intercalation reaction (equation 1). At higher rates (1C), the cell overpotential increases and therefore the intercalation capacity decreases. The inset in Figure 1c shows the color change of the graphite electrode at different SOCs, which can be used to monitor the homogeneity of the intercalation reaction across the electrode (time lapse video available in Supporting Information).[24] At the C/10 rate, the entire electrode first displays intercalation stage IIL ($Li_{0.25}C_6$, blue color), then reaches intercalation stage II ($Li_{0.50}C_6$, red color) before homogeneously attaining stage I ($Li_{1.00}C_6$, golden color), despite the small potential difference between stage I and II (120 and 80 mV vs. Li/Li^+). This is a consequence of the high in-plane conductivity of the graphite electrode, rendering the limited electronic contacting by the copper wire unproblematic. In contrast, at a rate of 1C the lithiation is only homogeneous at low SOCs ($Li_{0.25}C_6$, blue color) whereas the ohmic drop causes spatial inhomogeneity at higher SOCs as displayed by the simultaneous presence of blue, red and golden regions at the nominal composition of $Li_{0.5}C_6$. Therefore the *operando* EPR cell is considered to be representative of a "normal" cell design at moderate charging rates up to 1C.

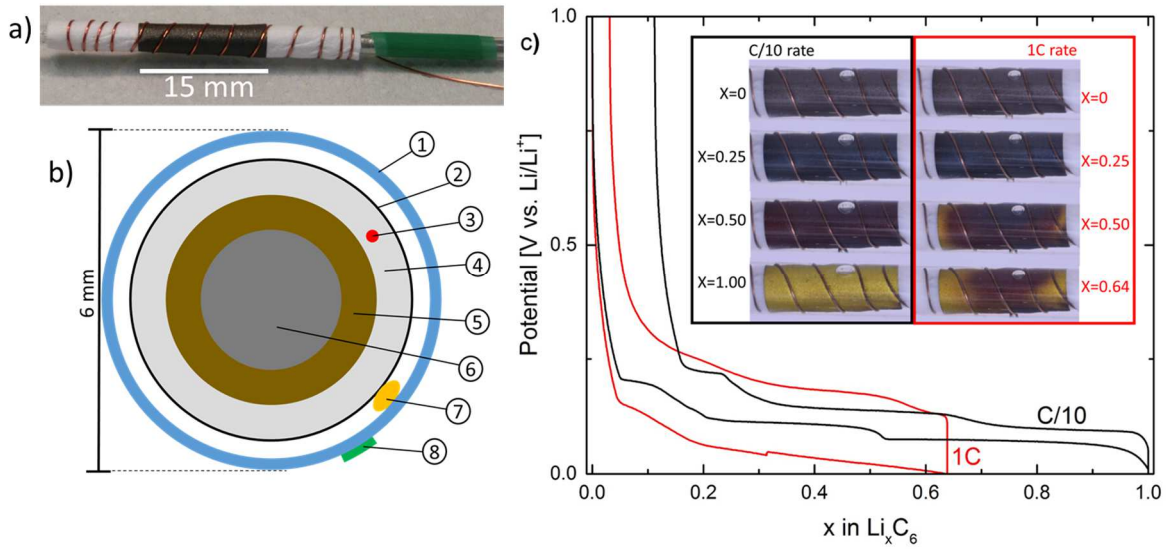

Figure 1 a) Photograph of the *operando* EPR cell showing the glass fiber separator (white), the graphite working electrode and the copper wire current collector, b) Cross section of the *operando* EPR cell with ① quartz glass tube, ② graphite working electrode, ③LFP reference electrode, ④ glass fiber separator, ⑤ LFP counter electrode, ⑥ aluminum wire as cathode current collector, ⑦ copper wire as anode current collector and ⑧ MnO on tape as EPR reference; c) Potential curve of C/10 (black) and 1C (red) cycle measured in the *operando* EPR cell; inset: optical images of graphite electrode in the *operando* EPR cell as a function of intercalation degree and rate.

Li Intercalation into Graphite

First, the reversible intercalation and deintercalation of lithium ions into graphite (equation 1) during a C/10 charge and C/5 discharge (Figure 2 a) at room temperature are investigated without the occurrence of any lithium metal plating. Going from pristine graphite (C_6) to fully intercalated LiC_6, the electronic conductivity of Li_xC_6 in c-direction (perpendicular to the graphene layers) increases by a factor of more than 2000[25–27], which influences the quality factor of the EPR resonator. To avoid correlated experimental artefacts, a phase and intensity correction is carried out based on an internal inert spin reference (MnO). All *operando* EPR spectra shown in this publication have already been phase and intensity corrected; exemplarily, uncorrected raw spectra and further details regarding the correction method can be found in the supplementary information (SI). The *operando* EPR spectra of Li_xC_6 (Figure 2b) all show one signal with a Dysonian line shape[28] and a signal width of about 0.15 mT which varies in intensity as a function of SOC. As expected, the EPR signal vanishes after the end of C/5 discharge, confirming the full reversibility of the lithium intercalation/deintercalation process. The signal intensity of the Li_xC_6 signal can be determined by directly fitting the first derivative *operando* EPR spectra with four fitting parameters, namely peak intensity, peak center, peak width and phase (see SI for details). Between C_6 and $Li_{0.5}C_6$ there is a linear correlation of the signal intensity and the intercalation capacity (or time in the constant current experiment) as shown in Figure 2c. In contrast, the signal intensity levels off at higher SOCs, hence not all additional electrons that accompany the Li intercalation (see equation 1) contribute to the EPR signal. This is probably caused by a shielding effect[22,29] due to the limited penetration depth of the microwave into the graphite particles. The penetration depth *d* decreases with increasing c-axis conductivity σ according to $d \propto \sqrt{\sigma^{-1}}$ from ≈190 µm for pristine graphite to only ≈4 µm for LiC_6 (see SI for details). Accordingly, at high SOCs parts of the graphite particles are not EPR active, which causes the Li_xC_6 signal intensity to level off. Such a non-linear effect is a possible limitation for quantitative *operando* EPR spectroscopy that always has to be considered during EPR data analysis. Fortunately, for the experiments carried out within this study the lithium metal signal always falls into the linear regime as discussed in the next section. In addition to this shielding effect, there is a short region of constant signal amplitude at a composition of around $Li_{0.5}C_6$ occurring in both charge and discharge. The physical origin of this behavior is currently under investigation.

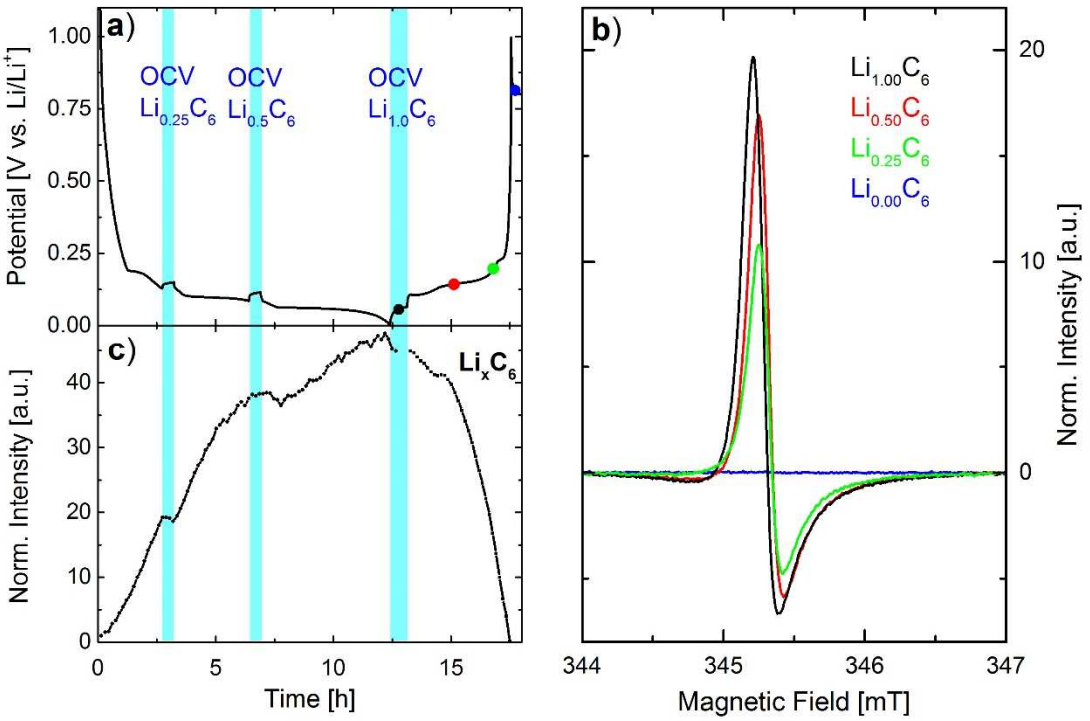

Figure 2 a) Potential curve of C/10 Li intercalation and C/5 Li deintercalation at room temperature; b) selected EPR spectra recorded during deintercalation at times indicated in a); c) Normalized intensity of graphite EPR signal (normalized by MnO reference intensity).

Forced Li Plating on LiC_6

In this section, the controlled lithium metal plating (equation 2) on fully intercalated graphite (LiC_6), to which we refer as "forced lithium plating", is investigated. This reaction could theoretically take place during the overcharge of a Li-ion cell, but this scenario is rather unlikely as the capacity per area (in mAh cm^{-2}) is typically higher for the graphite anode than for the cathode. We rather use forced lithium plating as a model experiment to independently study lithium plating while the LiC_6 compound does not change. Figure 3a shows the potential profile of the forced C/10 lithium metal plating on LiC_6 (five hours time limitation) and the C/5 lithium metal stripping, which after about seven hours passes over to lithium deintercalation from LiC_6. The first *operando* EPR spectrum (black line, Figure 3b), measured *before* the onset of lithium metal plating and consistent with the spectra shown in Figure 2b, only shows the broad Li_xC_6 signal. The other three spectra in Figure 3b, all measured *after* the onset of lithium metal plating, exhibit a second EPR signal that can be assigned to metallic lithium. The lithium metal EPR signal is very narrow (signal width ≈1/5 of Li_xC_6 signal) and its signal center is slightly upfield shifted in comparison to the Li_xC_6 signal. The Dysonian lineshape of the lithium metal signal does not change drastically over the course of the experiment. The intensity of both the Li_xC_6 and the lithium metal signal can be determined by simultaneously fitting the spectra with two Dysonian lines (see SI for details). The initial decrease (before first dashed vertical line) of the Li_xC_6 signal intensity (Figure 3b, grey markers) and the intermittent increase (around the second dashed vertical line) can be assigned to a partial shielding induced by lithium plating on top of the graphite particles (see Si for details). Only the second and stronger decrease of the Li_xC_6 signal is actually correlated with the electrochemical deintercalation reaction. This shielding is an indication for a very homogeneous plating reaction, forming a lithium metal film covering the graphite particles rather than discrete lithium metal particles. The onset of an observable lithium metal EPR signal agrees with the well know dip in the potential curve that is caused by the nucleation process (first dashed vertical line). The lithium metal signal intensity (Figure 3c, black dots) increases linearly during lithium plating, stays constant during OCV and decreases linearly during lithium stripping, indicating that the lithium plating/stripping process takes place in a linear EPR regime (see SI for details). The magenta lines in Figure 3c display the linear regression fits and their respective slopes. During lithium plating there is a constant exposure of fresh lithium metal surface to the electrolyte, which chemically reacts within seconds,[30] constantly consuming a certain fraction of the plated lithium metal to form a new solid electrolyte interphase (SEI) layer.[31] Effectively, the applied reductive current i_{red} consists of a lithium plating current $i_{Li\text{-}Plating}$ and an SEI forming current i_{SEI}. In contrast, during lithium stripping the entire applied oxidative current i_{ox} is carried by lithium metal stripping $i_{Li\text{-}Strip.}$, as this is virtually the only electrochemical oxidation occurring at ≈ 0 V vs. Li/Li^+. Therefore the comparison of the observed slopes as shown in Figure 3c (corrected for different C-rates) can be used to quantify the efficiency τ_{SEI} of the lithium plating and stripping reaction with respect to SEI losses to be τ_{SEI}=92% (= 0.090 h^{-1} x 2 / 0.195 h^{-1}). Furthermore it is possible to directly determine the amount of metallic lithium that gets electronically disconnected during the stripping process and remains within the electrode or separator as so called "dead lithium"[32,33] from Figure 3c. The efficiency of the lithium plating and stripping reaction with respect to dead lithium formation,

τ_{dead}, can be calculated as $\tau_{dead}=1 - n(Li_{dead})/n(Li_{plated})$ and equals 76% for the experiment shown in Figure 3, where $n(Li_{dead})$ and $n(Li_{plated})$ represent the amount of dead and plated Li, respectively, as extracted from the corresponding EPR signal amplitudes. The product of τ_{SEI} and τ_{dead} equals 69.9% which is very close to the electrochemically observable coulombic efficiency (CE) of the lithium plating/stripping process[34] of 70% (= Q_2/Q_1 where Q_1 and Q_2 refer to the lithium plating and stripping capacities, see Figure 3 a). To the best of our knowledge, this is the first time it has been achieved to deconvolute the coulombic efficiency into the quantitative contributions from both SEI and dead lithium formation to the coulombic inefficiency. The forced lithium plating process as shown in Figure 3 can also be used for the calibration of the lithium metal amount. As previously explained, the entire i_{ox} can be correlated with lithium metal oxidation. Therefore the slope of 0.195 h^{-1} and the applied current of 202 µA give rise to a calibration factor of 1036 µAh or 38.7 µmol per normalized intensity unit. This calibration procedure (see SI for details) has been used to quantify the amount of metallic lithium in the low temperature charging experiments discussed below.

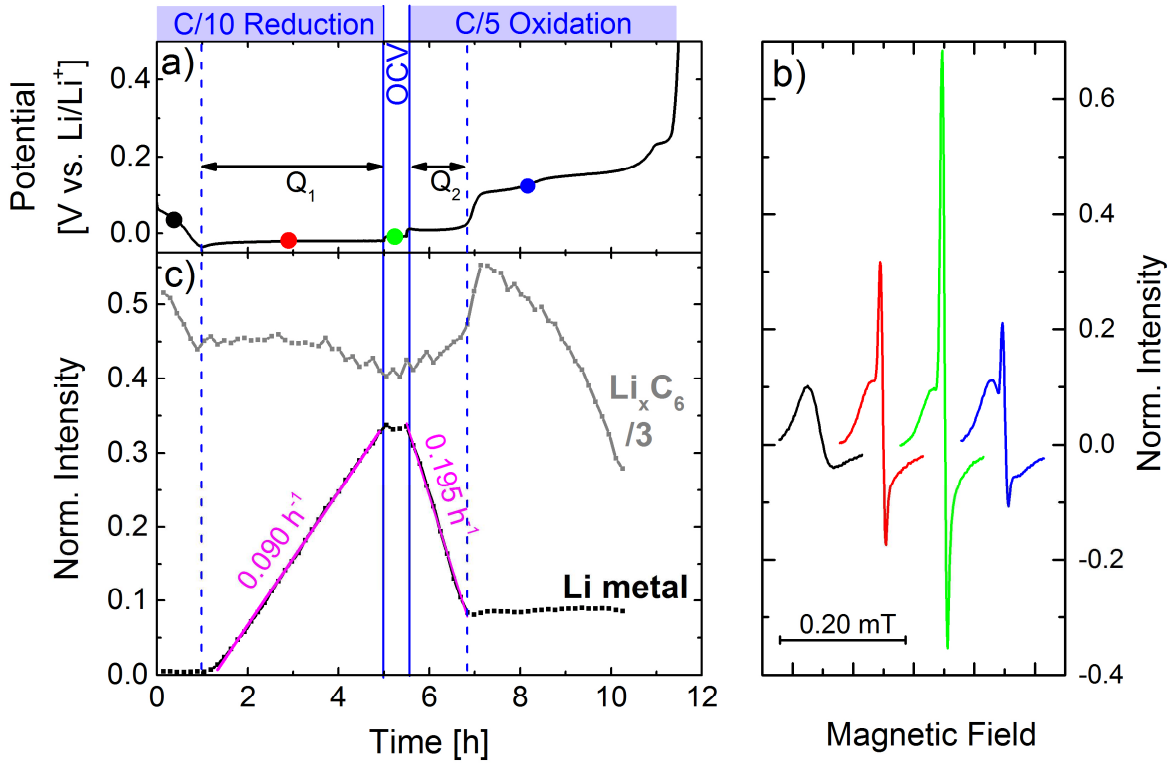

Figure 3 a) Potential curve of forced Li plating on preformed Li_1C_6 (C/10 reduction, 5 hours), followed by the subsequent Li stripping and Li deintercalation (C/5 oxidation) at room temperature. b) Selected EPR spectra recorded at times as indicated in a), spectra are shown with an x-axis offset. c) Normalized intensity of graphite (grey) and Li metal (black) EPR signal (normalized by MnO reference intensity); magenta lines represent linear regression of the Li metal signal intensity during Li plating and stripping with their respective slopes.

Li Plating During Low Temperature Charge

In this section, the low temperature charge of graphite electrodes is investigated. Cells are charged with different C-rates (C/10 to 1C) at a temperature of -20 °C to of 335 mAh g^{-1}, which is lower than the nominal graphite capacity of 372 mAh g^{-1}, to realistically mimick the low temperature charging process of a real LIB. In this case lithium intercalation into graphite (equation 1), lithium plating (equation 2) due to limited mass transfer and/or charge transfer kinetics and the chemical reintercalation of plated lithium metal into graphite (equation 3) all take place simultaneously. Figure 4a shows the potential profiles of the low temperature charge. For all C-rates the potential falls below 0 V vs. Li/Li^+ before the dip in the potential profile indicates the onset of Li metal plating. Figures 4c,d show selected *operando* EPR spectra recorded at different capacities for the C/5 and 1C charge. The first EPR spectrum measured during the C/5 charge (Figure 4c) before the onset of lithium plating only contains the broad Li_xC_6 signal, the next two spectra measured after the lithium plating onset also contain one narrow lithium metal signal. Due to the early lithium plating onset, all 1C EPR spectra (Figure 4d) show both a Li_xC_6 and a lithium metal signal. The lithium metal signals in Figures 4c,d actually consist of two separate very narrow signals with slightly different centers, which are well resolved for the 1C charge ($B_0(Li_2)$ - $B_0(Li_1)$ ≈ 0.04 mT) and poorly resolved for the C/5 charge ($B_0(Li_2)$ - $B_0(Li_1)$ ≈ 0.03 mT). The presence of two distinct lithium metal signals is probably caused by different locations of the lithium metal deposits within the cell (graphite electrode vs. separator) as discussed below. For the quantification of the lithium metal signals in Figure 4, a deviation method which is simpler and more robust than the previously used multi component fit is used (see SI for details). Figure 4b shows the amount of lithium metal as a function of the specific capacity. As expected, increasing the C-rate increases the amount of lithium metal plating and decreases the capacity from which on metallic lithium can be detected in the *operando* EPR spectra. For the two nominally identical C/2 cells (red and green curve in Figure 4b), the amount of detected lithium metal differs significantly. Still, both C/2 cells fall on the trend line if one plots the amount of lithium metal as determined by EPR versus the lithium plating onset as determined from the dip in the potential profile (inset Figure 4b). This indicates that the electrochemical reproducibility (all experiments shown in Figure 4 are measured in different cells) in the current cell design is not sufficient to give the exact same result in repeated experiments. Nonetheless, the *operando* EPR technique correctly detected the higher amount of lithium metal for the C/2-I cell (red curve) in comparison to the C/2-II cell (green curve). In summary, the *operando* EPR technique is well suited for the quantitative detection of lithium metal plating, but the current cell design still needs to be improved to obtain the required cell-to-cell reproducibility.

Figure 5a shows the fraction of the applied current that goes into lithium metal plating, obtained by differentiating the curves in Figure 4b. For all cells, the lithium plating current increases throughout the charge; for the 1C charge it even reaches a final value of ≈ 95%, meaning that lithium plating accounts for almost the entire current while the desired intercalation reaction hardly takes place anymore. To the best of our knowledge, this is the first demonstration of the time resolved and quantitative experimental determination of the lithium plating current during charging of a lithium ion battery. Figure 5b shows the chemical reintercalation of plated lithium during the OCV period

following the low temperature charge. As expected, the reintercalation rate is higher at 0°C compared to -20°C. The curves seem to consists of two different regions that might be caused by processes with different time constants.[17,18] We are currently working on a physics based model to properly fit the reintercalation curves and determine whether liquid and/or solid state diffusion are the rate-limiting step. Furthermore, it might also be possible to estimate the effective solid state diffusion coefficient for Li^+-ions in graphite for which values varying over several orders of magnitude have been reported.

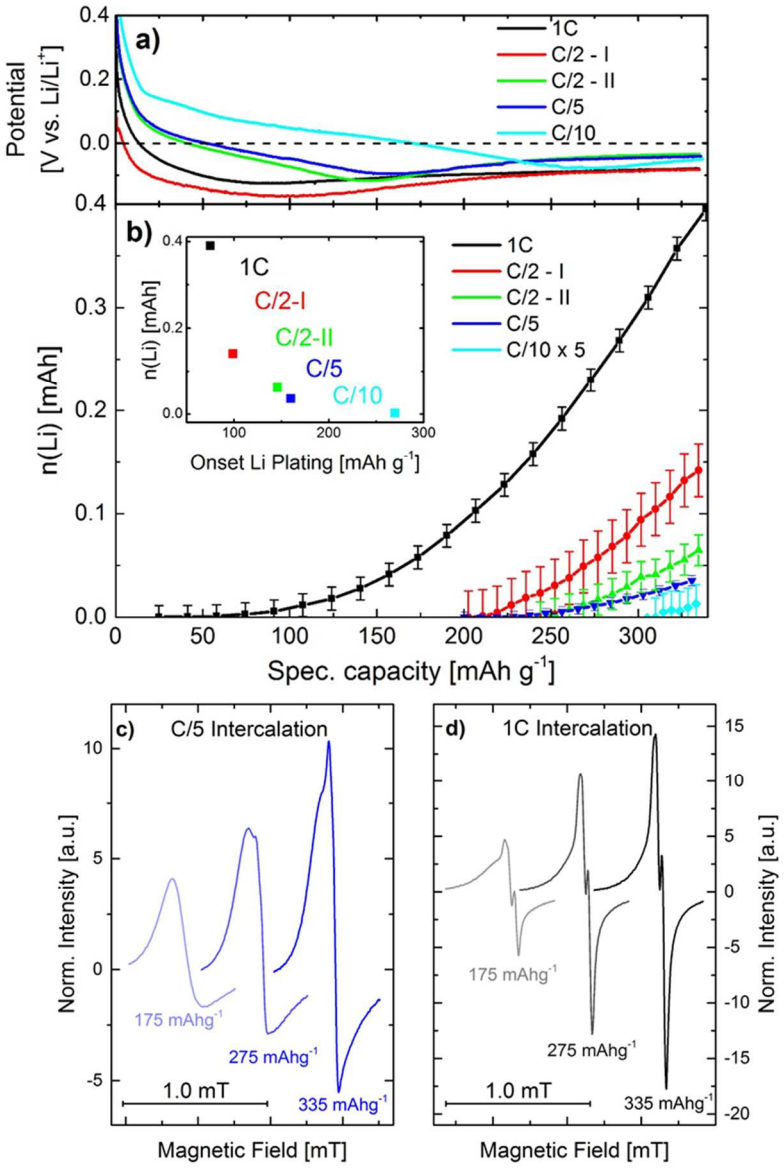

Figure 4 a) Potential curves of Li intercalation at –20°C at different C-rates. b) Amount of metallic Li as determined from *operando* EPR spectra as a function of intercalation capacity and applied C-rate. Inset: Correlation of final amount of plated Li (at 335 mAh g^{-1}) and the onset of Li plating (minimum in potential curves shown in Fig. 4a. c) and d) selected EPR spectra recorded during C/5 and 1C intercalation, respectively.

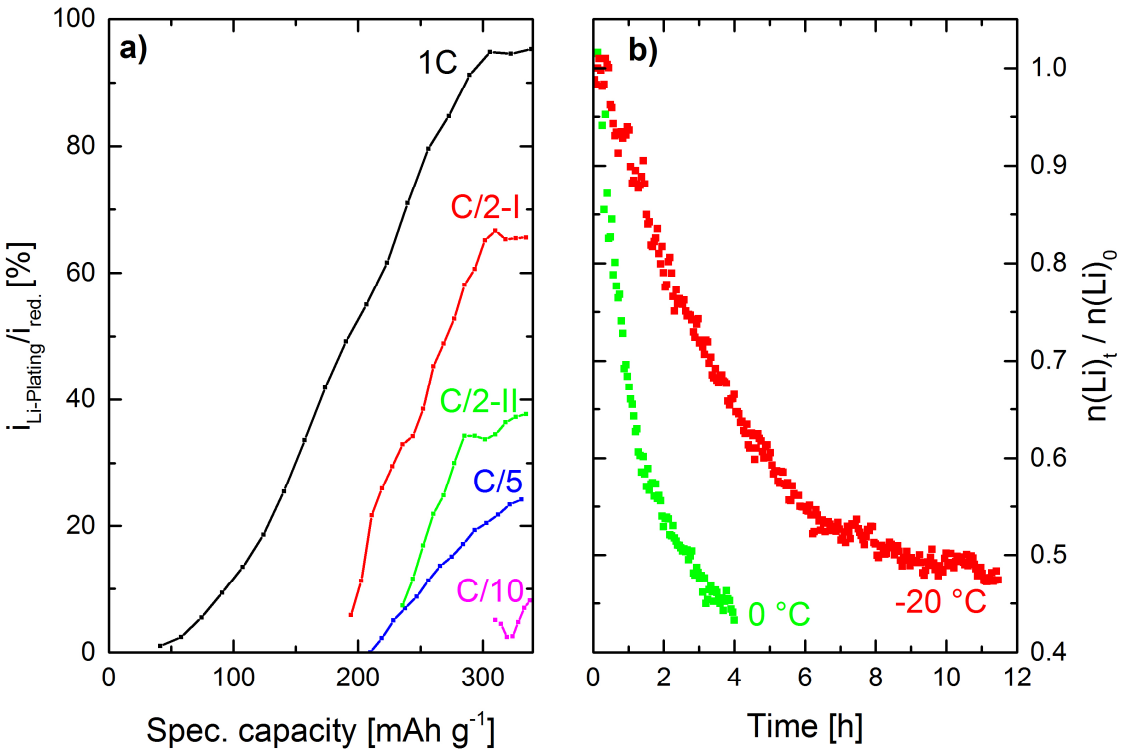

Figure 5 a) Fraction of the Li plating current of the applied total current ($i_{Li\text{-}Plating}/i_{red.}$) during charge at -20°C (same data set as Fig. 4b. b) Li metal reintercalation into graphite during OCV after low temperature charge at -20°C (red) and 0°C (green); for the reintercalation at 0°C, the temperature is increased directly after the end of the -20°C charge.

Physical interpretation of two distinct Li metal signals

Forced lithium plating produces a single lithium metal EPR signal at low rates (e.g. C/10, Figure 3b) and two clearly distinct EPR signal at high rates (Figure S5 in SI). During low temperature charge at high rates (e.g. 1C, Figure 4d) two lithium metal EPR signals emerge as well, whereas at low charging rates the low amount of lithium metal makes it difficult to distinguish between a single or two overlapping lithium metal signals. In all cases with two distinct lithium metal signals, the difference of the signal center ranges from 0.015 to 0.045 mT (corresponding to a shift of 40 to 120 ppm). The different shifts of these lithium metal EPR signals is probably caused by a shielding effect of the graphite electrode, which slightly reduces the magnetic field strength inside the porous graphite electrode in comparison to the separator (Figure 6a). To verify this hypothesis we prepared *ex situ* samples that either contained lithium dendrites encapsulated in a Celgard® separator ("Li@separator") or lithium metal homogeneously deposited within a graphite electrode ("Li@graphite"). The *ex situ* EPR spectra (Figure 6b) confirm that Li@graphite is shifted upfield for about 0.018 ± 0.005 mT (= 51 ppm) in comparison to Li@separator. In the *operando* EPR experiments the high field Li@graphite and the low field Li@separator signal always emerge simultaneously (within time and spectral resolution) after the onset of lithium plating. This is consistent with the fact that lithium plating is always initiated at the electrode/separator interphase before simultaneously propagating into the electrode and the separator phase.[2,35] The shielding effect of the graphite electrode might be caused by different susceptibilities, ring currents,[36,37] eddy currents[38] or a combination of these factors and is currently under investigation; in this respect, special challenges are the electronic[25,26] and magnetic[36] anisotropy of graphite intercalation compounds and the distribution of graphite crystallite orientations towards the external magnetic field.

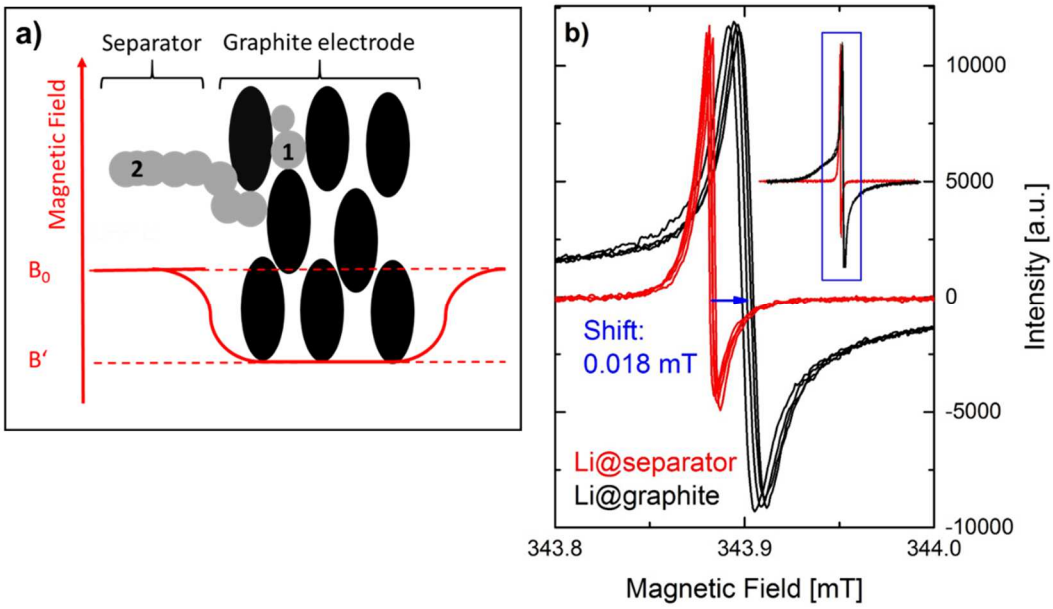

Figure 6 a) Scheme illustrating the physical origin of two Li metal signals observed in *operando* EPR spectra: partial shielding of external magnetic field inside the graphite electrode. b) *Ex situ* EPR spectra of Li dendrites inside the separator (red) and Li plated homogeneously within a graphite electrode (black). Inset: Zoom out of EPR spectra shown in main panel.

Conclusion and Outlook

In this study we introduced *operando* EPR spectroscopy as a novel technique for the investigation of the lithium plating reaction in LIBs. To the best of our knowledge, this is the first analytical technique capable of direct, time resolved and quantitative detection of lithium metal in a graphite electrode under realistic cell conditions. Time resolution can be as good as three minutes per spectrum. The achievable accuracy for the lithium metal quantification is not yet clear, but with the currently used simple and robust data analysis method an uncertainty of ≈3% with respect to the graphite capacity has been estimated (see SI for details). The mere (non-quantitative) detection limit will be significantly lower. It is also possible to deconvolute the coulombic inefficiency of the lithium plating/stripping process and quantify the contribution of dead lithium and SEI formation, which cannot be achieved with standard electrochemical techniques. Furthermore, the EPR spectra also contain spatial information regarding the location of lithium metal deposits (separator vs. electrode). Such data will be very useful for the validation of modeling/simulation based approaches[35,39–41] which have become powerful tools in LIB research but still contain uncertainties in the parametrization[41] and over-simplifying assumptions.[42] The major remaining challenge is the development of an improved cell design to minimize the cell-to-cell deviation. Nevertheless, *operando* EPR spectroscopy could become a valuable tool in Li-ion battery research with various applications like the optimization of fast charging procedures and the testing of electrolyte additives.

Materials and Methods

Electrode preparation and cell assembly

The graphite working electrodes with a composition of 90 wt-% graphite (SLP30, Timcal) and 10 wt-% polyvinylidene fluoride (PVDF) binder (Kynar HSV900, Arkema) were prepared by Mayer-rod coating (50 µm wetfilm thickness) of an *N*-methyl-2-pyrrolidone (Sigma Aldrich, 99.5 %) based ink with a solid content of 30 wt-% onto a Celgard C480 separator. The ink was prepared by mixing graphite, binder and solvent in a planetary centrifugal vacuum mixer (Thinky, USA) at 2000 rpm for 15 min. After solvent evaporation at room temperature, square electrodes (10 mm × 15 mm) were cut by a scalpel. The graphite loading was 2.0 $mg_{graphite}$ $cm^{-2}{}_{electrode}$ at a porosity of 60%.

The preparation of counter and reference electrode and the cell assembly of the *operando* EPR cell is explained in detail in our previous publications.[22,23] In short, the counter electrode was prepared using commercial lithium iron phosphate (LFP) as active material and PVDF as binder. The LFP counter electrode was directly coated onto the central aluminum wire (2 mm diameter, Alfa Aesar) which served both as mechanical support and counter electrode current collector. The capacity of the LFP counter electrode was oversized by a factor of three in comparison to the graphite working electrode in order to have enough electrochemically active lithium for the forced plating experiments and extended cycling. The reference electrode consisted of partially delithiated LFP ($Li_{0.5}FePO_4$) which was produced by chemical delithiation of commercial LFP using potassium peroxodisulfate (Sigma-Aldrich, 99.99%) as oxidizing agent. The reference electrode was directly coated onto a thin insulated aluminum wire (0.1 mm diameter, Goodfellow). All electrodes were dried under dynamic vacuum at 95°C for at least 12 hours in a glass oven (Büchi, Switzerland), and transferred for cell assembly into an argon-filled glove box (O_2 < 1 ppm, H_2O < 0.1 ppm; MBraun, Germany), carefully avoiding exposure to ambient air. For the assembly of the *operando* EPR cell, a separator (glass microfiber filter 691, VWR) and then the graphite working electrode were rolled around the central aluminum wire containing the LFP counter electrode. They were attached with a helically wound copper wire (Alfa Aesar, 99.9999% trace metal basis) which also serves as working electrode current collector. The LFP reference electrode was carefully introduced into the glass fiber separator. The cell was introduced into a quartz glass tube (6 mm outer diameter, 0.5 mm wall thickness, QSIL, Germany) and 200 µL of 1M lithium hexafluorophosphate ($LiPF_6$) in a mixture of ethylene carbonate (EC) and ethyl methyl carbonate (EMC) (LP57, BASF) were added as electrolyte. Afterwards the cell was sealed with a two component UV glue (UV glue 5023, BEST Klebstoffe, Germany) which had been dried over activated $CaCl_2$ in static vacuum for two weeks. A small quantity of manganese(II) oxide (Sigma, 99.99%) was used as an inert EPR reference material that was taped (Scotch® magic tape) directly onto the quartz glass tube in the same vertical position as the graphite working electrode.

Electrochemical testing

Electrochemical testing was done with a VMP2 or VMP3 potentiostat (Bio-Logic, France). In the entire study, the potential of the graphite electrode is measured against the partially lithiated LFP reference electrode. All potentials in this study are referenced to the Li/Li^+ scale by correcting the measured electrode potential for the potential of the partially lithiated LFP reference electrode (3.415 ± 0.005 V vs. Li/Li^+). The term "charge" refers to lithium intercalation into graphite, "discharge" refers to lithium deintercalation. The terms "oxidative/reductive current" are always defined with respect to the graphite working electrode. All cells first underwent a formation cycle with a C/5 charge and C/2 discharge (cut off potentials 0.01 V and 1.0 V vs. Li/Li^+). The experimentally determined C/2 deintercalation capacity was subsequently used as the reversible cell capacity for the *operando* EPR experiments in order to eliminate minor deviations from the nominal electrode size due to inaccurate cutting of the electrode. The first cycle coulombic efficiency was 86 ± 1% for all EPR cells, which is a typical formation loss for SLP30 graphite. After the formation cycle, the EPR cells were mounted in the resonator of the EPR spectrometer. For the forced lithium plating experiments cells were first charged to 0.01 V vs. Li/Li with a low rate and then lithium was plated with various C-rates (C/10 to 10C) to a nominal capacity of $Li_{1.5}C_6$ (e.g. five hours of lithium plating with a C/10 rate). For the low temperature experiments cells were charged with various C-rates (C/10 to 1C) with a capacity cut off at 335 mAh g^{-1} (nominally $Li_{0.9}C_6$) followed by an OCV period of at least 1.5 hours. Afterwards every cell underwent a forced lithium plating/stripping step in order to calibrate the lithium metal signal. Details regarding the low temperature cycling procedure and the calibration method can be found in the SI. Note that for every experiment that involved lithium plating a new cell was used.

Operando EPR experiments

EPR experiments were carried out on a Bruker X-band spectrometer. As is common practice, the EPR spectra were recorded as first derivatives of the signal with respect to the external magnetic field B_0. For the EPR spectra containing the graphite intercalation and lithium metal signal, the following settings were used: EPR Microwave power was set to 0.25 mW, sweeps were performed with 3 mT width and a center field of 340.5 mT; the field modulation frequency was set to 100 kHz and the modulation amplitude was 0.01 mT. The recording time per spectrum, which was adapted to the required temporal resolution, was 336 sec for a C/10 and C/5 rate and 86 sec for a C/2 and 1C rate. To correct the phase shift and changes of the resonator quality factor during the experiment, manganese(II) oxide was used as an inert EPR reference material. For the MnO EPR spectra the following settings were used: microwave power 1.0 mW, sweep width 600 mT, center field 340.5 mT, field modulation frequency 100 kHz, modulation amplitude 0.3 mT, recording time per spectrum of 86 sec for a C/10 and C/5 rate and 43 sec for a C/2 and 1C rate. EPR spectra were recorded continuously during cell cycling, alternating between narrow spectra showing the graphite intercalation compound and lithium metal, and broad spectra showing the MnO reference material. Further details regarding the phase and intensity correction can be found in the SI.

For low temperature experiments an evacuated glass dewar (8 mm inner diameter) was placed within the cavity of the EPR spectrometer. Liquid nitrogen was evaporated and cold nitrogen gas was passed over a heating coil and then through the dewar. The desired temperature was adjusted by controlling the evaporation rate and heating power. A thermocouple was taped directly onto the quartz glass tube 1 cm above the graphite working electrode in order to closely monitor the exact temperature. The liquid nitrogen reservoir lasted for about 16 hours if the cell was cooled to -20°C and actual temperature was always within ± 2°C of the desired value. The cell was given at least one hour to thermally equilibrate after cooling down to -20°C before starting electrochemical experiments.

Ex situ EPR experiment

The *ex situ* samples containing lithium metal encapsulated inside a separator ("Li@separator") were prepared by cycling a symmetrical lithium/lithium cell with three Celgard® C480 separators and LP57 electrolyte with a geometric current density of first 3.0 mA cm^{-2} and then 4.5 mA cm^{-2} for 10 cycles each (current always reversed after 30 minutes) in a pouch cell format under 1 bar atmospheric pressure. After cycling, the pouch cell was opened inside the argon filled glovebox and the central separator was recovered. It contained significant amounts of grey lithium dendrites which were visible by eye. The metallic nature of the grey deposits was confirmed by the vigorous gas evolution in contact with water.

The *ex situ* samples containing lithium metal homogeneously plated within a graphite electrode ("Li@graphite") was produced by slow C/10 forced lithium plating onto a fully lithiated graphite electrode. The forced lithium plating was terminate after five hours. These samples were prepared in a standard Swagelok cell with metallic lithium as counter and reference electrode, LP57 as electrolyte and SLP30 graphite on Celgard as working electrode (same electrode as for *operando* EPR experiments). After the forced lithium plating, the graphite electrode was harvested inside an argon filled glovebox. For each kind of *ex situ* sample two identical cells were cycled. 10 x 15 mm pieces were cut by scalpel and placed in EPR tubes closely resembling the concentric geometry of the *operando* EPR cell.

Every EPR tube contained both a Li@separator and a Li@graphite sample to exclude deviations in the signal center position due to differences in the EPR tube or other unaccounted factors. The two samples were placed on the same aluminum wire (resembling the operando EPR cell design) in different vertical positions, so that they could be measured after each other by changing the position of the EPR tube within the EPR resonator. Several *ex situ* EPR spectra were measured for every sample while rotating the EPR tube to exclude orientation effects. The exact signal center was determined by correcting for slight fluctuations of the microwave frequency, which was measured simultaneously using a microwave counter. The average signal center is 343.882 ± 0.004 mT for lithium dendrites in the separator and 343.900 ± 0.005 mT for lithium in the graphite electrode. The average difference is 0.018± 0.005 mT.

Acknowledgment

We thank Cyril Marino (Paul-Scherrer-Institute, Switzerland) for experimental support with the EPR experiments. We also thank Armin Siebel (TUM, Germany) for help with the time lapse video and Johannes Landesfeind (TUM, Germany) and Léonard Kröll (FZ Jülich) for helpful discussions on lithium plating and EPR data analysis. TUM gratefully acknowledges the funding by the Bavarian Ministry of Economic Affairs and Media, Energy, and Technology for its financial support under the auspices of the EEBatt and ExZellTUMII project.

References

1. Andre, D. *et al.* Future generations of cathode materials: an automotive industry perspective. *J. Mater. Chem. A* **3,** 6709–6732 (2015).
2. Gallagher, K. G. *et al.* Optimizing Areal Capacities through Understanding the Limitations of Lithium-Ion Electrodes. *J. Electrochem. Soc.* **163,** A138–A149 (2016).
3. Chandrasekaran, R. Quantification of bottlenecks to fast charging of lithium-ion-insertion cells for electric vehicles. *J. Power Sources* **271,** 622–632 (2014).
4. Keil, P. & Jossen, A. Charging protocols for lithium-ion batteries and their impact on cycle life-An experimental study with different 18650 high-power cells. *J. Energy Storage* **6,** 125–141 (2016).
5. Dahn, J. R. Phase diagram of LixC6. *Phys. Rev. B* **44,** 9170–9177 (1991).
6. Li, J. *et al.* Limiting factors for low-temperature performance of electrolytes in LiFePO 4/Li and graphite/Li half cells. *Electrochim. Acta* **59,** 69–74 (2012).
7. Hasan, M. F., Chen, C.-F., Shaffer, C. E. & Mukherjee, P. P. Analysis of the Implications of Rapid Charging on Lithium-Ion Battery Performance. *J. Electrochem. Soc.* **162,** A1382–A1395 (2015).
8. Cho, H. M., Choi, W. S., Go, J. Y., Bae, S. E. & Shin, H. C. A study on time-dependent low temperature power performance of a lithium-ion battery. *J. Power Sources* **198,** 273–280 (2012).
9. Ebner, M., Chung, D. W., García, R. E. & Wood, V. Tortuosity anisotropy in lithium-ion battery electrodes. *Adv. Energy Mater.* **4,** 1–6 (2014).
10. Li, Z., Huang, J., Yann Liaw, B., Metzler, V. & Zhang, J. A review of lithium deposition in lithium-ion and lithium metal secondary batteries. *J. Power Sources* **254,** 168–182 (2014).
11. Liu, Q. *et al.* Understanding of Undesirable Anode Lithium Plating Issues in Lithium-Ion Batteries. *RSC Adv.* **6,** 88683–88700 (2016).
12. Smart, M. C. & Ratnakumar, B. V. Effects of Electrolyte Composition on Lithium Plating in Lithium-Ion Cells. *J. Electrochem. Soc.* **158,** A379–A389 (2011).
13. Petzl, M. & Danzer, M. A. Nondestructive detection, characterization, and quantification of lithium plating in commercial lithium-ion batteries. *J. Power Sources* **254,** 80–87 (2014).
14. Uhlmann, C., Illig, J., Ender, M., Schuster, R. & Ivers-Tiffée, E. In situ detection of lithium metal plating on graphite in experimental cells. *J. Power Sources* **279,** 428–438 (2015).

15. Burns, J. C., Stevens, D. a. & Dahn, J. R. In-Situ Detection of Lithium Plating Using High Precision Coulometry. *J. Electrochem. Soc.* **162,** A959–A964 (2015).

16. Liu, Q. Q., Petibon, R., Du, C. Y. & Dahn, J. R. Effects of Electrolyte Additives and Solvents on Unwanted Lithium Plating in Lithium-Ion Cells. *J. Electrochem. Soc.* **164,** A1173–A1183 (2017).

17. Zinth, V. *et al.* Lithium plating in lithium-ion batteries at sub-ambient temperatures investigated by in situ neutron diffraction. *J. Power Sources* **271,** 152–159 (2014).

18. von Lüders, C. *et al.* Lithium plating in lithium-ion batteries investigated by voltage relaxation and in situ neutron diffraction. *J. Power Sources* **342,** 17–23 (2017).

19. Zhuang, L., Lu, J., Ai, X. & Yang, H. In-situ ESR study on electrochemical lithium intercalation into petroleum coke. *J. Electroanal. Chem.* **397,** 315–319 (1995).

20. Gotoh, K. *et al.* In situ 7Li nuclear magnetic resonance study of the relaxation effect in practical lithium ion batteries. *Carbon N. Y.* **79,** 380–387 (2014).

21. Arai, J. *et al.* In Situ Solid State 7Li NMR Observations of Lithium Metal Deposition during Overcharge in Lithium Ion Batteries. *J. Electrochem. Soc.* **162,** A952–A958 (2015).

22. Wandt, J. *et al.* Operando Electron Paramagnetic Resonance Spectroscopy – Formation of Mossy Lithium on Lithium Anodes During Charge/Discharge Cycling. *Energy Environ. Sci.* **8,** 1358–1367 (2015).

23. Wandt, J., Jakes, P., Granwehr, J., Gasteiger, H. A. & Eichel, R.-A. Singlet Oxygen Formation during the Charging Process of an Aprotic Lithium–Oxygen Battery. *Angew. Chemie Int. Ed.* **55,** 6892–6895 (2016).

24. Harris, S. J., Timmons, A., Baker, D. R. & Monroe, C. Direct in situ measurements of Li transport in Li-ion battery negative electrodes. *Chem. Phys. Lett.* **485,** 265–274 (2010).

25. Basu, S. *et al.* Synthesis and properties of lithium-graphite intercalation compounds. *Mater. Sci. Eng.* **38,** 275–283 (1979).

26. Tsuzuku, T. Anisotropic electrical conduction in relation to the stacking disorder in graphite. *Carbon N. Y.* **17,** 293–299 (1979).

27. Dresselhaus, M. S. & Dresselhaus, G. Intercalation compounds of graphite. *Adv. Phys.* **51,** 1–186 (2002).

28. Wagoner, G. Spin resonence of charge carriers in graphite. *Phys. Rev.* **118,** 647–653 (1960).

29. Bhattacharyya, R. *et al.* In situ NMR observation of the formation of metallic lithium microstructures in lithium batteries. *Nat. Mater.* **9,** 504–10 (2010).

30. Odziemkowski, M. & Irish, D. E. An Electrochemical Study of the Reactivity at the Lithium Electrolyte/Bare Lithium Metal Interface. *J. Electrochem. Soc.* **139,** 3063–3074 (1992).

31. Peled, E. the Electrochemical-Behavior of Alkali and Alkaline-Earth Metals in Non-Aqueous Battery Systems - the Solid Electrolyte Interphase Model. *J. Electrochem. Soc.* **126,** 2047–2051 (1979).

32. Yoshimatsu, I., Hirai, T. & Yamaki, J. Lithium Electrode Morphology during Cycling in Lithium Cells. *J. Electrochem. Soc.* **135,** 2422–2427 (1988).

33. Arakawa, M., Tobishima, S., Nemoto, Y. & Ichimura, M. Lithium electrode cycleability and morphology dependence on current density. *J. Power* **43–44,** 27–35 (1993).

34. Aurbach, D., Gofer, Y. & Langzam, J. The Correlation Between Surface Chemistry , Surface

Morphology , and Cycling Efficiency of Lithium Electrodes in a Few Polar Aprotic Systems. *J. Electrochem. Soc.* **136,** 3198–3205 (1989).

35. Arora, P. Mathematical Modeling of the Lithium Deposition Overcharge Reaction in Lithium-Ion Batteries Using Carbon-Based Negative Electrodes. *J. Electrochem. Soc.* **146,** 3543 (1999).

36. DiSalvo, F. J., Safran, S. A., Haddon, R. C., Waszczak, J. V. & Fischer, J. E. Large anisotropy and stage dependence of the magnetic susceptibility of alkali-graphite intercalation compounds. *Phys. Rev. B* **20,** 4883–4888 (1979).

37. Shabtai, E. *et al.* He NMR of He @ C 606 - and He @ C 706 - . New Records for the Most. *J. Am. Chem. Soc.* **120,** 6389–6393 (1998).

38. Auld, B. A. & Moulder, J. C. Review of advances in eddy current nondestructive evaluation. *J. Nondestruct. Eval.* **18,** 3–36 (1999).

39. Legrand, N., Knosp, B., Desprez, P., Lapicque, F. & Raël, S. Physical characterization of the charging process of a Li-ion battery and prediction of Li plating by electrochemical modelling. *J. Power Sources* **245,** 208–216 (2014).

40. Mastali, M., Farkhondeh, M., Farhad, S., Fraser, R. A. & Fowler, M. Electrochemical Modeling of Commercial LiFePO4 and Graphite Electrodes: Kinetic and Transport Properties and Their Temperature Dependence. *J. Electrochem. Soc.* **163,** A2803–A2816 (2016).

41. Ge, H. *et al.* Investigating Lithium Plating in Lithium-Ion Batteries at Low Temperatures Using Electrochemical Model with NMR Assisted Parameterization. *J. Electrochem. Soc.* **164,** A1050–A1060 (2017).

42. Landesfeind, J., Hattendorff, J., Ehrl, A., Wall, W. A. & Gasteiger, H. A. Tortuosity Determination of Battery Electrodes and Separators by Impedance Spectroscopy. *J. Electrochem. Soc.* **163,** A1373–A1387 (2016).

Supplementary Information

Quantitative and Time Resolved Detection of Lithium Plating and Reintercalation on Graphite Anodes in Lithium Ion Batteries

Author list in alphabetic order

Eichel[2,3], Gasteiger[1], Granwehr[2,4], Jakes[2], Wandt[1]

[1]Technische Universität München, Institute for Technical Electrochemistry, Germany
[2] Forschungszentrum Jülich, Institut für Energie- und Klimaforschung, Grundlagen der Elektrochemie (IEK-9), 52425 Jülich, Germany
[3] RWTH Aachen University, Institut für Physikalische Chemie, 52074 Aachen, Germany
[4] RWTH Aachen University, Institut für Technische und Makromolekulare Chemie, 52074 Aachen, Germany

* corresponding authors

Content

1. *Operando* EPR Spectra

During lithium intercalation into graphite the electronic conductivity increases for a factor of 10 along the a-axis (parallel to graphene sheets) and by a factor of more than 2000 along the c-axis (perpendicular to graphene sheets).[1–3] On the one hand, this makes LiC_6 an interesting compound as it has the lowest conductivity anisotropy σ_a/σ_c of all know graphite intercalation compounds of ≈ 14 in comparison to ≈ 3000 for pristine graphite.[3] On the other hand, the increasing conductivity lowers the quality factor of the resonator, which decreases the signal intensity, and causes a phase shift that alters the observed line shape of the EPR spectra. In order to correct these effects, manganese(II) oxide was used as an inert EPR reference that was taped to the outside of the quartz glass tube in the same vertical position as the graphite working electrode. Alternatingly, broad EPR spectra with 600 mT sweep width, showing the MnO reference and a signal arising from the LFP counter electrode, and narrow EPR spectra with 3 mT sweep width, showing the graphite intercalation and lithium metal signal, were measured as schematically shown in Figure S1.

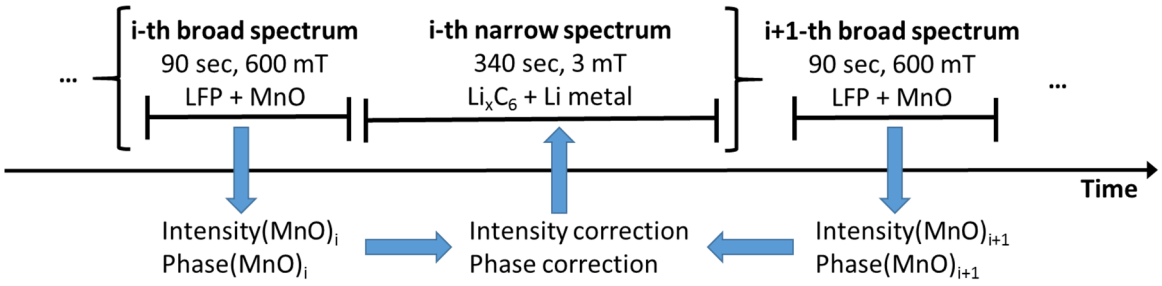

Figure S 1 Scheme of the sequence of wide and narrow operando EPR spectra.

The experimentally measured first derivative broad spectra were fitted with two (MnO and LFP) phase-shifted Lorentzian lines using[4]

$$I(B_0) = I_0 \left[\frac{\sin(\phi)}{\Delta^2+(B_0-B_{\mathrm{res}})^2} - 2(B_0 - B_{\mathrm{res}})\frac{\cos(\phi)+\sin(\phi)(B_0-B_{res})}{(\Delta^2+(B_0-B_{res})^2)^2}\right] \quad (1)$$

where I_0 is the signal amplitude, B_{res} the signal position, Δ the half width at half height and ϕ the phase that characterizes the asymmetry of the signal. The MnO phase and amplitude of the i^{th} and $(i+1)^{\mathrm{th}}$ spectrum were then used for the correction of the i^{th} narrow EPR spectrum (Figure S1). First, the phase of the i^{th} narrow EPR spectrum was corrected by the average of the i^{th} and $(i+1)^{\mathrm{th}}$ MnO phase using a numerical Hilbert transformation. Then, the phase corrected i^{th} narrow EPR spectrum was analyzed (either direct fitting or deviation method, see sections 2 and 3) to obtain the signal amplitudes of the graphite intercalation compound ($I_{\mathrm{Li}_x C_6,i}$) and, if present, the lithium metal ($I_{\mathrm{Li},i}$). Finally, in order to eliminate variations of the resonator quality factor, an intensity correction factor I_{ref} was calculated. This was done by dividing the averaged MnO amplitude of the i^{th} and $i+1^{\mathrm{st}}$ spectrum to the MnO amplitude of the first spectrum ($I_{\mathrm{MnO},1}$) according to $I_{ref,i} = (I_{\mathrm{MnO},i} + I_{\mathrm{MnO},i+1})/(2 * I_{\mathrm{MnO},1})$. The signal amplitudes $I_{\mathrm{Li}_x C_6,i}$ and $I_{\mathrm{Li},i}$ were then divided by $I_{ref,i}$ in order to obtain an intensity corrected measure for the amount of the graphite intercalation compound and lithium metal, respectively.

Figure S2 shows an example of the signal correction process for the first (Figure 2a,b) and the 20th spectrum (Figure 2c,d) measured during the C/10 deintercalation from LiC_6 at room temperature. Figure 2a shows the first broad *operando* EPR spectrum, which is dominated by the phase shifted first derivative Lorentzian line shape of the MnO signal. Figure 2b shows the first narrow *operando* EPR spectrum (black line), which has been subjected to a linear baseline subtraction, but before the phase and intensity correction, and the corresponding spectrum after phase and intensity correction (red line). For the first spectrum, the uncorrected and corrected spectrum look very similar (intensity correction factor 1.00, phase shift -0.14 rad) and display the expected Dysonian line shape. In contrast, for the 20th spectrum the Dysonian line shape only becomes visible after the correction process (intensity correction factor 1.17, phase shift +1.00 rad) whereas the as measured (baseline corrected) spectrum is distorted.

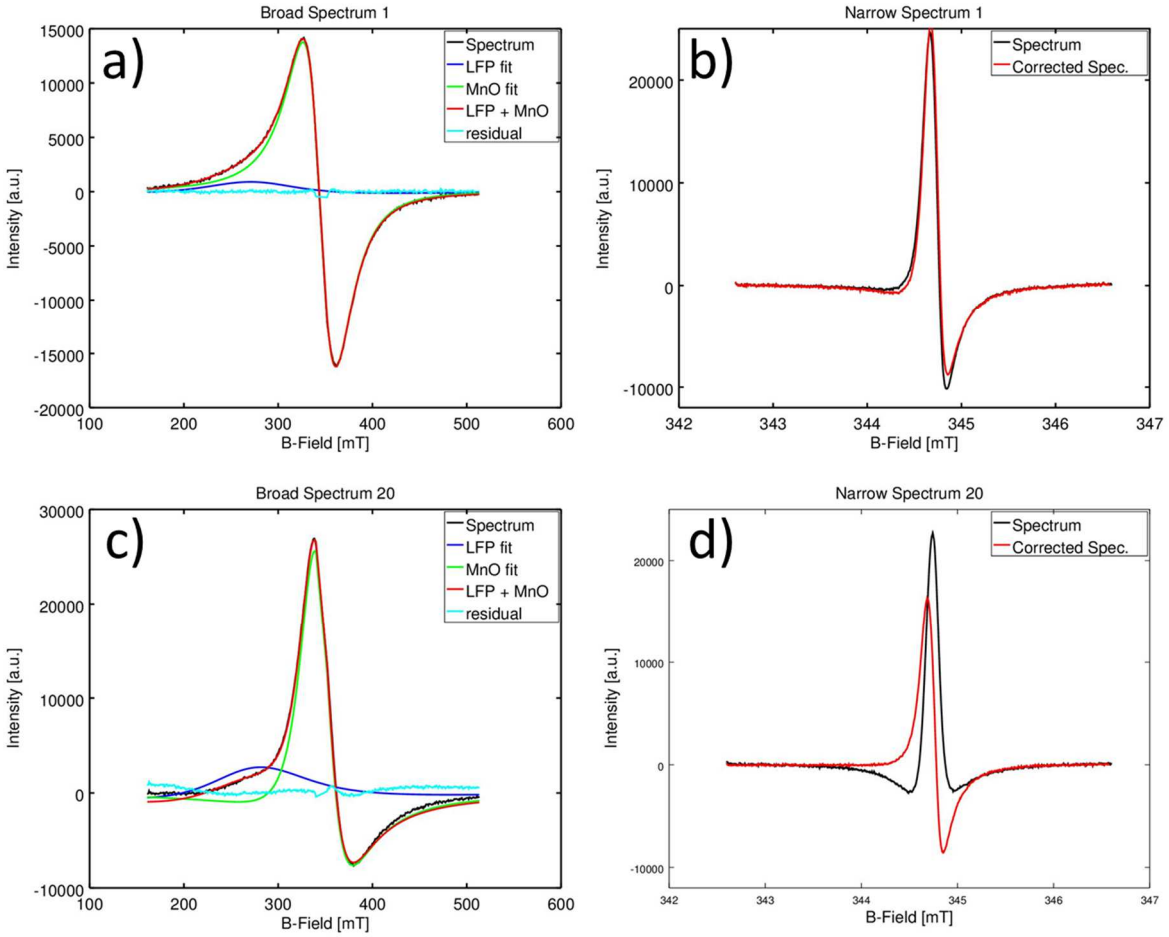

Figure S 2 Comparison of the measured with the intensity and phase corrected first (b) and 20th (d) narrow EPR spectrum (b and d). The correction is based on the MnO intensity and phase as determined in the respective broad spectrum (a and c).

2. Data analysis I: Multi component fit

In this section, data analysis via direct fitting of the phase corrected EPR spectra is shown.

<u>One signal component</u>

Figures S3 shows a phase corrected *operando* EPR spectrum containing a single signal component which can be assigned to the graphite intercalation compound (Li_xC_6), along with the fitted Dysonian curve using equation (1) and the respective residual.

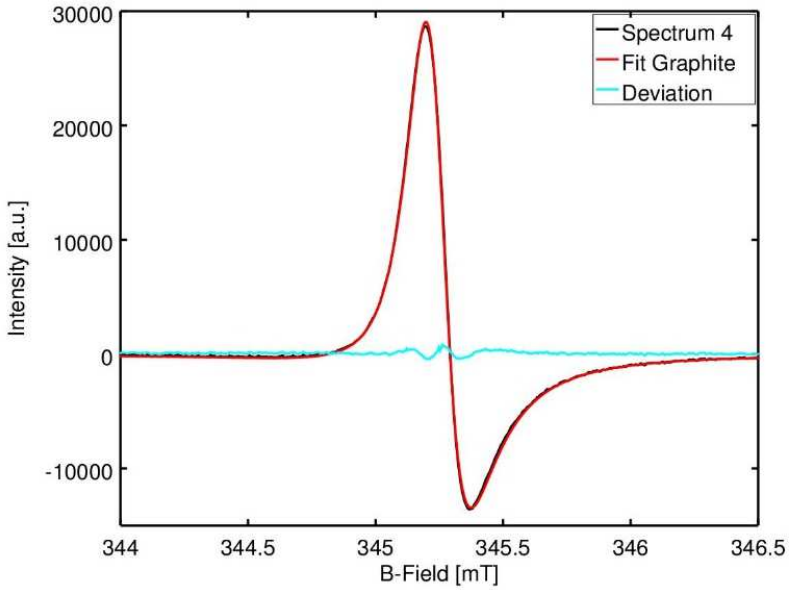

Figure S 3 *Operando* EPR spectrum of a graphite intercalation compound $Li_{0.5}C_6$ (black), the fit with a Dysonian line shape (red) and the residuals (cyan).

Two signal components

Figures S4 shows a phase corrected *operando* EPR spectrum containing two components recorded during the forced lithium plating onto Li_1C_6 with a C/10 rate. The broad component can be assigned to the graphite intercalation compound (Li_xC_6), the narrow component to metallic lithium. The two components are fitted simultaneously assuming two Dysonian lines and using equation (1). Figures S4a shows the phase corrected spectrum with the two fitted curves, Figures S4b shows the sum of the two fitted curves and the residual. In general, for spectra containing two components (Li_xC_6 and 1 x Li metal) simultaneous fitting is very robust, meaning that different input parameters (for signal position, width, phase and intensity) give the same result.

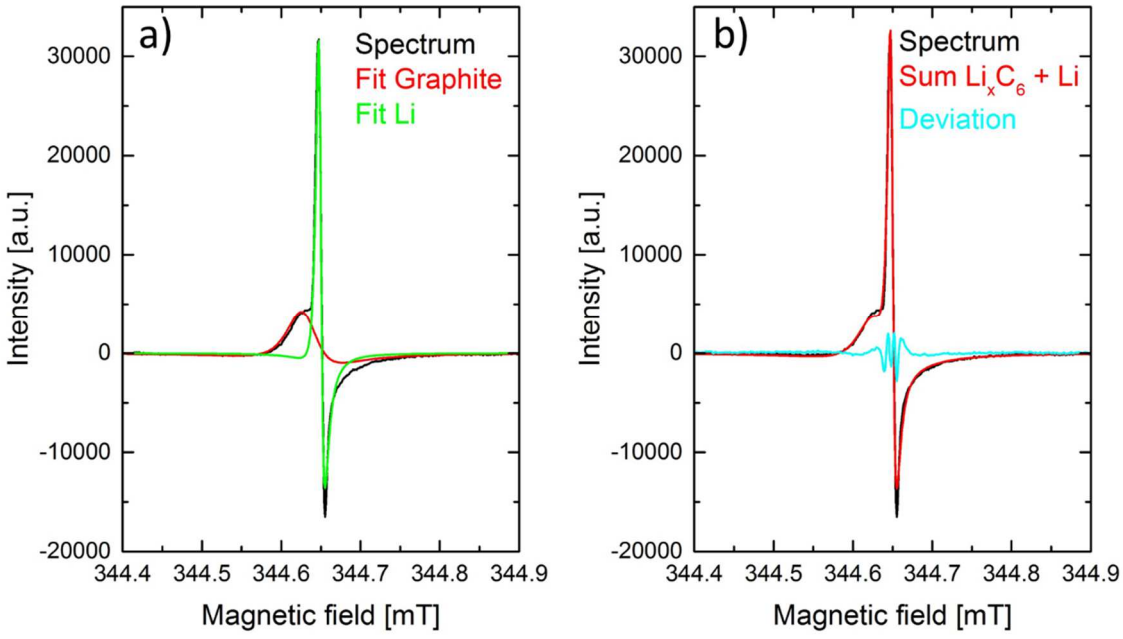

Figure S 4 a) Operando EPR spectrum (black) of an electrode containing LiC_6 and Li metal, plated with a C/10 rate, and fits of the LiC_6 signal (red) and the Li metal signal (green); b) Same EPR spectrum as in a) (black), sum of LiC_6 and Li metal fits (red) and the residuals (cyan).

Three signal components

Figures S5 shows a phase corrected *operando* EPR spectrum containing three components measured during the 10C forced lithium plating onto Li_1C_6. The broad component can be assigned to the graphite intercalation compound (Li_1C_6), the two narrow component to metallic lithium. The physical origin of two separate lithium metal EPR signals is discussed in the last section of the main paper. All three two components are fitted simultaneously using three Dysonian curves according to equation (1). Figures S5a shows the phase corrected spectrum with the three fitted curves, Figures S5b shows the sum of the three fitted curves and the residual. In general, for spectra containing three components (Li_xC_6 and 2 x Li metal), simultaneous fitting is only robust if the two lithium components both have a significant intensity and are clearly separated, as shown in Figure S5. Figure S6 shows the evolution of the lithium metal signal intensities during the 10C forced lithium plating experiment.

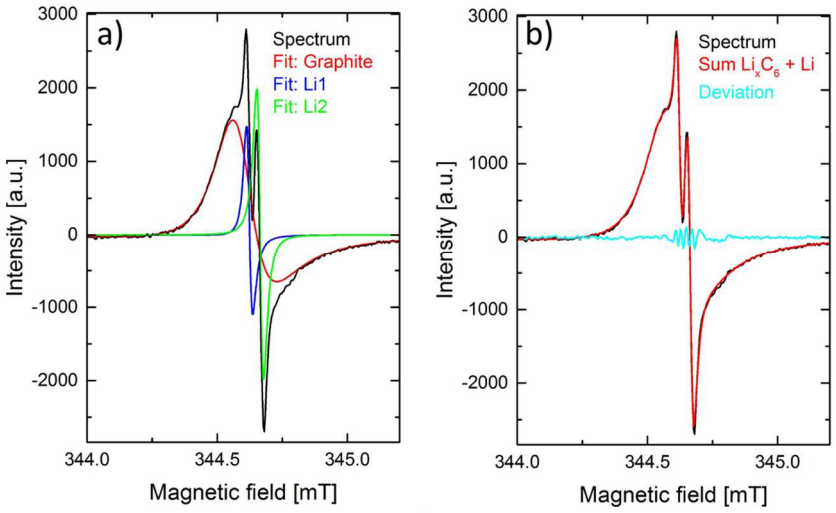

Figure S 5 a) Operando EPR spectrum (black) of an electrode containing LiC_6 and Li metal, plated with a 10C rate, and fits for the LiC_6 signal (red) and two Li metal signals (green and blue); b) Same EPR spectrum as in a) (black), sum of LiC_6 and both Li metal fits (red) and the residuals (cyan).

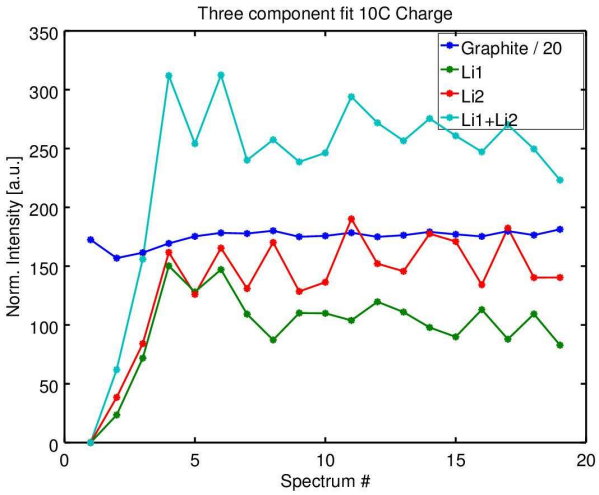

Figure S 6 Amplitude of graphite and Li signals obtained by direct three component fit for 10C forced Li plating at room temperature (see spectra in Fig. 5 of main paper and exemplary fit in Fig. S5).

3. Data analysis II: Deviation method

Working Principle of Deviation Method

The previously discussed multi-component fits work well for experiments with a high amount of lithium metal, which is the case for the forced lithium plating experiments as shown in Figure S4 and S5. In the low temperature charging experiments, it is complicated to obtain reliable multi component fits as i) the amount of lithium metal is generally lower and ii) the intercalation and lithium metal signals increase simultaneously. It was found that for the low temperature experiments the choice of the initial guess parameters and the boundaries have a significant impact on the fitting results, which were therefore less reliable.

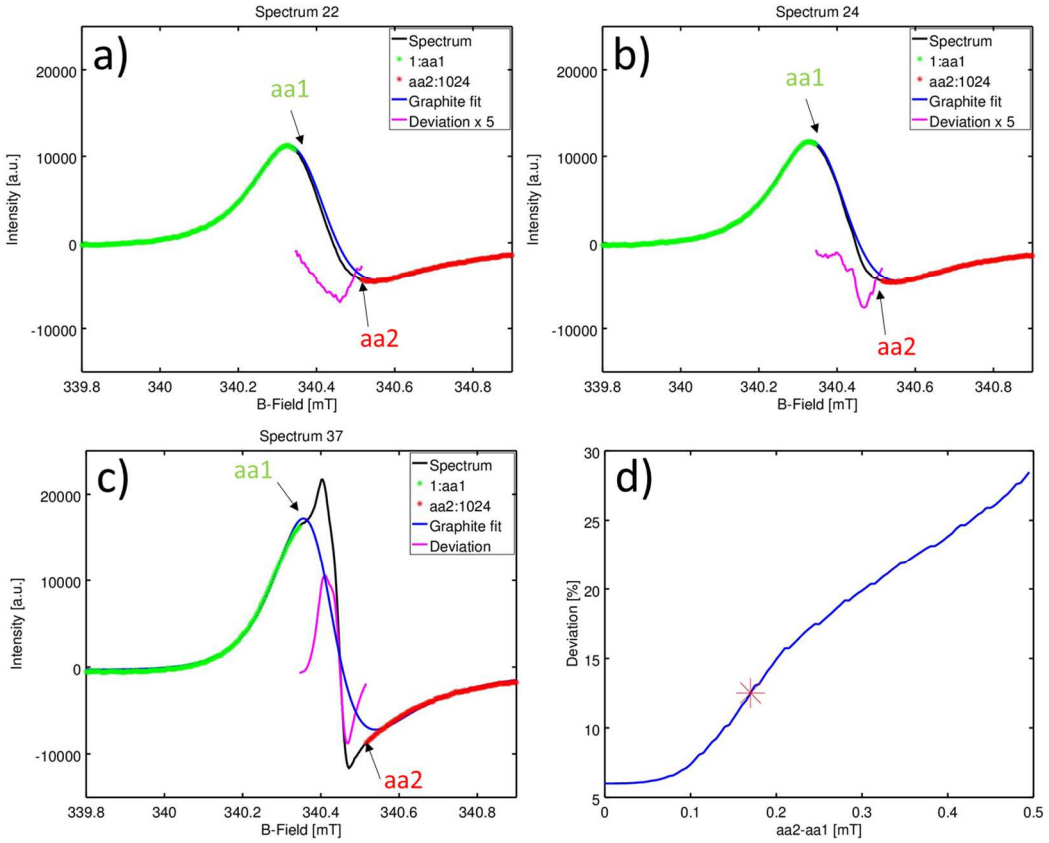

Figure S 7 a) to c) Operando EPR spectrum measured at -20 ° during battery charge (black), selection of data points for fitting of graphite signal (green and red), fitted graphite signal (blue) and difference between data and fit (pink). a) Spectrum immediately before the onset of Li metal plating. b) Spectrum immediately after the onset of Li metal plating. c) Spectrum at the end of charge, containing the maximum amount of Li metal. d) Deviation in fitting of a spectrum that does not contain a Li metal signal as a function of the gap (*aa*2 – *aa*1) not used for fitting. The red asterisk shows the *aa*2 – *aa*1 spacing which was used for data analysis.

As a consequence, the quantification of the lithium metal amount for the low temperature experiments was based on a different analysis method (Figure S7), which had to be i) simple and robust, ii) free of arbitrary parameter choices, and iii) independent of whether one or two lithium metal signal would exist in the spectrum. First the rather broad graphite spectrum was fitted with a single Dysonian line (fitted as phase shifted Lorentzian using formula S1, blue line in Figure S7 a to c).

For fitting of the graphite signal only the outer parts of the spectrum were used (green and red in Figure S7 a to c). The central part of the spectra was not used for fitting of the graphite signal to exclude co-fitting of the narrow lithium metal signal (Figure S7 c). The difference between the fitted graphite signal and the experimentally measured spectrum (pink line in Figure S7 a to c) was then used to quantify the amount of lithium metal according to

$$I_{Li} = \sqrt{\frac{1}{aa2-aa1}\sum_{aa1}^{aa2}(I(B_0) - f(B_0))^2} \quad (5)$$

where I_{Li} is the lithium metal signal amplitude in arbitrary units, $I(B_0)$ is the measured signal intensity of the EPR spectrum, $f(B_0)$ is the intensity of the graphite fit and $aa1$ and $aa2$ are the boundaries for the signal integration and also for fitting of the graphite signal. The choice of the $aa1$ and $aa2$ values was a compromise: For spectra recorded before the onset of lithium metal plating, the graphite fit gets better with decreasing the $aa2$–$aa1$ distance as shown in Figure S7 c. In contrast, once a significant lithium metal signal is present a certain aa2-aa1 distance is necessary in order to prevent co-fitting of the lithium metal signal. An $aa2$–$aa1$ distance of 0.17 mT, as indicated by the red asterisk in Figure S7 d, was used for all low temperature experiments except the C/10 charge.

For the C/10 charge the total amount of lithium plating was so low that it was possible to use the entire spectrum for fitting of the graphite signal (Figure S8). This increased the quality of the graphite fit, making it possible to detect significantly smaller lithium metal quantities.

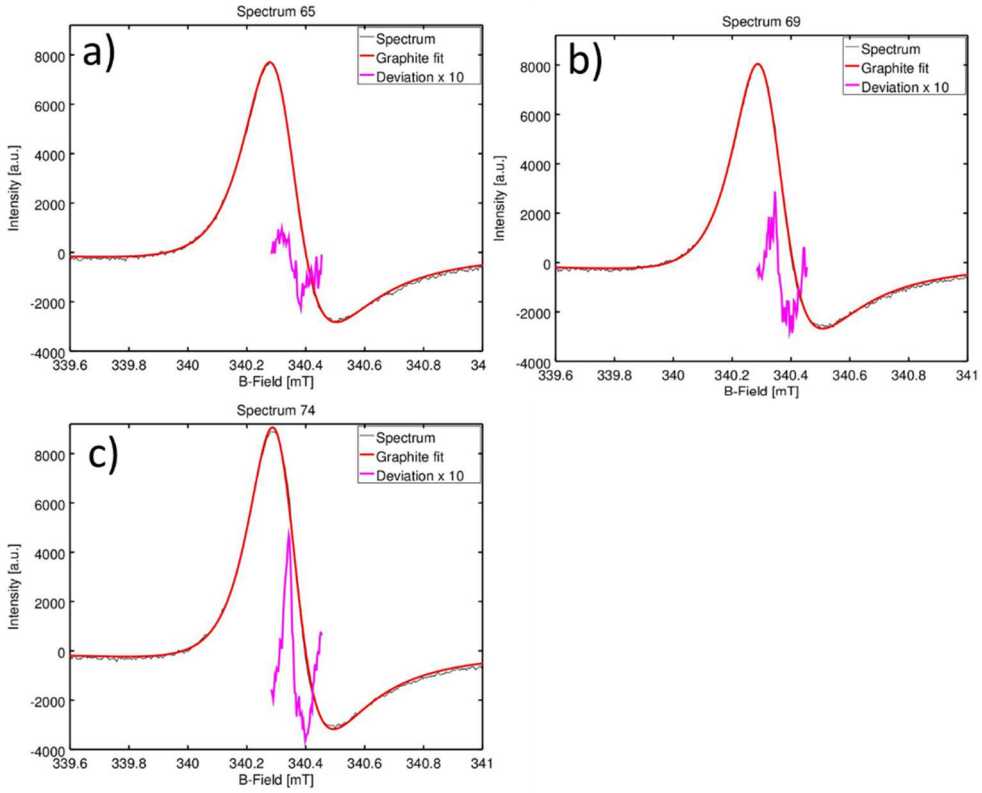

Figure S 8 Operando EPR spectrum measured at -20 ° during battery charge (black), fitted graphite signal (red) using the entire graphite spectrum for fitting, and difference between data and fit (pink). a) Spectrum directly before the onset of Li metal plating. b) Spectrum directly after the onset of Li metal plating. c) Spectrum at the end of charge containing the maximum amount of Li metal.

Identification of Lithium Plating Onset: Method A

Figure S7 a showed an EPR spectrum measured before the onset of lithium plating. In this case, the residual is simply due to imperfect fitting of the graphite signal and not to the presence of metallic lithium. This makes it necessary to define a criteria for the identification of the onset of lithium plating. Within this study, we used a simple and conservative approach and defined the onset of lithium metal plating as the first EPR spectrum, in which the residual unambiguously shows the typical first derivative EPR line shape of the lithium metal signal. Figure S9 a to d shows the spectra which were defined as the lithium plating onset for the C/2-I, C/2-II, C/5 and C/10 charge at -20 °C.

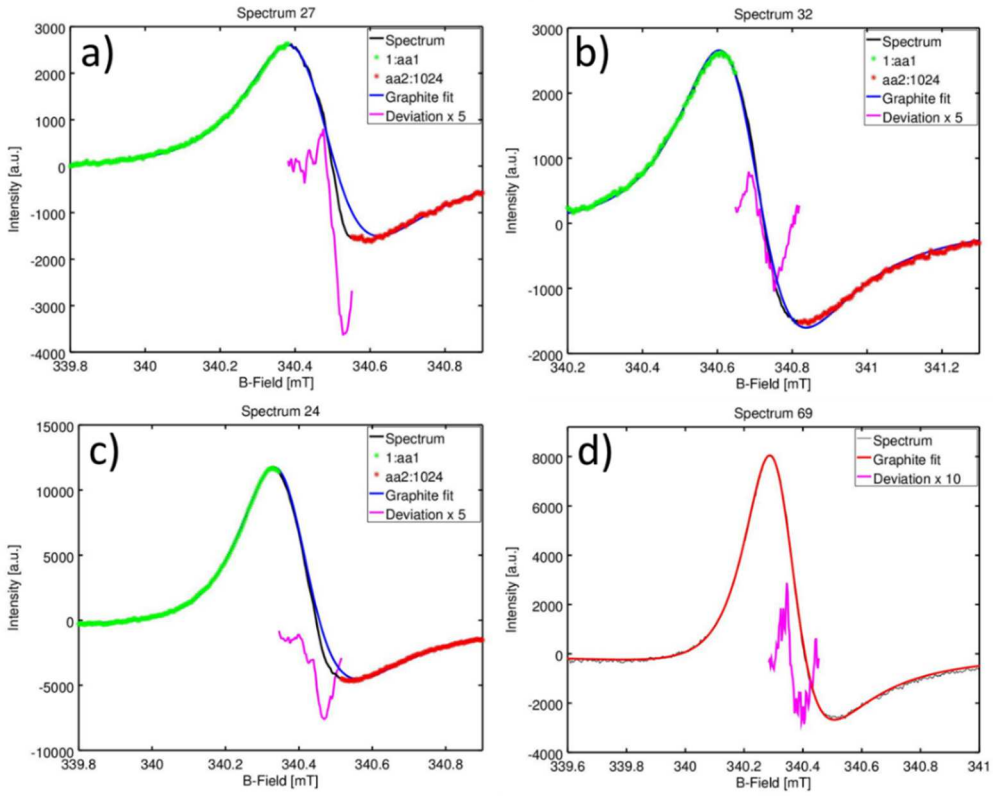

Figure S 9 Detection of Li plating onset in low temperature charging experiments (-20°C) by evaluating the shape of the deviation signal. a) C/2-I charge. b) C/2-II charge. c) C/5 charge. d) C/10 charge

Identification of Lithium Plating Onset: Method B

The cell which was charged with a 1C rate at -20 °C (black line in Figure 4 and 5 of main paper) contained an inert paramagnetic impurity with a narrow signal width. The signal intensity of this impurity was negligible in comparison to the lithium metal signal intensity, but it made the determination of the lithium metal plating onset difficult with the method described in the previous section ("Method A"). Therefore, for this cell the lithium plating onset was determined from difference spectra (spectrum(*n*+1)-spectrum(*n*)) in which the constant impurity is simply eliminated. Figure S10 shows the third difference spectrum (spect. 4 – spect. 3) which clearly displays two very narrow lithium metal signals in addition to the broader graphite signal.

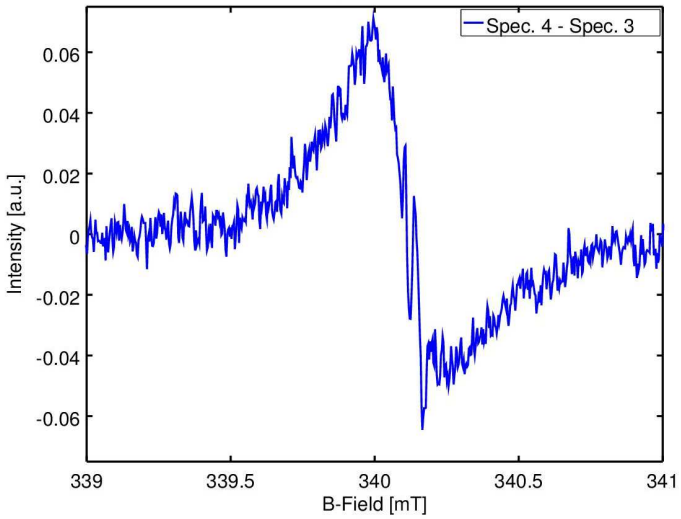

Figure S 10 Detection of Li plating onset in low temperature charging experiments (-20°C) with a 1C rate: Difference spectrum (4^{th} spectrum – 3^{rd} spectrum).

Identification of Lithium Plating Onset: Method C

A third possibility for the determination of the lithium plating onset are second derivative EPR spectra in which the narrower lithium metal signal is emphasized in comparison to the broader graphite signal. Second derivative EPR spectra were obtained by numerically differentiating the experimentally recorded first derivative spectra. A Savitzky-Golay filter (polynomial order of two, five point filter width) was used for smoothing before numerical differentiation. Since numerical differentiation also increases the noise this approach was only feasible for the C/5 and C/10 charging experiment as these spectra were of better signal-to-noise ration due to the longer recording time per spectrum (see Materials and Methods part in main paper). Figure S11 shows the second derivative spectra of the low temperature C/5 charge before and after the onset of lithium plating. In these second derivative EPR spectra a lithium metal signal can first be detected in spectrum 24 (red line, Figure S11). This is consistent with the lithium metal onset as determined by "Method A" (Figure S7b and Figure S9c).

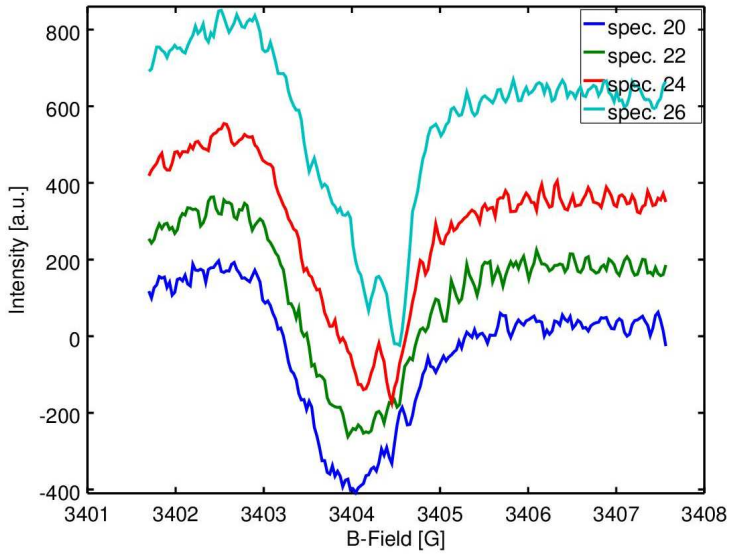

Figure S 11 Detection of Li plating onset in low temperature charging experiments (-20°C) with a C/5 rate: Selected 2nd derivative EPR spectra.

Baseline Correction and Accuracy

The first part (Working principle of Deviation Method) of this section explained a robust method for the determination of the amount of lithium metal I_{Li} in the dimension of arbitrary units. It is possible to quantify the lithium metal signal using a calibration procedure described in section 5 of the supplementary information. Figure S12 (main panel) shows the amount of lithium metal for all low temperature experiments determined by the deviation method in units of mAh's.

For each experiment, the colored dots indicate the spectrum in which lithium plating can first be detected. For the identification of the lithium plating onset, "Method A" was used for all cells except the 1C cell, for which "Method B" was used. As previously mentioned, the non-zero value before the onset of lithium plating is caused by imperfections of the graphite fit and is subtracted as constant baseline value. This background value is also used as constant error bar for the respective cell. The inset in Figure S12 shows the same data as the main panel after background subtraction and addition of the error bars and is identical to Figure 4b (main paper).

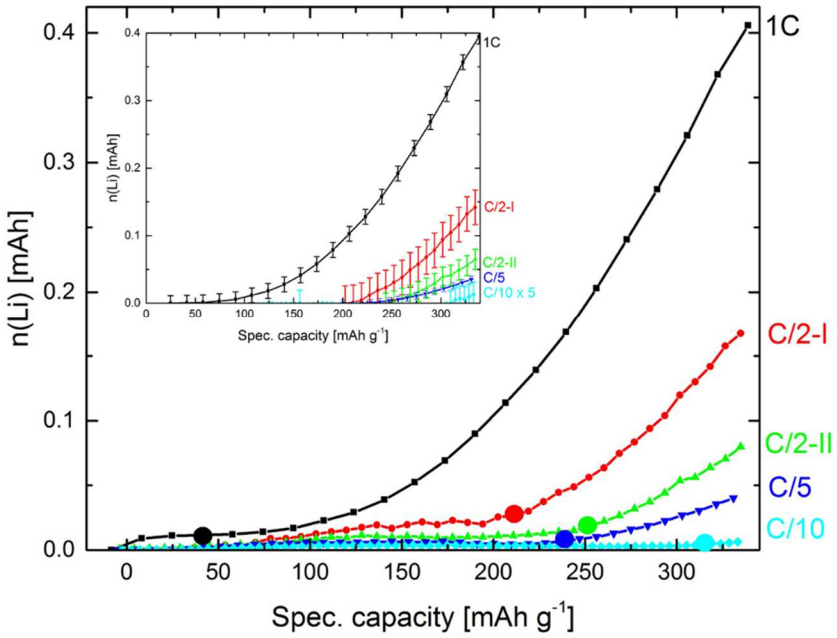

Figure S 12 Amount of Li metal during charge at -20 °C at different C-rates; the colored dots indicate the onset of the Li metal signal in the EPR spectra; inset: Baseline corrected amount of Li metal-

The cells shown in Figure S12 have a total capacity of 0.8 to 1.0 mAh. The cell C/2-I has a total capacity of 0.865 mAh and the error bars correspond to a capacity of ± 0.026 mAh or ± 3.0% of the cell capacity. Still this error is only a first approximation of the relative accuracy of the *operando* EPR technique for the lithium quantification. In order to properly determine the absolute accuracy, the results obtained by *operando* EPR will have to be compared to an independent analytical technique. The real accuracy might very well be better than the estimation of 3% if the imperfect fitting of the graphite signal really behaves like a constant background value; or the real accuracy might also be worse due to systematic errors, for example in the calibration procedure.

4. Comparison Multi Component Fit and Deviation Method

In the previous two sections, two different methods for the data analysis were explained, namely the direct multicomponent fits and the deviation method. Multicomponent fits are restricted to cells with high lithium metal intensity, which is mostly the case in forced lithium plating experiments. The deviation method can also be used for low amounts of lithium metal which is typically the case during "non-forced" lithium plating in low temperature experiments. For the low temperature charge with a 1C rate, the lithium metal amount is high enough to also apply the three component fit (one graphite, two lithium metal signals) as shown in Figure S13 a. The two different lithium metal signals develop similarly over the course of the experiment as shown in Figure S13 b. Also, both lithium metal signals first occur in the 4th spectrum (see Figure S10a).

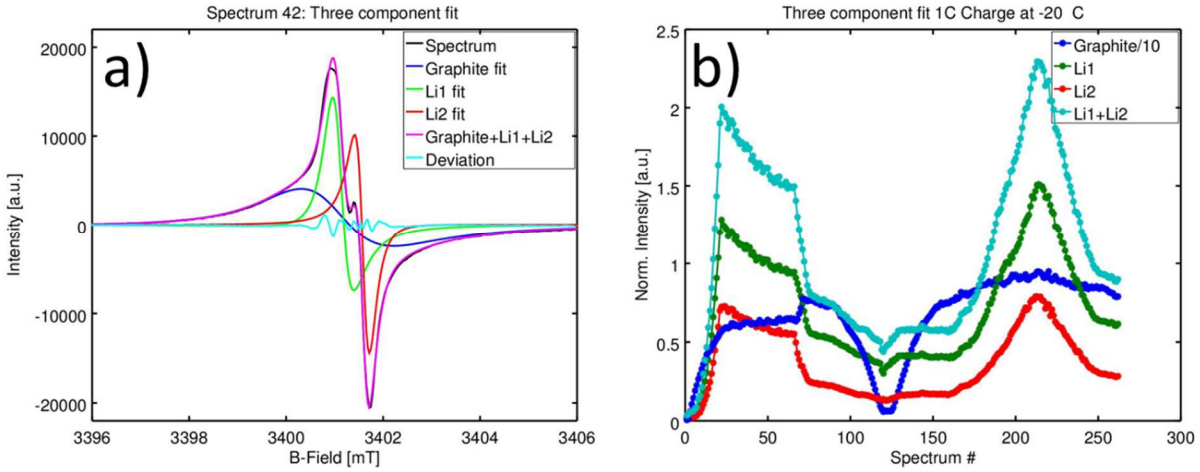

Figure S 13 a) Direct three component fit of operando EPR spectrum of 1C charge at -20 °C. b) Amplitude of graphite (blue), Li metal (red and green) and sum of Li metal (cyan) signals over the entire 1C charging experiment at -20 °C. The signal amplitudes are determined by a direct three component fit of the operando EPR spectra as shown in panel a).

Figure S14 a shows the comparison of the total lithium amount and lithium metal plating current as determined by the deviation method (black line) and the multi component fit (red line). The results obtained by these completely independent analysis methods agree well. Figure S14 b shows the lithium plating current, obtained by differentiating the curves shown in Figure S14 a. The lithium plating current can either be expressed in units of µA (left y-axis), or in % of the applied cell current (right y-axis). The lithium plating currents determined with the two different techniques agree very well expect for the very beginning and end. The deviation below 50 mAh g^{-1} is irrelevant as it is before the lithium plating onset, the reason for the slight deviation above 300 mAh g^{-1} is not yet clear.

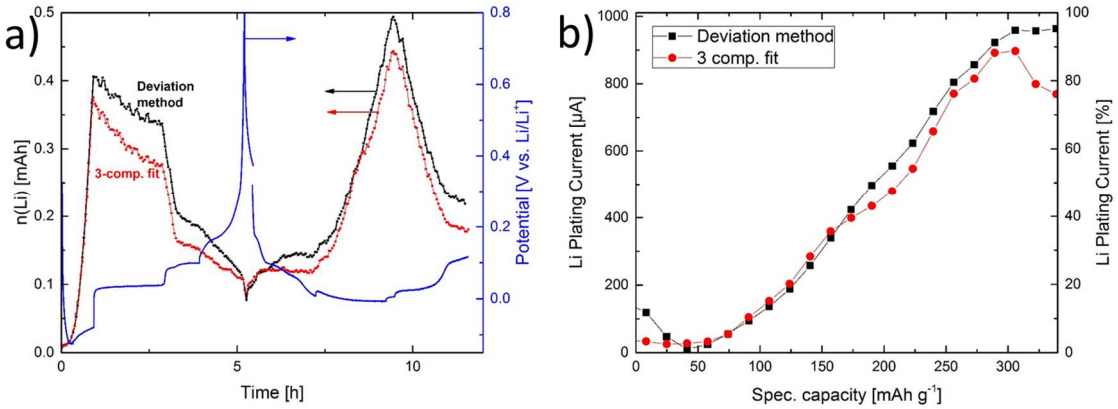

Figure S 14 Comparison of the results obtained by a direct three component fit (red) and the more robust deviation method (black). a) Amount of Li metal. b) Li plating current.

5. Low Temperature Charge: Electrochemical Procedure and Li Quantification

Table S1 and Figure S15 show details regarding the electrochemical procedure of the low temperature EPR experiments. In general, these experiments consisted of three parts, namely the formation cycle (steps 1 and 2), the actual low temperature *operando* EPR experiment (step 3) and the calibration cycle (steps 6 to 9). The EPR cell is mounted in the EPR resonator after the formation cycle. During the OCV period (steps 4 and 5) in between the actual experiment and the calibration cycle, the temperature was changed to room temperature.

Table S 1 Experimental details of low temperature charging experiments.

Step	Technique	Termination	Temperature	Set up
1	C/5 Intercal./Plating	10 mV vs. Li/Li$^+$	RT	Outside of resonator
2	C/2 Deintercal.	1.0 V vs. Li/Li$^+$		
3	C/*x* Intercalation (*x* = 1, 2, 5 or 10)	90% of $Q_{theo.}$	- 20 °C	Operando EPR
4	OCV	1.5 h		
5	OCV	1.5 h	RT	
6	C/2 Deintercal.	1.0 V vs. Li/Li$^+$		
7	C/2 Intercal.	1.8 h or 10 mV vs. Li/Li$^+$		
8	C/5 Plating	2 h		
9	C/5 Stripping	1.0 V vs. Li/Li$^+$		

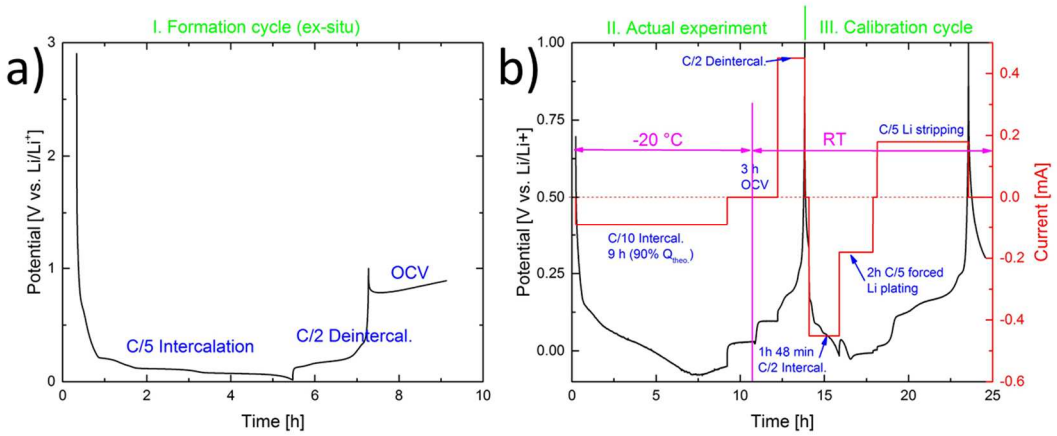

Figure S 15 a) Potential profile of formation cycle; b) Potential and current profile during *operando* EPR experiment.

During the calibration cycle, forced lithium plating (step 8) and lithium stripping (step 9) was carried out to determine the calibration factor. During lithium stripping in step 9, the entire applied oxidative current, i_{ox} can be assigned to electrochemical lithium metal oxidation (Li $\longrightarrow$ Li$^+$ + e$^-$) as explained in the main paper. Therefore the calibration factor *y* can be calculated by

$$y = \frac{i_{\mathrm{ox}}}{F\, m_{\mathrm{stripping}}} \qquad (3)$$

where i_{ox} is in units of [A], F is the Faraday constant in [As mol^{-1}] and $m_{stripping}$ is the slope of the amount of lithium metal plotted over time [a.u. s^{-1}] as shown in Figure S16a. The calibration factor y has the dimension of [mol a.u.$^{-1}$] and can be used for converting the lithium metal intensity from arbitrary units into moles. The calibration factor was independently determined for every cell to eliminate the influence of cell-to-cell deviations, which might be caused by small differences of the position within the resonator or the amount of electrolyte within the resonator.

For a few cells the slope of the lithium stripping step could not be properly determined (Figure S16b). In this case the slope of the lithium plating step is used for the determination of the calibration factor y as

$$y = m_{\mathrm{plating}} * 0.85 \tag{4}$$

where $m_{plating}$ is the slope of the plating step (Figure S16b).The constant factor 0.85 is the average ratio of $m_{\mathrm{plating}}/m_{\mathrm{stripping}}$ for cells where both values could be determined.

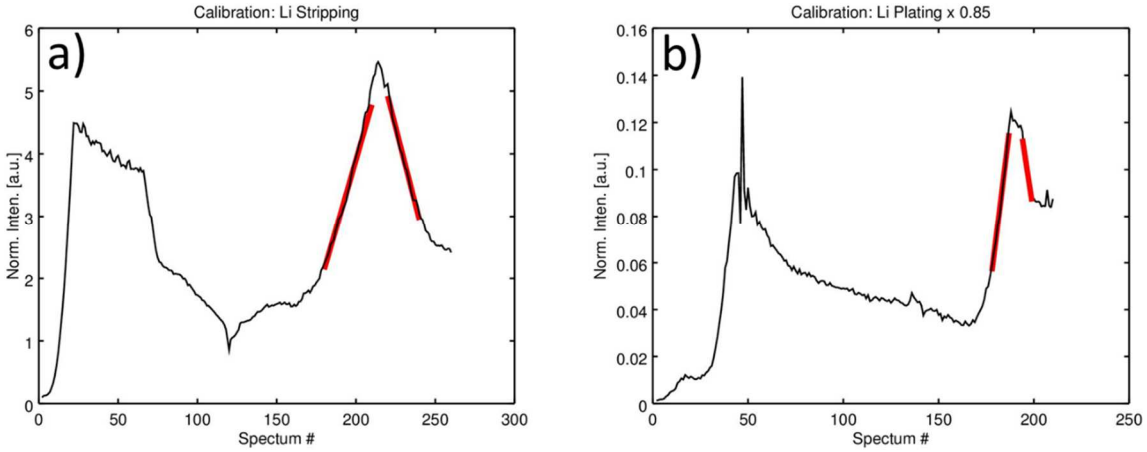

Figure S 16 Normalized intensity of Li metal signal during an *operando* EPR experiment, a) Example of a calibration cycle with a good Li plating and Li stripping step; b) Example of an calibration cycle with a good Li plating but an insufficient Li stripping step.

6. Non-linear effects and penetration depth

Quantitative EPR spectroscopy is based on the assumption that the signal amplitude is proportional to the number of contributing spins. In all experiments carried out in this study the lithium metal signal falls into such a linear regime. In every experiment in which a constant lithium platting/stripping current was applied (e.g. forced lithium plating) a linear increase/decrease of the lithium amount with time has been observed (Figure 3c, Figure S6 and Figure S8). In contrast, the graphite intercalation signal showed a non-linear behavior in two cases. In Figure 2c (main paper) the graphite signal intensity levels off at high SOCs during the constant current charge and in Figure 3c (main paper) the graphite signal intensity shows a decreases and subsequent increase while the amount of LiC_6 stays constant.

In conduction EPR spectroscopy, such non-linear effects are often caused by the limited penetration depth of the microwave (skin effect).[4] The penetration depth d of the microwave into an electronically conducting material, such as pristine graphite or Li_xC_6, can be calculated using[5]

$$d = \sqrt{\frac{1}{\pi f \sigma \mu_0 \mu_r}} \tag{2}$$

where f is the microwave frequency (= 9.63 GHz), σ the electronic conductivity of Li_xC_6, μ_0 the vacuum permeability (= 4π 10^{-7} m kg A^{-2} s^{-2}) and μ_r the relative permeability of Li_xC_6. The relative permeability of Li_xC_6 is anisotropic and varies with intercalation state[6] but for the calculation of the penetration depths the assumption of $\mu_r \approx 1$ is suitable. As previously mentioned, the electronic conductivity is also highly anisotropic and varies with the intercalation state; the following values have been reported for highly oriented pyrolytic graphite (HOPG): $\sigma_a(C_6) = 2.5 \cdot 10^4$ S cm^{-1}, $\sigma_c(C_6) = 8.3$ S cm^{-1}, $\sigma_a(LiC_6) = 25 \cdot 10^4$ S cm^{-1} and $\sigma_c(LiC_6) = 1.8 \cdot 10^4$ S cm^{-1}.[1–3] According to formula (2), these conductivities cause penetration depths of $d_a = 3$ µm and $d_c = 184$ µm for pristine graphite and $d_a = 1$ µm and $d_c = 4$ µm for LiC_6.

It is not entirely clear whether the shielding effect at high intercalation states observed in Figure 2c (main paper) occurs on the electrode or the graphite particle level. In the former case, the outer part of the concentric graphite electrode would shield the inner part of the electrode ("case I"), in the latter case the outer part of every graphite particle would shield the inner part of the same particle ("case II"). In order to evaluate these two cases it is helpful to compare the penetration depth with the electrode and graphite particle dimensions. A single SLP30 particle is potato shaped with dimensions of roughly 10 x 20 x 3 µm.[7] The electrode thickness is about 20 µm with a porosity of about 60%. A SOC dependent shielding mechanism on the electrode level ("case I") would be conceivable as the d_c penetration depth is higher than the electrode thickness of ≈ 20 µm for pristine graphite ($d_c = 184$ µm) but smaller for LiC_6 ($d_c = 4$ µm). Therefore, the outer part of the graphite electrode could shield off the inner part, but only at high intercalation states. But such a partial shielding effect on the electrode level would also cause a partial shielding of the lithium metal signal which is not observed in Figure 3c. The absence of lithium shielding in Figure 3c is highlighted by the constant signal amplitude of the dead lithium metal signal during the lithium deintercalation (after

the second vertical dashed line). If there had been a partial shielding of inner parts of the electrode the signal amplitude would increase during lithium deintercalation (=de-shielding) which is not observed. As a consequence, a shielding effect on the electrode level ("case I") is unlikely. The d_a penetration depth of 3 µm for pristine graphite and 1 µm for LiC_6 are both small in comparison to the lateral dimension of the SLP30 particles (≈ 10 x 20 µm). In contrast, the d_c penetration depth of 184 µm for pristine graphite and 4 µm for LiC_6 are both higher, if only slightly in the case of LiC_6, than the thickness of the SLP 30 particles (≈ 3 µm). Based on these numbers one would not expect a SOC dependent shielding effect where the outer part of every SLP30 particle shields off the inner part of the same particle ("case II") at high intercalation states. But this direct comparison of the SLP30 particle sizes to the above stated d_a and d_c penetration depths might be flawed, as they were calculated based on σ_a and σ_c conductivity values of highly oriented pyrolytic graphite (HOPG). In HOPG the individual crystallites, which are much smaller than the particle sizes,[8] are almost perfectly aligned within the graphite particle. If the crystallites are a little less oriented in SLP30, the conductivity anisotropy might be reduced and the effective penetration depth for LiC_6 in c-direction might be in between d_a and d_c values of HOPG of d_a = 1 µm and d_c = 4 µm. If this is the case the effective d_c penetration depth for SLP30 might fall below the average SLP30 particle thickness of 3 µm causing a "case II"-type shielding effect on the particle level. In summary, shielding effect observed in Figure 2 must be caused by limited penetration depth into graphite but it is not entirely clear whether it takes place on the electrode or the particle level.

References Supplementary Information

1. Tsuzuku, T. Anisotropic electrical conduction in relation to the stacking disorder in graphite. *Carbon N. Y.* **17,** 293–299 (1979).

2. Basu, S. *et al.* Synthesis and properties of lithium-graphite intercalation compounds. *Mater. Sci. Eng.* **38,** 275–283 (1979).

3. Dresselhaus, M. S. & Dresselhaus, G. Intercalation compounds of graphite. *Adv. Phys.* **51,** 1–186 (2002).

4. Wandt, J. *et al.* Operando Electron Paramagnetic Resonance Spectroscopy – Formation of Mossy Lithium on Lithium Anodes During Charge/Discharge Cycling. *Energy Environ. Sci.* **8,** 1358–1367 (2015).

5. Bhattacharyya, R. *et al.* In situ NMR observation of the formation of metallic lithium microstructures in lithium batteries. *Nat. Mater.* **9,** 504–10 (2010).

6. DiSalvo, F. J., Safran, S. A., Haddon, R. C., Waszczak, J. V. & Fischer, J. E. Large anisotropy and stage dependence of the magnetic susceptibility of alkali-graphite intercalation compounds. *Phys. Rev. B* **20,** 4883–4888 (1979).

7. Ghimbeu, C. M. *et al.* Influence of Graphite Characteristics on the Electrochemical Performance in Alkylcarbonate LiTFSI Electrolyte for Li-Ion Capacitors and Li-Ion Batteries. *J. Electrochem. Soc.* **160,** A1907–A1915 (2013).

8. Zaghib, K., Nadeau, G. & Kinoshita, K. Effect of Graphite Particle Size on Irreversible Capacity Loss. *J. Electrochem. Soc.* **147,** 2110 (2000).

3.1.3 Singlet Oxygen Formation In Lithium-Oxygen Batteries

This section presents the article "Singlet Oxygen Formation during the Charging Process of an Aprotic Lithium-Oxygen Battery" which was submitted in March 2016 and accepted for publication in the peer reviewed Journal *Angewandte Chemie International Edition* in April 2016. The article is reproduced within this thesis under the License Number 4117890260316. The publication was presented on international conferences, for example on the 230th Meeting of The Electrochemical Society/PRIME 2016 in Honolulu (USA) in October 2016 (Abstract Number: #A03-0319). The permanent weblink to the article is http://onlinelibrary.wiley.com/wol1/doi/10.1002/ange.201602142/abstract.

In this study we use *operando* EPR spectroscopy in combination with a chemical spin trap to prove the occurrence of singlet oxygen during the charging process of an aprotic lithium-oxygen cell. In the course of this study, an altered cell housing was developed which can be purged with oxygen within the cavity of the EPR spectrometer. We use tetramethyl-4-piperidone (4-Oxo-TEMP) as a spin trap which specifically reacts with singlet oxygen forming the stable and EPR active radical 4-Oxo-2,2,6,6-tetramethyl-1-piperidinyloxy (4-Oxo-TEMPO). This is the first use of this spin trap in a lithium-oxygen cell. Detailed background experiments and various additional analytical techniques are applied to confirm that the addition of 4-Oxo-TEMP does not alter the fundamental Li_2O_2 charging reaction. In this study we unambiguously demonstrate that singlet oxygen is formed if the charging potential exceeds 3.5 V vs. Li/Li^+; this onset potential is very similar to the thermodynamic threshold for singlet oxygen evolution of about 3.5 V. Furthermore, this potential is identical to the onset potential of the severe charging side reactions whose origin has been unclear so far (see Section 1.3). Considering its high reactivity, we propose that singlet oxygen evolution might be the long overlooked reason for the side reactions observed during charging.

In a recent publication, Mahne et al. confirm the occurrence of singlet oxygen evolution and also present experimental data which back our theory regarding its role in the charging side reactions.[153] In a comment to this article by Alan C. Luntz and Bryan McCloskey, the importance of the singlet oxygen discovery for the lithium-oxygen battery research is emphasized: *"If reactions of singlet O_2 are the underlying issue hindering reversibility, and its formation is a natural consequence of the $Li-O_2$ electrochemistry, then the current strategy for minimizing the parasitic chemistry must change."*[71]

Author contributions

H.G. and R.E. had the idea for this study. J.W. developed the special cell design used within this study. J.W. carried out the background experiments. J.W. and P.J. carried out the EPR experiments. J.W. wrote the manuscript. All authors discussed the data and commented on the results.

Lithium–Air Batteries

International Edition: DOI: 10.1002/anie.201602142
German Edition: DOI: 10.1002/ange.201602142

Singlet Oxygen Formation during the Charging Process of an Aprotic Lithium–Oxygen Battery

Johannes Wandt, Peter Jakes,* Josef Granwehr, Hubert A. Gasteiger, and Rüdiger-A. Eichel*

Abstract: *Aprotic lithium–oxygen ($Li–O_2$) batteries have attracted considerable attention in recent years owing to their outstanding theoretical energy density. A major challenge is their poor reversibility caused by degradation reactions, which mainly occur during battery charge and are still poorly understood. Herein, we show that singlet oxygen ($^1\Delta_g$) is formed upon Li_2O_2 oxidation at potentials above 3.5 V. Singlet oxygen was detected through a reaction with a spin trap to form a stable radical that was observed by time- and voltage-resolved in operando EPR spectroscopy in a purpose-built spectroelectrochemical cell. According to our estimate, a lower limit of approximately 0.5 % of the evolved oxygen is singlet oxygen. The occurrence of highly reactive singlet oxygen might be the long-overlooked missing link in the understanding of the electrolyte degradation and carbon corrosion reactions that occur during the charging of $Li–O_2$ cells.*

Since its discovery,[1] the aprotic lithium–air or lithium–oxygen ($Li–O_2$) battery has attracted huge interest as a possible "beyond-lithium-ion" technology owing to its outstanding theoretical energy density of 3460 $Wh\,kg^{-1}$.[2] The energy density on a system level—taking into account inactive cell components—has been predicted to lie between 250 and 500 $Wh\,kg^{-1}$, which exceeds a current lithium-ion battery by a factor of about 1.5 to 2.[3] The central problem for the development of a reversible $Li–O_2$ cell chemistry are parasitic side reactions causing the degradation of both the carbon electrode and the electrolyte upon battery cycling, thus leading to cell death within a few cycles.[4,5] In the reversible formation of Li_2O_2 ($2\,Li^+ + O_2 + 2\,e^- \rightarrow Li_2O_2$), an important measure to quantify the contribution of undesired side reactions is the e^-/O_2 ratio, which should ideally equal 2.00. However, several research groups found that, especially during charging, e^-/O_2 ratios significantly deviate from 2.00 for various combinations of solvents, conducting salts, and cathode materials.[6,7] The exact electrochemical or chemical nature of the side reactions during charge remains largely unclear, but some form of "nascent" oxygen produced during charging has been suggested to contribute to the degradation of several cell components.[8] This hypothesis is consistent with the observation that ^{13}C-labeled carbon electrodes show an onset of carbon corrosion at 3.5 V during Li_2O_2 oxidation, even though carbon is generally considered stable to potentials well above 4.0 V in the absence of Li_2O_2,[9] which led to the conclusion that *"the process of carbon decomposition involves Li_2O_2 or its intermediates of oxidation"*.[10]

Singlet oxygen (term symbol $^1\Delta_g$, hereafter $^1O_2$) could potentially be this reactive intermediate.[11] It is a strong oxidizing agent and known to form upon chemical oxidation of Li_2O_2, Na_2O_2, and a series of organic peroxides.[12,13] The thermodynamically reversible potential for $^1O_2$ evolution during the electrooxidation of Li_2O_2 can be estimated to be between 3.45 and 3.55 V, only about 0.5 V higher than its reversible potential to triplet oxygen (term symbol $^3\Sigma_g^-$), $U_0 =$ 2.96 V.[14] This estimate is derived from $U_0 + \Delta G(^3\Sigma_g^- \rightarrow {}^1\Delta_g)/2F$, in which F is the Faraday constant and $\Delta G(^3\Sigma_g^- \rightarrow {}^1\Delta_g)$ is the difference in Gibbs free energy between singlet and triplet oxygen; $\Delta G(^3\Sigma_g^- \rightarrow {}^1\Delta_g)$ can be estimated from $\Delta H(^3\Sigma_g^- \rightarrow {}^1\Delta_g) = 94\ kJ\,mol^{-1}$ and the assumption $0\ kJ\,mol^{-1} < -T\Delta S(^3\Sigma_g^- \rightarrow {}^1\Delta_g) < 20\ kJ\,mol^{-1}$.[15,16] The reversible potential for $^1O_2$ formation fits the observed onset potential for carbon corrosion well; however, the possibility of $^1O_2$ formation during charge in $Li–O_2$ batteries has been largely overlooked. To the best of our knowledge, there have been no experimental investigations and only a few mentions of $^1O_2$ in the context of $Li–O_2$ batteries. A potential of around 3.9 V[6,11,17–19] as the thermodynamic threshold for $^1O_2$ evolution has been stated, neglecting that the energy transfer takes place in a two-electron process and that $^1O_2$ evolution could therefore already occur at lower potentials, as shown above. Consequently, $^1O_2$ evolution was considered a less likely source of side reactions during charge.[6]

We herein present the first experimental investigation of $^1O_2$ formation during the charge of an aprotic $Li–O_2$ battery. The identification of $^1O_2$ is based on its reactivity towards a specific spin trap to form a stable radical that can be detected by in operando electron paramagnetic resonance (EPR) spectroscopy.[20]

Sterically hindered secondary amines have long been used to detect $^1O_2$.[21] Scheme 1 shows the reaction of 2,2,6,6-

[*] J. Wandt, H. A. Gasteiger
Technische Universität München
Chair for Technical Electrochemistry, Department of Chemistry and Catalysis Research Center (Germany)
E-mail: johannes.wandt@tum.de
P. Jakes, J. Granwehr, R.-A. Eichel
Forschungszentrum Jülich, Institut für Energie- und Klimaforschung
Grundlagen der Elektrochemie (IEK-9)
52425 Jülich (Germany)
E-mail: p.jakes@fz-juelich.de
R.-A. Eichel
RWTH Aachen University, Institut für Physikalische Chemie
52074 Aachen (Germany)
J. Granwehr
RWTH Aachen University
Institut für Technische und Makromolekulare Chemie
52074 Aachen (Germany)
Supporting information and the ORCID identification number(s) for the author(s) of this article can be found under http://dx.doi.org/10.1002/anie.201602142.

 © 2016 Wiley-VCH Verlag GmbH & Co. KGaA, Weinheim

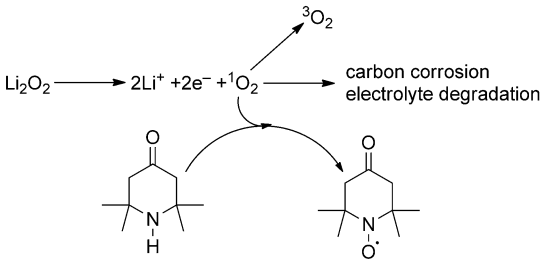

Scheme 1. Chemical reaction underlying the spin-trap approach: The reaction of 4-Oxo-TEMP with singlet oxygen forms the stable 4-Oxo-TEMPO radical, which is detected by in operando EPR spectroscopy. The trapping reaction is in kinetic competition with $^1O_2$ relaxation to triplet oxygen and other chemical reactions.

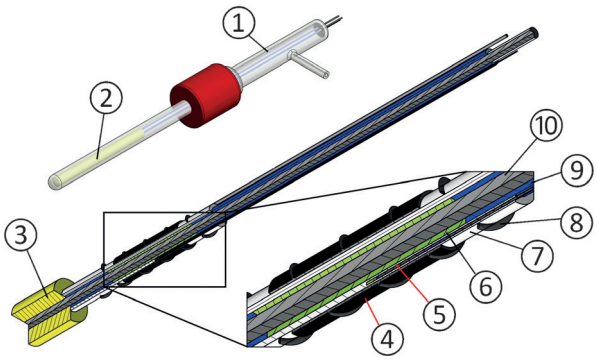

Figure 1. In operando EPR cell design. Top left: Cell housing with ① lid containing a connection for gas purging and three feed-through wires for contacting of working, counter, and reference electrodes; ② EPR tube containing the electrochemical cell. Center: Tubular electrochemical cell with ③ poly(tetrafluoroethylene) (PTFE) spacer. Bottom right: Cut through electrochemical cell, ④ Vulcan working electrode coated on Celgard separator, ⑤ reference electrode, ⑥ LFP counter electrode coated on Al wire (⑩), ⑦ glass-fiber separator, ⑧ Al wire (0.1 mm diameter) as working-electrode current collector, ⑨ PTFE tube, ⑩ Al wire (2.0 mm diameter) as counter electrode current collector.

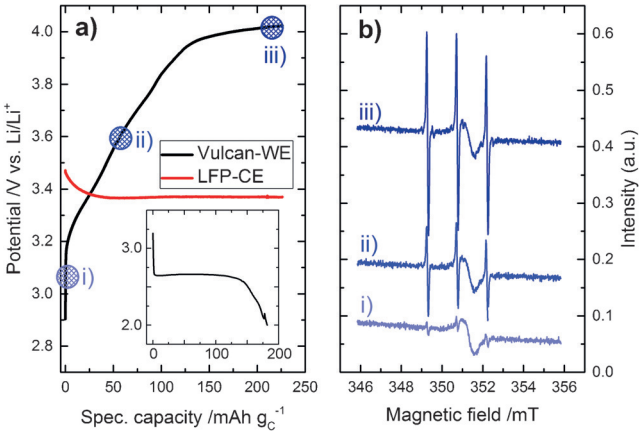

Figure 2. a) Charging curve ($i = 60\ mA\ g_C^{-1}$) of Li_2O_2 in an in operando EPR cell with 0.5 M LiTFSI in diglyme containing 0.1 M 4-Oxo-TEMP as a spin trap under an argon atmosphere; inset: previous discharge ($i = 120\ mA\ g_C^{-1}$) in a standard cell under an oxygen atmosphere. b) In operando EPR spectra (10 spectra averaged), recorded at the different charging potentials as indicated in (a).

tetramethyl-4-piperidone (4-Oxo-TEMP) with $^1O_2$ to form 4-Oxo-2,2,6,6-tetramethyl-1-piperidinyloxy (4-Oxo-TEMPO), which is a stable radical that can be identified by its characteristic EPR spectrum. 4-Oxo-TEMP is a very selective trapping agent for $^1O_2$,[22,23] especially as it does not react with superoxide radicals.[24] It is added to the electrolyte in a rather high concentration of 0.1 M, as the trapping reaction is in kinetic competition with $^1O_2$ relaxation to triplet oxygen, which is fast in liquid media ($\tau_{1/2} \approx 10^{-6}$–$10^{-3}$ s).[25,26] To investigate whether the spin trap reacted with Li_2O_2, discharged electrodes containing Li_2O_2 were stored either in standard electrolyte or 4-Oxo-TEMP-containing electrolyte. After storage, the same peroxide content was found in the electrode,[27] irrespective of the absence or presence of 4-Oxo-TEMP, thus ruling out a redox reaction. Furthermore, no dissolved peroxide species were found in the electrolyte, thus ruling out an acid–base reaction between Li_2O_2 and 4-Oxo-TEMP (see the Supporting Information). To verify that the presence of 4-Oxo-TEMP did not alter the electrochemical charging process, we determined the oxygen-evolution rates by on-line electrochemical mass spectrometry (OEMS; see the Supporting Information). In the presence of 4-Oxo-TEMP, Li_2O_2 oxidation proceeded normally up to a potential of about 3.9 V, when severe side reactions set in.

In operando EPR experiments were conducted with a custom spectroelectrochemical cell (Figure 1), which could be cycled directly within the cavity of the EPR spectrometer.[20] The housing was adapted to facilitate purging of the cell with gas, and a reference electrode was incorporated for potential-controlled experiments. The in operando EPR cell consisted of a Vulcan electrode containing Li_2O_2 coated on a Celgard separator, a glassfiber separator, chemically delithiated LFP as a counter electrode, and 0.5 M bis(trifluoromethane)sulfonimide lithium salt (LiTFSI) and 0.1 M 4-Oxo-TEMP in diglyme as the electrolyte (see the Supporting Information).

Figure 2 shows a typical charging curve recorded in the EPR cell. Only the charging step is done in the EPR cell; the prior discharge is carried out in a standard cell with the standard electrolyte (inset in Figure 2a), from which the Li_2O_2-containing Vulcan electrode is harvested. Figure 2b shows EPR spectra recorded in the in operando EPR cell during charge at positions indicated by the blue circles in Figure 2a. The initial spectrum shows a broad and featureless peak at $g = 2.0029$ from carbon dangling bonds and three narrow lines caused by a small amount of 4-Oxo-TEMPO impurity already present in the electrolyte. The later spectra clearly show the increased characteristic 1:1:1 triplet signal of 4-Oxo-TEMPO, which is the only EPR-active species formed during the entire charge process. The slanted baseline present in all three spectra can be assigned to a very broad EPR signal from the LFP counter electrode.

From the peak-to-peak amplitude of the EPR resonances (Figure 2b), it is possible to extract the relative amount of 4-Oxo-TEMPO (see the Supporting Information). Figure 3

 © 2016 Wiley-VCH Verlag GmbH & Co. KGaA, Weinheim

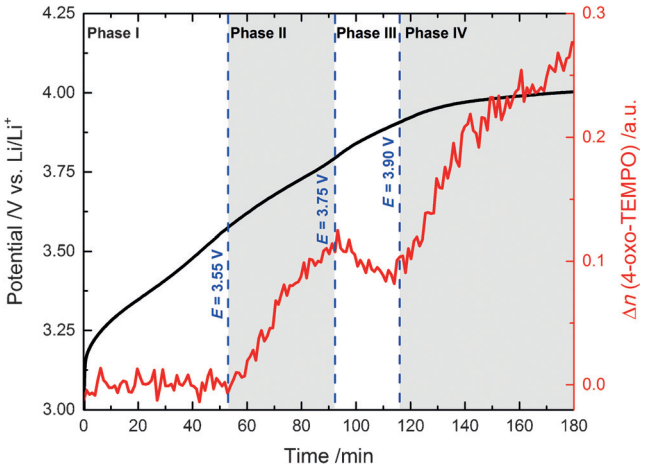

Figure 3. Voltage profile and EPR signal amplitude for 4-Oxo-TEMPO formed during the charging ($i = 60\ mA\ g_C^{-1}$) of Li_2O_2 with 0.5 M LiTFSI in diglyme containing 0.1 M 4-Oxo-TEMP as a spin trap.

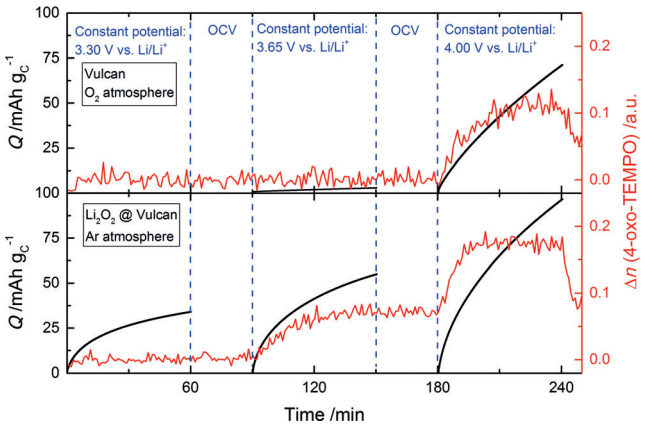

Figure 4. Charging capacity (black lines) and evolution of 4-Oxo-TEMPO EPR signal intensity (red lines) during potential stepping experiments. Top: Fresh Vulcan electrode without Li_2O_2 under oxygen (0.5 bar) and argon (0.5 bar). Bottom: Li_2O_2-containing Vulcan electrode under argon (1 bar). Electrolyte: 0.5 M LiTFSI in diglyme with 4-Oxo-TEMP.

shows the evolution of the 4-Oxo-TEMPO signal and the corresponding cell potential during charge, which can be separated into four distinct phases. During phase I and II, a normal charging process with Li_2O_2 oxidation as the main electrochemical reaction occurs, as indicated by the oxygen-evolution curve determined by OEMS (see Figure S6 in the Supporting Information). The 4-Oxo-TEMPO amount starts to increase once the electrode potential exceeds about 3.55 V, which is close to the thermodynamic threshold for $^1O_2$ formation (3.45–3.55 V), thus suggesting that this increase is caused by the reaction of the spin trap with $^1O_2$ (Scheme 1). During phase III, the 4-Oxo-TEMPO concentration decreases as a result of the $1\,e^-$ oxidation of the nitroxyl radical, a reaction known to occur in this potential range.[28–30] Above approximately 3.9 V during phase IV, another increase in the amount of 4-Oxo-TEMPO is accompanied by the consumption of oxygen, as seen in the OEMS data. The spin trap is electrochemically oxidized, which triggers a reaction with triplet oxygen to form 4-Oxo-TEMPO.[24,31] The presence of these four phases shows that a time- and voltage-resolved in operando EPR experiment is critical for unraveling the different mechanisms for the formation and decomposition of 4-Oxo-TEMPO (Figure 3).

To further provide evidence for the assignment of the electrochemical and chemical reactions to phases I–IV and that the increase in 4-Oxo-TEMPO during phase II is caused by $^1O_2$, we carried out potential-controlled experiments. Three different potentials were applied for 60 min each, with 30 min open-circuit (OCV) periods in between. The first potential of 3.3 V is below the thermodynamic threshold for $^1O_2$ formation, the second potential of 3.65 V is above this threshold but well within the stability window of the spin trap, and the third potential of 4.0 V is in the range in which the spin trap is electrochemically oxidized. The upper panel in Figure 4 shows that in the absence of Li_2O_2, 4-Oxo-TEMPO is only formed at 4.0 V, thus confirming that the increase observed during phase II in Figure 3 must be linked to Li_2O_2 oxidation. The fact that the oxidation of Li_2O_2 at 3.30 V does not yield 4-Oxo-TEMPO (lower panel in Figure 4) rules out the formation of 4-Oxo-TEMPO upon Li_2O_2 oxidation as a result of some unspecified side reaction. If the Li_2O_2 oxidation potential is then increased to 3.65 V, the formation of 4-Oxo-TEMPO sets in instantaneously, and can thus only be assigned to the reaction between $^1O_2$ and the spin trap.

In conclusion, in operando EPR data (Figures 3 and 4), in combination with OEMS data (see Figure S6), unambiguously show that $^1O_2$ is evolved at potentials above about 3.55 V in the charging process of aprotic Li–O_2 batteries. The EPR data were also reproduced in a second in operando EPR cell design with a conventional flat-cell configuration. The same four reaction phases with identical onset potentials were observed in the flat cell (see the Supporting Information).

To estimate the proportion of $^1O_2$, the amount of 4-Oxo-TEMPO formed in the range from 3.55 to 3.75 V (phase II, Figure 3) has been quantified by a calibration procedure with a known amount of 4-Oxo-TEMPO (see the Supporting Information). The total amount of evolved oxygen is estimated by the respective capacity and the e^-/O_2 ratio determined by OEMS. On the basis of the assumption that 100% of the $^1O_2$ formed during charging is converted into 4-Oxo-TEMPO, a lower limit of approximately 0.5% $^1O_2$ can be calculated. The real fraction of $^1O_2$ is most likely higher, as a significant part of the evolved $^1O_2$ will be quenched by the solvent or other side reactions before being trapped. However, this simple estimate already shows that $^1O_2$ is formed in substantial quantities. The close proximity of the onset potentials for $^1O_2$ evolution and carbon corrosion reactions at about 3.5 V suggests that $^1O_2$ as a highly reactive oxidizing species might play a central role in irreversible side reactions during the charging of Li–O_2 batteries. In a next step, it will first be necessary to quantify the extent to which $^1O_2$ is involved in parasitic side reactions during charge. Targeted counter measures can then be developed to eliminate $^1O_2$-induced side reactions and improve the reversibility and cycle life of Li–O_2 batteries.

 © 2016 Wiley-VCH Verlag GmbH & Co. KGaA, Weinheim

Acknowledgements

We thank Anna Freiberg (TUM), Cyril Marino (Paul-Scherrer-Institut, Switzerland), and Yi-Chun Lu (Chinese University of Hongkong) for contributions to the EPR cell design and Juan Herranz (Paul-Scherrer-Institut, Switzerland) for experimental support. TUM gratefully acknowledges financial support by the Bavarian Ministry of Economic Affairs and Media, Energy and Technology under the auspices of the EEBatt project. Forschungszentrum Jülich gratefully acknowledges financial support by the German Ministry of Education and Research (BMBF) within the framework of the MEET-HiEnD project.

Keywords: carbon corrosion · charging mechanism · EPR spectroscopy · lithium–air batteries · singlet oxygen

How to cite: *Angew. Chem. Int. Ed.* **2016**, *55*, 6892–6895
Angew. Chem. **2016**, *128*, 7006–7009

[1] K. M. Abraham, Z. Jiang, *J. Electrochem. Soc.* **1996**, *143*, 1–5.
[2] J. Christensen, P. Albertus, R. S. Sanchez-Carrera, T. Lohmann, B. Kozinsky, R. Liedtke, J. Ahmed, A. Kojic, *J. Electrochem. Soc.* **2012**, *159*, R1–R30.
[3] K. G. Gallagher, S. Goebel, T. Greszler, M. Mathias, W. Oelerich, D. Eroglu, V. Srinivasan, *Energy Environ. Sci.* **2014**, *7*, 1555–1563.
[4] S. A. Freunberger, Y. Chen, N. E. Drewett, L. J. Hardwick, F. Bardø, P. G. Bruce, *Angew. Chem. Int. Ed.* **2011**, *50*, 8609–8613; *Angew. Chem.* **2011**, *123*, 8768–8772.
[5] Y.-C. Lu, B. M. Gallant, D. G. Kwabi, J. R. Harding, R. R. Mitchell, M. S. Whittingham, Y. Shao-Horn, *Energy Environ. Sci.* **2013**, *6*, 750–786.
[6] B. D. McCloskey, D. S. Bethune, R. M. Shelby, T. Mori, R. Scheffler, A. Speidel, M. Sherwood, A. C. Luntz, *J. Phys. Chem. Lett.* **2012**, *3*, 3043–3047.
[7] N. Tsiouvaras, S. Meini, I. Buchberger, H. A. Gasteiger, *J. Electrochem. Soc.* **2013**, *160*, A471–A477.
[8] H. Beyer, S. Meini, N. Tsiouvaras, M. Piana, H. A. Gasteiger, *Phys. Chem. Chem. Phys.* **2013**, *15*, 11025–37.
[9] M. M. Ottakam Thotiyl, S. A. Freunberger, Z. Peng, P. G. Bruce, *J. Am. Chem. Soc.* **2013**, *135*, 494–500.
[10] D. G. Kwabi, N. Ortiz-Vitoriano, S. A. Freunberger, Y. Chen, N. Imanishi, P. G. Bruce, Y. Shao-Horn, *MRS Bull.* **2014**, *39*, 443–452.
[11] J. Hassoun, F. Croce, M. Armand, B. Scrosati, *Angew. Chem. Int. Ed.* **2011**, *50*, 2999–3002; *Angew. Chem.* **2011**, *123*, 3055–3058.
[12] Q. Li, F. Chen, W. Zhao, M. Xu, B. Fang, Y. Zhang, L. Duo, Y. Jin, F. Sang, *Bull. Korean Chem. Soc.* **2007**, *28*, 1656–1660.
[13] W. Adam, D. V. Kazakov, V. P. Kazakov, *Chem. Rev.* **2005**, *105*, 3371–3387.
[14] Y.-C. Lu, H. A. Gasteiger, M. C. Parent, V. Chiloyan, Y. Shao-Horn, *Electrochem. Solid-State Lett.* **2010**, *13*, A69–A72.
[15] F. Wilkinson, W. P. Helman, A. B. Ross, *J. Phys. Chem. Ref. Data* **1995**, *24*, 663.
[16] M. M. Richter, *Chem. Rev.* **2004**, *104*, 3003–3036.
[17] P. Bruce, S. Freunberger, L. Hardwick, J.-M. Tarascon, *Nat. Mater.* **2012**, *11*, 19–30.
[18] M. Balaish, A. Kraytsberg, Y. Ein-Eli, *Phys. Chem. Chem. Phys.* **2014**, *16*, 2801–2822.
[19] R. Black, J.-H. Lee, B. Adams, C. A. Mims, L. F. Nazar, *Angew. Chem. Int. Ed.* **2013**, *52*, 392–396; *Angew. Chem.* **2013**, *125*, 410–414.
[20] J. Wandt, C. Marino, P. Jakes, R. Eichel, H. A. Gasteiger, J. Granwehr, *Energy Environ. Sci.* **2015**, *8*, 1358–1367.
[21] Y. Lion, M. Delmelle, A. Van de Vorst, *Nature* **1976**, *263*, 442–443.
[22] R. Konaka, E. Kasahara, W. C. Dunlap, Y. Yamamoto, K. C. Chien, M. Inoue, *Free Radical Biol. Med.* **1999**, *27*, 294–300.
[23] Z.-Z. Ou, J.-R. Chen, X.-S. Wang, B.-W. Zhang, Y. Cao, *New J. Chem.* **2002**, *26*, 1130–1136.
[24] I. Rosenthal, C. M. Krishna, G. C. Yang, T. Kondo, P. Riesz, *FEBS Lett.* **1987**, *222*, 75–78.
[25] P. R. Ogilby, *Chem. Soc. Rev.* **2010**, *39*, 3181–3209.
[26] C. Schweitzer, R. Schmidt, *Chem. Rev.* **2003**, *103*, 1685–1757.
[27] K. U. Schwenke, M. Metzger, T. Restle, M. Piana, H. A. Gasteiger, *J. Electrochem. Soc.* **2015**, *162*, A573–A584.
[28] M. Kavala, R. Boča, L. Dlháň, V. Brezová, M. Breza, J. KožíŠek, M. Fronc, P. Herich, L. Švorc, P. Szolcsányi, *J. Org. Chem.* **2013**, *78*, 6558–6569.
[29] J. L. Hodgson, M. Namazian, S. E. Bottle, M. L. Coote, *J. Phys. Chem. A* **2007**, *111*, 13595–13605.
[30] B. J. Bergner, A. Schu, K. Peppler, A. Garsuch, J. Janek, *J. Am. Chem. Soc.* **2014**, *136*, 15054–15064.
[31] G. Nardi, I. Manet, S. Monti, M. A. Miranda, V. Lhiaubet-Vallet, *Free Radical Biol. Med.* **2014**, *77*, 64–70.

Received: March 1, 2016
Published online: April 26, 2016

 © 2016 Wiley-VCH Verlag GmbH & Co. KGaA, Weinheim

Angewandte Chemie
Eine Zeitschrift der Gesellschaft Deutscher Chemiker

Supporting Information

Singlet Oxygen Formation during the Charging Process of an Aprotic Lithium–Oxygen Battery

Johannes Wandt, Peter Jakes,* Josef Granwehr, Hubert A. Gasteiger, and Rüdiger-A. Eichel*

ange_201602142_sm_miscellaneous_information.pdf

Table of content:

Electrode/electrolyte preparation

The positive electrodes with a binder/carbon ratio of 0.5/1 g/g were prepared by Mayer-rod coating (100 µm wetfilm thickness) of an ink composed of Vulcan XC72 (Tanaka, Japan), isopropanol, and a lithium-ion exchanged Nafion solution (LITHion, Ion Power, USA) either onto a Celgard C480 separator or H1410 carbon paper (Freudenberg). For the H1410 electrodes, the coating process was repeated three times to achieve higher Vulcan loadings. The ink was prepared by adding Vulcan XC72 carbon to isopropanol (Sigma-Aldrich, 99.9%), and the mixture was sonicated for 20 minutes (Branson 250 probe-sonifier). Afterwards, LITHion solution (10.6%wt. in isopropanol) was added, and the ink was mixed with a spatula for half a minute. After solvent evaporation at room temperature, square electrodes (10 mm $\times$ 15 mm) were cut by a scalpel or 15 mm diameter cathode electrodes were punched out, dried under dynamic vacuum at 95°C for 12 hours in a glass oven (Büchi, Switzerland), and transferred for cell assembly into an argon-filled glove box (O_2 < 1 ppm, H_2O < 0.5 ppm; Jacomex, France), carefully avoiding exposure to ambient air. The Vulcan loading was 0.40 mg_{carbon} $cm^{-2}_{electrode}$ for C480 electrodes and about 1.2 mg_{carbon} $cm^{-2}_{electrode}$ for H1410 electrodes.

For counter and reference electrodes, chemically delithiated lithium iron phosphate (LFP) was used. Commercial LFP was stirred for 72 hours in an aqueous solution of potassium peroxodisulfate (Sigma-Aldrich) at room temperature. The amount of peroxodisulfate was adjusted to reach an LFP delithiation degree of 50 % for the reference electrode and of 100 % for the counter electrode. Afterwards, LFP was filtrated, thoroughly washed with deionized water, and dried under vacuum at 70 °C. The LFP-containing ink was prepared by dispersing chemically delithiated LFP (80 wt%), polyethylene oxide (PEO, M_v 400.000, Sigma-Aldrich, 10 wt%), and vapor grown carbon fibers (VGCF-H, Showa Denko, USA, 10 wt%) in deionized water and mixing them in a planetary centrifugal vacuum mixer (Thinky, USA) at 2000 rpm for 15 min. For EPR counter electrodes, the LFP ink was directly applied onto an aluminum wire (2 mm diameter, Alfa Aesar), which was constantly rotated during solvent evaporation to achieve a homogeneous LFP coating. Counter electrodes for the OEMS experiments were prepared by casting the slurry onto a H1410 carbon paper using the doctor blade method (RK Print Coat Instruments, UK) with a wetfilm thickness of 450 µm. LFP loadings were about 1.5 mg cm^{-1} for EPR counter electrodes and 6.5 mg cm^{-2} for OEMS counter electrodes. For EPR reference electrodes, the end of an insulated aluminum wire (0.1 mm diameter, Goodfellow) was simply dipped into the ink after mechanically removing 1 mm of the insulation at the tip of the wire. After solvent evaporation, LFP electrodes were dried for 72 hours at 55°C under dynamic vacuum and then directly transferred into an argon filled glove box.

Electrolytes were prepared with battery grade LiTFSI (Sigma-Aldrich, 99.99% trace metal basis), vacuum dried at 120◦C for 72 hours before use. Diethylene glycol dimethyl ether (Sigma-Aldrich, 99.5 %)

was purified by fractional distillation (25 cm Vigreux column) over metallic lithium and then stored over Sylobead MS 564C zeolites (3 Å, Grace Division).[1] For ether solvents, distillation is known to be critical in order to rule out side reactions induced by impurities.[2] 4-Oxo-TEMP (Sigma Aldrich, 95 %) was purified by double sublimation, which was necessary to reach a sufficiently low water content in the electrolyte and to remove 4-Oxo-TEMPO impurities. After prolonged storage (≥ 3 months), the 4-Oxo-TEMP had to be re-sublimated due to slow degradation forming 4-Oxo-TEMPO, as evidenced by a slight orange coloration and the characteristic EPR spectrum. The water content of the standard electrolyte (0.5 M LiTFSI in diglyme) was ≤ 5 ppm (Karl Fischer titration) and that of the spin trap electrolyte (0.5 M LiTFSI + 0.1 M 4-Oxo-TEMP in diglyme) was ≤ 10 ppm.

EPR Cell assembly and electrochemical testing

The discharge to produce Li_2O_2 was carried out in our standard Li-Oxygen cell design, which is described in detail elsewhere.[3] The standard cell was assembled with a lithium counter electrode, two Celgard C480 separators, the Vulcan working electrode, and 120 µL 0.5 M LiTFSI in diglyme. After assembly, the cell was purged with oxygen and discharged with a constant current of 120 mA g_{carbon}^{-1} to a cut-off potential of 2.00 V. Afterwards, the cell was purged with Argon and the Vulcan electrode containing Li_2O_2 was harvested inside the glovebox and used for EPR cell assembly. The reasons for carrying out the discharge in a separate cell with standard electrolyte are (i) that it rules out the possibility of side reactions involving the 4-Oxo-TEMP spin trap during discharge, and (ii) that it allows the use of a lithium counter electrode for the discharge, which would otherwise not be possible as 4-Oxo-TEMP is continuously reduced on metallic lithium, thereby forming hydrogen. It is also not possible to use prefilled electrodes (i.e., carbon electrodes with added Li_2O_2 particles) for the spin trap experiments, as potentials above 4.0 V are necessary to initiate the charging process with large Li_2O_2 particles, in contrast to the much lower potential required for electrochemically produced Li_2O_2.[4]

Figure 2 (main paper) shows a schematic drawing of the *in-operando* EPR cell used within this study, which has been adapted from our previous publication.[5] A tubular design with a concentric arrangement of the cell components is used to meet the geometric constrains of the EPR spectrometer. The central aluminum wire (2 mm diameter, 99.999 %, Alfa Aesar), coated with chemically delithiated LFP ($x \approx 0$ in Li_xFePO_4), serves as counter electrode current collector. PTFE heat shrink tubes (Adtech, United Kingdom) confine the LFP counter electrode (25 mm length) on both ends to prevent a short circuit. A glass-fiber separator (250 µm thickness, 35 mm length, glass microfiber filter 691, VWR) is rolled around the LFP counter electrode. The insulated reference electrode wire (0.1 mm diameter, 99.95 %, Goodfellow), containing partially delithiated LFP ($x \approx 0.5$ in Li_xFePO_4) as active material coated onto the tip of the wire where insulation has been mechanically removed, is inserted into the rolled glassfiber separator and attached to the central aluminium wire using BOPP tape (854PA, 3M). The Vulcan electrode (15 mm length, 10 mm width), which is coated directly onto a Celgard C480 separator, is assembled with the separator facing inwards. An aluminum wire (0.5 mm diameter, 99.999 %, Alfa Aesar) wound helically around the working electrode serves as working electrode current collector. The cell is enclosed by a quartz glass tube (10 mm outer diameter, 1 mm wall thickness, QSIL, Germany). The combination of an electrode coated directly onto the porous separator and the helically wound aluminum wire as current collector ensures ionic conduction between anode and cathode without shielding off the microwaves from the Vulcan working electrode. Electrolyte (250 µL) is added directly onto the glass-fiber separator inside the glass tube using an Eppendorf pipette. After cell assembly, the cell is closed with a glass lid through a ground-glass joint (GL 29, Bohlender, Germany) containing

three tungsten wires as feed-throughs for the working, the counter, and the reference electrode as well as a connection to a gas purging system through a second ground-glass joint (6 mm OD, Bohlender, Germany).

Electrochemical testing was done with a VMP2 or VMP3 potentiostat (Bio-Logic, France). For constant current experiments, the cell was charged at a rate of 60 mA g_{carbon}^{-1} for four hours. For potential stepping experiments, the Vulcan working electrode was polarized to 3.30, 3.65, and 4.00 V vs. Li/Li^+ for 60 minutes each, with intermittent OCV periods of 30 minutes. Note that all electrode potentials in this study are referenced to Li/Li^+ by correcting the measured electrode potentials for the potential of the partially lithiated LFP reference electrode (see Figure S*4*).

EPR spectroscopy and EPR data analysis

EPR spectra were recorded on a Bruker ElexSys E-540 continuous-wave (cw) X-band EPR spectrometer, equipped with a Bruker ER 4108 TMHS resonator operating at 9.819 GHz. The microwave power was set to 1.00 mW. Sweeps were performed over a range of 10 mT, with a center field of 348.0 mT. The cw EPR spectra were recorded as first derivatives of the signal with respect to the external magnetic field B_0. The field modulation frequency was set to 100 kHz and the modulation amplitude was 0.1 mT. EPR spectra were recorded continuously during cell operation. Each spectrum took 1 min to record, which represented the temporal resolution of the time-resolved EPR data.

The 4-Oxo-TEMPO signal was extracted from the peak-to-peak amplitude (ΔI_{pp}) of the first derivative EPR spectrum. If the EPR line width, expressed as the separation between first derivative extrema (ΔB_{pp}), remains constant during an experiment, ΔI_{pp} can be used as a direct measure of the relative 4-Oxo-TEMPO concentration. For changing ΔB_{pp} or to compare cells showing EPR signals with different ΔB_{pp}, the number of spins n is proportional to[6]

$$n \propto \Delta I_{pp} \Delta B_{pp}^2 \quad (1)$$

In fact, ΔB_{pp} of 4-Oxo-TEMPO is about 0.08 mT in argon atmosphere and about 0.2 mT in oxygen atmosphere (potential stepping experiment, upper panel in Figure 5 of main text). This EPR signal broadening is caused by dissolved oxygen[7] and would lead to a systematic underestimation of the 4-Oxo-TEMPO amount in the oxygen containing cell if only ΔI_{pp} would be considered.

By using a reference sample containing a known number of spins n_R with amplitude $\Delta I_{pp,R}$ and line width $\Delta B_{pp,R}$, the absolute number of spins of an unknown sample can be estimated as

$$n = n_R(\Delta I_{pp} \Delta B_{pp}^2)/(\Delta I_{pp,R} \Delta B_{pp,R}^2) \quad (2)$$

Since the cells used in these experiments show a very different loading of the resonator compared to a standard EPR tube, the reference signal was recorded using an identical cell that was loaded with a known amount of 4-Oxo-TEMPO. Nonetheless, the reproducibility of the cell design was not as good as for standard EPR samples, hence an error for the 4-Oxo-TEMPO concentration on the order of ±50% was estimated.

Kinetic considerations for the singlet oxygen deactivation and spin trapping

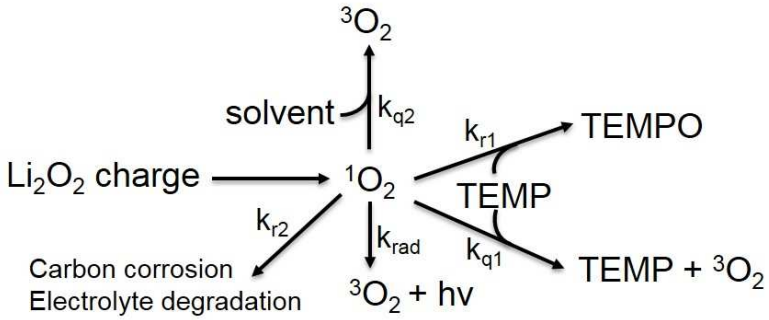

Figure S1 Proposed reaction scheme of the main chemical and physical deactivation mechanisms for singlet oxygen and the corresponding rate constants; (i) chemical reactions with the spin trap (k_{r1}) and other cell components (k_{r2}), (ii) electronic-to-vibrational energy transfer ("quenching") by the spin trap (k_{q1}) and the electrolyte solvent (k_{q2}) and (iii) radiative decay (k_{rad}).

Figure S*1* shows the main deactivation mechanisms for singlet oxygen in the 4-Oxo-TEMP containing electrolyte. The most common singlet oxygen deactivation process in solvents with high oxidation potential is electronical-to-vibrational energy transfer.[8] Both the electrolyte solvent (diethylene glycol dimethyl ether) and the spin trap 4-Oxo-TEMP contribute to the vibrational quenching of singlet oxygen. In addition, the spin trap can also react chemically with singlet oxygen to form the stable 4-Oxo-TEMPO radical, which is detected in the *in-operando* EPR experiment. Furthermore, singlet oxygen can undergo a radiative decay, emitting a photon at 1270 nm[9] or react chemically with various cell components.

The amount of singlet oxygen that is trapped by the spin trap to form 4-Oxo-TEMPO can be estimated using

$$n(\mathrm{TEMPO}) = n(^1\mathrm{O}_2)\,\frac{k_{r1}}{k_{r1}+k_{r2}+k_{q1}+k_{q2}+k_{rad}} \qquad (3)$$

The different rate constants *k* are introduced in Fig. S1. Notice that concentrations of reaction partners other than $^1O_2$ are implicitly included in the respective rate constant. Not all of the rate constants have been quantified in the literature for the solvents used in this study, therefore the present assessment provides only a lower boundary for the fraction of $^1O_2$ produced during charging of Li_2O_2.

Solving equation 9 for the amount of singlet oxygen gives

$$n(^1\mathrm{O}_2) = n(\mathrm{TEMPO})\,\frac{k_{\mathrm{r1}}+k_{\mathrm{r2}}+k_{\mathrm{q1}}+k_{\mathrm{q2}}+k_{\mathrm{rad}}}{k_{\mathrm{r1}}} \qquad (4)$$

The radiative decay is slow ($k_{rad} \approx 1\ s^{-1}$) and can be neglected.[8] The chemical reactions with the carbon electrode and with the electrolyte (k_{r2}) cannot be quantified since there are, to the best of our

knowledge, no kinetic data available. This does not imply that these chemical reactions are slow in comparison to the spin trapping and neglecting them will contribute to a systematic underestimation of the singlet oxygen fraction. The vibrational quenching by the spin trap (k_{q1}) can be neglected because the spin trap concentration (0.1 mol L^{-1}) is significantly lower than the solvent concentration (~7 mol L^{-1}) and the quenching constants k_{q1} and k_{q2} can be expected to be on the same order of magnitude. For the vibrational quenching of singlet oxygen, rate constants (k_{q2}) have been reported for various ether solvents as shown in

Table S1. Although no value for diethylene glycol dimethyl ether is reported, one can assume an averaged rate constant on the order of $k_{q2} \sim 3 \cdot 10^4\ s^{-1}$ due to the small deviation between the different ether solvents. Table S2 shows rate constants for the chemical reaction of singlet oxygen with various 2,2,6,6-tetramethylpiperdine spin traps in different solvents, which range from $< 1.0 \cdot 10^5\ L\ mol^{-1}\ s^{-1}$ to $4.0 \cdot 10^7\ L\ mol^{-1}\ s^{-1}$. For a spin trap concentration of 0.1 mol L^{-1}, the apparent rate constants k_{r1} for the chemical trapping reaction therefore range from $1.0 \cdot 10^4\ s^{-1}$ to $4.0 \cdot 10^6\ s^{-1}$. Comparing the rate constant for the solvent quenching reaction with the possible range for the chemical reaction with the spin trap shows that the trapping reaction is either of a similar speed or faster than the singlet oxygen deactivation. In any case, the simple relation

$$n(^1O_2) = n(\mathrm{TEMPO}) \tag{5}$$

would only be obtained if $k_{r1} >> k_{q1}, k_{q2}, k_{r2}, k_{rad}$. Even then, since O_2 forms on a surface a fast reaction could lead to a locally reduced concentration of the spin trap and therefore a locally reduced k_{r1}. This would cause spatially dependent kinetics and a correspondingly more complicated relation between $n(^1O_2)$ and n(TEMPO). Irrespective of the exact rate constants, the singlet oxygen fraction $n(^1O_2)/n(O_2)$ calculated by using eq. (12) and the total amount of O_2 obtained from electrochemical considerations represents only a lower limit of the actual singlet oxygen evolution rate.

Table S1 Quenching rate constants for singlet oxygen in several ether solvents. Rate constants were taken from a comprehensive review article.[10] The number of individual references for each solvent is given in the third column. The error margin represents the standard deviation between the different literature sources.

Solvent	k_q [10^4 s^{-1}]	Number of references
Diethyl ether	3.0 ± 0.3	4
1,1-Dimethylethyl methyl ether	3.2 ± 0.4	2
1,4-Dioxane	3.9 ± 0.7	4
Tetrahydrofuran	4.5 ± 0.7	5

Table S2 Rate constants for the chemical reaction with singlet oxygen and the respective solvents for several 2,2,6,6-tetramethylpiperidine spin traps.

Spin trap	Solvent	k_r [L mol^{-1} s^{-1}]	Reference
TEMP	C_6H_6/MeOH (80:20)	$4.0 \cdot 10^6$	[11]
	C_6H_6	$5.3 \cdot 10^5$	[12]
	CH_2Cl_2	$3.9 \cdot 10^5$	[13]
	CH_2Cl_2	$4.0 \cdot 10^5$	[14]
	EtOH	$1.6 \cdot 10^5$	[15]
4-Amino-TEMP	C_6H_6/EtOH	$1.8 \cdot 10^6$	[11]
4-Hydroxy-TEMP	C_6H_6/EtOH	$< 1.0 \cdot 10^5$	[11]
	C_6H_6/EtOH	$5.0 \cdot 10^5$	[16]
	$CHCl_3$	$< 2.0 \cdot 10^5$	[17]
	DMF	$5.0 \cdot 10^7$	[18]
	DMSO	$5.2 \cdot 10^6$	[19]
	EtOH	$8.0 \cdot 10^5$	[20]
	H_2O	$4.0 \cdot 10^7$	[20]

Quantification of 4-Oxo-TEMPO

To convert the relative amount (in arbitrary units) of 4-Oxo-TEMPO formed during phase II in the cell shown in Figure 4 (main paper) into a total amount (in mol), a simple calibration was carried out. An EPR spectrum of an electrolyte consisting of 0.5 M LiTFSI and 1 mM of the 4-Oxo-TEMPO radical (Sigma Aldrich) was measured in an *in-operando* EPR cell. The amount of 4-Oxo-TEMPO formed upon charge in phase II equals

$$n(\mathrm{TEMPO})_{\mathrm{PhaseII}} = \frac{\Delta A_{\mathrm{PhaseII}}}{A_{\mathrm{Calibration}}}\, n(\mathrm{TEMPO})_{\mathrm{Calibration}} \tag{6}$$

where $\Delta A_{\mathrm{PhaseII}}$ corresponds to the increase of the EPR signal intensity ($\Delta I_{pp}\ \Delta B_{pp}^2$) during phase II, $A_{\mathrm{Calibration}} = \Delta I_{\mathrm{pp,R}}\ \Delta B_{\mathrm{pp,R}}^2$ is the EPR signal intensity measured for the calibration cell and $n(\mathrm{TEMPO})_{\mathrm{Calibration}}$ is the respective amount of 4-Oxo-TEMPO. Assuming that an electrolyte volume of 200 µL is present within the EPR resonator, the amount of 4-Oxo-TEMPO formed in phase II can be calculated as $n(\mathrm{TEMPO})_{\mathrm{PhaseII}} = 1.4 \cdot 10^{-9}\ \mathrm{mol}$.

As discussed in the previous section, one can estimate the lower limit of the singlet oxygen evolution rate by assuming that every $^1O_2$ molecule is trapped, thus forming 4-Oxo-TEMPO (equation 12). Based on this assumption, the amount of $^1O_2$ formed during phase II can be expressed as $n(^1\mathrm{O}_2)_{\mathrm{PhaseII}} = 1.4 \cdot 10^{-9}\ \mathrm{mol}$.

The total amount of oxygen formed during phase II can be calculated from the respective capacity Q_{PhaseII} and the oxygen evolution rate of □3 e^-/O_2 (see section *Influence of 4-Oxo-TEMP on the Li_2O_2 electrochemistry*) as

$$n(\mathrm{O}_2)_{\mathrm{PhaseII}} = \frac{Q_{\mathrm{PhaseII}}}{3F} = 3.0 \cdot 10^{-7}\ \mathrm{mol} \tag{7}$$

where *F* is the Faraday constant. Comparing the amount of $^1O_2$ to the total amount of oxygen evolved during phase II gives a singlet oxygen fraction $n(^1O_2)/n(O_2) \approx 0.5$ %. As previously discussed, this number represents only a lower limit estimate and the real singlet oxygen fraction will most likely be higher.

Chemically delithiated LFP as counter and reference electrode material

LFP is used as counter and reference electrode material because 4-Oxo-TEMP is getting reduced at potentials lower than ≈ 2.0 V vs. Li/Li^+, thus ruling out the use of metallic lithium or LTO as counter electrode materials. Furthermore, LFP shows a very broad EPR signal of several thousand Gauss, which can easily be subtracted as baseline and therefore does not disturb the detection of the nitroxyl radical. As only the charge ($Li_2O_2 \rightarrow 2Li^+ + 2e^- + O_2$) is carried out in the *in-operando* EPR cell, LFP has to be chemically delithiated using potassium peroxodisulfate as oxidizing agent, as described in detail in section *Electrode/electrolyte preparation*. The voltage profile in Figure S*2* shows that the chemical delithiation was successful and that the LFP can be normally cycled with a first Li^+-intercalation capacity close to its theoretical value of 170 mAh g_{LFP}^{-1}.

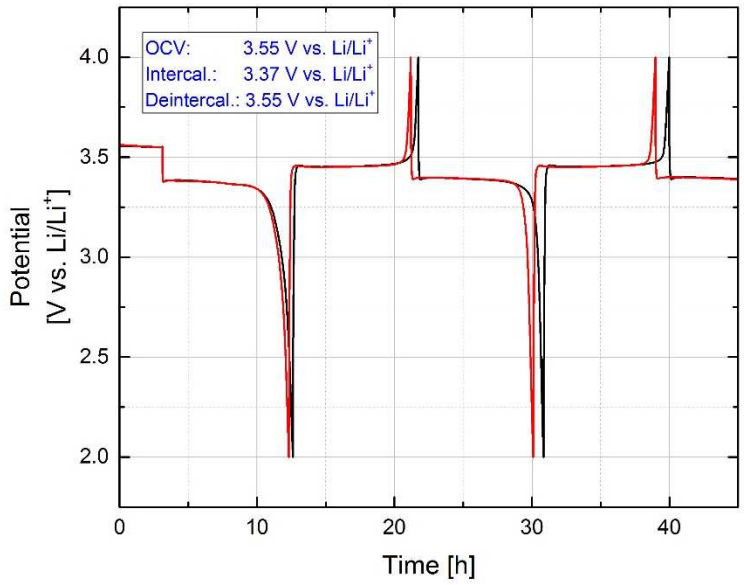

Figure S2 Voltage profile of chemically delithiated LFP (Li_0FePO_4) in a standard Swagelok cell with a metallic lithium counter electrode and 0.5 M LiTFSI in diglyme as electrolyte; constant current cycling with a C/10 rate between 2.0 V and 4.0 V. The two curves show two nominally identical cells. The active material loading is 12.7 mg_{LFP} cm^{-2}.

Figure S*3* shows that LFP can also be cycled normally in the presence of 0.1 M 4-Oxo-TEMP, both in argon and in oxygen atmosphere. The experiment was carried out in a two compartment cell, in which anode and cathode compartments are separated by a ceramic Li-ion conductor (Ohara glass).[21] In this way, it is possible to use lithium metal as counter electrode without altering the cell chemistry due to 4-Oxo-TEMP degradation, which would otherwise take place at the lithium electrode. Figure S2 and S3 show that chemically delithiated LFP can be used as a counter electrode material without interference with the cell chemistry at the oxygen electrode.

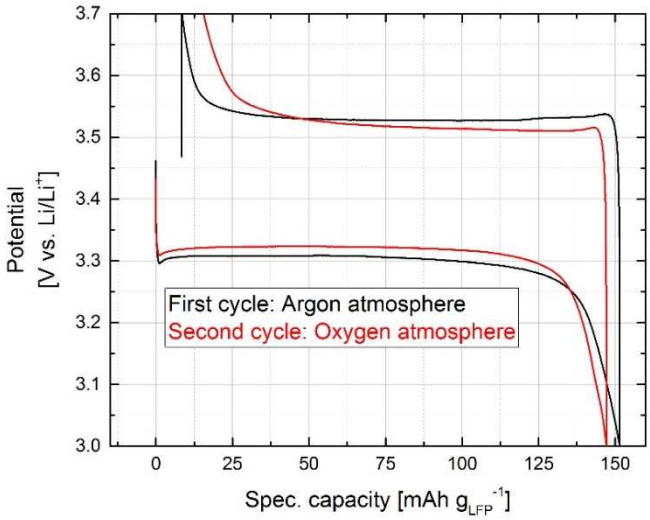

Figure S3 Voltage profile of chemically delithiated LFP (Li_0FePO_4) in a two compartment cell with a metallic lithium counter electrode and 0.5 M LiTFSI + 0.1 M 4-Oxo-TEMP in diglyme as catholyte and 0.5 M LiTFSI in diglyme as anolyte; constant current cycling with a C/50 rate between 2.0 V and 3.7 V. The C-rate was reduced due to the additional resistance of the ceramic Li-ion conductor. The active material loading is 12.4 mg_{LFP} cm^{-2}.

Figure S*4* shows that the open circuit potential of partially delithiated LFP ($Li_{0.5}FePO_4$) in standard and 4-Oxo-TEMP containing electrolyte is reproducible and stable in the relevant time scale at around 3.418 ± 0.005 V vs. Li/Li^+. Therefore, the partially delithiated LFP can be used as active material for the reference electrode and all potentials measured against the LFP reference electrode are corrected by adding 3.418 V to convert them to the Li/Li^+ scale.[22]

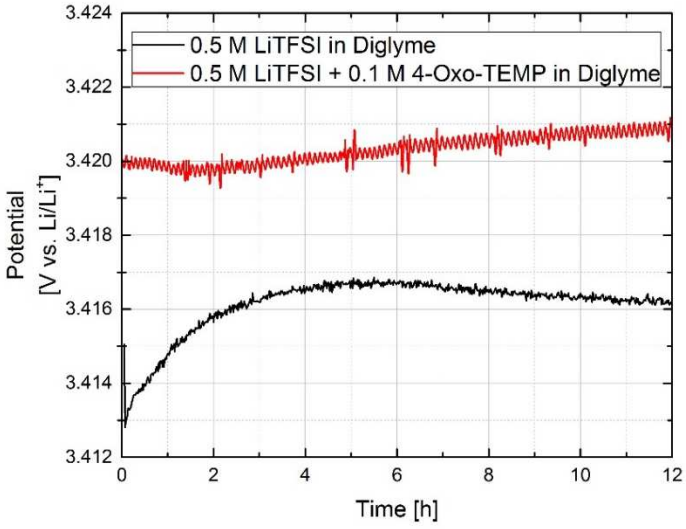

Figure S4 OCV of chemically delithiated LFP ($Li_{0.5}FePO_4$) versus a lithium counter electrode. The experiment with the standard electrolyte was carried out in a Swagelok cell; the experiment with 4-Oxo-TEMP containing electrolyte was carried out in a special cell in which the anode and cathode compartment are separated by a glass frit to prevent the contact of metallic lithium with 4-Oxo-TEMP (the voltage oscillation in the red curve is due to temperature fluctuation inside the glovebox).

Influence of 4-Oxo-TEMP on the Li_2O_2 electrochemistry

To rule out chemical reactions between Li_2O_2 and 4-Oxo-TEMP, Vulcan electrodes (H1410 support) were discharged in a standard cell, then the Li_2O_2 containing electrodes were harvested and finally stored either in 160 µL of standard electrolyte or electrolyte containing 0.1 M 4-Oxo-TEMP for two or four hours. After storage, the peroxide content was determined both in the electrode and in the electrolyte. The peroxide analysis was carried out photometrically based on the formation of the yellow $[Ti(O_2)]^{2+}$ complex as described in detail in a previous publication.[1] The peroxide contents are shown in Table S*3*.

Table S3 Peroxide content determined photometrically in the discharged Vulcan electrode and the electrolyte after 2 or 4 h storage in 4-Oxo-TEMP containing electrolyte or without exposure to 4-Oxo-Temp (≡ 0 h). The peroxide content is expressed as percentage of the theoretical amount based on the discharge capacity. The error margin represents the standard deviation between several identical cells.

Storage time electrode with 4-Oxo-TEMP	% (Li_2O_2)		Number of Cells
	electrode	electrolyte	
0 h	78.4 ± 1.1 %	-	4
2 h	79.4 ± 0.6 %	-0.1 ± 0.3 %	3
4 h	78.3 ± 0.6 %	-0.3 ± 0.2 %	3

In electrodes that were not stored in 4-Oxo-TEMP containing electrolyte, a peroxide yield of ≈78 % was found, which is in good agreement with our previous results.[1] Storage in 4-Oxo-TEMP containing electrolyte does not decrease the peroxide yield in the electrode, which rules out a redox reaction like a nucleophilic attack of the peroxide at the carbonyl group of the spin trap. Furthermore, no soluble peroxide species were found in the electrolyte, which also excludes peroxide protonation by the amine group of the spin trap. Therefore, one can conclude that Li_2O_2 is entirely stable in the presence of 4-Oxo-TEMP in the time scale of the *in-operando* EPR experiment.

In the next step, the cell chemistry during charge was characterized via on-line electrochemical mass spectrometry (OEMS)[23]. Figure S*5* shows the first discharge and charge of a cell consisting of a Vulcan electrode (H1410 support), two Celgard C480 separators, a Li counter electrode, and 120 µL of 0.5 M LiTFSI in diglyme as electrolyte, cycled at a current of 120 mA g_{carbon}^{-1} and between cut-off potentials of 2.0 V and 4.5 V vs. Li/Li^+. The oxygen consumption during discharge was monitored with a Baratron pressure transducer,[24] whereas gas evolution during charge was monitored by the OEMS. Both

voltage and oxygen evolution profiles and the averaged e^-/O_2 ratios of 2.16 during discharge and 2.58 during charge are consistent with the literature.[1,23,25] The deviation from the $2e^-/O_2$ line increases significantly after the potential exceeds □3.5 V, which might be caused by a change in the charging mechanism due to the evolution of $^1O_2$.

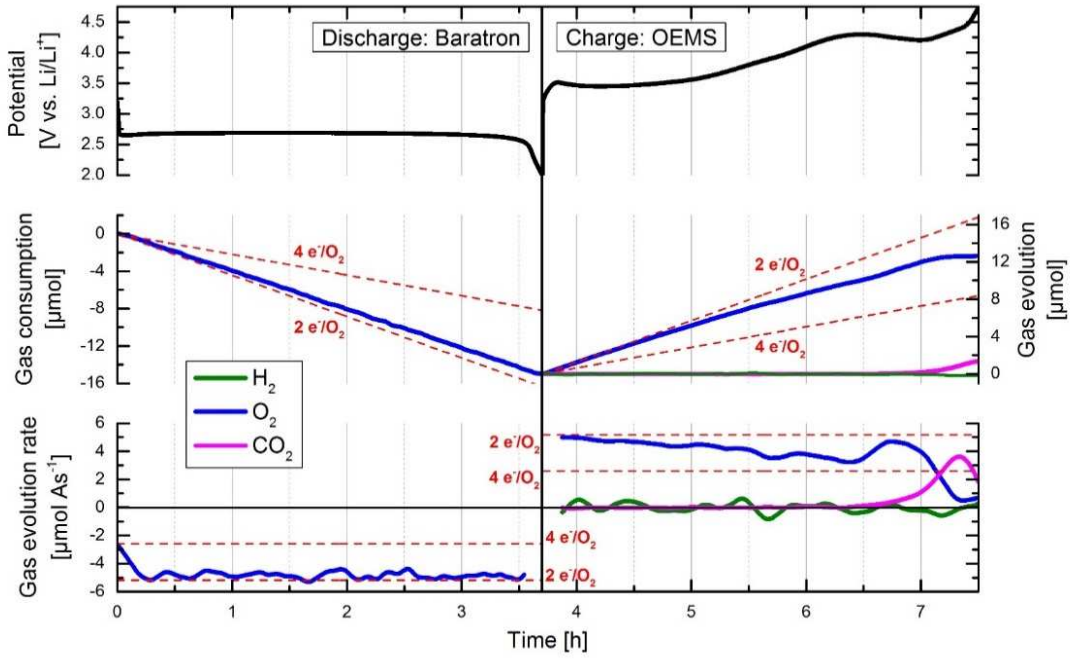

Figure S5 First cycle of a standard cell with a Vulcan working electrode (H1410 support) and a lithium metal counter electrode using 0.5 M LiTFSI in diglyme as electrolyte at a rate of 120 mA g_{carbon}^{-1} in the OEMS cell. The upper panel shows the voltage profile, the central panel the total amount of gas, and the lower panel the gas evolution/consumption rate. The oxygen consumption during discharge was detected via a pressure transducer, the gas evolution during charge with the OEMS. The discharge was conducted under 1 bar of O_2 and the charge under 1 bar of Ar.

Figure S *6* shows the charge of a cell consisting of a pre-discharged Li_2O_2-containing Vulcan electrode (H1410 support), two Celgard C480 separators, a delithiated LFP counter electrode and 120 µL of 0.5 M LiTFSI + 0.1 M 4-Oxo-TEMP in diglyme as electrolyte at a current of 120 mA g_{carbon}^{-1}. The OEMS cell does not contain a reference electrode, therefore the potential of the LFP counter electrode measured vs. Li/Li^+ at a comparable current rate was used for the potential correction. Between 3.0 and about 3.9 V, the potential and oxygen evolution profiles are similar in the absence (Figure S*5*) and the presence (Figure S *6*) of 4-Oxo-TEMP. In the presence of 0.1 M 4-Oxo-TEMP the charging potential is slightly increased, the reason of which is unclear. As already described above, the e^-/O_2 ratio is close to 2.0 at potentials smaller than 3.5 V also in the presence of 4-Oxo-TEMP and then starts to deviate at higher potentials. Between 3.0 and 3.9 V an average oxygen evolution rate of □3.0 e^-/O_2 was found in two repeated experiments for 4-Oxo-TEMP containing electrolyte. The slight increase of the oxygen evolution rate in the presence of the spin trap (3.0 e^-/O_2 vs. 2.6 e^-/O_2) is probably caused by (i) the slightly increased charging potential, (ii) the chemical trapping of $^1O_2$ by the spin trap, forming 4-Oxo-

TEMPO (see phase II in Figure 4, main paper), and (iii) the electrochemical oxidation of 4-Oxo-TEMPO at potentials above 3.75 V (see phase III in Figure 4, main paper). At potentials above 3.9 V oxygen starts to get consumed rather than evolved in the presence of 4-Oxo-TEMP and also the mass channels *m*/*z* =12, 15, 28, 44 increase. The oxygen consumption is caused by the electrochemical oxidation of the spin trap. It is known, that 1 e^--oxidation of the 2,2,6,6-tetramethylpiperidine based spin trap triggers a reaction with "normal" molecular triplet oxygen, forming the 4-Oxo-TEMPO radical,[26,27] which is also observed by *in-operando* EPR in the same potential range. The increase of the channels *m*/*z* =12, 15, 28, 44 is probably caused by the evolution of carbon dioxide, because the normalized increase of these channels (*m*/*z*(44) = 100 %, *m*/*z*(28) = 18 % and *m*/*z*(12) = 12 %) is similar to the expected fragmentation pattern according to the NIST database.[28] Considering the similar potential and oxygen evolution profiles and e^-/O_2 ratios in the absence and presence of 4-Oxo-TEMP, one can conclude that the addition of 0.1 M 4-Oxo-TEMP to the electrolyte does not significantly change the charging processes during Li_2O_2 oxidation up to a potential of about 3.9 V vs. Li/Li^+.

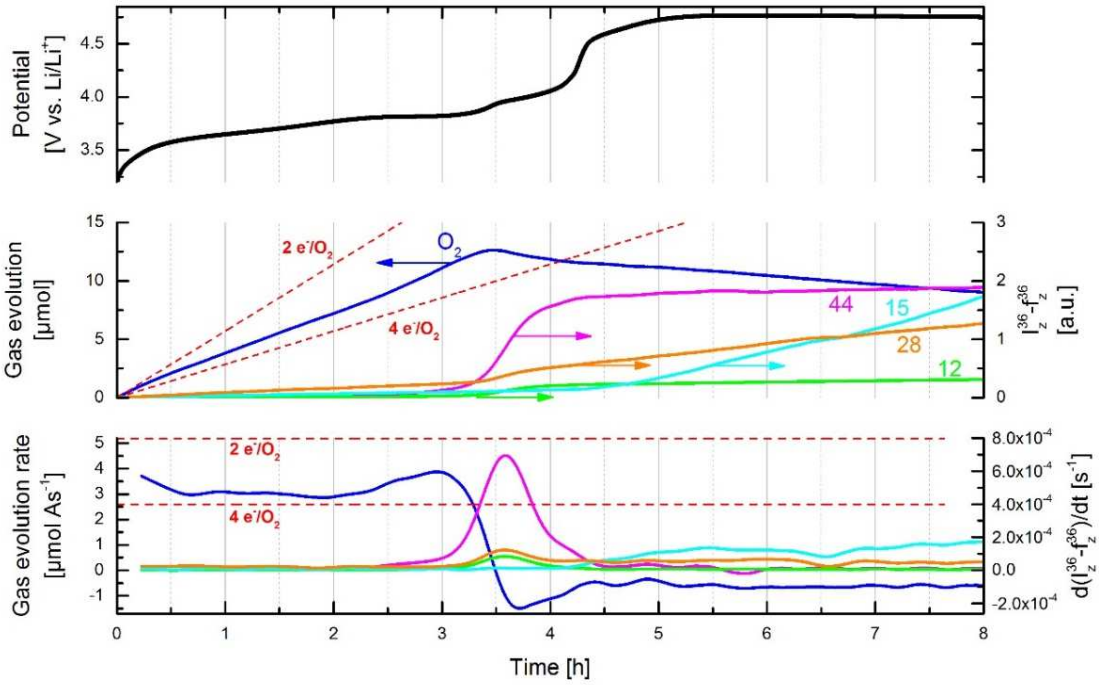

Figure S 6 Evolution of different chemical species monitered by OEMS during charge of a pre-discharged Li_2O_2-containing Vulcan electrode (H1410 support) and a chemically delithiated LFP counter electrode using 0.5 M LiTFSI in diglyme with 0.1 M 4-Oxo-TEMP as electrolyte at a rate of 120 mA g_{carbon}^{-1}. The upper panel shows the voltage profile, the central panel the total amount of gas and the lower panel the gas evolution rate. The charge was conducted under 1 bar of Ar.

Influence of magnetic field on charge during *in-operando* EPR experiments

During the *in-operando* EPR experiments, the electrochemistry takes place in the presence of an external magnetic field (maximum field strength of about B_0 =0 .35 T). To rule out that the magnetic field influences the charging process, an *in-operando* EPR cell consisting of a pre-discharged (Li_2O_2 containing) Vulcan electrode, a LFP counter electrode and 0.5 M LiTFSI in diglyme as electrolyte is charged with a constant current of 120 mA g_{carbon}^{-1}. During charging the magnetic field is repeatedly turned on and off for one minute each. The spectral density of the working electrode potential after Fourier transformation does not show any correlation with the switching frequency of the magnetic field of 120 s (Figure S*7*). This shows that the magnetic field applied during the *in-operando* EPR experiments has no detectable influence on the charging process.

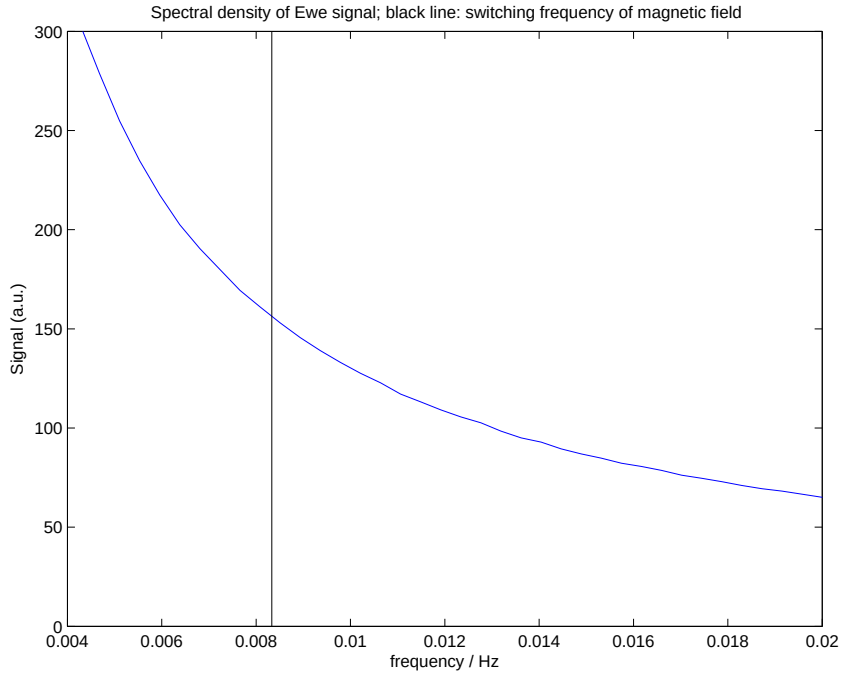

Figure S7 Spectral density of the working electrode potential during charging in the *in-operando* EPR cell. The magnetic field is repeatedly turned on and off for one minute each.

Potential and current profile during potential stepping experiments

Figure S*8* shows the working and counter electrode potentials and the current during the potential stepping experiments in the *in-operando* EPR cell in 4-Oxo-TEMP containing electrolyte (same cells as Figure 5 in the main paper). The cell shown in panel a) contains a fresh Vulcan electrode (no Li_2O_2) under oxygen atmosphere, the cell in panel b) comprises a Li_2O_2-containing pre-discharged Vulcan electrode under argon atmosphere.

During the potential stepping experiment, the Vulcan working electrode is polarized to a constant potential (3.30 V, 3.65 V and 4.00 V vs. Li/Li^+) for 60 minutes with intermittent OCV periods of 30 minutes. In the initial phase of each potential step, the counter electrode potentials deviates up to several hundred millivolts from the reversible potential. The fast potential drop and the subsequent relaxation in the beginning of a potential step are hard to predict, which prevents the use of the counter electrode as reference electrode. This highlights the importance of the LFP reference electrode for the potential stepping experiments to accurately polarize the Vulcan working electrode to the desired potential.

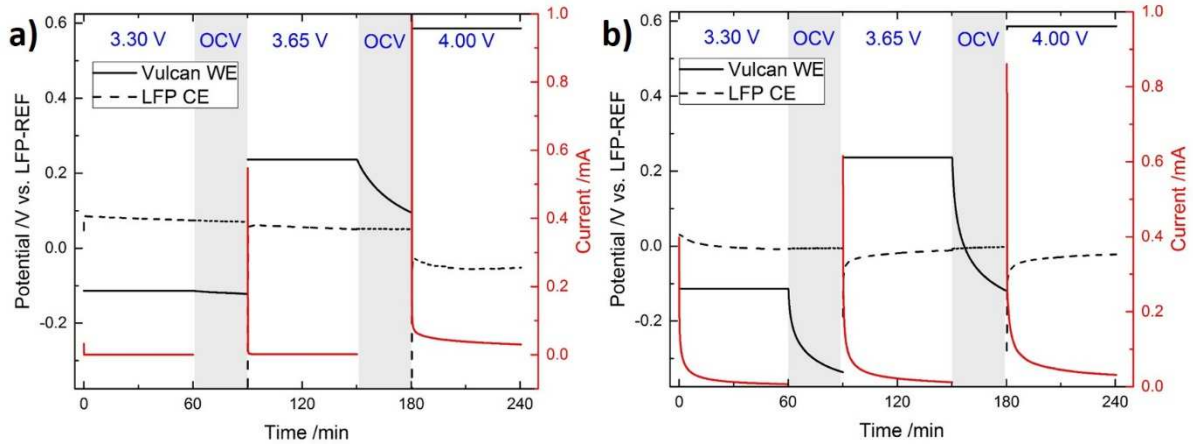

Figure S8 Potential stepping experiment in the *in-operando* EPR cell with an LFP counter and reference electrode and electrolyte containing 0.1 M 4-Oxo-TEMP. (a) Fresh Vulcan electrode (no Li_2O_2), oxygen atmosphere. (b) Pre-discharged Li_2O_2 containing Vulcan electrode, argon atmosphere. The blue numbers give the respective working electrode potentials in the Li/Li^+-scale and indicate the 30 minute OCV periods.

Reproduction of *in-operando* EPR experiments in flat cell design

A second *in-operando* EPR cell design was developed to confirm the reproducibility of the *in-operando* EPR experiments. In contrast to the rather unusual concentric arrangement of the working and counter electrode in the tubular cell design shown in Figure 2 (main paper), the second cell design is based on a conventional arrangement of flat electrodes as shown in Figure S9. The working electrode consists of Vulcan carbon and the counter electrode of chemically delithiated LFP. Both for the working and the counter electrode, the active materials are directly coated onto carbon paper (H1410, Freudenberg) with a size of 7 mm $\times$ 15 mm for Vulcan and 7.5 mm $\times$ 16 mm for LFP. The H1410 carbon paper serves as mechanical support and as current collector with a sufficiently high microwave permeability. The electrodes are sandwiched between two semi-circular PTFE tubes (length 45 mm, diameter 7.8 mm), which exactly fit into a quartz glass tube. In the upper end of the PTFE tubes 1 mm female contact pins (Buerklin, Germany) are embedded; the male contact pins are pushed through the upper end of the carbon paper into the female counterpart to electronically contact the working and the counter electrode. The same housing as for the tubular cell was used for placing the cell inside the EPR resonator (see Figure 2 main paper).

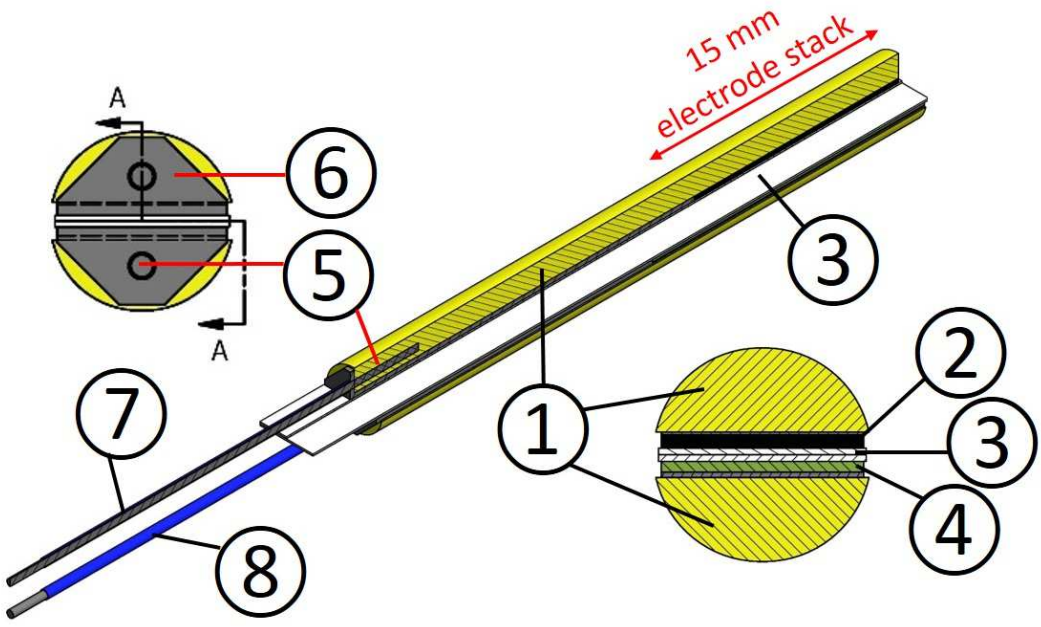

Figure S9 (*Central*) Overview of flat EPR cell. (*Lower right*) Cross section through lower part of flat cell where electrode stack is located (as indicated by the red arrow in the central image). (*Upper left*) Cross section through upper part of flat cell where the contact pins are located. ① Semicircular PTFE rods; ② Vulcan working electrode coated on H1410 carbon paper; ③ glassfiber separator; ④ LFP counter electrode coated on H1410 carbon paper; ⑤ female contact pins embedded into PTFE tubes; ⑥ Upper end of H1410 carbon paper, folded over and contacted with male contact pins; ⑦ working electrode current collector; ⑧ counter electrode current collector with PTFE heat shrink tube.

The flat EPR cell also showed a very good electrochemical performance. The reasons why the tubular cell design was used as the main EPR cell and the flat cell for the backup experiments are (i) the possibility to incorporate a reference electrode into the tubular cell (see previous section for the importance of the reference electrode for potential stepping experiments), which is not possible in the flat cell due to geometric constraints, and (ii) the better signal-to-noise ratio of the EPR spectra (by approximately a factor 100) in the tubular cell, which is probably due to the microwave absorption of the carbon paper in the flat cell. However, since the sampling rate of the EPR spectra significantly exceeds the rate of the EPR signal increase due to 4-Oxo-TEMPO formation, the signal-to-noise ratio can be increased at the expense of temporal resolution by calculating the moving average over a certain number of data points.

Figure S*10*a shows the potential profile and 4-Oxo-TEMPO concentration during charging (i = 120 mA g_C^{-1}) of a pre-discharged (Li_2O_2 containing) Vulcan electrode with a 4-Oxo-TEMP containing electrolyte in the flat EPR cell. The development of the 4-Oxo-TEMPO concentration shows the same four distinct phases, which have been identified in the tubular cell (Figure 4 in main paper). Also the onset potentials of phase II (~3.55 V) and phase III (~3.75 V) are very similar in the two cell designs. The onset potential of phase IV is seemingly shifted to higher voltage (~4.3 V). This is caused by a simultaneous potential drop of the LFP counter electrode, which is utilized to a high degree because of the large areal capacity of the Vulcan coated carbon paper working electrode. Accordingly, the potential correction transforming the measured cell potential into the Li/Li^+ scale overestimates the working electrode potential towards the end of the experiment (Figure S*10*b). The 4-Oxo-TEMPO concentration formed during phase II is approximately 0.2 mM, corresponding to a lower limit of □0.5% for the $^1O_2$ fraction formed during charge.

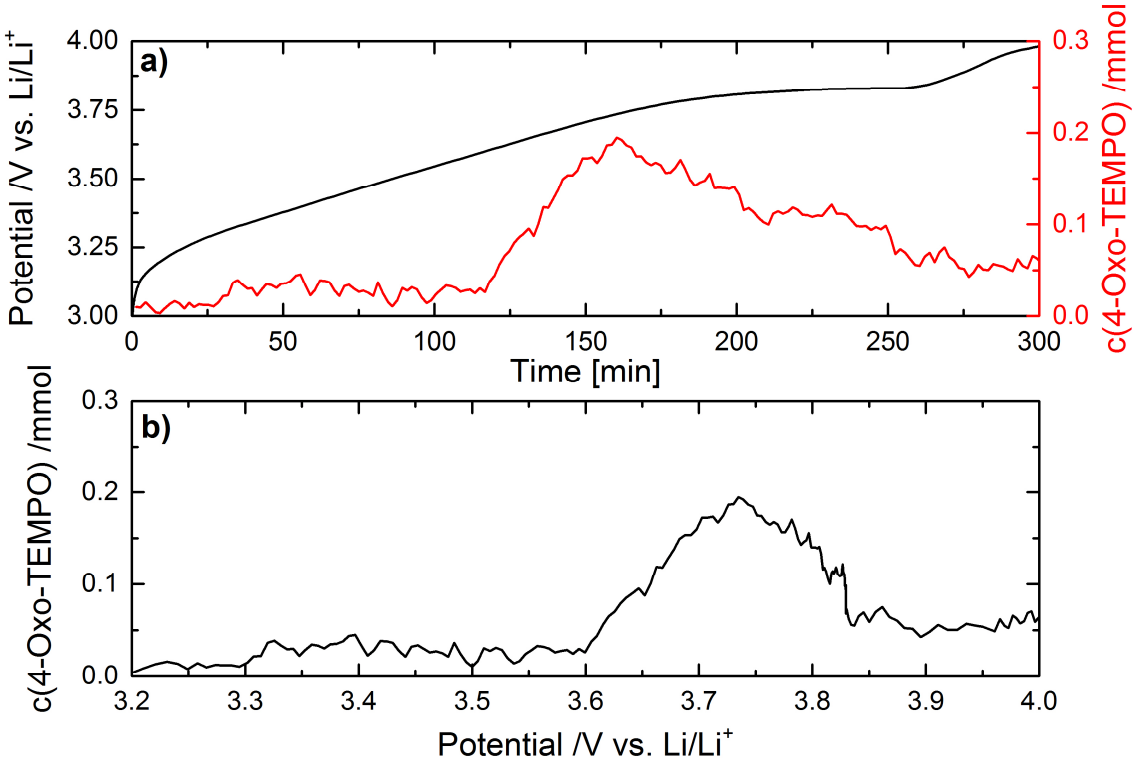

Figure S10 a) Potential profile and 4-Oxo-TEMPO concentration during charge of pre-discharged Vulcan electrode in 4-Oxo-TEMP containing electrolyte in the flat *in-operando* EPR cell design. Concentrations were calculated using a moving average over 17 individual data points. b) 4-Oxo-TEMPO concentration as a function of working electrode potential.

References Supplementary Information

[1] K. U. Schwenke, M. Metzger, T. Restle, M. Piana, H. A. Gasteiger, *J. Electrochem. Soc.* **2015**, *162*, A573–A584.

[2] K. U. Schwenke, S. Meini, X. Wu, H. A. Gasteiger, M. Piana, *Phys. Chem. Chem. Phys.* **2013**, *15*, 11830.

[3] S. Meini, M. Piana, N. Tsiouvaras, A. Garsuch, H. A. Gasteiger, *Electrochem. Solid-State Lett.* **2012**, *15*, A45–A48.

[4] S. Meini, N. Tsiouvaras, K. U. Schwenke, M. Piana, H. Beyer, L. Lange, H. a Gasteiger, *Phys. Chem. Chem. Phys.* **2013**, *15*, 11478–93.

[5] J. Wandt, C. Marino, P. Jakes, R. Eichel, H. A. Gasteiger, J. Granwehr, *Energy Environ. Sci.* **2015**, *8*, 1358–1367.

[6] D. T. Burns, B. D. Flockhart, *Philos. Trans. Phys. Sci. Eng.* **1990**, *333*, 37–48.

[7] M. Cipollone, C. di Palma, G. F. Pedulli, *Appl. Magn. Reson.* **1992**, *3*, 99–106.

[8] C. Schweitzer, R. Schmidt, *Chem. Rev.* **2003**, *103*, 1685–1757.

[9] W. Adam, D. V Kazakov, V. P. Kazakov, *Chem. Rev.* **2005**, *105*, 3371–87.

[10] F. Wilkinson, W. P. Helman, A. B. Ross, *J. Phys. Chem. Ref. Data* **1995**, *24*, 663.

[11] R. Ballardini, G. Beggiato, P. Bortolus, A. Faucitano, A. Buttafava, F. Gratini, *Polym. Degrad. Stab.* **1984**, *7*, 41–53.

[12] L. Y. Zang, Z. Y. Zhang, H. P. Misra, *Photochem. Photobiol.* **1990**, *52*, 677–83.

[13] R. E. Belford, G. Seely, D. Gust, T. A. Moore, N. J. Cherepy, S. Ekbundit, J. E. Lewis, S. H. Lin, *J. Photochem. Photobiol. A* **1993**, *70*, 125–133.

[14] X.-Z. Yang, Y. Chen, L. C. Dickinson, J. C. W. Chien, *Polym. Degrad. Stab.* **1988**, *20*, 1–35.

[15] K. Reszka, C. F. Chignell, *Photochem. Photobiol.* **1983**, *38*, 281–291.

[16] V. B. Ivanov, V. Y. Shlyapintokh, O. M. Khvostach, A. B. Shapiro, E. G. Rozantsev, *J. Photochem.* **1975**, *4*, 313–319.

[17] B. M. Monroe, *J. Phys. Chem.* **1977**, *81*, 1861–1864.

[18] S. Shukla, T. S. Srivastavat, *J. Photochem. Photobiol. A* **1989**, *48*, 249–257.

[19] A. E. Alegria, C. M. Krishna, R. K. Elespuru, P. Riesz, *Photochem. Photobiol.* **1989**, *49*, 257–265.

[20] Y. Lion, E. Gandin, A. Van de Vorst, *Photochem. Photobiol.* **1980**, *31*, 305–309.

[21] M. Metzger, C. Marino, J. Sicklinger, D. Haering, H. A. Gasteiger, *J. Electrochem. Soc.* **2015**, *162*, A1123–A1134.

[22] F. La Mantia, C. D. Wessells, H. D. Deshazer, Y. Cui, in *Electrochem. Commun.*, Elsevier B.V., **2013**, pp. 141–144.

[23] N. Tsiouvaras, S. Meini, I. Buchberger, H. A. Gasteiger, *J. Electrochem. Soc.* **2013**, *160*, A471–A477.

[24] M. Piana, J. Wandt, S. Meini, I. Buchberger, N. Tsiouvaras, H. A. Gasteiger, *J. Electrochem. Soc.* **2014**, *161*, A1992–A2001.

[25] B. D. McCloskey, D. S. Bethune, R. M. Shelby, T. Mori, R. Scheffler, A. Speidel, M. Sherwood, A. C. Luntz, *J. Phys. Chem. Lett.* **2012**, *3*, 3043–3047.

[26] I. Rosenthal, C. M. Krishna, G. C. Yang, T. Kondo, P. Riesz, *FEBS Lett.* **1987**, *222*, 75–78.

[27] G. Nardi, I. Manet, S. Monti, M. a Miranda, V. Lhiaubet-Vallet, *Free Radic. Biol. Med.* **2014**, *77*, 64–70.

[28] Mass Spectra, in *NIST Chem. WebBook, NIST Stand. Ref. Database Number 69, Eds. P.J. Linstrom W.G. Mallard*.

3.2 Operando X-Ray Absorption Spectroscopy Study

This section presents the article "Transition Metal Dissolution and Deposition in Li-Ion Batteries Investigated by *Operando* X-Ray Absorption Spectroscopy" which was submitted in October 2016 and accepted for publication in the peer reviewed Journal *Journal of Materials Chemistry A* in November 2016: *J. Mater. Chem. A*, 2016, 4, 18300 - Reproduced by permission of The Royal Society of Chemistry. The publication was presented on the conference Electrochemistry 2016 in Goslar (Germany) in September 2016. The permanent weblink to the article is http://pubs.rsc.org/en/content/articlelanding/2016/ta/c6ta08865a# !divAbstract.

In this study we investigate the transition metal dissolution from an NMC cathode and its subsequent deposition on the graphite anode by *operando* XAS spectroscopy. The experiments were carried out in two seperate synchrotron beamtimes at the European Synchrotron Radiation Facility (ESRF) in Grenoble (France) and the SOLEIL lightsource in Saint-Aubin (France) in April and July 2015. In the ESRF beamtime, method development was carried out and the iron dissolution from LFP cathodes was investigated (unpublished data). In the SOLEIL beamtime the data presented in this study were measured. We use a modified version of the previously developed *operando* XAS cell to which a reference electrode was added for the exact deconvolution of the cell potential into working and counter electrode potential. The cycling procedure, consisting of two charge discharge cycles between 3.0 and 4.6 V followed by a potential ramp and hold at 5.0 V, is a compromise between the limited experimental time and the desire to investigate both normal charge/discharge cycling and the influence of high cell potentials. The entire procedure lasts about 14 hours, the recording time for a single XAS spectrum (XANES) is about 24 minutes. Ideally, one could characterize all three NMC transition metals (Ni, Mn, Co) at the two relevant positions (anode and separator/electrolyte). Though, to achieve a reasonable time resolution we focus on recording manganese K-edge spectra in the graphite position. Manganese is chosen because it is considered to be the most detrimental transition metal with respect to the irreversible capacity loss on the anode side.[154] The diffusion time of transition metal ions from the cathode to the anode can be estimated to be around 20 minutes (diffusion coefficient of $> 1 \times 10^{-6}$ cm^2 s^{-1}, diffusion distance of 350 μm) which is fast in comparison to the overall time of the XAS experiment (14 hours). Effectively, by measuring the accumulation of transition metals on the anode one indirectly also observes the transition metal dissolution on the cathode side.

The average dissolution rate during charge/discharge cycling, as determined by *operando* XAS, is very similar to previously reported rates which were determined *ex situ* after 300 cycles, thereby confirming the validity of the more complex *operando* XAS experiments.[46] Increasing the cell potential above 4.6 V causes a significant increase of the transition metal dissolution rate. The main focus of this work is the determination of the oxidation state of "crossed-over" manganese deposits on the graphite electrode under real cell conditions. It is found that manganese deposits are always present in the oxidation state +2 as long as electrolyte is present and is only reduced to Mn(0) upon drying of the electrode. This is the first XAS study of the oxidation state of manganese deposits on the graphite anode under actual cell conditions and the change of oxidation state upon drying highlights the importance of adequate *operando* characterization techniques. These results are highly relevant for understanding the transition metal induced side reactions which are considered to be a major reason for the capacity loss of graphite/NMC cells.[45]

Author contributions

J.W., H.G. and M.T. developed the concept for this study. J.W. wrote the beamtime proposal and coordinated the project. J.W. and A.F. implemented the reference electrode and carried out the electrochemical experiments and the beamtime preparation. Participants ESRF beamtime: J.W., R.T., Y.G. and A.S. Participants SOLEIL beamtime: J.W., A.F., R.T. and R.J. R.T. carried out the XAS data analysis. J.W. and R.T. wrote the manuscript. All authors discussed the data and commented on the results.

Journal of Materials Chemistry A

COMMUNICATION

Transition metal dissolution and deposition in Li-ion batteries investigated by *operando* X-ray absorption spectroscopy†

Cite this: *J. Mater. Chem. A*, 2016, **4**, 18300

Received 12th October 2016
Accepted 8th November 2016

DOI: 10.1039/c6ta08865a

www.rsc.org/MaterialsA

Johannes Wandt,[a] Anna Freiberg,[a] Rowena Thomas,*[b] Yelena Gorlin,[a] Armin Siebel,[a] Roland Jung,[a] Hubert A. Gasteiger[a] and Moniek Tromp[c]

In Li-ion batteries the dissolution of transition metals from the cathode and their subsequent deposition on the anode are known to contribute to capacity fading. In this study, we investigate these processes using an NMC cathode and a graphite anode under operating conditions using X-ray absorption spectroscopy. The experiments are carried out in an *operando* cell, which allows both the time/voltage and spatially resolved determination of metal concentration and oxidation state of transition metal deposits on the graphite electrode. NMC shows a strong increase of the metal dissolution rate, if the upper cut off potential exceeds 4.6 V. Under operating conditions, the oxidation state of manganese, cobalt and nickel are found to be always +2 both on lithiated and delithiated graphite. In contrast, manganese is found to be present in the metallic state on lithiated graphite in the *ex situ* analysis, thus highlighting the importance of the *operando* characterization.

Electrification of the transport sector will be of vital importance for the containment of global warming and lithium ion batteries (LIB) are a key technology for the development of plug-in hybrid and electric vehicles. To achieve mass market penetration of battery electric vehicles, the driving range of BEVs will need to significantly increase. The necessary increase in the driving range has been recently estimated to require an increase in the energy density of Li-ion batteries by a factor of 2.5 over the next 15 years.[1] In a typical Li-ion cell, the single heaviest cell component is the cathode active material.[2] During recent years, intensive research has led to the development of a series of manganese-oxide based high energy density cathode materials such as layered $LiNi_{0.33}Mn_{0.33}Co_{0.33}O_2$ (NMC-111) or spinel structures like $LiMn_2O_4$ (LMO) or $LiNi_{0.5}Mn_{1.5}O_2$ (LNMO). While these materials offer good energy densities, a major problem for many manganese-oxide based cathode materials is the dissolution of manganese ions from the cathode which causes severe capacity fading in full cells.[3,4] Manganese ions dissolve in the electrolyte and accumulate on the anode, where they trigger irreversible side reactions leading to ongoing electrolyte reduction, SEI and impedance growth and the loss of cycleable lithium.[4–7] The fact that manganese induced side reactions on the anode side rather than structural damage of the cathode or loss of cathode material are the main cause for capacity fading is highlighted by the better capacity retention of LNMO half cells over LNMO full cells[8] and by the capacity recovery of NMC electrodes harvested from full cells at end of life.[4]

The mechanism of the detrimental effect of manganese accumulation on the graphite electrode is not yet fully understood. For a detailed understanding of these processes it is crucial to know the oxidation state of manganese species on the graphite electrode, which is still controversially discussed despite intensive research during recent years, with suggested manganese oxidation states ranging from Mn(0)[9,10] to Mn(III)[11] or even Mn(IV).[3] There are two different experimental approaches which are typically used for the investigation of manganese deposition on graphite which can be categorized by the manganese source: either manganese salts are intentionally added to the electrolyte[9,11–13] or manganese is dissolved directly from the cathode during normal cell operation.[3,6,14]

The presence of manganese species with oxidation states of +2 or even higher on graphite electrodes has been reported by several groups using either X-ray photoelectron (XPS)[3,11] or X-ray absorption spectroscopy (XAS).[6] Based on this observation, Zhan *et al.* proposed that the accumulation of manganese on graphite is caused by a metathesis reaction between Mn^{2+} and

[a]Technische Universität München, Chair of Technical Electrochemistry, Department of Chemistry and Catalysis Research Center, Germany

[b]Technische Universität München, Institute for Catalyst Characterization, Germany. E-mail: rowena.thomas@tum.de

[c]Van't Hoff Institute for Molecular Sciences, University of Amsterdam, Amsterdam, Netherlands

† Electronic supplementary information (ESI) available: Details regarding electrode preparation and cell assembly, electrochemical testing, experimental details regarding X-ray absorption spectroscopy and ICP-OES analysis, estimation of redox potentials in carbonate based electrolytes; additional manganese K-edge XAS spectra measured in the separator and graphite electrode and optical images of cycled graphite electrode. See DOI: 10.1039/c6ta08865a

This journal is © The Royal Society of Chemistry 2016

Li^+ containing SEI species rather than by an electrochemical reduction of Mn^{2+}.[6] Unfortunately, in these three publications[3,6,11] it is not clearly stated, whether the graphite electrodes were harvested in a lithiated or delithiated state before the *ex situ* analysis. To the best of our knowledge, the first experimental observation of metallic manganese on graphite electrodes was presented by Ochida *et al.* in 2012 using XPS.[15] Delacourt *et al.* also proposed that manganese is initially reduced to the metallic state at low potential on a copper model electrode, although their surface sensitive soft energy Mn L-edge XAS spectra only show Mn(II).[13] Gowda *et al.* identified Mn(0) in XAS spectra of lithiated graphite electrodes,[9] whereas Xiao *et al.* found both Mn(0) and MnF_2 nano-particles on the same graphite electrode (unknown state of charge).[10] Shkrob *et al.* were the first to point out that the seemingly contradictory information regarding manganese oxidations states might mainly be caused by differences in the state of charge at which the graphite electrodes are harvested before analysis. This was confirmed by their XAS results which showed reduced manganese on lithiated graphite electrodes and Mn(II) on delithiated graphite electrodes.[14]

In all of the above mentioned publications, the analytical investigation of the manganese oxidation state was carried out solely *ex situ* after preparation of the electrode. The details of sample preparation differ, but in general the electrodes are first harvested from the cycled cell, then washed in order to remove the conducting salt and ethylene carbonate and then dried. Without a doubt, *ex situ* data are very valuable and offer important insights into the mechanisms of manganese deposition and its oxidation state. Still, one cannot entirely rule out the possibility that the oxidation state changes during sample preparation. For example, Gowda *et al.* observed that washing the electrodes with dimethyl carbonate significantly decreased the amount of reduced manganese species.[9] Furthermore, the presence of electrolyte or electrolyte degradation products like hydrofluoric acid might also affect the oxidation states of the transition metals.

In order to address these issues and investigate the oxidation state of manganese on graphite under operating conditions, we performed time and spatially resolved *operando* XAS experiments with a special cell which is described in detail in our previous publication.[16] The cell has been slightly modified to allow the use of a reference electrode (see ESI and Fig. S1† for details). The cell consists of an NMC-111 positive electrode (120 μm thickness), a natural graphite negative electrode (170 μm thickness), two glassfiber separators (at a total compressed thickness of ≈400 μm) and 1 M $LiPF_6$ in EC/EMC (3 : 7) as electrolyte (for details see ESI†). The electrode arrangement and geometry of our *operando* cell design in combination with an X-ray beam focused onto a 140 × 1000 μm area allows the selective measurement of XANES or EXAFS spectra on either one of the two electrodes or in the separator region.[17]

Fig. 1a shows manganese K-edge XANES spectra measured in the *operando* XAS cell in these three different positions before the start of cell cycling. The raw spectra (not normalized) display the difference in signal intensity, reflected by the XAS edge height which is directly proportional to the amount of Mn in the beam. It is possible to continuously follow the manganese dissolution from the positive electrode during cell cycling by selectively monitoring manganese species deposited on the graphite counter electrode, as the diffusion time from cathode to anode (in the order of 500 s) is in the same order of magnitude as the time resolution of the XAS experiments (≈24 minutes per spectrum) and as transition metals are known to accumulate on the negative electrode rather than in the electrolyte.[14] The raw manganese K-edge XANES spectra (Fig. 1b) measured on the graphite electrode during battery cycling display a continuous increase of the manganese concentration upon cell cycling. The initial non-zero manganese concentration (lower panel of Fig. 1c) arises from impurities in the graphite electrode, the electrolyte, and the X-ray window. During cell charge/discharge cycling (Fig. 1c), manganese K-edge XANES spectra were mainly recorded in the graphite position in order to maximize the time/voltage resolution, justified by the fact that manganese is considered to be the most detrimental metal for graphite performance.[12] A single manganese K-edge spectrum (spectrum shown in Fig. S2†) was measured in the electrolyte (separator position) during the electrochemical procedure (pink star at ≈13 h in the lower panel of Fig. 1c) to confirm the above mentioned accumulation of manganese on the graphite electrode (see ESI† for details). Additionally, cobalt and nickel K-edge XAS spectra were also recorded before the start and after the end of the electrochemical procedure to determine their initial and final oxidation states as well as their concentration increase.

In the following section, we will first discuss the influence of the cell potential on the metal dissolution from the NMC electrode. In the second part we will discuss the oxidation states of manganese, nickel and cobalt species as observed on the graphite electrode. Furthermore, we consider the influence of the graphite potential on the transition metal oxidation states and the differences observed when comparing *operando* and *ex situ* spectra. Finally, we examine the implications of our findings for the capacity fading of full-cells.

Fig. 1c (lower panel) shows the increase of the manganese concentration on the graphite electrode upon cell cycling (upper panel) due to its dissolution from the NMC cathode, its diffusion through the separator, and its subsequent deposition on the anode. The manganese content in the graphite electrode was estimated by determining the Mn K edge XAS edge height of manganese solutions of known concentrations filled into our *operando* XAS cell (see ESI† for details). In the initial two cycles with an upper cut-off voltage of 4.6 V, the manganese concentration increases by 20 μmol h^{-1} $L_{electrode}{}^{-1}$ (≈0.34×10^{-9} mol h^{-1} or ≈1.0×10^{-9} mol per cycle) which equals a dissolution rate of ≈$0.0017\%_{Mn}$ per cycle when referring to the total manganese content in the NMC electrode (for details s. Section 6 of the ESI†). This manganese dissolution rate is essentially identical to our previous results for the same NMC material, where the manganese deposit on the graphite electrode was quantified after 230 cycles in the same potential range by post-mortem PGAA (prompt-gamma-activation analysis; s. Section 6 of the ESI† for details).[18]

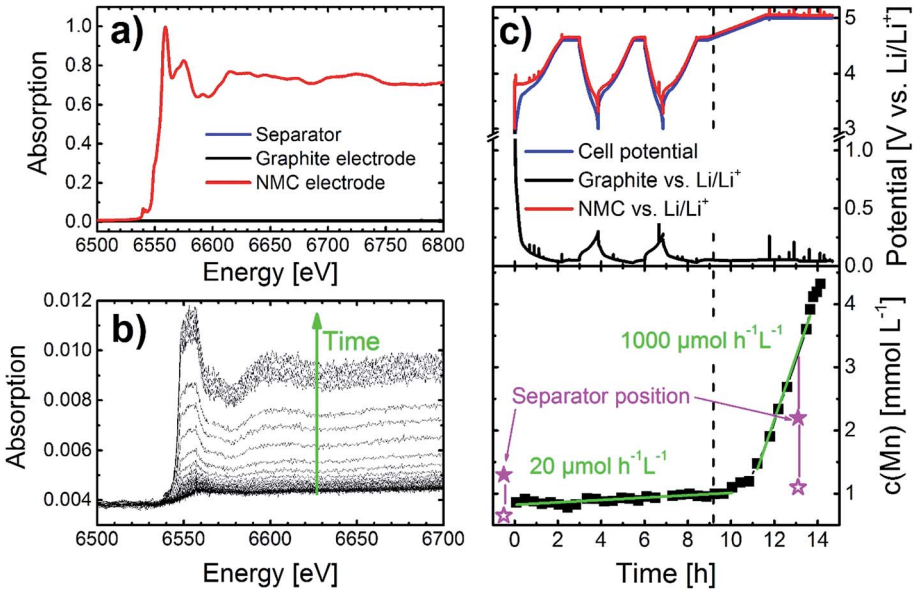

Fig. 1 Graphite/NMC full-cell data obtained in the operando XAS cell with 1 M $LiPF_6$ in EC/EMC (3 : 7) as electrolyte. (a) Initial Mn K-edge spectra (non-normalized) measured in the separator, the graphite electrode, and the NMC electrode position before electrochemical cycling, demonstrating the spatial resolution of the operando XAS cell. (b) Non-normalized operando Mn K-edge spectra measured on the graphite electrode during cell cycling (the first spectrum in (b) is a zoom into the graphite spectrum shown in (a)). (c) Upper panel: cell potential as well as individual electrode potentials *vs.* a metallic lithium reference electrode (*i.e., vs.* Li/Li^+) during cell cycling (see ESI† for detailed cycling procedure); lower panel: respective manganese concentrations on the graphite electrode as derived from the edge height of the operando Mn K-edge spectra (shown in (b)). The filled pink stars show the manganese concentration in the electrolyte (measured in the separator position); the empty pink stars show the theoretical manganese concentration which would be expected in the graphite position if there would be no accumulation on the graphite surface (considering the porosity of 50% of the graphite electrode, see ESI† for details).

When the NMC potential exceeds 4.6 V, the rate of manganese dissolution rapidly increases by a factor of ≈50 to 1000 mol h^{-1} L^{-1} (≡17×10^{-9} mol h^{-1}, s. Section 6 of the ESI†). The total metal dissolution over the course of the experiment (s. upper panel of Fig. 1c) determined by XAS (s. Section 6 of the ESI†) is 0.09 mol% for Mn, 0.26 mol% for Co, and 0.17 mol% for Ni. These amounts are within a factor of 2 of what we obtained by *ex situ* ICP-OES analysis (0.165 ± 0.015% for Mn, 0.125 ± 0.002% for Co and 0.116 ± 0.002% for Ni), which indicates that the XAS calibration procedure is reasonably accurate. In storage experiments with NMC-111 charged to 4.6 V, Gallus *et al.*[19] showed that the concentrations of Mn, Co, and Ni dissolved in the electrolyte are identical within roughly ±20%; on the other hand, after extended charge/discharge cycling of NMC-111/graphite cells between 3.0 and 4.6 V (including a CV step at 4.6 V to C/20), the amount of Mn deposited on the graphite electrode was twice as high as that of Co and Ni.[18] Unfortunately, no data are available for an extended potential hold at 5.0 V as was done in our XAS experiments. In general, the fact that the deposited/dissolved amounts of transition metals are within a factor of three points towards acidic corrosion as the governing metal dissolution mechanism at ≥4.6 V. In a recent study, it was shown by On-line Electrochemical Mass Spectrometry (OEMS) that at around 4.7 V significant amounts of protic species are formed upon electrolyte oxidation,[20] which could lead to a quasi homogeneous "etching" of the NMC material, resulting in a near stoichiometric dissolution/deposition of the three transition metals. Others have proposed that water might be produced by electrolyte oxidation at high potentials, which would lead to the formation of hydrofluoric acid from the $LiPF_6$ salt,[21] which in turn would trigger metal dissolution from transition metal oxide materials.[22,23] Manganese(III) disproportionation, which has also been suggested to contribute to the metal dissolution,[24,25] would cause a significantly increased manganese concentration in comparison to cobalt and nickel and is therefore likely negligible at potentials of ≥4.6 V.

In the following part we will discuss the oxidation state of manganese species deposited on the graphite electrode during the cycling procedure shown in Fig. 1c (upper panel). Fig. 2a and b compare the normalized reference Mn K-edge XANES spectra to the normalized Mn K-edge spectra measured *operando* on the graphite electrode (s. green line in Fig. 2b) at the end of the procedure shown in Fig. 1c (upper panel). Analyzing the edge position (see Section 5 of the ESI† for details), the oxidation state of the manganese species is predominantly +2 throughout the entire experiment (only final spectrum shown), independent of the graphite potential which varied between 80 mV and 250 mV *vs.* Li/Li^+. Although the edge position of the final *operando* Mn species is consistent with Mn^{2+} (s. red symbol in Fig. S3†), the structure of the XANES post-edge region differs from our Mn^{2+} references, which is not unexpected as this region depends strongly on the local geometry and ligand type around the Mn atom (s. Sections 4 and 5 of the ESI†). In the Mn^{2+} references, the Mn^{2+} is in an (close to) octahedral coordination sphere, whereas Mn^{2+} deposited on the graphite surface is not likely to be in such a geometry. The XANES spectra

 This journal is © The Royal Society of Chemistry 2016

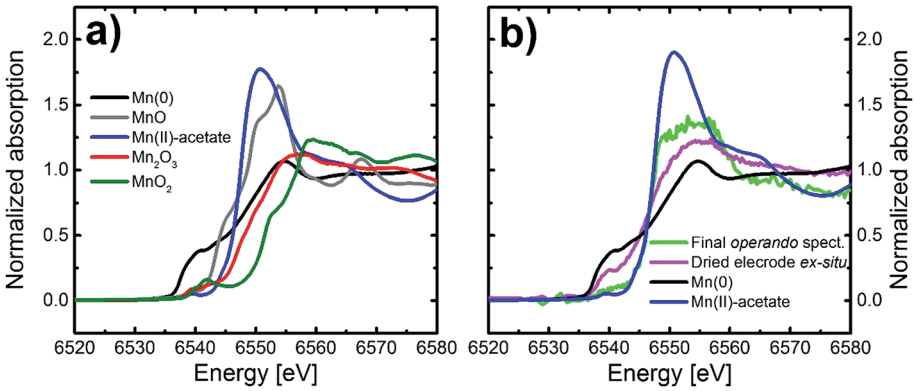

Fig. 2 (a) Mn K-edge spectra of reference compounds with different manganese oxidation states (s. also Sections 4 and 5 in the ESI†). (b) Final operando Mn K–edge spectrum (green line) measured in the operando cell on the lithiated graphite electrode at the end of the procedure shown in Fig. 1c (upper panel) and *ex situ* spectrum (pink line) of the same electrode after drying of the same electrode for 15 minutes under dynamic vacuum in the glovebox antechamber.

in fact indicate a lower symmetry based on the reduced main peak intensity and overall broadening. The spectrum also seems to differ from the *ex situ* spectra obtained by Gowda *et al.*[9] and Shkrob *et al.*,[14] with our data exhibiting a broader main peak. This is not surprising since our XANES spectra are recorded *operando* in the presence of electrolyte and those by the other authors *ex situ*, which will likely change the coordination geometry of the metal due to sample preparation. Unfortunately, we were not able to obtain full EXAFS spectra in a reasonable time scale at a sufficiently high signal/noise ratio, so we cannot deduce the local structure. The presence of Mn(II) on the lithiated graphite electrode is surprising, considering the low potential of lithiated graphite (80 mV and 250 mV *vs.* Li/Li^+), which is well below the Mn(0)/Mn(II) redox potential (s. Section 7 of the ESI†). Our observation of Mn(II) under operating conditions is also noteworthy because Gowda *et al.*[9] and Shkrob *et al.*[14] both found reduced manganese in their *ex situ* analysis on lithiated graphite (note, that in ref. 9 it is not entirely clear whether the *ex situ* XAS spectra were recorded in the absence or presence of electrolyte due to inconclusive experimental details). In order to rule out the possibility that the rather unusual cycling procedure of the cell shown in Fig. 1 is somehow responsible for the presence of Mn(II), a second cell was investigated after 22 "conventional" charge/discharge cycles between 3.0 and 4.6 V (s. Section 2 of the ESI†). *Operando* XANES spectra of the Mn K-edge were recorded while the graphite electrode was polarized to 0.095 V (cell charged, *i.e.*, graphite lithiated; s. pink line in Fig. S6†) or 1.5 V *vs.* Li/Li^+ (cell discharged, *i.e.*, graphite delithiated; s. green line in Fig. S6†), but independent of the graphite potential, the manganese oxidation state was again predominantly +2 under operating conditions, thus confirming the results shown in Fig. 2b (green line) for the *operando* XAS measurements on the graphite after polarization to 5 V.

After finishing the cycling procedure in the *operando* cell (s. Fig. 1c), the cell was brought back into the glove box and the graphite electrode was harvested in the lithiated state (*i.e.*, after the 200 minute cell potential hold at 5.0 V). The unwashed graphite electrode was dried in the antechamber for 15 minutes and then sealed again in an *operando* cell without a NMC counter electrode and without electrolyte. The subsequent *ex situ* Mn K-edge XANES spectrum measured on the dried graphite electrode (s. pink line in Fig. 2b) clearly shows a reduced manganese oxidation state which indicates the presence of Mn(0), in addition to Mn(II). The amounts of Mn(0) and Mn(II) present on the dried graphite electrode appear to be of a similar order of magnitude but further analysis to identify the species present was not possible from this data set. Again, for clarification, both the last *operando* spectrum consistent with the presence of Mn(II) (green line in Fig. 2b) and the *ex situ* spectrum showing a mixture of Mn(0) and Mn(II) (pink line in Fig. 2b) were measured on the same graphite electrode in the very same state of charge and using the same aluminized Kapton window, the only difference being the presence/absence of electrolyte. The fact that our *ex situ* data is consistent with the literature, *viz.*, showing reduced manganese, confirms that the observation of Mn(II) under operating conditions is not an artefact caused by our experimental set up. To the best of our knowledge, the XAS data presented here is the first experimental proof that manganese is predominantly present in oxidation state +2 on lithiated graphite under operating conditions and that it is being (partially) reduced during subsequent drying of the electrode which is actually unavoidable during *ex situ* sample preparation. This interpretation is supported by a simple optical observation: (i) directly after disassembling the cell in an argon filled glove box, the lithiated graphite electrode has a golden appearance, as one would expect for fully lithiated (*i.e.*, fully charged) graphite (s. Fig. S7a†); (ii) upon drying the top layer of the electrode for different periods of time, the surface quickly turns black (s. Fig. S7b–d†); (iii) scratching of the blackened surface of the graphite electrode shows that its inner parts still have the golden appearance characteristic of lithiated graphite (s. Fig. S7e†). Delacourt *et al.* have linked the appearance of a black conducting film on their model copper electrodes to the presence of metallic manganese,[13] which we believe is also the cause

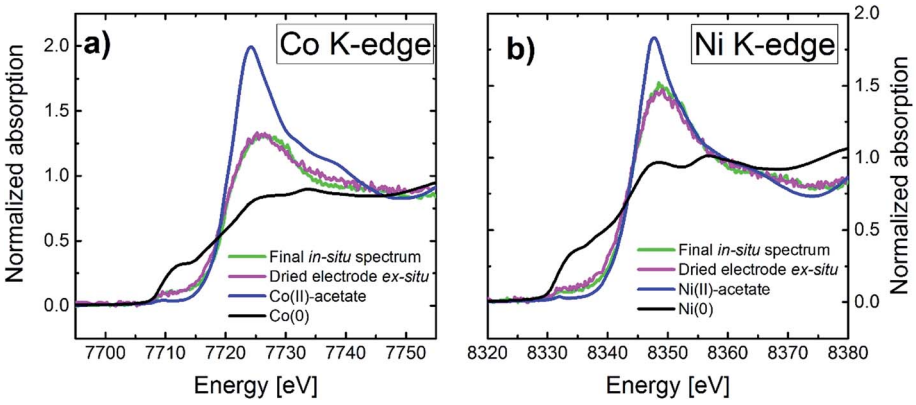

Fig. 3 K-edge spectra of (a) cobalt and (b) nickel measured at the lithiated graphite electrode at the end of the procedure shown in Fig. 1c (upper panel); for both metals the final operando spectrum measured in the operando XAS cell is compared with the *ex situ* spectrum of the same electrode after drying of the electrode for 15 minutes under dynamic vacuum in the glovebox antechamber.

for the black film observed on our graphite electrode. The observation that the black film is only present on the surface of the dried graphite electrode while the bulk of the graphite electrode is still golden, indicates the preferential manganese deposition on the graphite electrode surface which was facing the NMC electrode, an assumption which is consistent with XPS depth profiling data presented by Yang *et al.*[3]

When considering the question of why reduced manganese is only present in the *ex situ* analysis, a likely hypothesis is that under operating conditions Mn(II) is constantly reduced at the graphite electrode (the reduction rate limited by electron transfer through the SEI), but then rapidly reoxidized by electrolyte as suggested by Delacourt *et al.*[13] This would be consistent with XPS data published by Ochida *et al.*,[15] showing the oxidation of metallic manganese to MnO on delithiated graphite after a 24 hour hold at OCV and with DFT calculations by Han *et al.*,[26] showing that the oxidation of isolated Mn(0) by ethylene carbonate through a ring-opening reaction is exothermic. Thus, the different manganese oxidation state in *operando vs. ex situ* experiments could be explained by assuming that the reduction of Mn(II) on the graphite electrode is rate limiting (*i.e.*, sufficiently slowed down by the SEI), in which case the predominant manganese oxidation state would be +2 as long as electrolyte is available (*i.e.*, in the *operando* experiments), while it would gradually be reduced to an oxidation state of 0 in the absence of electrolyte (*i.e.*, in *ex situ* experiments). The suggested reduction of Mn(II) on the graphite electrode and subsequent re-oxidation by electrolyte corresponds to a Mn(II)/Mn(0) catalyzed redox cycle with a net reaction being continuous electrolyte reduction at the graphite electrode. In an actual battery cell the consequence would be ongoing active lithium loss and increased SEI formation. Accordingly, this Mn(II)/Mn(0) redox cycle might be the underlying mechanism causing the enhanced capacity fading and impedance rise typically observed for graphite/NMC full cells operating under conditions favoring transition metal dissolution (*e.g.* high cut-off potentials).[18]

Interestingly, both the *operando* (in the presence of electrolyte) and the *ex situ* (dried electrode) K-edge XANES spectra show that nickel and cobalt, which also accumulate on the graphite electrode, are always present in oxidation state +2 as shown in Fig. 3. This is surprising considering the more noble character of cobalt and nickel in comparison to manganese (see ESI† for details). The redox potentials for Co/Co^{2+} and Ni/Ni^{2+} are in the range of 2.2 to 2.5 V which is clearly above the potential for electrolyte reduction.[27] Accordingly, one would expect metallic cobalt and nickel both in the absence and presence of electrolyte; it is therefore not surprising that cobalt and nickel show the same oxidation state in the *operando* and *ex situ* spectra, but it is surprising that this oxidation state is +2 rather than zero. A possible reason for the trapping of cobalt and nickel in the +2 oxidation state might be the immobilization of cobalt and nickel in the outer SEI at a greater distance to the actual graphite surface, thus preventing their reduction to the metallic state. The influence of the exact site of the metal deposition within the graphite SEI on the oxidation state has been shown by an XPS depth profiling study carried out by Peled *et al.*,[28] where arsenic deposits from $LiAsF_6$ salt reduction were found to be mainly in oxidation state +III and +V in the outer SEI while they were dominated by As^0 near the graphite/SEI interface. For manganese, Shkrob *et al.* combined the results of electron paramagnetic resonance (EPR) spectroscopy and XAS to show that it is predominantly deposited on the inner SEI in a Li_2CO_3 matrix, thus enabling reduction of Mn^{2+} due to the close vicinity to the actual graphite surface.[14] To the best of our knowledge, there is no such information available for cobalt and nickel deposits. In the future, experiments which characterize the transition metal species in the SEI using high-quality K-edge EXAFS spectra at a micro-focus beamline, which would offer much higher flux and therefore a better signal-to-noise ratio, could clarify the chemical environment of manganese, cobalt and nickel compounds deposited on graphite under operating conditions.

In summary, we used time and spatially resolved XAS to study transition metal dissolution and deposition in Li-ions cells under operating conditions. This is, to the best of our knowledge, the first study of these processes under real cell conditions. The manganese dissolution rate was found to

 This journal is © The Royal Society of Chemistry 2016

drastically increase at potentials >4.6 V. Under operating conditions manganese deposits on the graphite electrode were always in oxidation state +2, independent of the state of charge. In contrast, *ex situ* analysis of the same lithiated graphite electrode showed reduced manganese species, indicating the presence of Mn(0), which is consistent with *ex situ* data in the literature. Cobalt and nickel deposits were always found in oxidation state +2 both in *operando* and *ex situ* spectra. We believe, that the change in the manganese oxidation state upon sample preparation clearly highlights the importance of using a dedicated *operando* technique in order to obtain a comprehensive picture of transition metal deposition on graphite anodes and its role in cell capacity fading.

Acknowledgements

We gratefully acknowledge Soleil for provision of beamtime (proposal number 20141256) and Dr Andrea Zitolo for his assistance using SAMBA. We thank Dominik Haering for experimental support during the beamtime. J. W. and R. T. gratefully acknowledge the financial support by the Bavarian Ministry of Economic Affairs and Media, Energy and Technology under the auspices of the EEBatt project. R. J. was supported by BMW AG, and Y. G. gratefully acknowledges the support of the Alexander von Humboldt Postdoctoral Fellowship and Carl Friedrich von Siemens Fellowship Supplement.

References

1 D. Andre, S.-J. Kim, P. Lamp, S. F. Lux, F. Maglia, O. Paschos and B. Stiaszny, *J. Mater. Chem. A*, 2015, **3**, 6709–6732.
2 F. T. Wagner, B. Lakshmanan and M. F. Mathias, *J. Phys. Chem. Lett.*, 2010, **1**, 2204–2219.
3 L. Yang, M. Takahashi and B. Wang, *Electrochim. Acta*, 2006, **51**, 3228–3234.
4 H. Zheng, Q. Sun, G. Liu, X. Song and V. S. Battaglia, *J. Power Sources*, 2012, **207**, 134–140.
5 K. Amine, Z. Chen, Z. Zhang, J. Liu, W. Lu, Y. Qin, J. Lu, L. Curtis and Y.-K. Sun, *J. Mater. Chem.*, 2011, **21**, 17754.
6 C. Zhan, J. Lu, A. J. Kropf, T. Wu, A. N. Jansen, Y.-K. Sun, X. Qiu and K. Amine, *Nat. Commun.*, 2013, **4**, 2437.
7 T. Joshi, K. Eom, G. Yushin and T. F. Fuller, *J. Electrochem. Soc.*, 2014, **161**, 1–33.
8 N. P. W. Pieczonka, Z. Liu, P. Lu, K. L. Olson, J. Moote, B. R. Powell and J.-H. Kim, *J. Phys. Chem. C*, 2013, **117**, 15947–15957.
9 S. R. Gowda, K. G. Gallagher, J. R. Croy, M. Bettge, M. M. Thackeray and M. Balasubramanian, *Phys. Chem. Chem. Phys.*, 2014, **16**, 6898–6902.
10 X. Xiao, Z. Liu, L. Baggetto, G. M. Veith, K. L. More and R. R. Unocic, *Phys. Chem. Chem. Phys.*, 2014, **16**, 10398–10402.
11 S. Komaba, T. Itabashi, T. Ohtsuka, H. Groult, N. Kumagai, B. Kaplan and H. Yashiro, *J. Electrochem. Soc.*, 2005, **152**, A937.
12 S. Komaba, N. Kumagai and Y. Kataoka, *Electrochim. Acta*, 2002, **47**, 1229–1239.
13 C. Delacourt, a. Kwong, X. Liu, R. Qiao, W. L. Yang, P. Lu, S. J. Harris and V. Srinivasan, *J. Electrochem. Soc.*, 2013, **160**, A1099–A1107.
14 I. A. Shkrob, A. J. Kropf, T. W. Marin, Y. Li, O. G. Poluektov, J. Niklas and D. P. Abraham, *J. Phys. Chem. C*, 2014, **118**, 24335–24348.
15 M. Ochida, Y. Domi, T. Doi, S. Tsubouchi, H. Nakagawa, T. Yamanaka, T. Abe and Z. Ogumi, *J. Electrochem. Soc.*, 2012, **159**, A961–A966.
16 Y. Gorlin, A. Siebel, M. Piana, T. Huthwelker, H. Jha, G. Monsch, F. Kraus, H. A. Gasteiger and M. Tromp, *J. Electrochem. Soc.*, 2015, **162**, A1146–A1155.
17 Y. Gorlin, M. U. M. Patel, A. Freiberg, Q. He, M. Piana, M. Tromp and H. A. Gasteiger, *J. Electrochem. Soc.*, 2016, **163**, A930–A939.
18 I. Buchberger, S. Seidlmayer, A. Pokharel, M. Piana, J. Hattendorff, P. Kudejova, R. Gilles and H. A. Gasteiger, *J. Electrochem. Soc.*, 2015, **162**, A2737–A2746.
19 D. R. Gallus, R. Schmitz, R. Wagner, B. Hoffmann, S. Nowak, I. Cekic-Laskovic, R. W. Schmitz and M. Winter, *Electrochim. Acta*, 2014, **134**, 393–398.
20 M. Metzger, J. Sicklinger, D. Haering, C. Kavakli, C. Stinner, C. Marino and H. A. Gasteiger, *J. Electrochem. Soc.*, 2015, **162**, A1227–A1235.
21 H. Yang, G. V. Zhuang and P. N. Ross, *J. Power Sources*, 2006, **161**, 573–579.
22 J. C. Hunter, *J. Solid State Chem.*, 1981, **39**, 142–147.
23 D. Aurbach, M. Levi, K. Gamulski, B. Markovsky, G. Salitra, E. Levi, U. Heider, L. Heider and R. Oesten, *J. Power Sources*, 1999, **81–82**, 472–479.
24 Y. Xia and M. Yoshio, *J. Electrochem. Soc.*, 1996, **143**, 825–833.
25 D. H. Jang, Y. J. Shin and S. M. Oh, *J. Electrochem. Soc.*, 1996, **143**, 2204–2211.
26 Y.-K. Han, K. Lee, S. Kang, Y. S. Huh and H. Lee, *Comput. Mater. Sci.*, 2014, **81**, 548–550.
27 R. Jung and H. A. Gasteiger, 2016, manuscript in preparation.
28 D. Bar-Tow, E. Peled and L. Burstein, *J. Electrochem. Soc.*, 1999, **146**, 824.

This journal is © The Royal Society of Chemistry 2016

Electronic Supplementary Material (ESI) for Journal of Materials Chemistry A.
This journal is © The Royal Society of Chemistry 2016

Supporting Information

Transition metal dissolution and deposition in Li-ion batteries investigated by operando x-ray absorption spectroscopy

Johannes Wandt[1], Anna Freiberg[1], Rowena Thomas[#], Yelena Gorlin[1], Armin Siebel[1], Roland Jung[1], Hubert A. Gasteiger[1], Moniek Tromp[2]

[1]Technische Universität München, Chair of Technical Electrochemistry, Department of Chemistry and Catalysis Research Center, Germany

[2] Van't Hoff Institute for Molecular Sciences, University of Amsterdam, Amsterdam, Netherlands

Table of content

1) Electrode preparation and cell assembly

Cathodes based on commercial $LiNi_{0.33}Mn_{0.33}Co_{0.33}O_2$ (NMC) active material were prepared by dispersing NMC (96wt%), polyvinylidene difluoride (PVdF, KynarHSV 900, Arkema, France) (2 wt%), and carbon black (Super C65, TIMCAL, Switzerland) (2 wt%) in N-methyl-2-pyrrolidone (NMP, Sigma Aldrich, Germany) and mixing them altogether in a planetary centrifugal vacuum mixer (Thinky, USA) at 2000 rpm for 15 min. The resulting viscous slurry with a solid content of 1.9 g/mL was cast onto a thin aluminum foil (thickness 18 µm, MTI corporation, USA) using the doctor blade method (RK Print Coat Instruments, UK) with a wet-film thickness of 240 µm. Graphite electrodes were produced analogously, using a mixture of 90 wt% graphite (Timcal, Germany) and 10 wt% PVdF binder in NMP (solids content of 0.88 g/ml) and a copper foil as current collector (10µm, MTI corporation, USA). After drying at room temperature, electrodes with a size of 10×10 mm (squares) were punched out and dried under dynamic vacuum for 12 hours at 120 °C (Büchi, Switzerland) and transferred into an Argon filled glove box (MBRAUN). Active material loadings were about 14.8 mg cm^{-2} for graphite and 18.0 mg cm^{-2} for NMC electrodes. NMC electrodes were compressed at a pressure of 130 MPa to a thickness of 125 µm and a porosity of 30%; graphite electrodes were used without compression (170 µm thickness, 50% porosity).

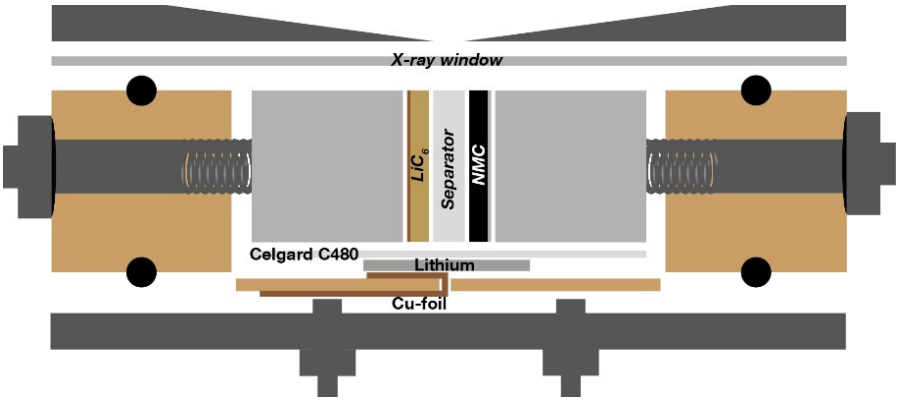

Figure S1 Schematic drawing of the spectro-electrochemical *operando* XAS cell showing the incorporation of the reference electrode. A detail exploded view and description of the cell design is provided in reference [1].

The XAS cell design is described in detail elsewhere.[1] It has been slightly modified in comparison to the work by Gorlin *et al.*[1] in order to accommodate a metallic lithium reference electrode as shown in Figure S1. The lithium reference electrode was placed in a central position underneath the electrode stack and contacted through a screw in the back

plate of the cell. The x-ray window consisted of an aluminized 12 µm Kapton® foil (aluminized side placed towards the cell exterior) and an additional 25 µm Kapton® foil (placed on top of the aluminum layer) to prevent mechanical damage of the thin aluminum layer. The cell was assembled with two glassfiber separators (250 µm uncompressed thickness, glass microfiber filter 691, VWR) and 300 µL electrolyte (1 M $LiPF_6$ in EC/EMC 3:7, BASF).

2) Electrochemical testing

Electrochemical testing was carried out using a Biologic SP200 battery cycler. Two different cycling procedures were used within this project. For the *operando* procedure (s. Fig. 1), the cell was mounted in the XAS sample stage directly after assembly and then cycled for two cycles between 3.0 and 4.6 V with a C/2 CCCV charge (C/20 current cut off) and 1C CC discharge followed by a single CC charge to 4.6 V followed by another CV step. The discharge capacities in the first two cycles were 174 $mAhg_{NMC}^{-1}$ and 169 mAh g_{NMC}^{-1}, respectively. The potential was then increased with a sweep rate of 2.5 mV min^{-1} to 5.0 V, where it was held for 200 minutes. A second cell ("conventional cycling procedure") was cycled inside the glovebox for 22 cycles between 3.0 and 4.6 V: after a C/10 formation cycle, the cell was cycled with a C/2 CCCV charge (C/20 current cut off) and 1C CC discharge. The last cycle showed a discharge capacity retention of 169 mAh g_{NMC}^{-1}, which is comparable to the performance in a standard Swagelok cell.[2] After cycling, the cell was sealed in a pouch bag inside the glove box and transported to the synchrotron in the charged state, thus eliminating the possibility of oxygen intrusion. After mounting the cell in the sample stage, XAS spectra were recorded in the charged state (graphite potential +0.095 V vs. Li/Li^+) and in the entirely discharged state (graphite potential +1.5 V vs. Li/Li^+).

3) XAS experiments

The X-ray absorption spectra were measured at the SAMBA beamline, a hard X-ray bending magnet beamline at Soleil synchrotron, France. The acquisition time for each spectrum presented in this work was approximately 24 minutes. The synchrotron was operating in multibunch top up mode. A sagittaly focusing double crystal monochromator consisting of two Si 220 crystals was used to select the incoming energy and the beam was focused using Pd coated mirrors before being cut with slits to achieve a beam size of 100 micrometer in the horizontal and approximately 1000 micrometer in the vertical dimension. The cells were

assembled as described above, and measured in fluorescence mode, with an energy selective Canberra 35-element monolithic planar Ge pixel array detector to collect the photons. Photon energies were calibrated using the first peak in the first derivative of the pure metal foils, which were measured in fluorescence before and after the operando studies, and background corrections of the spectra were carried out using the IFEFFIT software package.[3,4]

4) Manganese K-edge spectrum of electrolyte

Figure S2 shows a manganese K-edge spectrum measured in the electrolyte (separator position, pink line) during the 5 V constant potential step as indicated in Figure 1c (main paper). The oxidation state of the dissolved manganese is clearly +2 which is consistent with the literature.[5]

The XAS spectra, which are measured in the graphite position actually show a superposition of manganese deposited on the surface of the graphite particles and manganese species dissolved in the electrolyte which is contained within the pores of the graphite electrode (50% porosity). It is therefore only possible to reliably determine the oxidation state of manganese deposits on the graphite electrode, if the spectrum measured in the graphite position is dominated by manganese deposits rather than by dissolved manganese species. The edge jump measured in the separator (Figure S2) corresponds to a manganese concentration of about 2.2 mmolar (s. filled pink star at ≈13 h in the lower panel of Fig. 1c). If the concentration of the dissolved manganese species were constant across the entire cell, the dissolved manganese species would correspond to a ≈1.1 mmolar concentration in the graphite position considering the porosity of the graphite electrode of 50% (s. empty pink star at ≈13 h in the lower panel of Fig. 1c). If one interpolates the manganese concentration determined in the graphite position directly before and after the separator spectrum to the time at which the separator spectrum was measured, one contains a manganese concentration of 3.2 mmolar for the graphite position. Therefore, at this point in time (about 13 hours) the higher limit for the contribution of dissolved manganese to the spectrum measured in the graphite position can be estimated to be about 25% (=1.1/(1.1+3.2)). The real contribution of the dissolved manganese will be significantly smaller due to two reasons: Firstly, the above estimation is based on the assumption that the concentration of dissolved manganese is identical (1.1 mmolar) for electrolyte contained within the pores of

the graphite electrode and the separator. In reality, the manganese is being released into the electrolyte at the NMC electrode and then diffuses through the separator to the graphite electrode. As this diffusion is driven by a concentration gradient, the manganese concentration has to be lower in the electrolyte contained in the graphite electrode in comparison to the electrolyte contained in the separator, which is closer to the NCM electrode. Secondly, the fact that manganese is being accumulated in the graphite electrode means that it is being extracted from the electrolyte. As a direct consequence, the manganese concentration in the electrolyte contained within the porous graphite electrode is further reduced in comparison to the respective concentration in the separator. Therefore, the manganese K-edge spectra measured within the graphite electrode during the 5V hold step can reliably be assigned to manganese deposits.

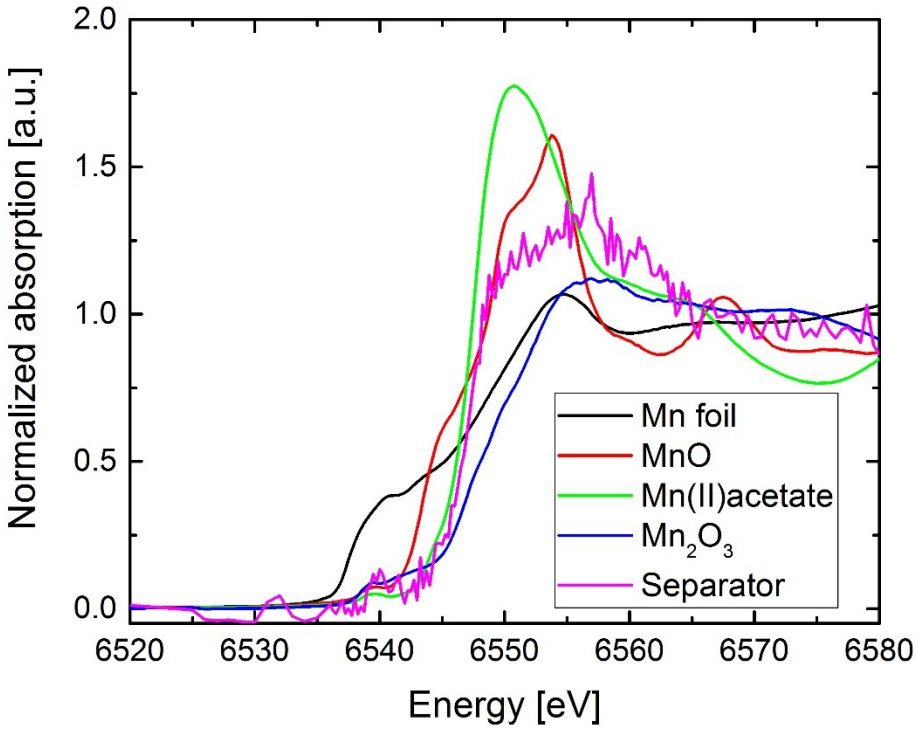

Figure S2 Mn K-edge spectra of reference compounds as well as *operando* spectrum measured in the electrolyte (= separator position) at the beginning of the 5 V potential hold after the initial charge/discharge cycles in the operando XAS cell. The exact time at which the *operando* spectrum was measured is indicated by the pink star at the right-hand-side of the lower panel of Figure 1c (main text).

The situation is a little less clear in the initial spectra due to the lower difference in the manganese concentration measured in the graphite position (0.9 mmolar) in comparison to the electrolyte (1.3 mmolar, or 0.65 mmolar considering 50 % porosity of the graphite

electrode; see full and empty pink star near 0 h in the lower panel of Fig. 1c). Accordingly, the contribution of dissolved manganese to the first manganese spectrum measured in the graphite position can be estimated to be about 42% (=0.65/(0.65+0.9)). Nevertheless, the main conclusion derived from the manganese spectra in the graphite position, that the manganese deposits are always present in oxidation state +2 irrespective of the graphite potential, is in no way hampered by the slight contribution of dissolved manganese in the initial spectra.

5) Analysis of manganese oxidation states

The edge positions of the Mn samples were determined by taking the position of the second peak in the 1st derivative of the K-edge XANES spectra. In Figure S3 the edge positions of all Mn references (black points) are plotted against formal oxidation state in order to more clearly see the trend in edge shifts. From this it is clear that the edge position of the final *operando* graphite spectrum (red point) is consistent with the values obtained for a formal oxidation state of +2. A linear fit is not possible due to the rather wide range of edge values for a single oxidation state, as demonstrated by the values obtained for Mn^{2+}, due to the fact that the edge values for transition metals also depend on geometry and ligand coordination.[6] The relatively poor signal-to-noise ratio for the 1st derivative spectrum of the ex situ sample makes assigning a precise edge position difficult, this is further discussed below. The references measured were as follows: Mn foil (Mn(0)), MnO (Mn(II)), $Mn(CH_3COO)_2 \cdot 4\,H_2O$ (Mn(II)), manganocene (Mn(II)), Mn_2O_3 (Mn(III)), MnO_2 (Mn(IV)), and pristine NMC material (Mn(IV)). All Mn references were purchased from Sigma-Aldrich (Germany), with the exception of the NMC material (see above). Pellets were prepared using boron nitride as a diluent and measured in transmission. The 1st derivative XANES spectrum of the ex situ graphite sample (Figure S4, blue line) shows a broad peak at the edge position (6542-6550 eV) which has intensity spanning the edge position for Mn(0) and Mn(II), as depicted here by spectra from a Mn foil (black line) and $Mn(II)(CH_3COO)_2 \cdot 4\,H_2O$ (red line). Therefore, we believe a combination of Mn(0) and Mn(II) is present, both in significant amounts. This is supported by an examination of the associated XANES spectra (Figure S4), which shows that the rising edge is located between those of Mn foil and $Mn(II)(CH_3COO)_2 \cdot 4\,H_2O$. Unfortunately, due to the data quality and lack of suitable reference spectra further analysis by principle components analysis is not possible.

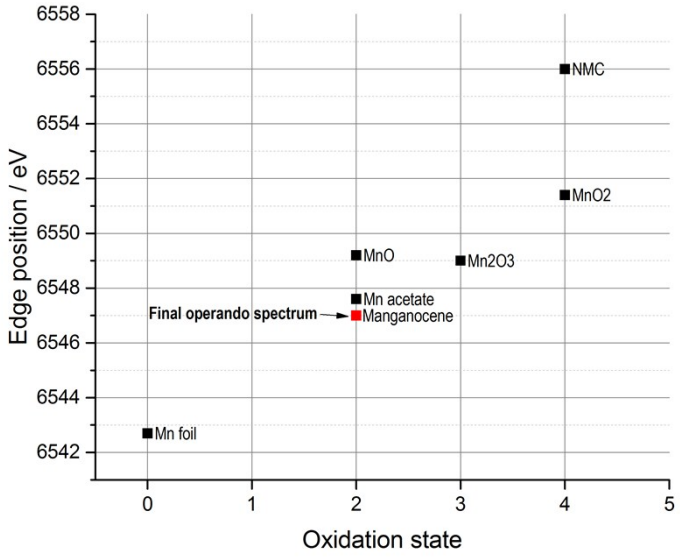

Figure S3 Edge position in Mn K-edge spectra for several reference compounds (black dots) as a function of their formal oxidation state and the final *operando* spectrum measured on the graphite electrode (red dot, see Figure 2b in main text). The final *operando* spectrum occurs at the same energy as manganocene, so the two data points are overlaid.

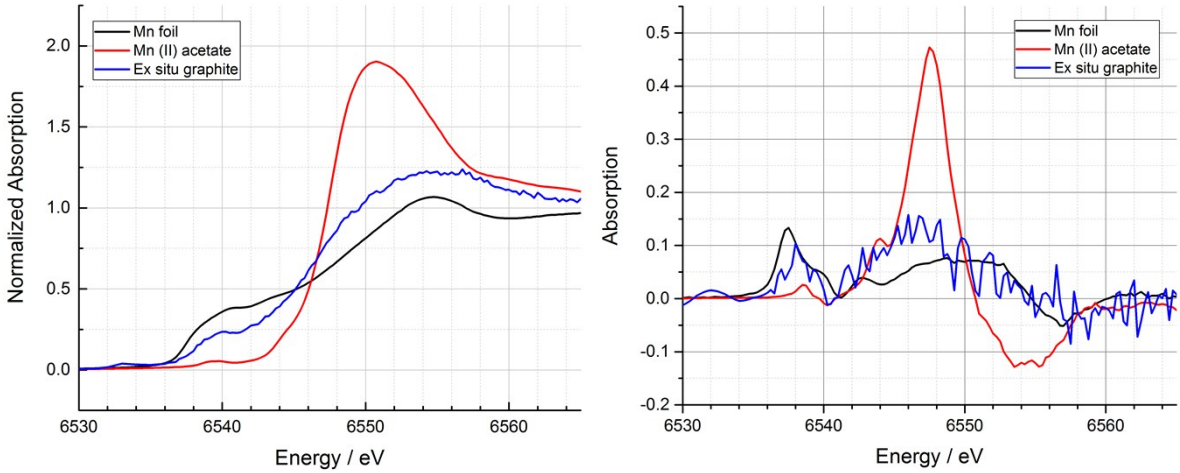

Figure S4 Mn K-edge XANES spectra (left) and the 1st derivative Mn K-edge XANES spectra (right) of the ex situ graphite sample overlaid with the spectra of Mn (II) acetate and Mn foil reference samples to demonstrate relative edge positions.

6) Quantification of transition metal deposition on graphite

In order to quantify the amount of transition metal deposited on the graphite electrode calibration curves (Figure S5) were measured containing manganocene, cobaltocene and nickelocene (all Sigma-Aldrich) in concentrations of zero (≡ background signal for pure electrolyte), 0.4, 4 and 20 mM dissolved in LP57 electrolyte. The calibration curves were measured directly in the *operando* XAS cell in the same geometry, thus eliminating the necessity of performing a correction for differences in x-ray penetration depths. For the calibration measurements, the cells contained only two glass fiber separators and no electrodes The calibration can be used to convert experimentally determined edge jumps into concentrations (in mol L^{-1}). The experimentally determined transition metal concentrations are all in the low mmolar range, which is close to the detection limit for the XAS experiment; furthermore, the manganese and cobalt calibration curves show no ideal linear behavior in this concentration range (Figure S5). Accordingly, the transition metal concentrations determined by XAS will contain an error which cannot be exactly determined due to the non-linear behavior of the calibration curve in the relevant concentration range. Nevertheless, they present a reasonable estimate for the transition metal concentration.

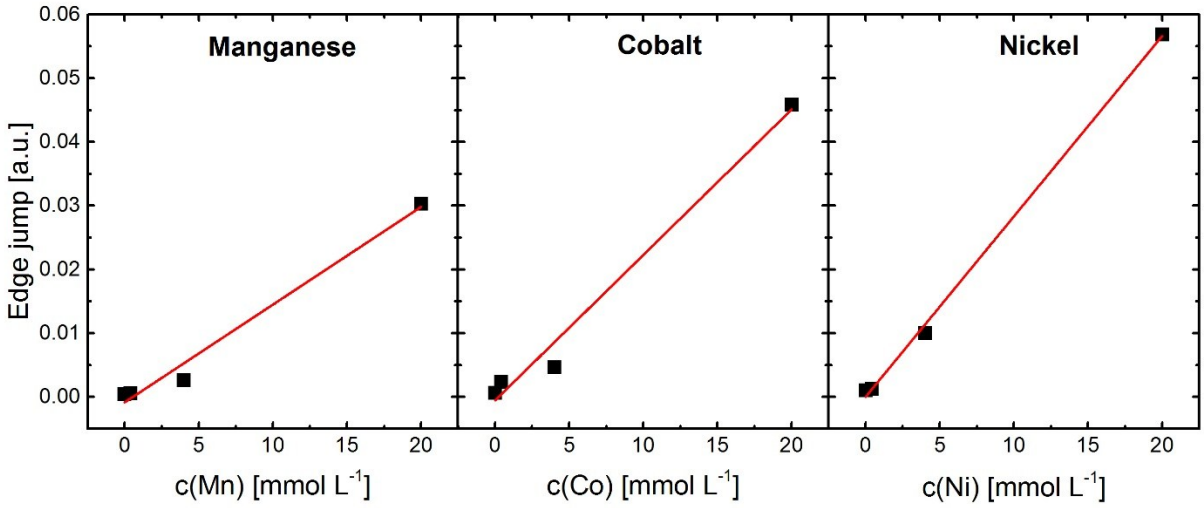

Figure S5 Calibration curves of manganocene, cobaltocene and nickelocene dissolved in LP57 electrolyte in concentrations of zero (= pure electrolyte), 0.4, 4 and 20 mM measured directly in the operando XAS cell.

By comparing the initial and the final XAS spectra measured in the operando cell, concentration increases during cycling of ≈ 3, 9, and 6 mmol L^{-1} were found for Mn, Co, and Ni, respectively (the Mn concentration increase is shown in the lower panel of Figure 1, main text). From this concentration increase, the total amount of each metal deposited on the

graphite electrode (in mol) can be calculated considering the volume of the graphite electrode, which equals 10 mm × 10 mm × 0.17 mm = 17 ·10^{-6} L. The relative amount of the dissolved transition metals can be calculated by dividing by the total amount of each transition metal in the NMC electrode (containing 17.08 mg $LiNi_{0.33}Mn_{0.33}Co_{0.33}O_2$ for this cell with a molecular weight of 96.46 g/mol), which is 59 · 10^{-6} mol for Mn, Co and Ni. Accordingly, the concentration increases over the entire course of the experiment (3, 9 and 6 mmol L^{-1} for Mn, Co and Ni) can be converted into dissolution fractions of 0.09, 0.26 and 0.17% of the total metal content in the NMC electrode. These values agree within a factor of two with *ex-situ* ICP-OES analysis (0.165 ± 0.015 % for Mn, 0.125 ± 0.002 % for Co and 0.116 ± 0.002 % for Ni) of harvested electrodes as explained in the next section.

For manganese, it is also possible to extract dissolution rates from the time resolved *operando* experiments shown in Figure 1 (main text). For the first two cycles between 3.0 and 4.6 V, an average dissolution rate of 0.34 · 10^{-9} mol h^{-1} can be estimated (based on the slope of 20 μmol h^{-1} L^{-1} shown in the lower panel of Fig. 1c multiplied by the graphite electrode volume of 17 ·10^{-6} L) which for an approximate cyle time of 3.5 h (s. upper panel of Fig. 1c) corresponds to a manganese loss of ≈1.0 · 10^{-9} mol/cycle or ≈0.0017%$_{Mn}$/cycle. This may be compared to a previous study, where the same NMC material was cycled in a NMC/graphite full-cell in the same potential range (3.0/4.6 V) at similar conditions (1C CCCV charge (C/20 cut-off) and 1C discharge vs. 0.5C CCCV charge (C/20 cut-off) and 1C CC discharge in the present study), resulting in a total amount of Mn deposited on the graphite electrode of 0.35%$_{Mn}$ of the total Mn content of the NMC electrode (measured by post-mortem prompt-gamma-activation analysis).[2] If normalized by the number of cycles, the latter value equates to ≈0.0015%$_{Mn}$/cycle, which is in excellent agreement with our XAS based measurements. At potentials above 4.6 V, the manganese dissolution rate equals 17 · 10^{-9} mol h^{-1} (based on the now higher slope of 1000 μmol h^{-1} L^{-1} shown in the lower panel of Fig. 1c multiplied by the graphite electrode volume of 17 ·10^{-6} L), which is ≈50-fold higher than the rate found between 3.0 and 4.6 V.

In order to verify the amount of transition metal deposition on the graphite counter electrode with a second analytical technique, two nominally identical cells were cycled with the same procedure as shown in Figure 1c (upper panel). Directly after the end of the procedure, the graphite electrodes were harvested in the charged state, at the end of the

200 minute hold at 5 V. The copper current collector and glass fiber residue were removed and the graphite coating was immersed in 1 mL 65 %HNO_3 (analytical grade, Sigma Aldrich) for one week. The determination of the manganese, cobalt and nickel concentration in HNO_3 was then carried out by ICP-OES (Mikroanalytisches Labor Pascher, Remagen, Germany). The thus quantified metal content of the graphite electrode –expressed as fraction of the total metal content in the NMC electrode – amounts to 0.165 ± 0.015 % for Mn, 0.125 ± 0.002 % for Co and 0.116 ± 0.002 % for Ni, respectively (the error corresponds to the standard deviation from analyzing the graphite electrode harvested from the two nominally identical cells). For all three metals, the contents determined via *operando* XAS and ICP-OES are consistent within a factor of two (s. above). Note, however, that the trend is inverted, with cobalt showing the highest concentration in the XAS determination and manganese showing the highest concentration in the ICP-OES determination. It is not entirely clear whether the XAS or ICP-OES analysis is more accurate as both techniques contain possible sources of error which are difficult to quantify. One can therefore only conclude that the dissolution rate is in the same order of magnitude for all three transition metals without knowing exactly which metal shows the highest dissolution rate. In comparison, Gallus *et al.*[7] found very similar manganese, cobalt and nickel contents in the electrolyte after storage experiments whereas the post-mortem PGAA analysis by Buchberger et al.[2] found the manganese content to be twice as high as that of cobalt and nickel.

7) Estimation of redox potentials in carbonate based electrolytes

It is not possible to state exact potentials for the expected Mn(II), Co(II) and Ni(II) reduction potential vs. Li/Li^+ because, to the best of our knowledge, there is no consistent data for the redox potentials of these transition metals in carbonate based electrolytes. According to the standard electrode potential series in aqueous electrolyte, the Mn(0)/Mn(II) potential is about 900 mV more negative than the respective values for cobalt and nickel. If the redox potentials are corrected for the different solvation energies in water and ethylene carbonate,[8] the resulting redox potential of Mn(0)/Mn(II) is 690 mV more negative than Ni(0)/Ni(II) and 1100 mV more negative than Co(0)/Co(II). Accordingly, in carbonate based solutions the same trend in redox potentials holds true as in aqueous solutions with manganese being the least noble metal.

8) Mn-K edge spectra on graphite electrode after "conventional" cycling

For a description of the cycling procedure see Section 2 in the supplementary information.

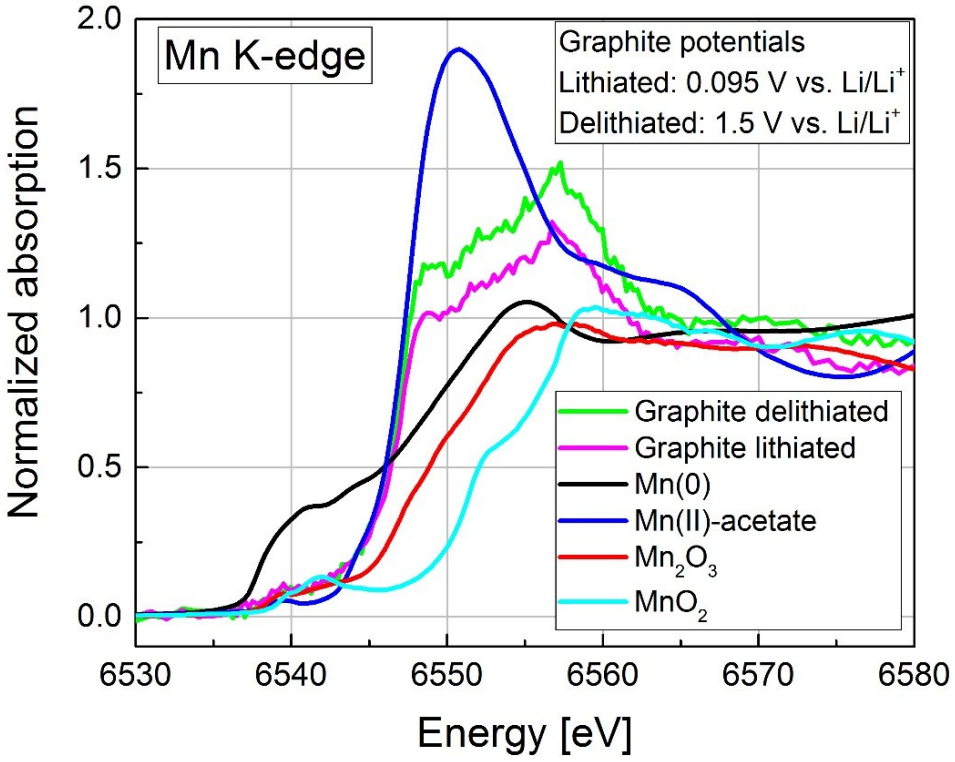

Figure S6 Mn K-edge spectra of reference compounds and *operando* spectra of the graphite electrode either in the lithiated (at 0.095 V vs. Li/Li^+) or delithiated (at 1.5 V vs. Li/Li^+) state. The *operando* spectra were obtained with a Graphite/NMC *operando* XAS cell after 22 "conventional cycles" between 3.0 V and 4.6 V with 1M $LiPF_6$ in EC/EMC as electrolyte.

9) Optical images of lithiated graphite electrodes

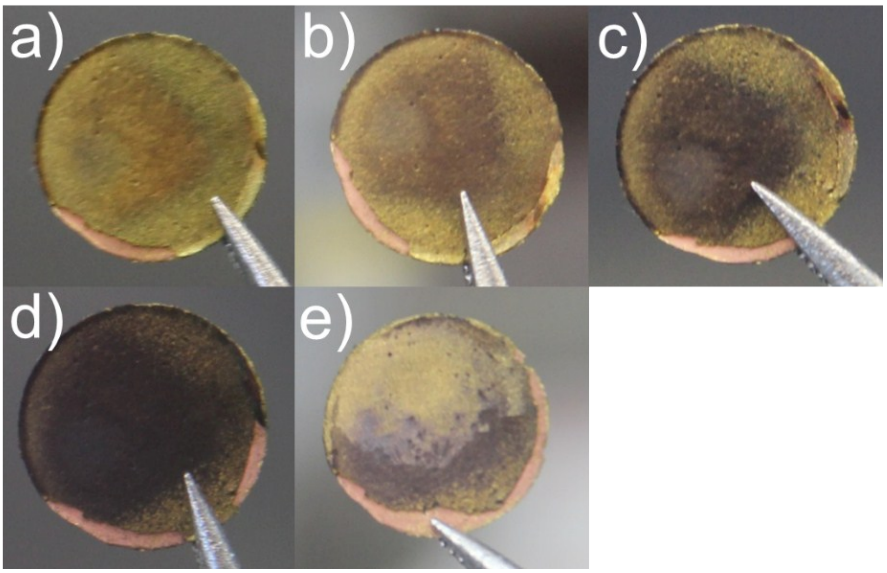

Figure S7 Graphite electrode harvested inside the glove box from Swagelok T-cells after finishing the same procedure which was conducted for the *operando* XAS measurements (s. upper panel of Fig. 1c in the main manuscript. The Images show the top side of the graphite electrode which had faced the NMC electrode during cycling: **a)** directly after harvesting the graphite electrode from the cell inside the glove box, **b)** after drying for 40 minutes in the glove box, **c)** after drying for 80 minutes in the glove box, **d)** after drying for 2 days in the glove box, and, **e)** after scratching off the top layer of the graphite electrode with a scalpel after two days of drying in the glove box.

References

[1] Y. Gorlin, A. Siebel, M. Piana, T. Huthwelker, H. Jha, G. Monsch, F. Kraus, H. A. Gasteiger, M. Tromp, *J. Electrochem. Soc.* **2015**, *162*, A1146–A1155.

[2] I. Buchberger, S. Seidlmayer, A. Pokharel, M. Piana, J. Hattendorff, P. Kudejova, R. Gilles, H. A. Gasteiger, *J. Electrochem. Soc.* **2015**, *162*, A2737–A2746.

[3] B. Ravel, M. Newville, *J. Synchrotron Radiat.* **2005**, *12*, 537–541.

[4] M. Newville, *J. Synchrotron Radiat.* **2001**, *8*, 322–324.

[5] A. Jarry, S. Gottis, Y.-S. Yu, J. Roqué-Rosell, C. Kim, J. Cabana, J. Kerr, R. Kostecki, *J. Am. Chem. Soc.* **2015**, *137*, 3533–3539.

[6] M. Tromp, J. Moulin, G. Reid, J. Evans, *AIP Conf. Proc.* **2007**, *882*, 699–701.

[7] D. R. Gallus, R. Schmitz, R. Wagner, B. Hoffmann, S. Nowak, I. Cekic-Laskovic, R. W. Schmitz, M. Winter, *Electrochim. Acta* **2014**, *134*, 393–398.

[8] Y.-K. Han, K. Lee, S. Kang, Y. S. Huh, H. Lee, *Comput. Mater. Sci.* **2014**, *81*, 548–550.

3.3 In Situ Neutron Diffraction Study

This section presents the article "Aging Behavior of Lithium Iron Phosphate Based 18650-type Cells Studied by *In Situ* Neutron Diffraction" which was submitted in November 2016 and accepted for publication in the peer reviewed Journal *Journal of Power Sources* in January 2017. The article is reproduced within this thesis under the License Number 4117990789961. The publication was presented on international conferences, for example on the 231st Meeting of The Electrochemical Society in New Orleans (USA) in May 2017 (Abstract Number: #318). The permanent weblink to the article is http://www.sciencedirect.com/science/article/pii/S0378775317301441.
This project is carried out in cooperation with a commercial cell producer who provided the 18650 cells and also the electrode active material and electrode sheets as used in the 18650 cells. This is a unique opportunity to study the behavior of commercially produced high quality cells and in addition carry out fundamental studies on the electrode and active material level. The best cells investigated in this study have a relative capacity retention of over 90% after almost 5000 cycles without an excess of electrolyte; such a cell quality cannot be achieved in a university laboratory.
In this study, two sets of identical cells, which only differ in the kind of graphite used as anode active material, are investigated by neutron diffraction and electrochemical characterization. Neutron diffraction experiments were carried out at the SPODI beamline at the neutron source FRMII in four rapid access beamtimes with a measuring time of 6 hours per cell. The molar fractions of different active material phases are determined by Rietveld analysis and systematically compared to the remaining electrochemical capacity. The loss of active lithium is the only reason for capacity fading in all investigated cells. The two different carbons differ both in cyclic and calendaric aging. The different cyclic aging can probably be assigned to partially irreversible lithium plating which is favored by one of the carbons because of its higher tortuosity on an electrode level. The reason for the different cyclic aging is not clear so far.

Author contributions

S.Sc. provided the 18650 cells. N.P., J.W. and S.Se. wrote beamtime proposals. M.M. and O.O. carried out the neutron diffraction experiments. N.P. carried out the Rietveld analysis. J.W. carried out the electrochemical characterization. J.W. and N.P. prepared the manuscript. All authors discussed the data and commented on the results.

Journal of Power Sources 345 (2017) 85–96

Contents lists available at ScienceDirect

Journal of Power Sources

journal homepage: www.elsevier.com/locate/jpowsour

Aging behavior of lithium iron phosphate based 18650-type cells studied by *in situ* neutron diffraction

Neelima Paul [a, *, 1], Johannes Wandt [b, 1], Stefan Seidlmayer [a], Sebastian Schebesta [c], Martin J. Mühlbauer [a, d, e], Oleksandr Dolotko [a], Hubert A. Gasteiger [b], Ralph Gilles [a]

[a] Heinz Maier-Leibnitz Zentrum (MLZ), Technische Universität München, 85747 Garching, Germany
[b] Chair of Technical Electrochemistry, Technische Universität München, 85748 Garching, Germany
[c] VW-VM Forschungsgesellschaft mbH & Co. KG, 73479 Ellwangen, Germany
[d] Institute for Applied Materials (IAM), Karlsruhe Institute of Technology (KIT), Hermann-von-Helmholtz-Platz 1, 76344 Eggenstein-Leopoldshafen, Germany
[e] Helmholtz-Institute Ulm for Electrochemical Energy Storage (HIU), P.O. Box, 76021 Karlsruhe, Germany

HIGHLIGHTS

- Aging in MCMB/LFP and NC/LFP cells was investigated by neutron diffraction.
- NC/LFP cell lost capacity on storage whereas the MCMB/LFP cell showed no loss.
- After 4750 cycles, the relative capacity losses were much lower for the MCMB/LFP cell.
- Entire capacity loss upon formation, cycling and storage is due to active lithium loss.
- Structural degradation and active material isolation could be excluded.

ARTICLE INFO

Article history:
Received 12 November 2016
Received in revised form
13 January 2017
Accepted 31 January 2017

Keywords:
Lithium-ion batteries
Neutron diffraction
In-situ studies
Aging
Graphite
Lithium iron phosphate

ABSTRACT

The aging behavior of commercially produced 18650-type Li-ion cells consisting of a lithium iron phosphate (LFP) based cathode and a graphite anode based on either mesocarbon microbeads (MCMB) or needle coke (NC) is studied by *in situ* neutron diffraction and standard electrochemical techniques. While the MCMB cells showed an excellent cycle life with only 8% relative capacity loss (i.e., referenced to the capacity after formation) after 4750 cycles and showed no capacity loss on storage for two years, the needle coke cells suffered a 23% relative capacity loss after cycling and a 11% loss after storage. Based on a combination of neutron diffraction and electrochemical characterization, it is shown that the entire capacity loss for both cell types is dominated by the loss of active lithium; no other aging mechanisms like structural degradation of anode or cathode active materials or deactivation of active material could be found, highlighting the high structural stability of the active material and the excellent quality of the investigated cells.

© 2017 Elsevier B.V. All rights reserved.

1. Introduction

Since their commercialization by Sony in 1991, Li-ion batteries have become the main power source for portable consumer electronics. Due to their constant improvement in terms of cost, energy density and lifetime [1,2], Li-ion batteries have also started spreading into new markets like hybrid electric (HEV) and electric vehicles (EV) or grid storage within the last couple of years [3,4]. To be cost competitive with other energy storage technologies, the lifetime of Li-ion cells is a critical value: while a life time of 2–3 years is sufficient for most consumer electronic applications [5], a lifetime of 15 years and cycle life over 1000 charge/discharge cycles are required for battery electric vehicles (BEVs) [6]; even longer cycle life of over 5.000–10.000 charge/discharge cycles is required for grid storage applications [7]. In order to reach these targets, a detailed understanding of the undesired side reactions contributing to capacity fading is mandatory. Recently, a broad variety of analytical techniques has been used to unravel the underlying

* Corresponding author.
E-mail address: Neelima.Paul@frm2.tum.de (N. Paul).
[1] Authors N.P and J.W contributed equally to this work.

http://dx.doi.org/10.1016/j.jpowsour.2017.01.134
0378-7753/© 2017 Elsevier B.V. All rights reserved.

chemical, physical and mechanical processes taking place during charge, discharge (cyclic aging) and storage (calendar aging) of Li-ion batteries [8]. For many of these analytical techniques, *in situ*/*in operando* setups have been developed which offer several advantages in comparison to *ex-situ* analysis: i) enabling the detection of unstable reaction intermediates [9] or phases [10], ii) avoiding the risk of altering the sample, e.g., the state of charge or the oxidation state, during sample preparation [11], and iii) offering the possibility to continue with cell cycling following the analysis. Most spectroscopy and microscopy based *in situ*/*in operando* techniques require special cell designs which are transparent for either electromagnetic waves, magnetic fields, and/or electrons [12–15], thus rendering them unsuitable for the investigation of commercial Li-ion cells with generally impenetrable metal casing/housing. There are, however, degradation mechanisms which can only be studied in large-format cells, e.g., effects related to current collector tab positioning [16], cell geometry [17], or inhomogeneous heat distribution [18,19]. A powerful analytical technique for the *in situ*/*in operando* study of commercial Li-ion cells is neutron diffraction. Rietveld analysis of neutron diffractograms can be used to determine the atomic structure, lattice parameters, and particle size of crystalline anode (e.g. graphite) and cathode active materials (e.g. spinels, layered metal oxides, or phospho-olivines). In this respect, an important advantage of neutron diffraction over X-ray diffraction (XRD) is the higher penetration depth of neutrons in comparison to X-rays, making neutron diffraction truly bulk sensitive and suitable for large cell formats, whereas XRD is only suitable for thin samples [20]. Furthermore, neutron diffraction shows a much higher sensitivity for light elements like lithium than XRD.

Only few *in situ*/*in operando* neutron diffraction studies on commercial Li-ion cells have been published so far, typically based on cells with graphite anodes and a variety of cathode active materials like $LiCoO_2$ (LCO) [16,21–24], $LiMn_2O_4$ (LMO) [25], $LiMn_{0.33}Co_{0.33}Ni_{0.33}O_2$ (NMC) [10,16,26,27], and $LiFePO_4$ (LFP) [16,28–30]. These have focused on topics like structural changes within the cathode active material [22,26], metal doping [29,30], local inhomogeneities [16,25,31], or lithium plating on graphite [27]. While there are neutron diffraction studies on cell aging for commercial graphite/LCO cells [23,24], to the best of our knowledge no such data is available for graphite/LFP cells.

In this work, we carry out a detailed investigation of the aging mechanism in commercially produced 18650-type cells with a graphite/LFP cell chemistry. A total of four cells are investigated in this study which differ either in the type of graphite used as anode active material – mesocarbon microbeads (MCMB) versus needle coke (NC) - or in the cell history. One cell of each graphite anode material was cycled for 4750 cycles at a C-rate of 1 h^{-1} at 23 °C and one cell was stored for about two years at 20% state-of-charge (SOC) at 23 °C. For all four cells we systematically compare the electrochemically determined remaining discharge capacity with the active lithium inventory derived from *in situ* neutron diffraction. With this approach it is possible to differentiate several aging mechanisms, namely i) active lithium loss, ii) particle isolation, further on referred to as particle deactivation, due to loss of ionic and/or electronic contact, and, iii) destruction of bulk electrode material (metal dissolution or irreversible phase transformation). Loss of active lithium has frequently been described to occur in Li-ion cells and may have several reasons, for example ongoing SEI formation or irreversible Li-plating [32,33]. Active lithium loss can be identified if the loss of active lithium inventory measured by neutron diffraction corresponds to the electrochemically determined discharge capacity loss. The second main capacity fading mechanism is particle deactivation, resulting in an effective loss of active material. This can either be caused by the loss of ionic contact due to gassing [34], drying out [35], or pore blocking [36] or by the loss of electronic contact due to particle delamination from the current collector [10,18] or particle cracking [37]. Particle deactivation has been observed in previous studies in aged commercial Li-ion cells by the presence of lithiated "uncharged" cathode active material [25] and/or of totally unlithiated graphite anode active material in charged cells [23,25]. The third main capacity fading mechanism is the chemical destruction of electrode active material, which could either be due to an irreversible phase transformation or to transition metal dissolution. Examples of the former are the conversion of layered LCO to spinel LCO [22] or the destruction of the spinel structure of $LiMn_2O_4$ [25] upon cycling. Phase transformations can easily be recognized by the appearance of new peaks in the neutron diffractograms which cannot be assigned to the original electrode materials. Transition metal dissolution has frequently been linked to capacity fading of Li-ion cells. It has been reported that under certain circumstances 3–4% of the iron can dissolve from LFP active material which would cause a direct and stoichiometric capacity loss [38]. If cathode active material loss due to transition metal dissolution is occurring to a significant extent, the observed lithium inventory would stay constant while the electrochemically determined remaining capacity would decrease. The dissolution of transition metals from the cathode can also indirectly contribute to the capacity fading of Li-ion cells by catalyzing electrolyte reduction at the graphite anode, causing a loss of active lithium and an increase in cell impedance [39]. As this is a catalytic process, already a very small amount of transition metal dissolution, whose corresponding direct stoichiometric capacity loss would be negligible, can cause a substantial capacity loss [40]. Note that in the framework of this study, the transition metal triggered capacity loss on the anode side would be observed as increased active lithium loss, rather than constituting an independent capacity loss mechanism.

2. Experimental

2.1. Cell information

The cylindrical 18650-type graphite/LFP prototype cells were provided by the battery producer (VW-VM Forschungsgesellschaft mbH & Co. KG, a joint venture between Volkswagen and VARTA Microbattery GmbH). Each cell consisted of a LFP cathode, an organic carbonate based electrolyte with $LiPF_6$ as conducting salt, a standard polyolefin separator, and a graphite anode made of either mesocarbon microbeads or needle coke. In both types of cells identical LFP cathodes were used. The cathode consisted of 90 wt% active material, 5 wt% binder and 5 wt% conductive additive (3 wt% graphite and 2 wt% SuperC) and was coated on both sides of an Al-foil current collector; all cells contained a total of 10.75 g LFP (2.4 wt % carbon coating), resulting in a theoretical cell capacity Q_{theo} of 1.678 Ah (based on an achievable capacity of 160 mAh g_{LFP}^{-1}, see Supporting Information). The amount of anode active material was adjusted to obtain an anode/cathode capacity ratio of 1.25 considering the specific capacities of MCMB (330 mA g^{-1}) and needle coke (349 mAh g^{-1}). The anodes consisted of 97 wt% of graphite active material, 2.5 wt% binder and 0.5 wt% conductive additive coated on both sides of a Cu-foil current collector. The BET surface area of the pure powders was 2.4 m^2 g^{-1} for MCMB and 1.9 m^2 g^{-1} for needle coke.

After the cell assembly, all cells were subjected to a proprietary formation procedure and the thus obtained preformed cells were then either stored for two years (at 20% SOC and 23 °C) or cycled for 4750 cycles (at a C rate of 1 h^{-1} at 23 °C) by the battery producer. Of each cell type, three identical cells were cycled. The observed discharge capacities for the three identical cells were always within 0.4% for both cell types, exemplifying the very good reproducibility

of the commercially produced cells. After long term cycling/storage, four cells (cycled vs. stored and MCMB vs. needle coke) were examined by neutron diffraction and subjected to further electrochemical characterization like impedance spectroscopy and cycling at different C-rates. The total time span between cell assembly and the here described neutron diffraction and electrochemical experiments was about 24 months. No neutron diffraction analysis was conducted directly after cell formation, as this study was initiated only after the cycling/storage experiments had been completed. Fig. 1 gives an overview of the chronological sequence of electrochemical and neutron diffraction experiments as well as the nomenclature used within this work to refer to the different points in time at which the various tests were conducted. The term "pristine cell" refers to the cells directly after assembly before formation (with the theoretical capacity of 1.678 Ah), whereas after formation the cells are called "preformed cell". This distinction is crucial because the major capacity fading already occurs during the formation cycles, as discussed later. After the long term cycling/storage tests, the cells are referred to as "cycled cells" and "stored cells", respectively.

2.2. Neutron diffraction

The neutron powder diffractograms were measured in Debye-Scherrer geometry under ambient conditions at the high-resolution powder diffractometer SPODI, MLZ Garching [41]. Neutrons with wavelength of $\lambda = 1.5483$ Å from the Ge (551) monochromator were incident on the cell with a rectangular illumination cross section of 40 × 30 mm^2. The scattered neutrons were collected by a neutron detector array of 80 vertical position sensitive detectors [41,42]. The cells were rotated around their cylindrical axis during the measurement to reduce texture effects in the diffraction pattern. Five diffractograms were measured for each cell with an acquisition time of about 1 h 10 min each, depending on monitor rate/neutron flux. Therefore, the total integration time for the averaged plotted diffractograms for each cell was approximately 6 h. The edges of the cell (about 10 mm) at the top and bottom were not illuminated by the neutron beam. Thus, averaged information from the central part of the cylindrical cell (central 45 mm of total 65 mm height) is obtained from these diffractograms. Pictures of the powder diffractometer, the mounted cells as well as a schematic of the neutron diffraction set-up can be seen in Fig. 2. Multiphase, sequential Rietveld refinement of structural models for the neutron diffraction data has been carried out with the FullProf software package [43]. The instrumental resolution function was determined with a $Na_2Ca_3Al_2F_{14}$ reference material and used to calculate half widths of the reflections. A Thompson-Cox-Hastings pseudo-Voigt function was used to describe the peak profile shape. A linear interpolation between selected data points in non-overlapping regions was used to fit the background. For the steel housing and the current collectors, a structure independent (Le Bail) profile fit was used due to the strong preferred orientations of crystallites in these materials. This was done in order to obtain a better quality multi-phase pattern refinement of the neutron diffractogram.

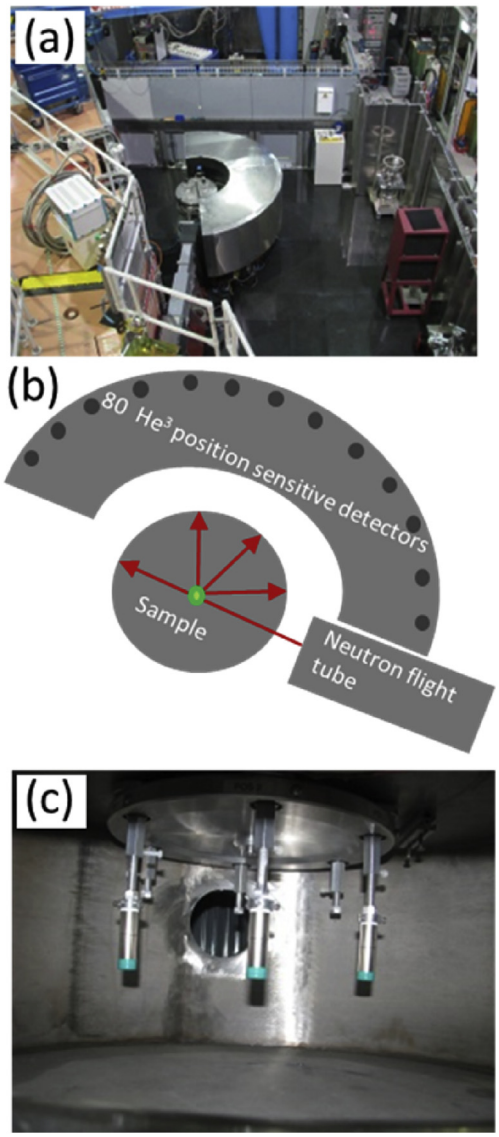

Fig. 2. a) The neutron diffractometer SPODI with the Ge (551) monochromator and the detector array around the sample chamber, **b)** schematic representation of the experimental set-up, and, **c)** the positioning of the cylindrical 18650-type Li-ion cells inside the sample changer.

2.3. Electrochemical techniques

The formation procedure of the cells was carried out by the battery producer; details regarding the formation procedure are

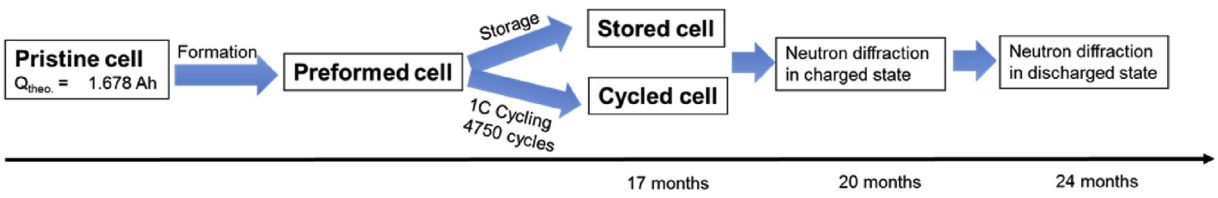

Fig. 1. Schematic showing the chronological sequence of electrochemical and neutron diffraction experiments as well as the nomenclature used to refer to the different conditions of the cells.

proprietary and are thus not being disclosed. After formation, the MCMB cells had a reversible capacity of 1.230 Ah and the needle coke cells of 1.150 Ah; all C-rates used within this work relate to these capacities of the preformed cells. Long term cycling (ca. 4750 cycles) at 23 °C was performed by the battery producer with a CCCV charge to 3.6 V (constant current (CC) charging at 1C to 3.6 V, followed by a constant voltage (CV) hold at 3.6 V until a current corresponding to C/20 is reached) and a CC discharge to 2.0 V with a rate of 1C using a Maccor battery tester. Prior to the neutron diffraction experiments in the charged state, the cells were charged with the above described cycling procedure; on the other hand, prior to neutron diffraction experiments in the discharged state, the cells were discharged with a C/5 rate followed by a CV hold at 2.0 V (with a C/20 cut-off) in order to ensure that the cells are fully discharged. Potentiostatic electrochemical impedance spectroscopy (PEIS) was carried out with a 5 mV perturbation amplitude in the frequency range from 300 kHz to 100 mHz on fully charged cells. Impedance spectra were fitted with the EC-Lab software package (Biologic, France) to determine high frequency and charge transfer resistances. Charging and discharging before the neutron diffraction experiments and the impedance spectroscopy was carried out with a Biologic VMP3 potentiostat.

2.4. Morphology of MCMB and needle coke

The scanning electron microscopy (SEM) images of the pristine MCMB and NC powder were recorded on a JEOL JCM-6000 (secondary electron imaging, 15 kV accelerating voltage). The MCMB powder, shown in Fig. 3a and b, consists of spherical particles with an average particle diameter of approximately 10 μm and the surface of these particles shows significant roughness in the submicrometer range. In contrast, the needle coke powder shown in Fig. 3c and d, consists of anisotropic flake shaped particles with a larger particle size, broader size distribution and a rather smooth particle surface in comparison to the MCMB.

3. Results

3.1. Electrochemical characterization

Table 1 shows the absolute discharge capacities measured at a 1C rate and normalized capacities with respect to the pristine (Q_{dis}/Q_{theo}) and preformed capacities ($Q_{dis}/Q_{preformed}$) for the MCMB and NC cells in their preformed, stored and cycled states, whereby Q_{theo} = 1.678 Ah is based on the theoretical LFP capacity of 160 mAh g^{-1}_{LFP} as previously described.

Fig. 4a shows the relative change of the discharge capacities of the graphite/LFP cells as a function of time and cycle number (CC charge at 1C with a CV hold at 3.6 V until a C/20 cut-off and 1C discharge to 2.0 V at 23 °C), normalized by the discharge capacity of the preformed cells (1.230 Ah for MCMB and 1.150 Ah for the NC; see Table 1). The cycled MCMB cell (light green line) shows a linear drop in capacity versus cycle number, with a relative capacity loss of 8.2% over 4750 cycles; in contrast, the capacity fading rate for the needle coke cell (light blue line) is substantially higher during the initial 1000 cycles before gradually leveling off to a capacity fading rate which is similar to the MCMB cells, resulting in an overall relative capacity loss of 23.1% over 4750 cycles. After two years of

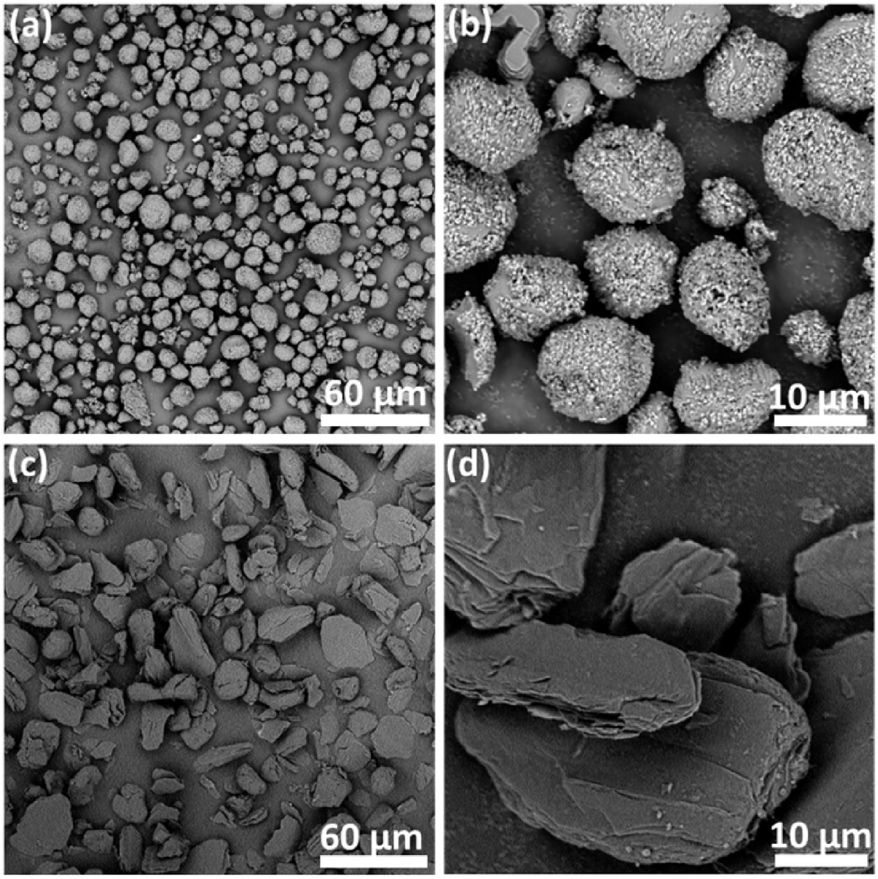

Fig. 3. **a)** and **b)** show SEM images of the pristine MCMB powder, whereas **c)** and **d)** show SEM images of the pristine needle coke powder at two different magnifications.

Table 1
Absolute discharge capacities (Ah) measured at a 1C rate (Q_{dis}; 2nd column), as well as the capacities normalized either to the theoretical capacity (Q_{theo} = 1.678 Ah) of the LFP capacity-limited cells (Q_{dis}/Q_{theo}; 3rd column) or to the capacity after formation ($Q_{dis}/Q_{preformed}$; 4th column). The 5th column shows capacity loss after storage or cycling in comparison to the capacity of the preformed cell.

State of cells	Q_{dis} [Ah]	Q_{dis}/Q_{theo} [%]	$Q_{dis}/Q_{preformed}$ [%]	Relative Q-change [%]
Preformed MCMB	1.230	73.3	≡100.0	
Stored MCMB	1.249	74.4	101.5	+1.5
Cycled MCMB	1.130	67.3	91.8	−8.2
Preformed NC	1.150	68.5	≡100.0	
Stored NC	1.025	61.1	89.1	−10.8
Cycled NC	0.884	52.8	76.9	−23.1

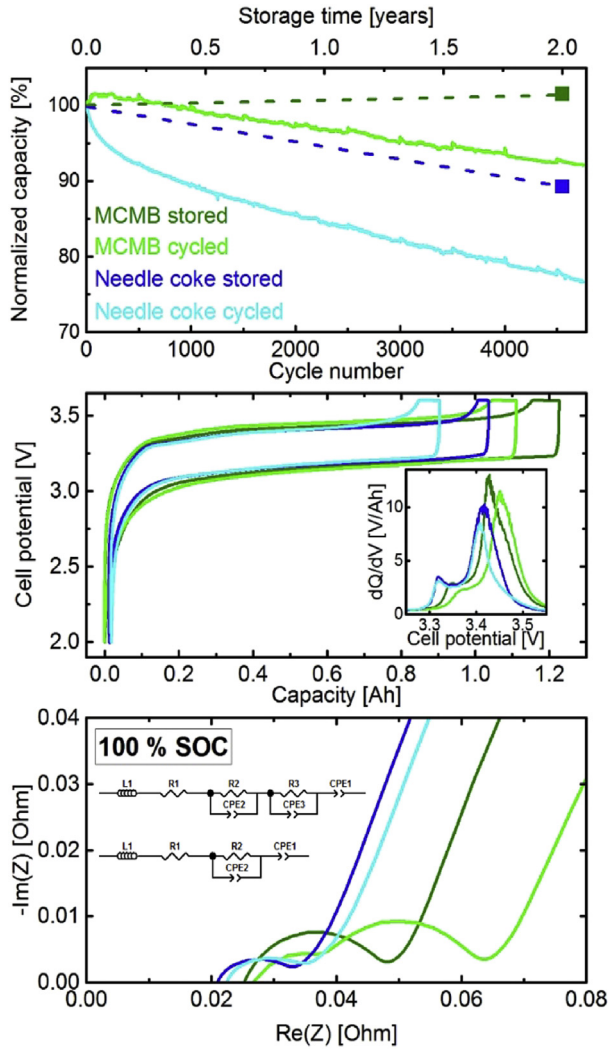

Fig. 4. a) solid lines: Relative discharge capacities (referenced to the capacity after formation; see Table 1) of the 18650 graphite/LFP cells at 23 °C as a function of cycle number (CC charge at 1C to 3.6 V with a CV hold at 3.6 V until a C/20 current cut-off and 1C CC discharge to 2.0 V); solid symbols: relative capacity loss after storage at 20% SOC and 23 °C for 2 years (the dashed lines are a guide to the eye). **b)** Potential profiles recorded with a 1C CCCV charge/1C CC discharge rate at 23 °C after the long term storage or cycling experiments; the inset shows the corresponding dQ/dV plot for the charging curves; **c)** PEIS of the long term stored and cycled cells acquired at 100% SOC (5 mV perturbation at frequencies between 300 kHz and 0.1 Hz) and corresponding equivalent circuits.

storage at 20% SOC and 23 °C for 2 years, the relative capacity of the MCMB cell increased by 1.5% (dark green square), whereas it decreased by 10.8% for the needle coke cell (dark blue square). The potential profiles of the stored and cycled cells (Fig. 4b) are typical for LFP/graphite cells and show features which can be assigned to the staging behavior of the graphite anode. The polarization is slightly higher for the two MCMB cells than for the two needle coke cells. This is more apparent in the dQ/dV plot of these data (inset Fig. 4b), which shows that there is a cycling induced polarization increase (comparing the cycled vs. the stored cell) of approximately 23 mV for the MCMB anode material, whereas there is no noticeable difference in the polarization for the needle coke cells.

Potentiostatic electrochemical impedance spectroscopy (PEIS) data together with the equivalent circuits used for fitting the PEIS data are depicted in Fig. 4c. The stored MCMB cell and both needle coke cells were fitted with one R/Q element (as shown in the lower equivalent circuit), while the cycled MCMB cell clearly displayed two semi-circles in the Nyquist plot and was thus fitted with two R/Q elements (as shown in the upper equivalent circuit). All four cells show similar high frequency resistances of about 20 mΩ and a first semi-circle which can be assigned to predominantly reflect the charge-transfer resistance of the graphite anode (as shown recently [44], the semi-circle in the full-cell impedance of an LFP/graphite cell mostly derives from the graphite anode). This apparent charge-transfer resistance is ≈ 26 mΩ and ≈29 mΩ for the stored and cycled MCMB cells versus only ≈14 mΩ and ≈15 mΩ for the stored and cycled needle coke cells. The higher charge transfer resistance of the MCMB cells in comparison to the needle coke cells is in line with the higher polarization observed in the potential profiles (Fig. 4b). The cycled MCMB cell also shows an additional smaller semicircle with a resistance of ≈16 mΩ which is not present in the stored MCMB cell. Based on its diameter (16 mΩ) and the frequency of its maximum (2710 Hz), the capacitance of this additional semi-circle equals 3700 μF. Considering a typical double layer capacitance in the order of 10 μF cm^{-2}, an effective interfacial area of 370 cm^2 can be calculated, which is in good agreement with the geometric area of the current collector foils in a 18650 cell but significantly smaller than the electrode material surface area ($140 \cdot 10^3$ cm^2 for a graphite mass of 7 g and a BET area of 2 m^2 g^{-1}) [45,46]. Accordingly, the additional semi-circle in the cycled MCMB cell can most likely be assigned to an increased contact resistance between the active material and the current collector foil. For the cycled MCMB cell this additional resistance of ≈16 mΩ corresponds to an additional IR drop of ≈20 mV at a current of 1.230 A (= 1C rate), which is very close to the observed polarization increase of 23 mV for the cycled MCMB cell in comparison to the stored MCMB cell (Fig. 4b).

Furthermore, to test whether the slight polarization increases affect the discharge capacities, all cells were cycled with a C/50 rate between 2.0 and 3.6 V (data not shown). For all four cells, the discharge capacities in the C/50 cycle are identical with the 1C discharge capacities within 5%, implying that resistive effects (often associated with capacity roll-over fading) [36] do not contribute to capacity fading.

3.2. Neutron diffraction

In situ neutron diffraction is used to obtain detailed structural information about the anode and cathode materials without opening the cell. It has to be noted, however, that averaged information from the central part of the cylindrical cell (central 45 mm of total 65 mm height) is obtained. From the neutron diffraction data it is possible to identify crystalline phases in the Li-ion cells and also to calculate their respective weight fractions and lattice parameters. A high background is observed for all cells due to the incoherent scattering of neutrons by the hydrogen atoms present in the organic electrolyte and separator. This background has no angularly dependance and is similar for both cells irrespective of their state of charge.

3.2.1. Discharged cell

Neutron diffraction data for the four different cells in their discharged state is presented in Fig. 5, along with their Rietveld refinements. The steel casing as well as the Al and Cu current collectors show their respective reflections with similar intensities in all four cells. Reflections of $LiFePO_4$ and graphite, as expected for a lithiated cathode and a delithiated anode, are also present in all four cells. However, reflections of $FePO_4$ are also present in all cells, implying that a significant portion of $FePO_4$ in the cathode has not been converted to $LiFePO_4$, even after fully discharging the cell. From Rietveld refinement of the neutron diffraction data shown in Fig. 5, weight fractions of $LiFePO_4$ and $FePO_4$ were obtained and converted into their molar ratios: LFP/FP molar ratios are 75:25 for the stored MCMB cell, 67:33 for the cycled MCMB cell, 58:42 for the stored needle coke cell, and 55:45 for the cycled needle coke cell. In all cells, the total absence of peaks belonging to lithiated graphite (Li_xC_6 with $x \neq 0$) is an indication for the complete extraction of lithium from the anode during discharging. This clearly proves the absence of regions with inactive lithiated graphite (due to particle isolation or electrode delamination, etc.).

It should be noted that due to the extremely weak and multiple reflections of the $LiFePO_4$ and $FePO_4$ phases (see Fig. 5c and f), the purpose of the refinement was not to determine lattice parameters with high accuracy, but rather to calculate and compare the molar fractions of the $LiFePO_4$ and $FePO_4$ phases in the discharged state of the stored and cycled cells. Still, the structural stability of the LFP cathode material is confirmed by the constant and fixed angular position of the $LiFePO_4$ (221) reflections, as exemplified in Fig. 5c and f. Within the accuracy of the experiment, the lattice parameters of cathode ($LiFePO_4$ and $FePO_4$) remain unchanged for all cells. We take the maximum error value obtained from the fitting as the general error value for all lattice parameters displayed in Tables 2 and 3.

For the MCMB and needle coke graphites present in the discharged cells it is possible to determine lattice parameters *a* and *c* as shown in Table 2. Both lattice parameters are identical for the stored and cycled MCMB cell. The cycled needle coke cell shows a

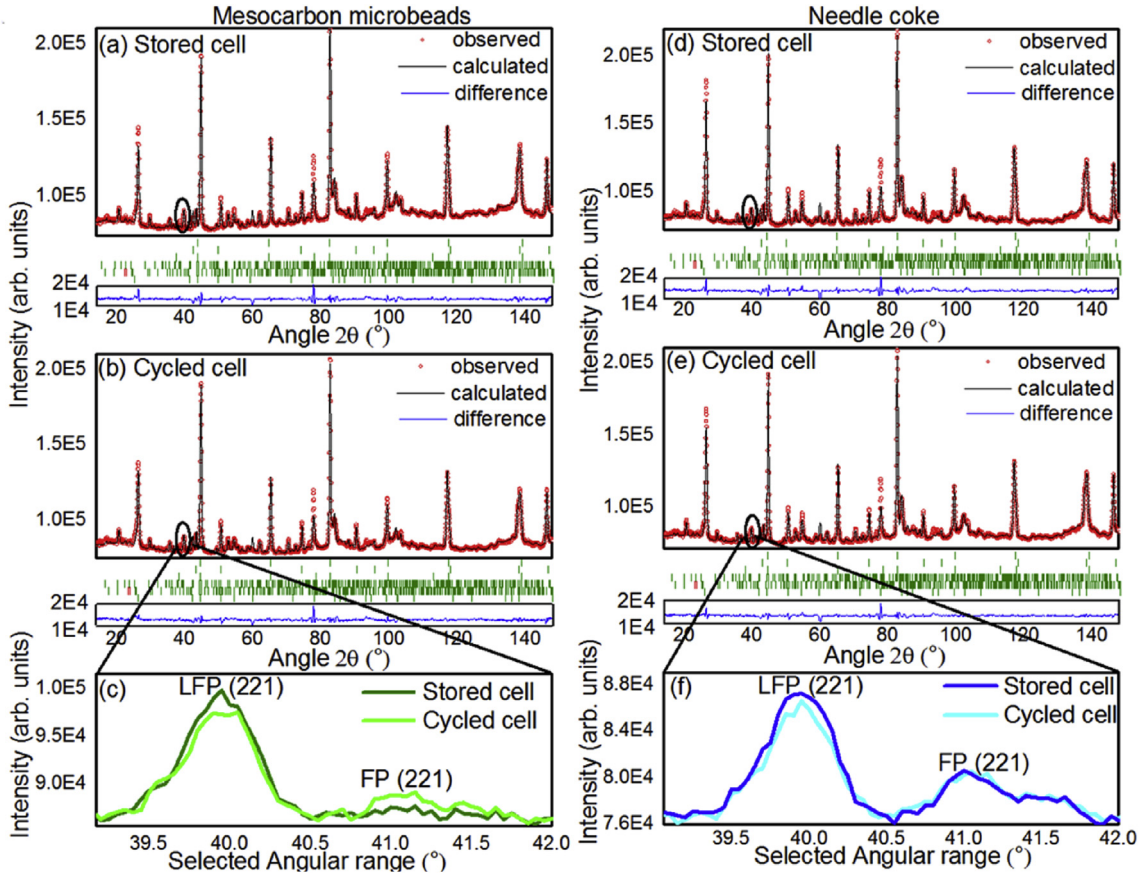

Fig. 5. Neutron diffraction data with full angular range of the graphite/LFP cells measured in the fully discharged state (discharged at a C/5 CC rate to 2.0 V with a CV hold at 2.0 V to a C/20 cut-off). **a)** Stored MCMB cell, **b)** cycled MCMB cell, **d)** stored needle coke cell, **e)** cycled needle coke cell. Experimental data are shown in red circles along with their Rietveld refinements (black line). The blue lines mark the difference between data and fit. Vertical bars (green) above the blue line indicate Bragg reflections corresponding to the crystalline phases in the cell (from top to bottom: Fe, Cu, Al, $LiFePO_4$, $FePO_4$, and graphite). **c)** and **f)** Selected angular range of neutron diffraction data focusing on the relatively weak LFP (221) reflection and the even weaker FP (221) reflection for the MCMB cells (c) and needle coke cells (f) (these are the only reflections from the cathode active material which do not overlap with reflections from other components). (For interpretation of the references to colour in this figure legend, the reader is referred to the web version of this article.)

Table 2
Lattice parameters for MCMB and needle coke cells as determined by Rietveld refinement of the neutron diffractograms of the discharged cells (data from Fig. 5). Lattice parameters of conventional LCO/graphite cell are also shown for comparison.

State of cells	Graphite- *a* [Å]	Graphite - *c* [Å]
Stored MCMB	2.462 ± 0.004	6.756 ± 0.004
Cycled MCMB	2.462 ± 0.004	6.756 ± 0.004
Stored Needle coke	2.462 ± 0.004	6.736 ± 0.004
Cycled Needle coke	2.462 ± 0.004	6.729 ± 0.004
Graphite literature ref. [23]	2.463	6.722

Table 3
Lattice parameters determined by Rietveld refinement of the neutron diffractograms of the charged cells by fitting the data according to the structural model of the LiC_{12} phase. Literature values corresponding to the LiC_{12} phase in LCO/graphite cells are shown for comparison.

State of cells	$LiC_{12} - a$ [Å]	$LiC_{12} - c$ [Å]
Stored MCMB	4.294 ± 0.004	7.074 ± 0.004
Cycled MCMB	4.293 ± 0.004	7.070 ± 0.004
Stored Needle coke	4.295 ± 0.004	7.043 ± 0.004
Cycled Needle coke	4.285 ± 0.004	7.037 ± 0.004
Lithiated graphite - literature ref. [23]	4.294 (fresh and fatigued)	7.034 (fresh)/7.038 (fatigued)

slightly reduced lattice parameter *c* in comparison to the stored cell, the reason of which is not clear. In contrast, an earlier neutron diffraction study found a slight increase of the lattice parameter for a cycled graphite anode [23]. A comparatively larger *c* parameter for the MCMB based cells in comparison to that in the needle coke and conventional graphite based cells is also observed in the X-ray diffraction pattern of their pristine powders (not shown here).

3.2.2. Charged cell

In the charged state, the cathode is delithiated, whereas the anode is lithiated. The diffraction data of the four cells in the charged state are shown in Fig. 6 along with their Rietveld refinements. In the stored and cycled MCMB cells, reflections of $FePO_4$, LiC_6, and LiC_{12} are clearly visible. From Rietveld refinement, weight fractions of LiC_6 and LiC_{12} were obtained and converted into their molar ratios: LiC_6/LiC_{12} molar ratios are 23:77 for the stored MCMB cell and 12:88 for the cycled MCMB cell. In the two needle coke cells, both $FePO_4$ and LiC_{12} phases are present, whereas the LiC_6 reflections are very weak in the stored and almost absent in the cycled needle coke cell. The different intensities of the LiC_6 phase can be rationalized based on the remaining capacities of the respective cells: LiC_6 corresponds to a $SOC_{graphite}$ of 100% and LiC_{12} to a $SOC_{graphite}$ of 50%; however, when considering the anode/cathode balancing factor of 1.25, the complete LiC_{12} phase would correspond to an SOC of the cell of $SOC_{cell} = 62.5\%$,. Accordingly, only at cell capacities above 62.5% referenced to the theoretical cell capacity one would expect to observe the formation of the LiC_6 phase (together with the LiC_{12} phase).

A comparison with Table 1 (3rd column) thus suggests that the LiC_6 phase should be present in the charged state in the stored and cycled MCMB cells (Q_{dis}/Q_{theo} of 74.4% and 67.3%, respectively), as indeed is demonstrated by the neutron diffraction data shown in Fig. 6c. On the other hand, the low relative capacities observed in the charged state of the stored and cycled needle coke cells (Q_{dis}/Q_{theo} of 61.1% and 52.8%, respectively) should not allow the formation of the LiC_6 phase, which again is confirmed by the neutron diffraction data shown in Fig. 6f. By the same token, at cell capacities below 62.5% one would expect a mixture of LiC_{12} and lithiated graphite of the general composition LiC_x, with $x > 12$ (e.g., LiC_{18} or LiC_{24}). The transition from LiC_6 to LiC_{12} is a two-phase mechanism resulting in two clearly separated peaks at $2\theta = 24.2°$ and $2\theta = 25.3°$ in the neutron diffractograms, as clearly observed for the MCMB cells in Fig. 6c. The mechanism of the transition from LiC_{12} to lower lithiation degrees (e.g., LiC_{18}, LiC_{24}) is more complicated, and it is still controversially discussed whether it is a combination of several sequential two-phase transitions or rather a continuous single phase mechanism [47,48]. Independent of the underlying mechanism, the further delithiation of LiC_{12} causes a continuous shift of the corresponding reflection to higher angular values, as observed for the cycled needle coke cell (light blue line in Fig. 6f). Due to this more complicated mechanism, it is not possible to extract molar ratios of the different lithiated graphite phases from neutron diffraction for cells in which the LiC_6 phase is not present, as is the case for the cycled and stored needle coke cells.

In all four cells, the absence of any $LiFePO_4$ peaks within the accuracy of the neutron experiment is an indication for the complete extraction of lithium from the cathode during charging. In addition, all charged cells show a small peak at $2\theta = 26.5°$, which has the same intensity in all four charged cells and an angular position which is overlapping with the C (002) signal of graphite. This peak is not observed/resolved in the discharged state of the cells, because of the high intensity of the C (002) reflection from the delitiated graphite active material. As the relative intensity of this carbon signal is identical for all cells and as its weight fraction matches the amount of conductive carbon present in the cathode (SuperC), one can most likely assign this signal to the conductive carbon in the cathode, which shows negligible lithium intercalation and thus remains unlithiated even in the charged cells. One may note that the shoulder at $2\theta = 25.9°$ is due to the $FePO_4$ (111) reflection and not due to a LiC_x phase with $x > 12$. Accordingly, the entire MCMB and needle coke present in the anode is lithiated during charge, thus ruling out the presence of electrochemically inactive anode material.

Table 3 shows the lattice parameters of the LiC_{12} phase as determined by Rietveld refinement of the neutron diffraction data shown in Fig. 6 according to the structural model of the LiC_{12} phase. For the MCMB cells there is no difference in lattice parameters between the cycled and the stored cell, confirming the structural stability of the MCMB graphite upon cycling. The reduction in the lattice parameter for the cycled needle coke cell as compared to the stored cell is probably due to the onset of its transition from the LiC_{12} phase to a phase with a lower lithiation degree as discussed above.

3.3. Active lithium content from $Q_{discharge}$, the $LiFePO_4/FePO_4$ ratio, and the LiC_6/LiC_{12} ratio

As described in the previous section, the Rietveld refinement of the neutron diffraction data gives the molar ratios of $LiFePO_4/FePO_4$ (LFP/FP) for the discharged cells and of LiC_6/LiC_{12} for the charged cells (both after cycling and after storage), which are summarized in Table 4. Neutron diffraction experiments could not be carried out for the cells directly after formation (i.e., the preformed cells in Fig. 1), because the formation was done several years prior to the here described neutron diffraction analysis. It is possible to use the molar ratios of LFP/FP and LiC_6/LiC_{12} to determine the active lithium inventory (*LI*). The active lithium inventory equals the amount of electrochemically active lithium, which is either contained in the LFP cathode when the cell is discharged or in the lithiated graphite anode (as phases of LiC_6, LiC_{12}, ect.) when the cell is charged. The LI can best be expressed as percentage of the initial amount of active lithium, which is introduced into the pristine cell by the LFP cathode.

The thus defined active lithium inventory derived from the LFP/FP ratio of the discharged cells is denoted as $LI_{LFP/FP}$ and simply

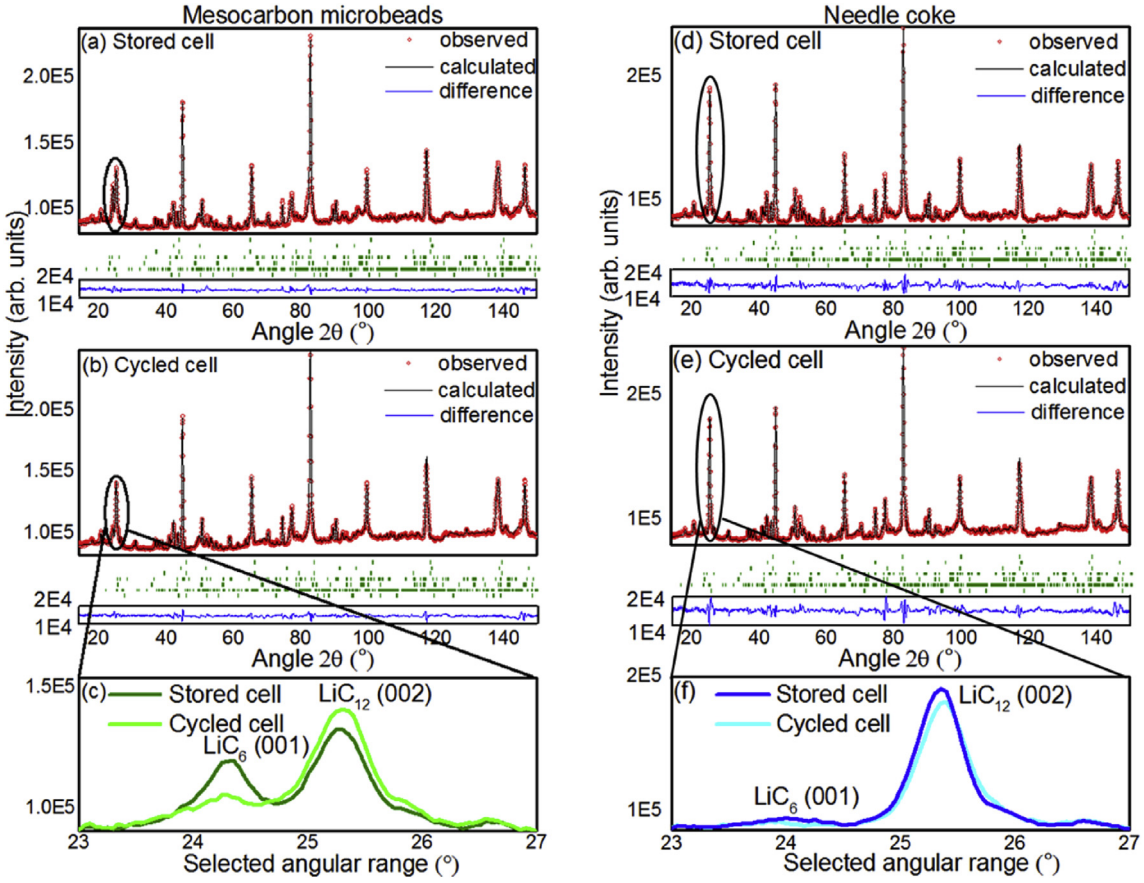

Fig. 6. Neutron diffraction data with full angular range of the graphite/LFP cells measured in the fully charged state (charged at a 1C CC rate to 3.6 V with a CV hold at 3.6 V to a C/20 cut-off). a) Stored MCMB cell, b) cycled MCMB cell, d) stored needle coke cell, e) cycled needle coke cell. Experimental data are shown in red circles along with their Rietveld refinements (black line). The blue lines mark the difference between data and fit. Vertical bars (green) above the blue line indicate Bragg reflections corresponding to crystalline phases in the cell (from top to bottom: Fe, Cu, Al, LiC_{12}, LiC_6, $FePO_4$, and graphite. c) and f) Selected angular range of neutron diffraction data focusing on the LiC_6 (001) and LiC_{12} (002) reflections for the MCMB cells (c) and needle coke cells (f). (For interpretation of the references to colour in this figure legend, the reader is referred to the web version of this article.)

Table 4
Molar ratios of $LiFePO_4/FePO_4$ and of LiC_6/LiC_{12} for stored and cycled cells, as obtained from refinement of the neutron diffraction data for the discharged cells and the charged cells, respectively. Due to their low remaining capacity, LiC_6/LiC_{12} ratios could not be determined for the needle coke cells.

State of cells	$LiFePO_4/FePO_4$	LiC_6/LiC_{12}
Stored MCMB	75/25	23/77
Cycled MCMB	67/33	12/88
Stored Needle coke	58/42	n.a.
Cycled Needle coke	55/45	n.a.

equals

$$LI_{LFP/FP} = y(LFP) \quad (1)$$

where y(LFP) is the molar fraction of LFP (in %) obtained by *in situ* neutron diffraction analysis of the discharged cells (ranging from 55% to 75%, as shown in Table 4). For example, the molar LFP/FP ratio of 75/25 determined for the stored MCMB cell corresponds to a y(LFP) value of 75% and an active lithium inventory of $LI_{LFP/FP} = 75\%$.

To derive the LI from the anode side is not as straightforward, because over the entire SOC range several different phases of lithiated graphite (LiC_6, LiC_{12} as well as phases with lower lithium content) [27,48] and a pure graphite phase can be present, so that the lithium content can only be determined if the fraction of all the different phases present can be quantified. Unfortunately, only the LiC_6 and the LiC_{12} have sufficiently different lattice spacings to allow a deconvolution of their diffraction peaks, while the phases with lower lithium content either have a poorly defined stoichiometry and/or overlap with the LiC_{12} diffraction [27]. Therefore, it is only possible to quantify the content of lithium in graphite if its state of charge is higher than 50%, i.e., only if all lithium is contained in the LiC_6 and the LiC_{12} phases. In addition, it needs to be taken into account that the graphite electrode is typically capacitively oversized [47]. Clearly defined LiC_6 and LiC_{12} diffractions without visible diffractions from lower lithiated phases and graphite in the discharged state can only be observed for the stored/cycled MCMB cells. In this case, the sum of the LiC_6 and LiC_{12} molar fractions equals the total amount of graphite active material, so that the active lithium inventory denoted as $LI_{LiC6/LiC12}$ and can be calculated by

$$LI_{LiC6/LiC12} = [y(LiC_6)/2 + 50\%]^*B \quad (2)$$

where $y(LiC_6)$ is the molar fraction of LiC_6 in % (ranging from 12% to 23%, as shown in Table 4) and B is the anode/cathode balancing factor, which is 1.25 for the cells investigated in this study. Due to the capacitively larger graphite anode (i.e., the balancing factor of >1), a LiC_6 phase fraction of 100% cannot be obtained even if 100%

of the electrochemically active lithium were still present (based on Eq. (2), the maximum molar fraction of LiC_6 for B = 1.25 is 60%). Accordingly, a LiC_6/LiC_{12} ratio of 12/88 as determined for the cycled MCMB cell in its charged state corresponds to $y(LiC_6) = 12\%$, which based on Eq. (2) equates to an active lithium inventory of $LI_{LiC6/LiC12} = 70\%$. The active lithium inventory values determined by neutron diffraction analysis either from the LFP/FP ratio measured in discharged cells ($LI_{LFP/FP}$; using Eq. (1)) or from the LiC_6/LiC_{12} ratio measured in charged cells ($LI_{LiC6/LiC12}$; using Eq. (2)) are summarized in the second and third column of Table 5.

The fourth and fifth column in Table 5 shows the electrochemically determined remaining discharge capacities (*RDC*) of the different cells, expressed as percentage of the initial theoretical capacity (1.678 Ah; see Fig. 1). The values in the fourth column (RDC_{1C}) were measured with the same discharge procedure which was used for the long term cycling by the battery producer (also shown in the third column of Table 1). The values in the fifth column (RDC_{CCCV}) were measured with the same discharge procedure which was used to prepare the cells for neutron diffraction experiments in the discharged state (same charging procedure, but followed by a C/5 discharge to 2.0 V with a CV hold until C/20), so that they can be directly compared to the $LI_{LFP/FP}$ values. In summary, the RDC_{CCCV} values can be used for comparison with the active lithium inventory determined by the LFP/FP ratio and the LiC_6/LiC_{12} ratio. On the other hand, the RDC_{1C} values can be used to compare the capacity of the stored and cycled cells to that of the preformed cells (for which no RDC_{CCCV} data is available). Note, that the discharge capacities measured with the two different protocols (i.e., RDC_{1C} and RDC_{CCCV}) are very similar, thus confirming that impedance build-up effects (i.e. increased impedance over time, which would result in a so-called capacity roll-over) [36] do not contribute significantly to the capacity fading, as was already discussed in the previous section.

4. Discussion

In the following sections the different mechanisms contributing to capacity fading will be discussed for i) the preformed cells which only show formation loss, ii) the stored cells which show a sum of formation loss and calendar aging, and, iii) the cycled cells which show a sum of the formation loss and cyclic aging. For the preformed cells it is only possible to compare their discharge capacity to the theoretical LFP capacity in the pristine cells, as no neutron diffraction experiments were carried out in between formation and storage/long term cycling (see Fig. 1). In contrast, for the stored and cycled cells it is possible to compare neutron diffractograms and the corresponding LFP/FP and LiC_6/LiC_{12} fractions to their electrochemically determined capacities.

Table 5
Active lithium inventory derived from the molar LFP/FP ratio in the discharged cells ($LI_{LFP/FP}$) and the LiC_6/LiC_{12} ratio in the charged cells ($LI_{LiC6/LiC12}$), both determined from the neutron diffraction data. The remaining capacities after storage/cycling are the electrochemically determined discharge capacities normalized by the theoretical capacity of the pristine cells (1.678 Ah) and obtained from two different cycling procedures: i) RDC_{1C} is the discharge capacity obtained when cycling the cells at the same procedure as used in the long term cycling test (Fig. 4: CC charge at 1C with a CV hold at 3.6 V until a C/20 cut-off and 1C discharge to 2.0 V at 23 °C); ii) RDC_{CCCV} is the discharge capacity obtained with the same charging procedure, but followed by a C/5 discharge to 2.0 V with a CV hold until C/20.

State of cells	Lithium inventory		Remaining capacity	
	$LI_{LFP/FP}$	$LI_{LiC6/LiC12}$	RDC_{1C}	RDC_{CCCV}
Preformed MCMB	–	–	73.3%	–
Stored MCMB	75%	76%	74.4%	75.2%
Cycled MCMB	67%	70%	67.3%	67.0%
Preformed needle coke	–	–	68.5%	–
Stored needle coke	58%	n.a.	61.1%	61.8%
Cycled needle coke	55%	n.a.	52.8%	53.0%

4.1. Formation loss

After formation, the remaining discharge capacities RDC_{1C} are 73.3% for the MCMB cells and 68.5% for the needle coke cells (Table 5). Accordingly, the irreversible capacity loss during the formation process amounts to 26.7% for the MCMB cells and 31.5% for the needle coke cells. The irreversible capacity loss in the first cycles is generally exclusively caused by the consumption of active lithium for the solid electrolyte interphase (SEI) formation on the graphite electrode. A capacity loss during formation on the order of 30% is surprisingly high, as typical graphite anode materials usually show a significantly lower first-cycle irreversible capacity loss of about 10% [49,50]. Considering the oversized anode (balancing factor of 1.25), one would expect an irreversible capacity of about 12.5% of the theoretical cell capacity. The reason for the much higher capacity loss during formation is unclear, but must be related to the specific formation procedure applied to these commercial cells, which consumes more active lithium and thus forms a thicker SEI, presumably in order to reduce subsequent capacity losses during cell cycling. In this way, one obtains a cell with a lower initial capacity, but lower capacity fading during storage/cycling, as exemplified by the very low relative capacity loss of only 8% for the MCMB cell during the subsequent 4750 cycles (Fig. 4a). The relatively high formation loss in these commercial cells is an interesting finding as this information is usually not readily available for commercial cells, for which only a nominal capacity in units of *Ah* is stated, without revealing what fraction of the active cathode material is actually used (i.e., in terms of mAh g^{-1}_{LFP}). This "shifting" of capacity loss into the formation process also has to be taken into account when comparing the cycling performance of commercial cells with lab-built Swagelok or coin cells. In academic studies, a typical formation procedure consists of a few slow cycles (e.g. C/10 or C/20) at room temperature, during which the irreversible capacity loss would range from 10 to 15%. Further capacity losses due to continuing growth of the anode SEI would then take place during cell cycling and would therefore lead to a higher *apparent* capacity fading in comparison to commercial cells with identical cell chemistry.

Unfortunately, the formation procedures for commercial cells are essentially always proprietary, and the question remains, whether the formation related capacity losses of 26.7% and 31.5% observed for the graphite/LFP cells investigated in the present study are representative of commercial cells or whether they are unusually high. While this information is not made public by battery producers, some answers can be found in two other neutron diffraction studies, which report the LFP/FP ratios for "fresh" (meaning "preformed" in our nomenclature) commercially produced graphite/LFP cells. Rodriguez et al. found a LFP/FP ratio of 75/25 for a 2.6 Ah 18650-type cell and Bobrikov et al. found a value of 57/43 (with a significant uncertainty) for a 2.0 Ah prismatic cell [28,30]. The corresponding formation related capacity losses of 25% and 43 ± 10%, respectively, indicate that the formation losses of the cells investigated in our study seem to be within the range observed for other commercial graphite/LFP cells.

4.2. Calendar aging

Upon two years of storage (at 20% SOC, 23 °C), the remaining discharge capacity RDC_{1C} of the MCMB cell increases from 73.3% to 74.4% (Table 5), which means that there is no calendar aging for this cell. The reason for the slight capacity increase upon storage is

consistent with data recently published by Kassem et al. and Li et al., who also found a slight capacity increase in commercially produced cylindrical graphite/LFP cells after one year of storage at different SOCs [51–53]. For the stored MCMB cell, the remaining discharge capacity of $RDC_{CCCV} = 75.2\%$ is in excellent agreement with the active lithium inventory determined by neutron diffraction from the LFP/LP ratio of $LI_{LFP/FP} = 75\%$ and from the LiC_6/LiC_{12} ratio of $LI_{LiC6/LiC12} = 76\%$ (Table 5), meaning that active lithium loss accounts for the entire capacity loss of the stored MCMB cell.

In contrast, the needle coke cell shows a significant calendar aging, with the remaining discharge capacity decreasing from $RDC_{1C} = 68.5\%$ after formation to 61.1% after storage (Table 5). The active lithium inventory determined by the LFP/FP ratio of $Li_{LFP/FP} = 58\%$ slightly overestimates the capacity loss in comparison to the electrochemically observed remaining capacity of $RDC_{CCCV} = 61.8\%$. There is no indication for the contribution of particle deactivation by electronic/ionic insulation to capacity fading, as no $LiFePO_4$ is observed in the charged cell and no LiC_6/LiC_{12} (or other lithiated phases) are observed in the discharged cell. One can conclude that active lithium loss is most likely also the sole contributor to capacity fading in the stored needle coke cell, which is again consistent with results published by Kassem et al. [52,53]. The difference between the lithium inventory $Li_{LFP/FP}$ and the remaining discharge capacity is probably due to the fitting error of the neutron diffraction data, which is estimated to be about 3% from the fitting software for each of the fitted phases (LFP and FP in this case).

At the current stage, the reason for the different calendar aging behavior of the stored MCMB and the stored needle coke cells is not clear. Interestingly, the stored MCMB cell shows both a higher polarization (Fig. 4b) and a higher charge transfer resistance (Fig. 4c) than the stored needle coke cell (25.7 mΩ vs. 14.0 mΩ, respectively). This might be an indication for the formation of a more passivating SEI layer on the MCMB in comparison to the needle coke, which on the one hand increases the charge transfer resistance, but on the other hand more effectively suppresses further electrolyte reduction, thereby lowering the corresponding capacity loss. Or, in other words, the higher charge transfer resistance and lower calendar aging of the MCMB cell might be two sides of the same coin. Furthermore, the different calendar aging might also be influenced by the nature of the exposed graphite planes which strongly depend on the local arrangement of crystallite grains [49]. In normal flake-like graphite as needle coke, the majority (>90%) of the exposed graphite layers are basal planes [54] while MCMB shows a higher fraction of exposed edge planes [49]. It is known that the SEI on edge and basal planes differs both in chemical composition and especially thickness [55–57]. Based on x-ray photoelectron spectroscopy (XPS) Peled et al. reported a thickness of 2 nm for basal and 30 nm for edge plane SEI [56]. The thicker SEI on the edge plane is probably a consequence of either solvent co-intercalation during charge, which is not possible on basal planes [58,59], and/or the constant expansion and contraction of graphite perpendicular to the edge planes during cycling. Newman and co-workers showed that there is also a difference in the passivation behavior of the edge and basal plane SEI on highly oriented pyrolytic graphite (HOPG) and they concluded that the SEI on basal planes might be thin enough to permit limited electron tunneling [60]. Accordingly, the higher fraction of basal planes might contribute to the significant calendar aging of the stored needle coke cell while the stored MCMB cell does not show any calendar aging. We are currently carrying out further experiments to thoroughly investigate which chemical, physicochemical, and/or structural/mechanical properties are responsible for the different passivation and calendar aging behavior of the MCMB and needle coke graphite.

4.3. Cyclic aging

Upon cycling for 4750 cycles, the remaining discharge capacity RDC_{1C} decreases from 73.3% to 67.3% for the MCMB cell (Table 5), corresponding to a capacity loss of 6% if referenced to the theoretical capacity or of 8.2% if referenced to the capacity of the preformed cell (Table 1). The essentially perfect correspondence of the active lithium inventory deduced from the LFP/LP ratio ($LI_{LFP/FP}$) = 67% with the remaining discharge capacity $RDC_{CCCV} = 67.0\%$ clearly indicates that the capacity fading during cycling of the MCMB cell can be accounted quantitatively by active lithium loss, excluding effects caused by particle isolation/degradation and impedance growth effects.

For the cycled needle coke cell, the remaining discharge capacity RDC_{1C} decreases from 68.5% to 52.8%, corresponding to a capacity loss of 15.7% if referenced to the theoretical capacity or of 23.1% if referenced to the preformed cell. In principle, these capacity losses contain contributions from calendar aging and cyclic aging, but a clear deconvolution is not possible on the basis of our experiments. The comparison of the active lithium inventory deduced from the LFP/LP ratio of $LI_{LFP/FP} = 55\%$ with the remaining discharge capacity $RDC_{CCCV} = 53.0\%$ shows that, within the error of the neutron diffraction analysis, the entire capacity fading can be accounted for by active lithium loss. And again, there is no indication for the occurrence of other aging mechanisms, as no new phases in the diffraction patterns emerge, the lattice parameters of all active materials stay constant and no lithium containing inactive particles are observed.

The reason for the faster loss of active lithium upon cycling in the needle coke cell in comparison to the MCMB cell is currently being investigated in our labs. In this respect, it is very important to understand which processes contribute to the loss of active lithium in each cell. The linear decrease of the cell capacity with cycling number as observed for the MCMB cell (Fig. 4a) is typical for active lithium loss due to the constant repair of a small fraction of the anode SEI caused by the slight expansion and contraction of the graphite particles upon lithium intercalation and deintercalation [61]. In contrast, the higher initial rate of capacity fading upon cycling observed for the needle coke cell (Fig. 4a) might be an indication for the presence of a second process contributing to the loss of active lithium during the initial 1000 cycles, for example partial lithium plating during charge.

4.4. Active lithium loss analysis via the LFP/FP ratio versus the LiC_6/LiC_{12} ratio

For the graphite/LFP cells investigated in this study, the lithium inventory can, in general, be determined by neutron diffraction based on the molar ratio of LFP/FP (measured in the discharged state) or through the LiC_6/LiC_{12} ratio (measured in the charged state). Theoretically, the values of $LI_{LFP/FP}$ and $LI_{LiC6/LiC12}$ should give identical results, as they both determine the same parameter, namely the amount of active lithium. Indeed, for the MCMB cells, the $LI_{LFP/FP}$ and $LI_{LiC6/LiC12}$ values agree within 1% for the stored cell and within 3% for the cycled cell (Table 5). Note, that one would only expect identical results for the $LI_{LFP/FP}$ and $LI_{LiC6/LiC12}$ values for cells in which active lithium loss is the only mechanism contributing to capacity fading, as is the here. While LFP/FP and LiC_6/LiC_{12} ratios should ideally give identical results, there are some considerations which might render one of them advantageous for LFP/FP based cells.

As already discussed, the lithiation/delithiation process of graphite is only a two phase mechanism for higher lithiation degrees ($x > 0.5$ in Li_xC_6) [47,48]. Accordingly, the lithium inventory can only be determined through the LiC_6/LiC_{12} ratio as long as the

cell capacity is higher than $0.5^{*}Q_{theo.}{}^{*}B$, where $Q_{theo.}$ is the theoretical capacity of the pristine cell and B is the cell balancing factor. This limitation is the reason why the $LI_{LiC6/LiC12}$ ratio cannot be determined for the needle coke cells in the present study. In contrast, the lithiation/delithiation of LFP is a two phase mechanism of triphylite ($LiFePO_4$) and the heterosite ($FePO_4$) over the entire capacity range; therefore, the triphylite/heterosite phase ratio can be used for the determination of the $LI_{LFP/FP}$ independent of the remaining capacity. Another advantage of the analysis via the LFP/FP ratio over that of the LiC_6/LiC_{12} ratio is that the former can also be used to determine the lithium inventory and the active lithium loss, if the anode/cathode balancing factor is unknown, which is usually the case for commercial cells (compare equations (1) and (2)).

5. Conclusion and outlook

In this study, the capacity fading processes in four commercially produced 18650-type graphite/LFP cells, which differed either in the kind of graphite active material or the applied type of aging, were investigated *in situ* with neutron diffraction. All four cells showed a rather high formation loss in the order of 30% (27% for an MCMB based anode and 31% for a needle coke based anode) and excellent cycling stability thereafter, with relative capacity losses (referring to the capacity after formation) of only ≈8% for the MCMB cell and ≈23% for the needle coke cell during 4750 cycles. Upon two years of storage, the MCMB cell showed no measurable capacity loss, while the needle coke cell lost ≈11% of its relative capacity.

The comparison of neutron diffraction experiments in the charged and discharged state with electrochemical characterization reveals that the entire capacity loss upon formation, cycling, and storage is solely due to active lithium loss. Based on the neutron diffractograms, the contribution of other aging mechanisms like deactivation and active material isolation/destruction can be excluded. The slower calendar aging of the MCMB cell in comparison to the needle coke cell is probably due to the formation of an SEI layer which provides better passivation, reflected by the higher cell impedance of the MCMB cells. The slower cyclic aging of the MCMB cell in comparison to the needle coke cell is probably caused by different mechanisms of active lithium loss: The decrease of discharge capacity with cycle number indicates that in the MCMB cell the entire active lithium loss is caused by ongoing SEI repair, while in the needle coke cell a second mechanism might contribute to active lithium loss in the first 1000 cycles, the origin of which is currently under investigation.

Acknowledgements

This work was financially supported by the Bavarian Ministry of Economic Affairs and Media, Energy and Technology under the auspices of the EEBatt project. The authors thank the Heinz Maier-Leibnitz Zentrum (MLZ) for granting beam time at FRM II.

Appendix A. Supplementary data

Supplementary data related to this article can be found at http://dx.doi.org/10.1016/j.jpowsour.2017.01.134.

References

[1] B. Nykvist, M. Nilsson, Nat. Clim. Chang. 5 (2015) 329–332.
[2] J.-M. Tarascon, Philos. Trans. A. Math. Phys. Eng. Sci. 368 (2010) 3227–3241.
[3] F.T. Wagner, B. Lakshmanan, M.F. Mathias, J. Phys. Chem. Lett. 1 (2010) 2204–2219.
[4] D. Andre, S.-J. Kim, P. Lamp, S.F. Lux, F. Maglia, O. Paschos, B. Stiaszny, J. Mater. Chem. A 3 (2015) 6709–6732.
[5] S.J. Harris, P. Lu, J. Phys. Chem. C 117 (2013) 6481–6492.
[6] USABC, USABC Goals for Advanced Batteries for EVs - CY2020 Commercializaton, can be found under, 2015. http://www.energy.gov/sites/prod/files/2014/05/f15/APR13_Energy_Storage_d_III_Adv_Battery_Dev_0.pdf.
[7] U.S. Department of Energy, Grid Energy Storage, can be found under http://energy.gov/sites/prod/files/2014/09/f18/Grid Energy Storage December 2013.pdf, accessed September 2016.
[8] P.P.R.M.L. Harks, F.M. Mulder, P.H.L. Notten, J. Power Sources 288 (2015) 92–105.
[9] J. Wandt, P. Jakes, J. Granwehr, H.A. Gasteiger, R.-A. Eichel, Angew. Chem. Int. Ed. 55 (2016) 6892–6895.
[10] X.-L. Wang, K. An, L. Cai, Z. Feng, S.E. Nagler, C. Daniel, K.J. Rhodes, A.D. Stoica, H.D. Skorpenske, C. Liang, et al., Sci. Rep. 2 (2012) 1–7.
[11] J. Wandt, A. Freiberg, R. Thomas, Y. Gorlin, A. Siebel, R. Jung, H.A. Gasteiger, M. Tromp, J. Mater. Chem. A 4 (2016) 18300–18305.
[12] Y. Gorlin, A. Siebel, M. Piana, T. Huthwelker, H. Jha, G. Monsch, F. Kraus, H.A. Gasteiger, M. Tromp, J. Electrochem. Soc. 162 (2015) A1146–A1155.
[13] J. Wandt, C. Marino, P. Jakes, R. Eichel, H.A. Gasteiger, J. Granwehr, Energy Environ. Sci. 8 (2015) 1358–1367.
[14] F. Poli, J.S. Kshetrimayum, L. Monconduit, M. Letellier, Electrochem. Commun. 13 (2011) 1293–1295.
[15] N. Tsiouvaras, S. Meini, I. Buchberger, H.A. Gasteiger, J. Electrochem. Soc. 160 (2013) A471–A477.
[16] A. Senyshyn, M.J. Mühlbauer, O. Dolotko, M. Hofmann, H. Ehrenberg, Sci. Rep. (2015) 1–9.
[17] R.S. Rubino, H. Gan, E.S. Takeuchi, J. Electrochem. Soc. 148 (2001) A1029–A1033.
[18] T. Waldmann, S. Gorse, T. Samtleben, G. Schneider, V. Knoblauch, M. Wohlfahrt-Mehrens, J. Electrochem. Soc. 161 (2014) A1742–A1747.
[19] M. Fleckenstein, O. Bohlen, M.A. Roscher, B. Bäker, J. Power Sources 196 (2011) 4769–4778.
[20] M.A. Rodriguez, D. Ingersoll, D.H. Doughty, JCPDS Adv. X-ray Anal. 45 (2002) 182–187.
[21] M.A. Rodriguez, D. Ingersoll, S.C. Vogel, D.J. Williams, Electrochem. Solid-State Lett. 7 (2004) A8.
[22] N. Sharma, V.K. Peterson, M.M. Elcombe, M. Avdeev, A.J. Studer, N. Blagojevic, R. Yusoff, N. Kamarulzaman, J. Power Sources 195 (2010) 8258–8266.
[23] O. Dolotko, A. Senyshyn, M.J. Mühlbauer, K. Nikolowski, F. Scheiba, H. Ehrenberg, J. Electrochem. Soc. 159 (2012) A2082–A2088.
[24] A. Senyshyn, M.J. Mühlbauer, K. Nikolowski, T. Pirling, H. Ehrenberg, J. Power Sources 203 (2012) 126–129.
[25] L. Cai, K. An, Z. Feng, C. Liang, S.J. Harris, J. Power Sources 236 (2013) 163–168.
[26] O. Dolotko, A. Senyshyn, M.J. Mühlbauer, K. Nikolowski, H. Ehrenberg, J. Power Sources 255 (2014) 197–203.
[27] V. Zinth, C. von Lüders, M. Hofmann, J. Hattendorff, I. Buchberger, S. Erhard, J. Rebelo-Kornmeier, A. Jossen, R. Gilles, J. Power Sources 271 (2014) 152–159.
[28] M.A. Rodriguez, M.H. Van Benthem, D. Ingersoll, S.C. Vogel, H.M. Reiche, Powder Diffr. 25 (2010) 143–148.
[29] C.W. Hu, N. Sharma, C.-Y. Chiang, H.-C. Su, V.K. Peterson, H.W. Hsieh, Y.F. Lin, W.C. Chou, B.Y. Shew, C.H. Lee, J. Power Sources 244 (2013) 158–163.
[30] I.A. Bobrikov, A.M. Balagurov, C.W. Hu, C.H. Lee, T.Y. Chen, S. Deleg, D.A. Balagurov, J. Power Sources 258 (2014) 356–364.
[31] A. Senyshyn, M.J. Mühlbauer, O. Dolotko, M. Hofmann, T. Pirling, H. Ehrenberg, J. Power Sources 245 (2014) 678–683.
[32] A.J. Smith, J.C. Burns, X. Zhao, D. Xiong, J.R. Dahn, J. Electrochem. Soc. 158 (2011) A447–A452.
[33] J.C. Burns, D.A. Stevens, J.R. Dahn, J. Electrochem. Soc. 162 (2015) A959–A964.
[34] R. Bernhard, S. Meini, H.A. Gasteiger, J. Electrochem. Soc. 161 (2014) A497–A505.
[35] R.P. Day, J. Xia, R. Petibon, J. Rucska, H. Wang, A.T.B. Wright, J.R. Dahn, J. Electrochem. Soc. 162 (2015) A2577–A2581.
[36] J.C. Burns, A. Kassam, N.N. Sinha, L.E. Downie, L. Solnickova, B.M. Way, J.R. Dahn, J. Electrochem. Soc. 160 (2013) A1451–A1456.
[37] K. Ishidzu, Y. Oka, T. Nakamura, Solid State Ionics 288 (2016) 176–179.
[38] M. Koltypin, D. Aurbach, L. Nazar, B. Ellis, Electrochem. Solid-State Lett. 10 (2007) A40.
[39] H. Zheng, Q. Sun, G. Liu, X. Song, V.S. Battaglia, J. Power Sources 207 (2012) 134–140.
[40] C. Delacourt, A. Kwong, X. Liu, R. Qiao, W.L. Yang, P. Lu, S.J. Harris, V. Srinivasan, J. Electrochem. Soc. 160 (2013) A1099–A1107.
[41] M. Hoelzel, A. Senyshyn, N. Juenke, H. Boysen, W. Schmahl, H. Fuess, Nucl. Instrum. Methods Phys. Res. Sect. A Accel. Spectrom. Detect. Assoc. Equip. 667 (2012) 32–37.
[42] R. Gilles, B. Krimmer, H. Boysen, H. Fuess, Appl. Phys. A 74 (2002) S148–S150.
[43] T. Roisnel, J. Rodríquez-Carvajal, Mater. Sci. Forum 378–381 (2001) 118–123.
[44] S. Solchenbach, D. Pritzl, E.J.Y. Kong, J. Landesfeind, H.A. Gasteiger, J. Electrochem. Soc. 163 (2016) A2265–A2272.
[45] M. Gaberscek, J. Moskon, B. Erjavec, R. Dominko, J. Jamnik, Electrochem. Solid-State Lett. 11 (2008) A170–A174.
[46] J. Landesfeind, J. Hattendorff, A. Ehrl, W.A. Wall, H.A. Gasteiger, J. Electrochem. Soc. 163 (2016) A1373–A1387.
[47] J.R. Dahn, Phys. Rev. B 44 (1991) 9170–9177.
[48] A. Senyshyn, O. Dolotko, M.J. Mühlbauer, K. Nikolowski, H. Fuess, H. Ehrenberg, J. Electrochem. Soc. 160 (2013) A3198–A3205.

[49] G. Chung, S. Jun, K. Lee, M. Kim, J. Electrochem. Soc. 146 (1999) 1664–1671.
[50] S. Hossain, Y.K. Kim, Y. Saleh, R. Loutfy, J. Power Sources 114 (2003) 264–276.
[51] D. Li, D.L. Danilov, J. Xie, L. Raijmakers, L. Gao, Y. Yang, P.H.L. Notten, Electrochim. Acta 190 (2016) 1124–1133.
[52] M. Kassem, J. Bernard, R. Revel, S. Pélissier, F. Duclaud, C. Delacourt, J. Power Sources 217 (2012) 574.
[53] M. Kassem, C. Delacourt, J. Power Sources 235 (2013) 159–171.
[54] K. Zaghib, G. Nadeau, K. Kinoshita, J. Electrochem. Soc. 147 (2000) 2110.
[55] D. Bar-Tow, E. Peled, L. Burstein, J. Electrochem. Soc. 146 (1999) 824.
[56] E. Peled, D. Bar Tow, A. Merson, A. Gladkich, L. Burstein, D. Golodnitsky, J. Power Sources 97–98 (2001) 52–57.
[57] E. Peled, D. Golodnitsky, A. Ulus, V. Yufit, Electrochim. Acta 50 (2004) 391–395.
[58] J.O. Besenhard, M. Winter, J. Yang, W. Biberacher, J. Power Sources 54 (1995) 228–231.
[59] M. Inaba, Z. Siroma, A. Funabiki, Z. Ogumi, T. Abe, Y. Mizutani, M. Asano, Langmuir 12 (1996) 1535–1540.
[60] M. Tang, J. Newman, J. Electrochem. Soc. 159 (2012) A1922–A1927.
[61] D. Li, D.L. Danilov, L. Gao, Y. Yang, P.H.L. Notten, Electrochim. Acta 190 (2016) 445–455.

Supporting information

Aging behavior of lithium iron phosphate based 18650-type cells studied by *in situ* neutron diffraction

Neelima Paul[#a]*, Johannes Wandt[#b], Stefan Seidlmayer[a], Sebastian Schebesta[c], Martin J. Mühlbauer[a,d,e] , Oleksandr Dolotko[a], Hubert A. Gasteiger[b] and Ralph Gilles[a]

[a]*Heinz Maier-Leibnitz Zentrum (MLZ), Technische Universität München, 85747 Garching, Germany,* [b]*Chair of Technical Electrochemistry, Technische Universität München, 85748 Garching, Germany,* [c]*VW-VM Forschungsgesellschaft mbH & Co. KG, 73479 Ellwangen, Germany,* [d]*Institute for Applied Materials (IAM), Karlsruhe Institute of Technology (KIT), Hermann-von-Helmholtz-Platz 1, 76344 Eggenstein-Leopoldshafen,* [e]*Helmholtz-Institute Ulm for Electrochmical Energy Storage (HIU), P.O. Box, 76021 Karlsruhe, Germany*
** Corresponding author - Neelima.Paul@frm2.tum.de ,[#] Authors N.P and J.W contributed equally to this work*

LFP active material

The theoretical cell capacity Q_{theo}. of 1.678 Ah for the 18650 cells was calculated from the amount of LFP active material (10.75 g) and the achievable capacity of 160 mAh g_{LFP}^{-1}. This value was determined experimentally by cycling a pristine LFP electrode in a Swagelok half-cell (lithium counter and reference electrode, glass fiber separator, 80 µL LP57 electrolyte) with a C/10 rate between 2.0 and 4.0 V vs. Li/Li^+ as shown in Figure S1. The determined specific capacity of 160 mAh g_{LFP}^{-1} is slightly lower than the theoretical value of 170 mAh g_{LFP}^{-1} but well within the range of what is typically observed in practical LFP cells.[S1–S3] For a proper analysis of the neutron diffraction data, it is important whether the "missing" 10 mAh g_{LFP}^{-1} are due to the presence of electrochemically inactive LFP or to other side phases (e.g., Li_2CO_3, Fe_2O_3). Therefore, LFP electrodes were harvested from Swagelok half-cells either in the fully lithiated or fully delithiated state and *ex situ* x-ray diffraction (inset Figure S1) was used to determine the LFP/FP phase fractions. Within the accuracy of the XRD analysis, the lithiated sample only contained $LiFePO_4$ and no $FePO_4$ whereas the situation was the opposite for the delithiated sample. This indicates that the entire LFP in the electrode is electrochemically active and the achievable capacity of 160 mAh g_{LFP}^{-1} corresponds to a change of the LFP/FP ratio from 100/0 to 0/100.

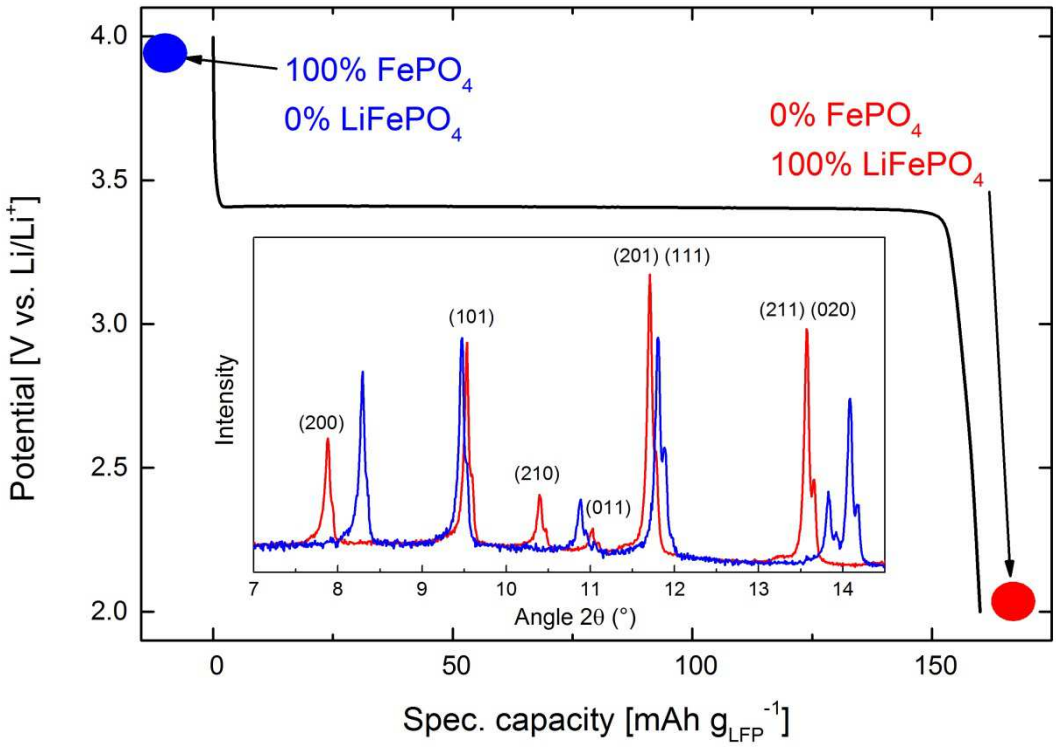

Figure S1: Determination of achievable LFP capacity measured in a half cell with a Li counter electrode at a C/10 discharge rate; inset: ex-situ XRD of harvested LFP electrodes in the fully lithitated (red) or fully delithiated state (blue) (Bragg reflections of LFP are indexed).

References

S1. Zaghib, K., Shim, J., Guerfi, a., Charest, P. & Striebel, K. a. Effect of Carbon Source as Additives in $LiFePO_4$ as Positive Electrode for Lithium-Ion Batteries. *Electrochem. Solid-State Lett.* **8,** A207 (2005).

S2. Fongy, C., Jouanneau, S., Guyomard, D., Badot, J. C. & Lestriez, B. Electronic and Ionic Wirings Versus the Insertion Reaction Contributions to the Polarization in $LiFePO_4$ Composite Electrodes. *J. Electrochem. Soc.* **157,** A1347–A1353 (2010).

S3. Fongy, C., Gaillot, A.-C., Jouanneau, S., Guyomard, D. & Lestriez, B. Ionic vs Electronic Power Limitations and Analysis of the Fraction of Wired Grains in $LiFePO_4$ Composite Electrodes. *J. Electrochem. Soc.* **157,** A885–A891 (2010).

.

4 Conclusion and Outlook

The development of an electrochemical battery cell for *operando* EPR spectroscopy was the main goal of this PhD thesis. We successfully developed a concentric cell design which shows good overall electrochemical performance in combination with good spectroscopic properties. We could show that it is possible to semi-quantitatively monitor the formation of lithium dendrites on lithium metal anodes by exploiting the surface sensitivity due to the skin-effect. To the best of our knowledge this is the first *operando* EPR study in the field of lithium-ion battery research.

We also developed a technique based on *operando* EPR spectroscopy to quantitatively detect lithium metal plating on graphite anodes. The complex method development has been completed and we already applied this technique for a first study of the low temperature charging process of lithium-ion cells. In order to use *operando* EPR spectroscopy for validation of numerical simulations of lithium plating, it will be necessary to improve the electrochemical reproducibility of the current cell design. In this respect, lithium plating is a very challenging reaction because it is very sensitive to minor deviations in the cell geometry, e.g. the distance between working and counter electrode. In order to achieve a perfectly homogeneous current distribution, it will be necessary to i) obtain a uniform pressure distribution and ii) reduce the ratio of the electrode edge in comparison to the electrode surface for the graphite electrode. We also measured a large quantity of high quality EPR data of the lithium intercalation into graphite. So far, the data analysis has focused on the lithium metal signal while the graphite EPR signal was rather considered as a disturbing signal. In fact, this data is also the first *operando* EPR study on the lithium intercalation reaction and might give new insights into electronic and magnetic properties of graphite intercalation compounds and especially the staging model at lower lithiation degrees ($x \leq 0.5$ in Li_xC_6).

In another study we applied *operando* EPR in combination with a chemical spin trap to show that singlet oxygen is evolved in significant quantities during the charging process of aprotic lithium-oxygen batteries. This discovery opens new venues for the mitigation of irreversible side reactions taking place during battery charge. These side

reactions cause electrolyte degradation and carbon corrosion and result in fast cell failure. Other research groups have already started exploring new experimental approaches and there are first promising results with catalytic singlet oxygen scavengers as electrolyte additives, which show an improved cell reversibility.[153] Furthermore, it would be interesting to investigate whether singlet oxygen is formed in the charging process of aprotic sodium-oxygen batteries which received alot attention in recent years.[155] It has also been suggested that part of the oxygen evolved from layered lithium oxide cathode materials at high charging potentials might be singlet oxygen;[51] so far, there is no direct experimental data proofing this theory right or wrong. The working potential of these transition metal oxides is well above 4.0 V vs. Li/Li^+ which significantly exceeds the stability limit of the 4-Oxo-TEMP spin trap. The only possibility to investigate singlet oxygen evolution from these lithium-ion cathode materials is the detection of the characteristic singlet oxygen chemiluminescence at 633 or 1270 nm.[156]

We successfully applied *operando* XAS spectroscopy to investigate the transition metal dissolution and redeposition in NMC/graphite cells. We could show that the oxidation state of manganese deposits is +2 under operating conditions and 0 in the *ex situ* analysis, highlighting the necessity for adequate *operando* characterization techniques. The oxidation state of +2 under operating conditions is rather surprising considering the highly reducing potential of the graphite electrode. A possible interpretation is the occurrence of a catalytic Mn(0)/Mn(II) cycle causing ongoing electrolyte reduction. Further experimental evidence is necessary to support this hypothesis. In this respect, the combination of artificially added transition metal salts with On-line electrochemical mass spectrometry (OEMS) would be a promising approach.

In the last part of this thesis, we investigated the aging mechanism of commercially produced 18650 cells by *in situ* neutron diffraction. Based on neutron diffraction and electrochemical characterization, we could show that all the capacity loss can be assigned to active lithium loss. The amount of active lithium loss depended on the graphite type which was used as anode active material. Needle coke showed a higher cycling and calendaric aging in comparison to mesocarbon microbeads. The reason for the different aging behaviors of these two carbons is currently under investigation in our laboratory.

List of Figures

List of Tables

References

[1] Y. Nishi, *The Electrochemical Society Interface* **2016**, *25*(3), 71–74.

[2] M. S. Whittingham, *Science* **1976**, *192*(4244), 1126–1127.

[3] M. S. Whittingham, *Progress in Solid State Chemistry* **1978**, *12*(1), 41–99.

[4] K. Mizushima, P. Jones, P. Wiseman, J. B. Goodenough, *Materials Research Bulletin* **1980**, *15*(6), 783–789.

[5] M. Thackeray, W. David, P. Bruce, J. Goodenough, *Materials Research Bulletin* **1983**, *18*(4), 461–472.

[6] K. Brandt, *Solid State Ionics* **1994**, *69*(3-4), 173–183.

[7] G. E. Blomgren, *Journal of The Electrochemical Society* **2017**, *164*(1), A5019–A5025.

[8] R. Fong, U. Von Sacken, J. R. Dahn, *Journal of The Electrochemical Society* **1990**, *137*(7), 2009–2013.

[9] E. J. Berg, C. Villevieille, D. Streich, S. Trabesinger, P. Novák, *Journal of The Electrochemical Society* **2015**, *162*(14), A2468–A2475.

[10] D. Andre, S.-J. Kim, P. Lamp, S. F. Lux, F. Maglia, O. Paschos, B. Stiaszny, *Journal of Materials Chemistry A* **2015**, *3*(13), 6709–6732.

[11] B. Dunn, H. Kamath, J.-M. Tarascon, *Science* **2011**, *334*(6058), 928–935.

[12] "Antarctic CO2 Hit 400 PPM For First Time in 4 Million Years", http://www.climatecentral.org/news/antarctica-co2-400-ppm-million-years-20451, accessed on 16.05.2017.

[13] J.-R. Petit, J. Jouzel, D. Raynaud, N. I. Barkov, J.-M. Barnola, I. Basile, M. Bender, J. Chappellaz, M. Davis, G. Delaygue, et al., *Nature* **1999**, *399*(6735), 429–436.

[14] "CO2 emissions from fuel combustion - Highlights", International Energy Agency (2016), https://www.iea.org/publications/freepublications/publication/CO2EmissionsfromFuelCombustion-Highlights-2016.pdf, accessed on 17.05.2017.

[15] O. Gröger, H. A. Gasteiger, J.-P. Suchsland, *Journal of The Electrochemical Society* **2015**, *162*(14), A2605–A2622.

[16] B. Nykvist, M. Nilsson, *Nature Climate Change* **2015**, *5*(4), 329–332.

[17] P. Keil, A. Jossen, *Journal of Energy Storage* **2016**, *6*, 125–141.

[18] N. Williard, W. He, C. Hendricks, M. Pecht, *Energies* **2013**, *6*(9), 4682–4695.

[19] A. Lerf, *Dalton Transactions* **2014**, *43*(27), 10276–10291.

[20] P. Arora, Z. Zhang, *Chemical Reviews* **2004**, *104*(10), 4419–4462.

[21] J. Dahn, *Physical Review B* **1991**, *44*(17), 9170.

[22] M. S. Dresselhaus, G. Dresselhaus, *Advances in Physics* **2002**, *51*(1), 1–186.

[23] A. Senyshyn, O. Dolotko, M. Mühlbauer, K. Nikolowski, H. Fuess, H. Ehrenberg, *Journal of The Electrochemical Society* **2013**, *160*(5), A3198–A3205.

[24] F. DiSalvo, S. Safran, R. Haddon, J. Waszczak, J. Fischer, *Physical Review B* **1979**, *20*(12), 4883.

[25] T. Tsuzuku, *Carbon* **1979**, *17*(3), 293–299.

[26] S. Basu, C. Zeller, P. Flanders, C. Fuerst, W. Johnson, J. Fischer, *Materials Science and Engineering* **1979**, *38*(3), 275–283.

[27] E. Peled, *Journal of The Electrochemical Society* **1979**, *126*(12), 2047–2051.

[28] M. Nie, D. Chalasani, D. P. Abraham, Y. Chen, A. Bose, B. L. Lucht, *The Journal of Physical Chemistry C* **2013**, *117*(3), 1257–1267.

[29] Y. Ein-Eli, B. Markovsky, D. Aurbach, Y. Carmeli, H. Yamin, S. Luski, *Electrochimica Acta* **1994**, *39*(17), 2559–2569.

[30] D. Aurbach, *Journal of Power Sources* **2000**, *89*(2), 206–218.

[31] Q. Liu, C. Du, B. Shen, P. Zuo, X. Cheng, Y. Ma, G. Yin, Y. Gao, *RSC Advances* **2016**, *6*(91), 88683–88700.

[32] F. Ronci, P. Reale, B. Scrosati, S. Panero, V. Rossi Albertini, P. Perfetti, M. Di Michiel, J. Merino, *The Journal of Physical Chemistry B* **2002**, *106*(12), 3082–3086.

[33] K. Zaghib, M. Dontigny, A. Guerfi, P. Charest, I. Rodrigues, A. Mauger, C. Julien, *Journal of Power Sources* **2011**, *196*(8), 3949–3954.

[34] H.-G. Jung, M. W. Jang, J. Hassoun, Y.-K. Sun, B. Scrosati, *Nature Communications* **2011**, *2*, 516.

[35] E. Buiel, J. Dahn, *Electrochimica Acta* **1999**, *45*(1), 121–130.

[36] "The Rechargeable Battery Market and Main Trends 2015-2025" by Christophe Pillot (Avicenne Energy), https://de.slideshare.net/ChristophePILLOT/c-pillot-june-2016-64406919, accessed on 06.06.2017.

[37] C. M. Julien, A. Mauger, K. Zaghib, H. Groult, *Inorganics* **2014**, *2*(1), 132–154.

[38] A. K. Padhi, K. Nanjundaswamy, J. B. Goodenough, *Journal of the Electrochemical Society* **1997**, *144*(4), 1188–1194.

[39] L. Lu, X. Han, J. Li, J. Hua, M. Ouyang, *Journal of Power Sources* **2013**, *226*, 272–288.

[40] K. Xu, *Chemical Reviews* **2014**, *114*(23), 11503–11618.

[41] K. Xu, *Chemical Reviews* **2004**, *104*(10), 4303–4418.

[42] J. Burns, R. Petibon, K. Nelson, N. Sinha, A. Kassam, B. Way, J. Dahn, *Journal of The Electrochemical Society* **2013**, *160*(10), A1668–A1674.

[43] D. Y. Wang, J. Xia, L. Ma, K. Nelson, J. Harlow, D. Xiong, L. Downie, R. Petibon, J. Burns, A. Xiao, et al., *Journal of The Electrochemical Society* **2014**, *161*(12), A1818–A1827.

[44] N. Yabuuchi, Y. Makimura, T. Ohzuku, *Journal of The Electrochemical Society* **2007**, *154*(4), A314–A321.

[45] H. Zheng, Q. Sun, G. Liu, X. Song, V. S. Battaglia, *Journal of Power Sources* **2012**, *207*, 134–140.

[46] I. Buchberger, S. Seidlmayer, A. Pokharel, M. Piana, J. Hattendorff, P. Kudejova, R. Gilles, H. A. Gasteiger, *Journal of The Electrochemical Society* **2015**, *162*(14), A2737–A2746.

[47] D. R. Gallus, R. Schmitz, R. Wagner, B. Hoffmann, S. Nowak, I. Cekic-Laskovic, R. W. Schmitz, M. Winter, *Electrochimica Acta* **2014**, *134*, 393–398.

[48] M. Metzger, J. Sicklinger, D. Haering, C. Kavakli, C. Stinner, C. Marino, H. A. Gasteiger, *Journal of The Electrochemical Society* **2015**, *162*(7), A1227–A1235.

[49] J. C. Hunter, *Journal of Solid State Chemistry* **1981**, *39*(2), 142–147.

[50] B. Strehle, K. Kleiner, R. Jung, F. Chesneau, M. Mendez, H. A. Gasteiger, M. Piana, *Journal of The Electrochemical Society* **2017**, *164*(2), A400–A406.

[51] R. Jung, M. Metzger, F. Maglia, C. Stinner, H. A. Gasteiger, *Journal of The Electrochemical Society* **2017**, *164*(7), A1361–A1377.

[52] H.-J. Noh, S. Youn, C. S. Yoon, Y.-K. Sun, *Journal of Power Sources* **2013**, *233*, 121–130.

[53] J.-H. Kim, S.-T. Myung, C. Yoon, S. Kang, Y.-K. Sun, *Chemistry of Materials* **2004**, *16*(5), 906–914.

[54] Z. Lu, D. MacNeil, J. Dahn, *Electrochemical and Solid-State Letters* **2001**, *4*(11), A191–A194.

[55] C. Johnson, J. Kim, C. Lefief, N. Li, J. Vaughey, M. Thackeray, *Electrochemistry Communications* **2004**, *6*(10), 1085–1091.

[56] B. Scrosati, J. Garche, *Journal of Power Sources* **2010**, *195*(9), 2419–2430.

[57] F. Luo, B. Liu, J. Zheng, G. Chu, K. Zhong, H. Li, X. Huang, L. Chen, *Journal of The Electrochemical Society* **2015**, *162*(14), A2509–A2528.

[58] X. Zuo, J. Zhu, P. Müller-Buschbaum, Y.-J. Cheng, *Nano Energy* **2017**, *31*, 113–143.

[59] W. Xu, J. Wang, F. Ding, X. Chen, E. Nasybulin, Y. Zhang, J.-G. Zhang, *Energy & Environmental Science* **2014**, *7*(2), 513–537.

[60] M. Arakawa, S.-i. Tobishima, Y. Nemoto, M. Ichimura, J.-i. Yamaki, *Journal of Power Sources* **1993**, *43*(1-3), 27–35.

[61] D. Aurbach, I. Weissman, H. Yamin, E. Elster, *Journal of The Electrochemical Society* **1998**, *145*(5), 1421–1426.

[62] J.-I. Yamaki, S.-I. Tobishima, K. Hayashi, K. Saito, Y. Nemoto, M. Arakawa, *Journal of Power Sources* **1998**, *74*(2), 219–227.

[63] A. Aryanfar, D. Brooks, B. V. Merinov, W. A. Goddard III, A. J. Colussi, M. R. Hoffmann, *The Journal of Physical Chemistry Letters* **2014**, *5*(10), 1721–1726.

[64] J.-N. Chazalviel, *Physical Review A* **1990**, *42*(12), 7355.

[65] C. Brissot, M. Rosso, J.-N. Chazalviel, S. Lascaud, *Journal of the Electrochemical Society* **1999**, *146*(12), 4393–4400.

[66] J. Steiger, D. Kramer, R. Mönig, *Electrochimica Acta* **2014**, *136*, 529–536.

[67] J. Steiger, D. Kramer, R. Mönig, *Journal of Power Sources* **2014**, *261*, 112–119.

[68] J. K. Stark, Y. Ding, P. A. Kohl, *Journal of The Electrochemical Society* **2013**, *160*(9), D337–D342.

[69] M. Dollé, L. Sannier, B. Beaudoin, M. Trentin, J.-M. Tarascon, *Electrochemical and Solid-State Letters* **2002**, *5*(12), A286–A289.

[70] P. C. Howlett, D. R. MacFarlane, A. F. Hollenkamp, *Electrochemical and Solid-State Letters* **2004**, *7*(5), A97–A101.

[71] A. C. Luntz, B. D. McCloskey, *Nature Energy* **2017**, *2*, 17056.

[72] K. M. Abraham, Z. Jiang, *Journal of The Electrochemical Society* **1996**, *143*(1), 1–5.

[73] J. Christensen, P. Albertus, R. S. Sanchez-Carrera, T. Lohmann, B. Kozinsky, R. Liedtke, J. Ahmed, A. Kojic, *Journal of the Electrochemical Society* **2011**, *159*(2), R1–R30.

[74] K. G. Gallagher, S. Goebel, T. Greszler, M. Mathias, W. Oelerich, D. Eroglu, V. Srinivasan, *Energy & Environmental Science* **2014**, *7*(5), 1555–1563.

[75] C. O. Laoire, S. Mukerjee, K. Abraham, E. J. Plichta, M. A. Hendrickson, *The Journal of Physical Chemistry C* **2009**, *113*(46), 20127–20134.

[76] C. O. Laoire, S. Mukerjee, K. Abraham, E. J. Plichta, M. A. Hendrickson, *The Journal of Physical Chemistry C* **2010**, *114*(19), 9178–9186.

[77] L. Johnson, C. Li, Z. Liu, Y. Chen, S. A. Freunberger, P. C. Ashok, B. B. Praveen, K. Dholakia, J.-M. Tarascon, P. G. Bruce, *Nature Chemistry* **2014**, *6*(12), 1091–1099.

[78] K. Abraham, *Journal of The Electrochemical Society* **2015**, *162*(2), A3021–A3031.

[79] Y. Wang, Z. Liang, Q. Zou, G. Cong, Y.-C. Lu, *The Journal of Physical Chemistry C* **2016**, *120*(12), 6459–6466.

[80] Y.-C. Lu, Y. Shao-Horn, *The Journal of Physical Chemistry Letters* **2012**, *4*(1), 93–99.

[81] S. Kang, Y. Mo, S. P. Ong, G. Ceder, *Chemistry of Materials* **2013**, *25*(16), 3328–3336.

[82] S. Ganapathy, B. D. Adams, G. Stenou, M. S. Anastasaki, K. Goubitz, X.-F. Miao, L. F. Nazar, M. Wagemaker, *Journal of the American Chemical Society* **2014**, *136*(46), 16335–16344.

[83] B. D. McCloskey, A. Valery, A. C. Luntz, S. R. Gowda, G. M. Wallraff, J. M. Garcia, T. Mori, L. E. Krupp, *The Journal of Physical Chemistry Letters* **2013**, *4*(17), 2989–2993.

[84] S. A. Freunberger, Y. Chen, N. E. Drewett, L. J. Hardwick, F. Bardé, P. G. Bruce, *Angewandte Chemie International Edition* **2011**, *50*(37), 8609–8613.

[85] B. McCloskey, A. Speidel, R. Scheffler, D. Miller, V. Viswanathan, J. Hummelshøj, J. Nørskov, A. Luntz, *The Journal of Physical Chemistry Letters* **2012**, *3*(8), 997–1001.

[86] B. McCloskey, D. Bethune, R. Shelby, T. Mori, R. Scheffler, A. Speidel, M. Sherwood, A. Luntz, *The Journal of Physical Chemistry Letters* **2012**, *3*(20), 3043–3047.

[87] N. Tsiouvaras, S. Meini, I. Buchberger, H. A. Gasteiger, *Journal of The Electrochemical Society* **2013**, *160*(3), A471–A477.

[88] M. Piana, J. Wandt, S. Meini, I. Buchberger, N. Tsiouvaras, H. A. Gasteiger, *Journal of The Electrochemical Society* **2014**, *161*(14), A1992–A2001.

[89] M. M. Ottakam Thotiyl, S. A. Freunberger, Z. Peng, P. G. Bruce, *Journal of the American Chemical Society* **2012**, *135*(1), 494–500.

[90] D. Kwabi, N. Ortiz-Vitoriano, S. Freunberger, Y. Chen, N. Imanishi, P. Bruce, Y. Shao-Horn, *MRS Bulletin* **2014**, *39*(05), 443–452.

[91] A. C. Luntz, B. D. McCloskey, *Chemical Reviews* **2014**, *114*(23), 11721–11750.

[92] Y. Chen, S. A. Freunberger, Z. Peng, O. Fontaine, P. G. Bruce, *Nature Chemistry* **2013**, *5*(6), 489–494.

[93] M. Noked, M. A. Schroeder, A. J. Pearse, G. W. Rubloff, S. B. Lee, *Journal of Physical Chemistry Letters* **2016**, *7*(2), 211–215.

[94] S. A. Freunberger, Y. Chen, Z. Peng, J. M. Griffin, L. J. Hardwick, F. Bardé, P. Novák, P. G. Bruce, *Journal of the American Chemical Society* **2011**, *133*(20), 8040–8047.

[95] B. J. Bergner, A. Schürmann, K. Peppler, A. Garsuch, J. Janek, *Journal of the American Chemical Society* **2014**, *136*(42), 15054–15064.

[96] Z. Peng, S. A. Freunberger, Y. Chen, P. G. Bruce, *Science* **2012**, *337*(6094), 563–566.

[97] W. Zhang, Y. Shen, D. Sun, Z. Huang, Y. Huang, *Advanced Energy Materials* **2017**, (1602938 (1), 1–16.

[98] K. M. Abraham, *ECS Transactions* **2008**, *3*(42), 67–71.

[99] F. Mizuno, S. Nakanishi, Y. Kotani, S. Yokoishi, H. Iba, *Electrochemistry* **2010**, *78*(5), 403–405.

[100] Y.-C. Lu, H. A. Gasteiger, E. Crumlin, R. McGuire, Y. Shao-Horn, *Journal of the Electrochemical Society* **2010**, *157*(9), A1016–A1025.

[101] Y.-C. Lu, H. A. Gasteiger, M. C. Parent, V. Chiloyan, Y. Shao-Horn, *Electrochemical and Solid-State Letters* **2010**, *13*(6), A69–A72.

[102] M. Eswaran, N. Munichandraiah, L. Scanlon, *Electrochemical and Solid-State Letters* **2010**, *13*(9), A121–A124.

[103] B. D. McCloskey, D. Bethune, R. Shelby, G. Girishkumar, A. Luntz, *The Journal of Physical Chemistry Letters* **2011**, *2*(10), 1161–1166.

[104] D. Aurbach, M. Daroux, P. Faguy, E. Yeager, *Journal of Electroanalytical Chemistry and Interfacial Electrochemistry* **1991**, *297*(1), 225–244.

[105] C. Zhan, J. Lu, A. J. Kropf, T. Wu, A. N. Jansen, Y.-K. Sun, X. Qiu, K. Amine, *Nature Communications* **2013**, *4*.

[106] I. A. Shkrob, A. J. Kropf, T. W. Marin, Y. Li, O. G. Poluektov, J. Niklas, D. P. Abraham, *The Journal of Physical Chemistry C* **2014**, *118*(42), 24335–24348.

[107] M. Roberts, J. J. Biendicho, S. Hull, P. Beran, T. Gustafsson, G. Svensson, K. Edström, *Journal of Power Sources* **2013**, *226*, 249–255.

[108] R. Gerald II, J. Sanchez, C. Johnson, R. Klingler, J. Rathke, *Journal of Physics: Condensed Matter* **2001**, *13*(36), 8269.

[109] C. von Lüders, V. Zinth, S. V. Erhard, P. J. Osswald, M. Hofmann, R. Gilles, A. Jossen, *Journal of Power Sources* **2017**, *342*, 17–23.

[110] F. Blanc, M. Leskes, C. P. Grey, *Accounts of Chemical Research* **2013**, *46*(9), 1952–1963.

[111] H. Ge, T. Aoki, N. Ikeda, S. Suga, T. Isobe, Z. Li, Y. Tabuchi, J. Zhang, *Journal of The Electrochemical Society* **2017**, *164*(6), A1050–A1060.

[112] P. Harks, F. Mulder, P. Notten, *Journal of Power Sources* **2015**, *288*, 92–105.

[113] O. Pecher, J. Carretero-González, K. J. Griffith, C. P. Grey, *Chemistry of Materials* **2016**.

[114] M. U. Patel, R. Demir-Cakan, M. Morcrette, J.-M. Tarascon, M. Gaberscek, R. Dominko, *ChemSusChem* **2013**, *6*(7), 1177–1181.

[115] A. Deb, U. Bergmann, S. Cramer, E. J. Cairns, *Electrochimica Acta* **2005**, *50*(25), 5200–5207.

[116] J. Nelson, S. Misra, Y. Yang, A. Jackson, Y. Liu, H. Wang, H. Dai, J. C. Andrews, Y. Cui, M. F. Toney, *Journal of the American Chemical Society* **2012**, *134*(14), 6337–6343.

[117] S. Axnanda, E. J. Crumlin, B. Mao, S. Rani, R. Chang, P. G. Karlsson, M. O. Edwards, M. Lundqvist, R. Moberg, P. Ross, et al., *Scientific Reports* **2015**, *5*, 9788.

[118] V. Zinth, C. von Lüders, M. Hofmann, J. Hattendorff, I. Buchberger, S. Erhard, J. Rebelo-Kornmeier, A. Jossen, R. Gilles, *Journal of Power Sources* **2014**, *271*, 152–159.

[119] D. Austen, P. Given, D. Ingram, M. Peover, *Nature* **1958**, *182*(4652), 1784–1786.

[120] R. Bagchi, A. Bond, F. Scholz, *Electroanalysis* **1989**, *1*(1), 1–11.

[121] L. Dunsch, *Journal of Solid State Electrochemistry* **2011**, *15*(7-8), 1631–1646.

[122] L. Zhuang, J. Lu, X. Ai, H. Yang, *Journal of Electroanalytical Chemistry* **1995**, *397*(1-2), 315–319.

[123] R. Bhattacharyya, B. Key, H. Chen, A. S. Best, A. F. Hollenkamp, C. P. Grey, *Nature Materials* **2010**, *9*(6), 504–510.

[124] F. Poli, J. S. Kshetrimayum, L. Monconduit, M. Letellier, *Electrochemistry Communications* **2011**, *13*(12), 1293–1295.

[125] L. Zhuang, J. Lu, *Review of Scientific Instruments* **2000**, *71*(11), 4242–4248.

[126] S. Meini, M. Piana, N. Tsiouvaras, A. Garsuch, H. A. Gasteiger, *Electrochemical and Solid-State Letters* **2012**, *15*(4), A45–A48.

[127] R. Allendoerfer, G. Martinchek, S. Bruckenstein, *Analytical Chemistry* **1975**, *47*(6), 890–894.

[128] I. Rosenthal, C. M. Krishna, G. Yang, T. Kondo, P. Riesz, *FEBS Letters* **1987**, *222*(1), 75–78.

[129] M. Cuisinier, P.-E. Cabelguen, S. Evers, G. He, M. Kolbeck, A. Garsuch, T. Bolin, M. Balasubramanian, L. F. Nazar, *The Journal of Physical Chemistry Letters* **2013**, *4*(19), 3227–3232.

[130] T. A. Pascal, K. H. Wujcik, J. Velasco-Velez, C. Wu, A. A. Teran, M. Kapilashrami, J. Cabana, J. Guo, M. Salmeron, N. Balsara, et al., *The Journal of Physical Chemistry Letters* **2014**, *5*(9), 1547–1551.

[131] Y. Gorlin, A. Siebel, M. Piana, T. Huthwelker, H. Jha, G. Monsch, F. Kraus, H. A. Gasteiger, M. Tromp, *Journal of The Electrochemical Society* **2015**, *162*(7), A1146–A1155.

[132] Y. Gorlin, M. U. Patel, A. Freiberg, Q. He, M. Piana, M. Tromp, H. A. Gasteiger, *Journal of The Electrochemical Society* **2016**, *163*(6), A930–A939.

[133] M. A. Rodriguez, D. Ingersoll, D. Doughty, *Adv. X-Ray Anal* **2002**, *45*, 182–187.

[134] M. Fleckenstein, O. Bohlen, M. A. Roscher, B. Bäker, *Journal of Power Sources* **2011**, *196*(10), 4769–4778.

[135] T. Waldmann, S. Gorse, T. Samtleben, G. Schneider, V. Knoblauch, M. Wohlfahrt-Mehrens, *Journal of The Electrochemical Society* **2014**, *161*(10), A1742–A1747.

[136] A. Senyshyn, M. J. Mühlbauer, O. Dolotko, M. Hofmann, H. Ehrenberg, *Scientific Reports* **2015**, *5:18380*, 1–9.

[137] M. A. Rodriguez, D. Ingersoll, S. C. Vogel, D. J. Williams, *Electrochemical and Solid-State Letters* **2004**, *7*(1), A8–A10.

[138] N. Sharma, V. K. Peterson, M. M. Elcombe, M. Avdeev, A. J. Studer, N. Blagojevic, R. Yusoff, N. Kamarulzaman, *Journal of Power Sources* **2010**, *195*(24), 8258–8266.

[139] L. Cai, K. An, Z. Feng, C. Liang, S. J. Harris, *Journal of Power Sources* **2013**, *236*, 163–168.

[140] R. Gilles, G. Artus, J. Saroun, H. Boysen, H. Fuess, *Physica B: Condensed Matter* **2000**, *276*, 87–88.

[141] M. Hofmann, R. Schneider, G. Seidl, J. Rebelo-Kornmeier, R. Wimpory, U. Garbe, H.-G. Brokmeier, *Physica B: Condensed Matter* **2006**, *385*, 1035–1037.

[142] A. Senyshyn, M. Mühlbauer, K. Nikolowski, T. Pirling, H. Ehrenberg, *Journal of Power Sources* **2012**, *203*, 126–129.

[143] O. Dolotko, A. Senyshyn, M. Mühlbauer, K. Nikolowski, F. Scheiba, H. Ehrenberg, *Journal of The Electrochemical Society* **2012**, *159*(12), A2082–A2088.

[144] A. Senyshyn, M. Mühlbauer, O. Dolotko, M. Hofmann, T. Pirling, H. Ehrenberg, *Journal of Power Sources* **2014**, *245*, 678–683.

[145] Y. S. Cohen, Y. Cohen, D. Aurbach, *The Journal of Physical Chemistry B* **2000**, *104*(51), 12282–12291.

[146] K. Nishikawa, T. Mori, T. Nishida, Y. Fukunaka, M. Rosso, T. Homma, *Journal of The Electrochemical Society* **2010**, *157*(11), A1212–A1217.

[147] D. R. Ely, R. E. García, *Journal of The Electrochemical Society* **2013**, *160*(4), A662–A668.

[148] E. Markevich, G. Salitra, F. Chesneau, M. Schmidt, D. Aurbach, *ACS Energy Letters* **2017**.

[149] M. C. Smart, B. L. Lucht, S. Dalavi, F. C. Krause, B. V. Ratnakumar, *Journal of The Electrochemical Society* **2012**, *159*(6), A739–A751.

[150] C. Uhlmann, J. Illig, M. Ender, R. Schuster, E. Ivers-Tiffée, *Journal of Power Sources* **2015**, *279*, 428–438.

[151] J. Burns, D. Stevens, J. Dahn, *Journal of The Electrochemical Society* **2015**, *162*(6), A959–A964.

[152] M. Zier, F. Scheiba, S. Oswald, J. Thomas, D. Goers, T. Scherer, M. Klose, H. Ehrenberg, J. Eckert, *Journal of Power Sources* **2014**, *266*, 198–207.

[153] N. Mahne, B. Schafzahl, C. Leypold, M. Leypold, S. Grumm, A. Leitgeb, G. A. Strohmeier, M. Wilkening, O. Fontaine, D. Kramer, C. Slugovc, S. M. Borisov, S. A. Freunberger, *Nature Energy* **2017**, *2*, 1–9.

[154] S. Komaba, N. Kumagai, Y. Kataoka, *Electrochimica Acta* **2002**, *47*(8), 1229–1239.

[155] P. Hartmann, C. L. Bender, M. Vračar, A. K. Dürr, A. Garsuch, J. Janek, P. Adelhelm, *Nature Materials* **2013**, *12*(3), 228–232.

[156] C. Schweitzer, R. Schmidt, *Chemical Reviews* **2003**, *103*(5), 1685–1758.

Acknowledgments

First of all I want to thank my PhD supervisor Prof. Hubert A. Gasteiger for the great opportunity to work in his group for the last few years and the invaluable support and guidance throughout this time. You created a unique scientific environment at the Chair of Technical Electrochemistry, both with respect to the available equipment and the open and inspiring work atmosphere. Furthermore, I want to thank Michele Piana for first recruiting me in the course of my Master's Thesis back in 2012 and Veronika Pichler for administrative assistance.

I thank all current group members at the Chair for Technical Electrochemistry for the great collaboration, helpful discussions and your part in the above mentioned work atmosphere. I want to especially mention the outstanding young scientist Anna Freiberg for her contribution to several of my projects. I also want to include former group members Stefano Meini, Cuneyt Kavakli, Rebecca Bernhard, Uta Schwenke, Juan Herranz, Nikolaos Tsiouvaras, Johannes Hattendorff, Irmgard Buchberger, Rowena Thomas and Yelena Gorlin. Special thanks goes to Cyril Marino who shared his vast hands on experience in battery research with me.

I want to thank my former students Hartmut Rauch, Felix Riewald and Daniel Göhl for their passionate work during their Bachelor and Master's Theses projects.

I further want to thank all external partners for the successful collaborations. Special thanks goes to Prof. Rüdiger-A. Eichel, Prof. Josef Granwehr and Peter Jakes from the Institute of Energy and Climate Research - Fundamental Electrochemistry (IEK-9) at the Forschungszentrum Jülich (Germany) for countless nights of EPR experiments and data analysis. I also thank Moniek Tromp from the Van't Hoff Institute for Molecular Sciences at the University of Amsterdam (Netherlands), Ralph Gilles and his team at the Heinz Maier-Leibnitz Zentrum (MLZ) in Munich (Germany) and Sebastian Schebesta from the VW-VM Forschungsgesellschaft mbH & Co. KG (Ellwangen, Germany).

Furthermore, I thank Alexander Ogrodnik (Technical University of Munich) and Ethan Crumlin from the Advanced Light Source at the Lawrence Berkeley National Laboratory (Berkeley, USA) for the exciting joint research projects. I also thank Prof. Yi-Chun Lu (Chinese University of Hongkong) for her help with the *operando* EPR cell development and interesting discussions on all aspects of lithium-oxygen batteries.

I also want to thank Jake Christensen, Timm Lohmann, Paul Albertus, Christina

Johnston, Reinhardt Klein and Ram Subbaraman for introducing me to lithium-ion battery research at the Robert Bosch LLC Research Center in Palo Alto (USA) back in 2013.
Last but not least, I gratefully acknowledge financial support by the Bavarian Ministry of Economic Affairs and Media, Energy and Technology under the auspices of the EEBatt project. I also thank the German Academic Exchange Service (DAAD) and the ECS Europe Section for conference travel grants for the 2016 ECS PRiME in Honolulu (USA) and the 231st ECS meeting in New Orleans (USA).